

MHD STABILITY LIMITS IN THE TCV TOKAMAK

THÈSE N° 2399 (2001)

PRÉSENTÉE AU DÉPARTEMENT DE PHYSIQUE

ÉCOLE POLYTECHNIQUE FÉDÉRALE DE LAUSANNE

POUR L'OBTENTION DU GRADE DE DOCTEUR ÈS SCIENCES

PAR

Holger REIMERDES

Diplom-Physiker, Universität Bayreuth, Allemagne
et de nationalité allemande

acceptée sur proposition du jury:

Dr A. Pochelon, directeur de thèse
Prof. R. Chawla, rapporteur
Prof. F. Porcelli, rapporteur
Dr O. Sauter, rapporteur
Prof. M. Q. Tran, rapporteur
Prof. H. Zohm, rapporteur

Lausanne, EPFL
2001

*“Par une belle matinée de mai, une svelte amazone,
montée sur une somptueuse jument alezane, parcourait,
au milieu des fleurs, les allées du bois ...”*

J. Grand dans “La Peste” de A. Camus

Version abrégée

Les instabilités magnétohydrodynamiques (MHD) peuvent limiter les performances du tokamak et dégrader le confinement du plasma. Le *Tokamak à Configuration Variable* (TCV), unique pour sa capacité de produire une large variété de formes de plasma, a été utilisée pour analyser diverses instabilités et pour comparer leur comportement aux prédictions théoriques. Ces instabilités sont des perturbations du champ magnétique qui s'étendent habituellement jusqu'au bord du plasma où elles peuvent être détectées avec des bobines magnétiques. Des anneaux de sondes magnétiques, installés à l'intérieur de la chambre à vide de TCV, permettent l'observation de ces fluctuations magnétiques. La structure et l'évolution temporelle des modes de déformation cohérents sont extraites en utilisant plusieurs méthodes numériques.

En plus de l'installation du diagnostique magnétique et de la mise en place de méthodes d'analyse des signaux, les thèmes de cette thèse se concentrent sur quatre instabilités qui imposent des limites de stabilité locales et globales. Toutes ces instabilités sont pertinentes au fonctionnement d'un réacteur à fusion et une compréhension profonde de leur comportement est nécessaire pour l'optimisation d'un tel réacteur.

Les dents de scie, qui sont des oscillations de relaxation centrales communes à la plupart des scénarios standards de tokamak, ont un effet important sur les paramètres centraux du plasma. Dans TCV, des balayages systématiques de la forme du plasma ont montré une forte dépendance du comportement des dents de scie avec l'élongation κ et la triangularité δ , les décharges à haut κ et à bas δ menant à des dents de scie plus courtes et des chutes de dents de scie plus petites. Cette dépendance sur la forme est augmentée par l'application de chauffage électronique cyclotronique (ECH) au centre, celui-ci augmentant ou diminuant la période des dents de scie selon la forme de plasma. La réponse à la puissance de chauffage supplémentaire est déterminée par le rôle de la MHD idéale ou résistive dans le déclenchement de la chute de la dent de scie. Pour les formes de plasmas où le chauffage additionnel central raccourcit les dents de scie, la basse limite expérimentale du gradient de pression à l'intérieur de la surface $q = 1$ est conforme aux prédictions de la MHD idéale. La diminution observée de cette limite avec l'élongation est également en accord qualitatif avec la théorie MHD idéale.

Les *edge localised modes* (ELMs), observés dans les décharges ohmiques de confinement amélioré de TCV, sont précédés par des oscillations magnétiques cohérentes. Les précurseurs des petits ELMs, supposés être de *type III*, et les précurseurs des plus grands ELMs, précédemment désignés sous le nom de *large* ELMs de TCV, montrent les mêmes caractéristiques, ce qui permet d'identifier ces deux genres d'ELMs comme étant du même

type III, selon la classification en usage. La structure poloïdale et toroïdale du mode est compatible avec une surface de flux résonnante proche du bord de plasma. Au contraire des modes MHD conventionnels, qui démarrent simultanément partout le long du tore, ces précurseurs démarrent à une position toroïdale aléatoire d'où ils croissent en amplitude et en étendue toroïdale jusqu'à l'envahissement de la totalité de la circonférence toroïdale. De ce fait, l'asymétrie causant la localisation toroïdale du précurseur d'ELM doit être intrinsèque au plasma. Les mesures de rayons X mous prouvent que le précurseur localisé coïncide toujours avec la présence d'un mode $m = 1$ central, qui peut habituellement être associé au mode qui précède ou succède à la dent de scie. Une comparaison entre les phases indique une corrélation avec le maximum du mode central qui précède la position toroïdale du précurseur d'ELM et suggère, en conséquence, un couplage jusqu'ici inaperçu entre les modes centraux et les ELMs.

Les plasmas allongées promettent plusieurs avantages, parmi lesquels des limites plus élevées de beta et du courant. Pendant des expériences consacrées à une augmentation de l'élongation du plasma, une nouvelle limite disruptive, bien au-dessous la limite de courant conventionnelle correspondant à $q_a > 2$, est rencontrée pour $\kappa > 2.3$. Cette limite, qui est précédée par un mode de type "kink", s'avère conforme aux calculs de stabilité MHD idéale. Les observations de TCV fournissent, donc la première confirmation expérimentale d'une déviation à la loi d'échelle linéaire de Troyon, la limite de beta, à haute élongation et à haut courant normalisé, une déviation prévue il y a déjà plus de 10 ans.

En plus de la limite de beta idéale, plusieurs autres événements MHD ont été observés dans les plasmas fortement allongés. D'une part, le mode axisymétrique qui se manifeste par des événements de déplacement verticaux impose une limite de courant inférieure. Cette limite opérationnelle est en bon accord avec le taux de croissance théorique du mode axisymétrique. D'autre part, on observe parfois des disruptions mineures provoquées par des bouffées de modes de déchirement localisés près de la surface $q = 1$, qui sont déstabilisés par des profils de courant central plat, typique des plasmas fortement allongés.

Les modes de déchirement néoclassiques (NTMs), qui sont observés limiter le beta dans un certain nombre de tokamaks, résultent d'une perturbation hélicoïdale du courant provoquée par un îlot germe (*seed island*) préexistant. Les NTMs $m/n = 2/1$ ont été identifiés dans des décharges de TCV qui se caractérisent par une basse collisionnalité électronique ν_{e*} , une collisionnalité ionique ν_* moyenne, une valeur moyenne de beta et des profils de pression et de courant fortement piqués. Contrairement aux autres tokamaks, où les dents de scie, les *fishbones* ou les ELMs peuvent produire des îlots germe, dans TCV, l'îlot germe est fourni par un mode de déchirement conventionnel. L'îlot montre clairement une phase de croissance conventionnelle et une phase néoclassique. Les résultats de TCV fournissent les premières observations claires d'un tel mécanisme de déclenchement qui pourrait également expliquer la présence des NTMs "sans trigger"

observés dans d'autres expériences. La croissance lente de l'îlot germe permet également une mesure de la largeur critique d'îlot w_{crit} , qui est observée augmenter avec la densité.

En conclusion, plusieurs limites de stabilité globales et locales sont analysées. Ces instabilités peuvent limiter le gradient de pression et de ce fait, les performances du plasma. Les résultats présentés indiquent plusieurs caractéristiques précédemment inaperçues sur des instabilités pourtant communément observées. Puisque la plupart de ces nouvelles observations peuvent être expliquées par la théorie, elles en améliorent les capacités prédictives, ce qui a son importance en regard des grandes expériences à venir. Les expériences sur TCV ont également montré des interactions nouvelles entre différentes instabilités, ce qui ajoute à la complexité déjà étoffée des phénomènes MHD dans les plasmas de fusion.

Abstract

Magnetohydrodynamic (MHD) instabilities can limit the performance and degrade the confinement of tokamak plasmas. The *Tokamak à Configuration Variable* (TCV), unique for its capability to produce a variety of poloidal plasma shapes, has been used to analyse various instabilities and compare their behaviour with theoretical predictions. These instabilities are perturbations of the magnetic field which usually extend to the plasma edge where they can be detected with magnetic pick-up coils as magnetic fluctuations. A spatially dense set of magnetic probes, installed inside the TCV vacuum vessel, allows for a fast observation of these fluctuations. The structure and temporal evolution of coherent modes is extracted using several numerical methods.

In addition to the setup of the magnetic diagnostic and the implementation of analysis methods, the subject matter of this thesis focuses on four instabilities which impose local and global stability limits. All of these instabilities are relevant for the operation of a fusion reactor and a profound understanding of their behaviour is required in order to optimise the performance of such a reactor.

Sawteeth, which are central relaxation oscillations common to most standard tokamak scenarios, have a significant effect on central plasma parameters. In TCV, systematic scans of the plasma shape have revealed a strong dependence of their behaviour on elongation κ , and triangularity δ , with high κ and low δ leading to shorter sawteeth with smaller crashes. This shape dependence is increased by applying central electron cyclotron heating (ECH), which increases or decreases the sawtooth period, depending on the plasma shape. The response to additional heating power is determined by the role of ideal or resistive MHD in triggering the sawtooth crash. For plasma shapes where additional heating and consequently, a faster increase of the central pressure shortens the sawteeth, the low experimental limit of the pressure gradient within the $q = 1$ surface is consistent with ideal MHD predictions. The observed decrease of this limit with elongation is also in qualitative agreement with ideal MHD theory.

Edge localised modes (ELMs), occurring in TCV Ohmic high-confinement mode discharges, were observed to be preceded by coherent magnetic oscillations. The precursors prior to small ELMs, believed to be of *type III*, and prior to larger ELMs, previously referred to as TCV *large* ELMs, show the same characteristics, which allows for an identification of both ELMs to be of *type III* according to the usual classification scheme. The detected poloidal and toroidal mode structures are consistent with a resonant flux surface close to the plasma edge. Unlike conventional MHD modes, these precursors start at a random toroidal location and then grow in amplitude and toroidal extent until they

encompass the whole toroidal circumference. Thus, the asymmetry causing and maintaining the toroidal localisation of the ELM precursor, must be intrinsic to the plasma. Soft X-ray measurements show that the localised precursor always coincides with a central $m = 1$ mode, which can usually be associated with the sawtooth pre- or postcursor mode. A comparison of the phases indicates a correlation with the maximum of the central mode preceding the toroidal location of the ELM precursor and, therefore, a hitherto unobserved coupling between central modes and ELMs.

Highly elongated plasmas promise several advantages, among them higher current and beta limits. During TCV experiments dedicated to an increasing of the plasma elongation, a new disruptive current limit, at values well below the conventional current limit corresponding to $q_a > 2$, was encountered for $\kappa > 2.3$. This limit, which is preceded by a kink-type mode, is found to be consistent with ideal MHD stability calculations. The TCV observations, therefore, provide the first experimental confirmation of a deviation of the linear Troyon-scaling of the ideal beta limit with normalised current at high elongation, which was predicted over 10 years ago.

In addition to the ideal beta limit, several other MHD events are observed in highly elongated plasmas. The axisymmetric mode causes vertical displacement events and thereby, imposes a lower current limit. This operational limit is in good agreement with theoretical predictions of the growth rate of the axisymmetric mode. Furthermore, minor disruption are occasionally observed. They are caused by bursts of tearing modes located close to the $q = 1$ surface, which are destabilised by flat central current profiles, typical for highly elongated plasmas.

Neoclassical tearing modes (NTMs), which have been observed to limit the achievable beta in a number of tokamaks, arise from a helical perturbation of the bootstrap current caused by an existing seed island. Neoclassical $m/n = 2/1$ tearing modes have been identified in TCV discharges which are characterised by a low electron collisionality ν_{e*} , a medium ion collisionality ν_{*} , a medium value of beta and strongly peaked pressure and current profiles. In contrast to other tokamak experiments, where sawteeth, fishbones or ELMs generate the seed island, the required seed island is provided by a conventional tearing mode. The island clearly shows a conventional and a neoclassical growth phase. The TCV results provide the first clear observations of such a trigger mechanism which could also explain the occurrence of “triggerless” NTMs observed in other experiments. The slowly growing seed island also allows a measurement of the critical seed island width w_{crit} , which is observed to increase with increasing density.

In conclusion, several local and a global stability limits are analysed. These instabilities can limit the pressure gradient and thereby, the performance of the plasma. The presented results reveal several previously unobserved features of commonly observed instabilities. Since the most of the new observations can be explained by theory, they improve the

predictive capabilities with respect to new experiments. The experiments have also shown some new interactions among different instabilities, which add to the already crowded complexities of MHD phenomena in fusion plasmas.

Contents

1	Introduction	1
1.1	Nuclear fusion	1
1.1.1	Magnetic confinement	3
1.1.2	Tokamak principle	3
1.1.3	Plasma heating	7
1.1.4	Power plant concept	9
1.2	Motivation for the thesis	11
1.3	Outline of the thesis	12
2	Magnetohydrodynamic theory	15
2.1	MHD equations	15
2.2	Ideal MHD	17
2.2.1	Frozen flux	18
2.2.2	Tokamak equilibrium	18
2.2.3	Stability analysis	20
2.3	Ideal instabilities	22
2.3.1	Pressure driven modes	22
2.3.2	Current driven modes	25
2.3.3	Beta limit	28
2.3.4	Axisymmetric mode	28
2.4	Resistive Instabilities	28
2.4.1	Magnetic Islands	29
2.4.2	Tearing modes	31
2.4.3	Resistive internal kink mode	33
3	The TCV experiment	35
3.1	Tokamak	35
3.1.1	Plasma shaping and control	36
3.1.2	Plasmas	38
3.1.3	First wall	38

3.2	Electron cyclotron heating system	40
3.3	Diagnostics	41
3.3.1	Far-infrared interferometer	42
3.3.2	Thomson scattering	43
3.3.3	Soft X-ray emissivity measurements	44
3.4	Equilibrium reconstruction	45
3.5	Concluding remarks	47
4	Fast magnetic fluctuation diagnostic	49
4.1	Probe arrangement	49
4.2	Magnetic probe	51
4.2.1	Construction	51
4.2.2	Calibration	52
4.2.3	Frequency response	53
4.3	Signal processing	57
4.3.1	Amplifying chain	57
4.3.2	Acquisition	58
4.4	Concluding remarks	58
5	Magnetic fluctuation analysis	61
5.1	Perturbation of the magnetic field	61
5.1.1	Decomposition into modes	61
5.1.2	Plasma rotation	62
5.1.3	Geometry of magnetic field lines	63
5.2	Numerical techniques for the mode analysis	64
5.2.1	Temporal analysis	64
5.2.2	Spatial analysis	67
5.2.3	Spatiotemporal analysis	69
5.3	Modelling of magnetic islands	71
5.3.1	Perturbation current density	72
5.3.2	Reconstruction of the magnetic perturbation	73
5.3.3	Identification of the experimental mode structure	76
5.4	Island width	78
5.4.1	Cylindrical approximation	78
5.4.2	Reconstruction of the island geometry	79
5.4.3	Confinement degradation	82
5.5	Concluding remarks	82

6	Sawtooth oscillations	83
6.1	Introduction into sawteeth	83
6.2	Sawtooth period and crash amplitude	84
6.3	Density dependence of sawtooth instability	85
6.4	Shape dependence of sawtooth instability	86
6.4.1	Experiment	86
6.4.2	Variations of sawtooth characteristics	89
6.4.3	Comparison with a sawtooth model	91
6.4.4	Shape dependence of ideal central beta limit	95
6.5	Concluding remarks	97
7	Edge localised modes	99
7.1	Introduction into ELMs	99
7.1.1	Phenomenology	99
7.1.2	Current understanding	100
7.1.3	ELMs in TCV	101
7.2	Observation of precursor oscillations	101
7.2.1	Experiments	101
7.2.2	Toroidal measurements	102
7.2.3	Poloidal measurements	107
7.3	Toroidal asymmetry of the precursor	109
7.3.1	Toroidal mode structure	109
7.3.2	Toroidal asymmetry	110
7.4	Concluding remarks	112
8	Stability limits in highly elongated plasmas	115
8.1	Introduction into elongated plasmas	115
8.1.1	Properties of elongated plasmas	115
8.1.2	High elongation in TCV	116
8.2	MHD activity in highly elongated plasmas	117
8.2.1	Vertical displacement events	118
8.2.2	Minor disruptions	120
8.2.3	Mode disruptions	121
8.3	MHD stability in highly elongated plasmas	121
8.3.1	Operational diagram	122
8.3.2	Axisymmetric mode	123
8.3.3	Tearing modes	124
8.3.4	Ideal MHD stability limit	125

8.4	Concluding remarks	126
9	Neoclassical tearing modes	129
9.1	Introduction into neoclassical tearing modes	129
9.1.1	Bootstrap current	129
9.1.2	Neoclassical effects on the island growth	130
9.1.3	Triggering mechanisms	131
9.2	Observation of neoclassical tearing modes	132
9.2.1	Mode structure	133
9.2.2	Identification as a neoclassical tearing mode	136
9.3	Seeding by conventional tearing modes	137
9.4	Onset of neoclassical tearing modes in TCV	140
9.4.1	Discharge parameters and profiles	140
9.4.2	Critical island width	140
9.5	Concluding remarks	142
10	Conclusion and outlook	145

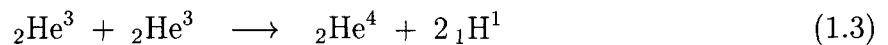
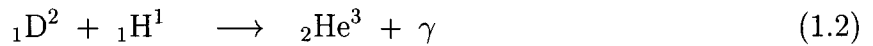
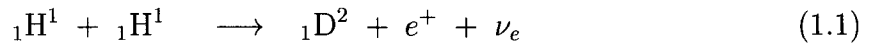
Chapter 1

Introduction

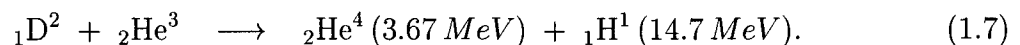
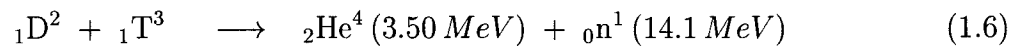
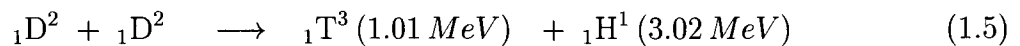
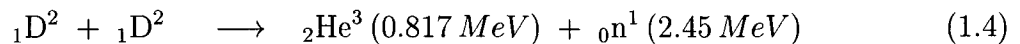
The development of nuclear fusion as a commercial source of energy has motivated researchers for several decades. It has the potential to offer a practically inexhaustible and inherently safe source of energy. It also has the advantage of not producing either greenhouse gases or long-lived radioactive waste.

1.1 Nuclear fusion

Nuclear fusion is the process which supplies the sun with energy. By a series of reactions namely,



hydrogen fuses to form helium. The nuclear rearrangement results in a reduction of the total mass and consequently in a release of energy. However, the β^+ -decay (equation 1.1) involves the weak interaction and therefore, has a very small cross-section. For an energy production on earth the weak interaction has to be avoided. Alternative reactions involve the heavier hydrogen isotopes deuterium (D) and tritium (T),



Of all of these reactions the D-T reaction (equation 1.6) has the highest cross section at the lowest deuteron energy (figure 1.1) and is, therefore, the most promising. Deuterium is a plentiful resource, its natural abundance in hydrogen being one part in 6700. The water of the oceans would provide enough deuterium for approximately 10^{11} times today's

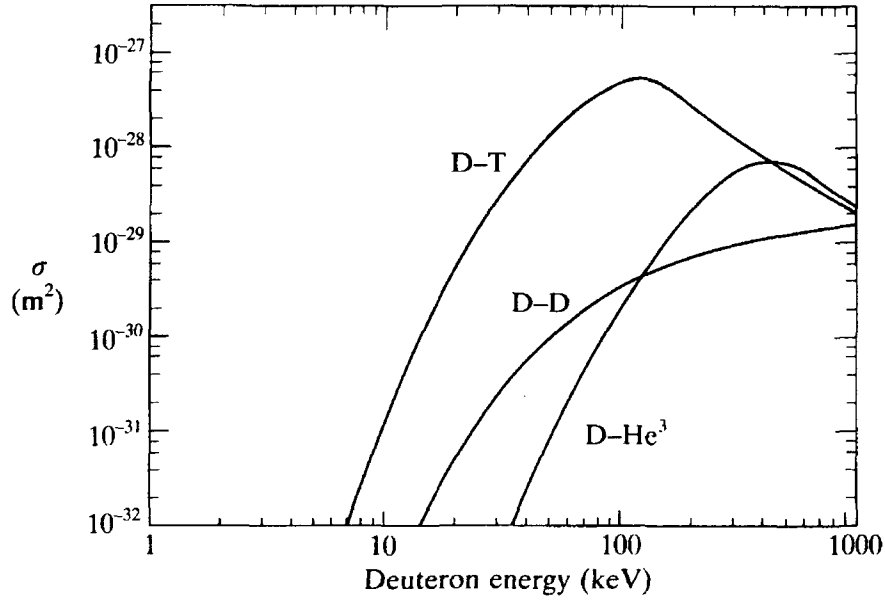
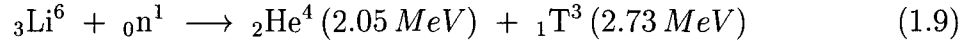
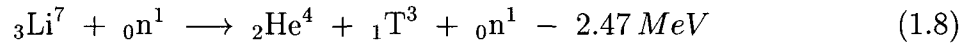


Figure 1.1: Cross-sections for the fusion reactions D-T, D-D and D-He³. For the D-D reaction the sum of the cross-sections of both reactions is given [1].

annual global electricity consumption [1]. However, unlike deuterium, tritium is virtually non existent in nature. It is radioactive with a half life of 12.3 years. It can, however, be produced from Lithium using the neutron induced fission reactions,



and could, therefore, be bred in the reactor. The relative abundance of the two Lithium isotopes Li⁶ and Li⁷ are 7.4% and 92.6% respectively. Natural resources of Lithium including the Lithium dissolved in sea water are estimated to meet the global energy consumption for 10⁶ – 10⁷ years [1]. Thus, nuclear fusion promises a practically inexhaustible source of energy.

A main obstacle for the fusion reaction is the Coulomb repulsion of the positively charged nuclei. To overcome the Coulomb barrier the nuclei require high kinetic energies. The cross-section for the D-T reaction reaches a maximum at a deuteron energy of 100 keV (see figure 1.1). Nevertheless, even at this high energy the probability of Coulomb scattering is much higher than that of a fusion reaction. Nuclei with sufficient energy have to be confined for many elastic collisions before they undergo a fusion reaction. This constraint precludes the use of high energy particle beams. The most promising solution is to heat a deuterium-tritium mixture until the thermal velocities are sufficiently high for fusion reactions to become likely. This process is referred to as thermonuclear fusion. The optimum temperature is lower than that corresponding to the maximum of the cross-section for the

D-T reaction since the required reactions occur in the high energy tail of the Maxwellian velocity distribution. The optimum energy of approximately 10 keV corresponds to 116 million degrees Celsius.

1.1.1 Magnetic confinement

At the temperatures required for fusion reactions the hydrogen isotopes are fully ionised. The electrostatic charge of the ions is neutralised by the presence of an equal number of electrons resulting in a neutral gas called plasma. In order to maintain this temperature the contact between the plasma and material walls has to be minimised. A possible method is to confine the plasma in a magnetic field. Owing to the Lorentz force, charged particles moving in a magnetic field follow helical trajectories around the magnetic field lines. The radial extent, or gyro radius, of this trajectory for a particle species s of mass m_s and charge q_s , is,

$$\rho_s = \frac{m_s v_{\perp}}{q_s B} \quad (1.10)$$

with v_{\perp} being the velocity perpendicular to the magnetic field B . For a homogeneous velocity distribution v_{\perp} can be expressed by the temperature, $v_{\perp} = (2kT/m_s)^{1/2}$. The particle motion perpendicular to the magnetic field is highly restricted, which is the basis of magnetic confinement, whereas there are no restrictions for the motion along the field lines. However, collisions among particles introduce a diffusive cross field transport and also give rise to a resistivity in the parallel direction.

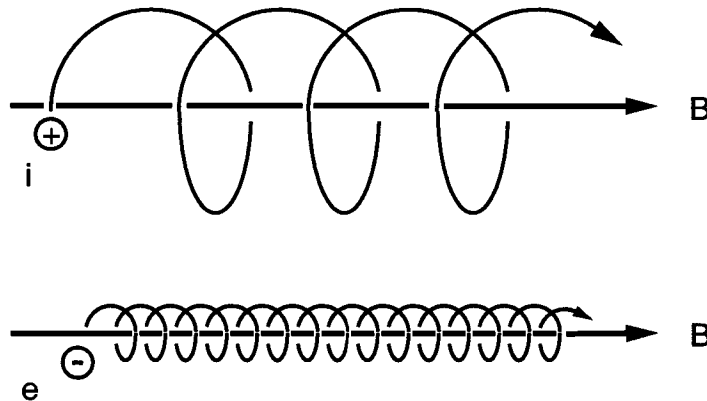


Figure 1.2: Trajectories of charged particles in a homogeneous magnetic field B .

1.1.2 Tokamak principle

A straight magnetic field configuration suffers from plasma losses at both ends, which can be avoided by closing the magnetic field lines. The simplest configuration with closed field lines is a torus. Unfortunately, a purely toroidal field is not homogeneous. The gradient

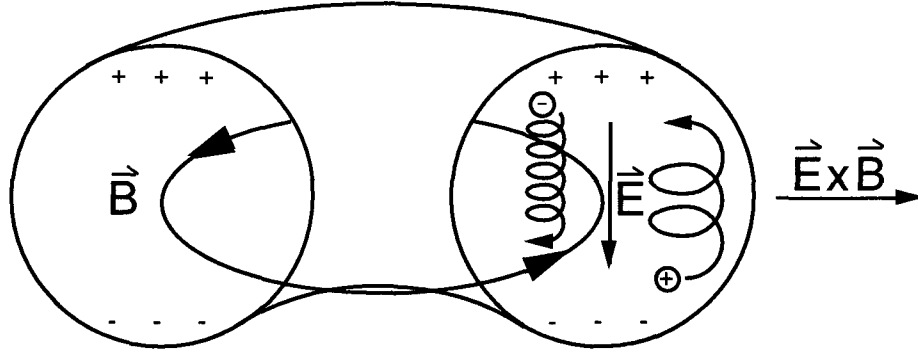


Figure 1.3: Particle drift motions in a toroidal magnetic field. The inhomogeneous field leads to a separation of charges. The resulting electrical field combined with the toroidal field cause an outward expulsion of the plasma particles.

of the field amplitude and the curvature of the field lines lead to drift motions of ions and electrons in opposite vertical directions, thus, resulting in a separation of charge and consequently, an electric field. The electric field is perpendicular to the magnetic field and causes an outward $\vec{E} \times \vec{B}$ -drift motion of the entire plasma (figure 1.3).

The outward drift motion can be avoided by twisting the magnetic field lines, so that each field line passes the upper and lower part of the torus. Then, an averaging along the path of particles, which follows the magnetic field line, leads to a cancelling of the vertical drift motions and avoids the build up of an electric field. Therefore, a combination of toroidal and poloidal magnetic fields can form a suitable trap for a plasma. In the so-called tokamak, the Russian acronym for “Toroidalnaja Kamera s Magnitnymi Katushkami” or “toroidal chamber with magnetic coils”, a toroidal plasma column is confined by a toroidal field B_{tor} , produced by external coils and a poloidal field B_{pol} , produced by a current that flows in the plasma. The toroidal geometry and the plasma pressure lead to a force trying to expand the plasma ring. This force is balanced by applying a vertical magnetic field B_v , which interacts with the toroidal plasma current to give an inward force. A schematic of the coil and field configuration is shown in figure 1.4. The original ideas were put forward in 1951 by Igor Tamm and Andrei Sacharov. The breakthrough of the tokamak concept was obtained in 1968 by research performed under the leadership of Lev Artsimovich at the Kurchatov Institute where a tokamak achieved much higher plasma temperatures than were reached in any other magnetic configuration at the time [2]. The confirmation of these results by a team from Culham Laboratory in 1969 triggered a boom in tokamak experiments.

The plasma current is usually induced by transformer action in which a central solenoid acts as the primary coil and the plasma ring as a single secondary winding (see figure 1.4).

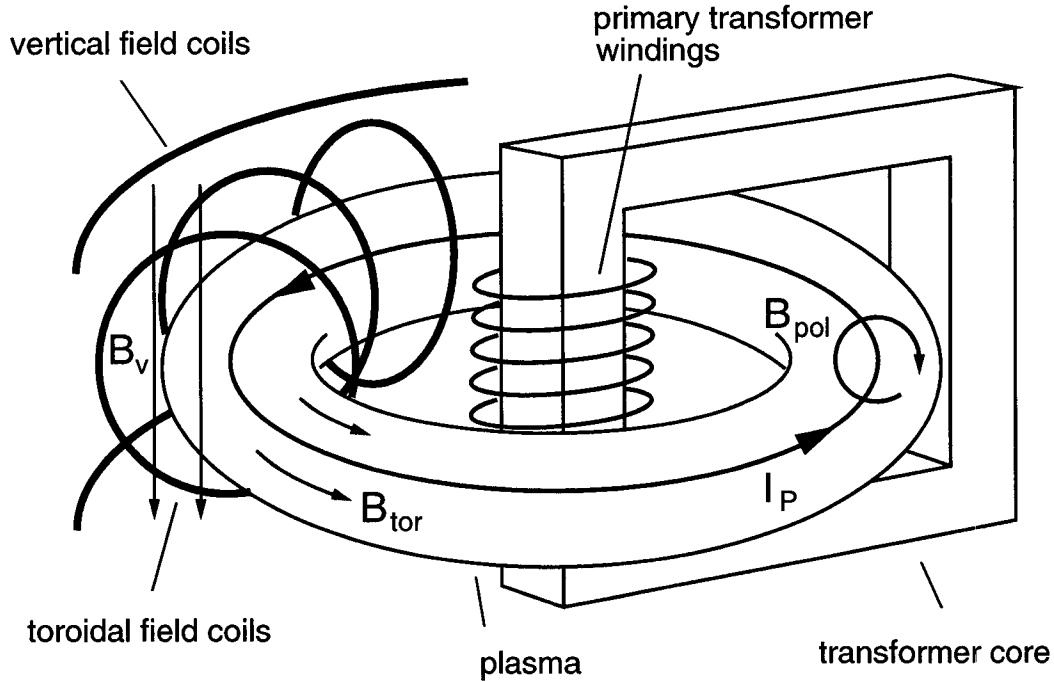


Figure 1.4: Schematic of the coil configuration of a tokamak. The plasma is the single secondary loop of a transformer. The induced plasma current is necessary for a stable confinement.

The tokamak configuration has the advantage of retaining the toroidal symmetry. On the other hand the induction of the plasma current allows only for pulsed operation. A major effort is being undertaken to develop alternative ways of driving the plasma current, such as wave or particle beam driven currents, which allow for a continuous tokamak operation.

The magnetic structure thus generated in a tokamak consists of an infinite set of nested toroidal magnetic surfaces, the so-called *flux surfaces*. The twist of the field lines in each surface is characterised by the safety factor q , where

$$q = \frac{\Delta\varphi}{2\pi}. \quad (1.11)$$

Here $\Delta\varphi$ denotes the change in the toroidal angle φ , associated with a change of 2π in poloidal angle when following the field lines on a magnetic surface. If $q = m/n$ with m and n being integers the magnetic field line joins up on itself after m toroidal and n poloidal rotations. These rational values of q play an important role in stability. A field line with $q = 2$ is illustrated in figure 1.5. The profile of q or equivalently B_{pol} or J , the current density, is also a crucial parameter for magnetohydrodynamic (MHD) stability (see chapter 2) as well as for the transport properties of the plasma.

In modern tokamaks additional poloidal field coils carrying a toroidal current allow the shaping of the poloidal plasma cross section. It has been shown that the plasma shape also influences the stability and transport properties of the plasma. Elongated and triangular

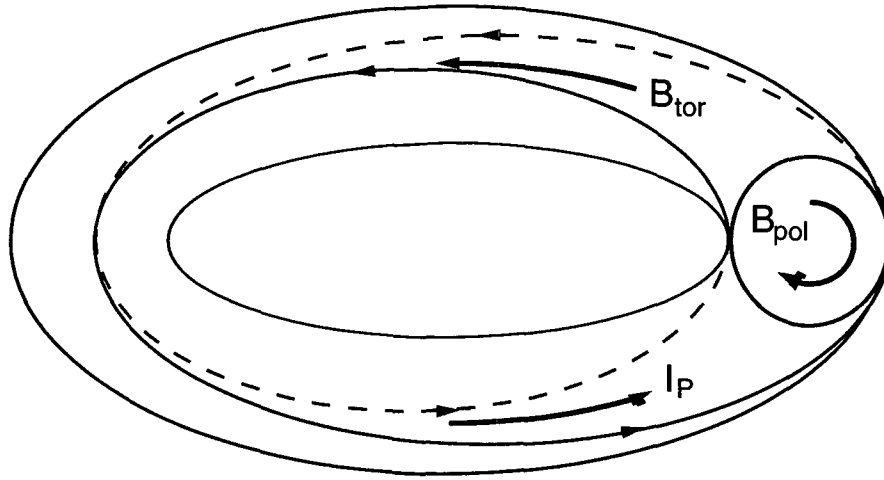


Figure 1.5: A schematic of a field line on a $q = 2$ magnetic surface.

plasma shapes, for example, show properties superior to those of circular plasmas. The definitions used in this work for the shape parameters elongation κ , and triangularity δ , are shown in figure 1.6. In addition to shaping the poloidal field coils are also used to control the position of the plasma.

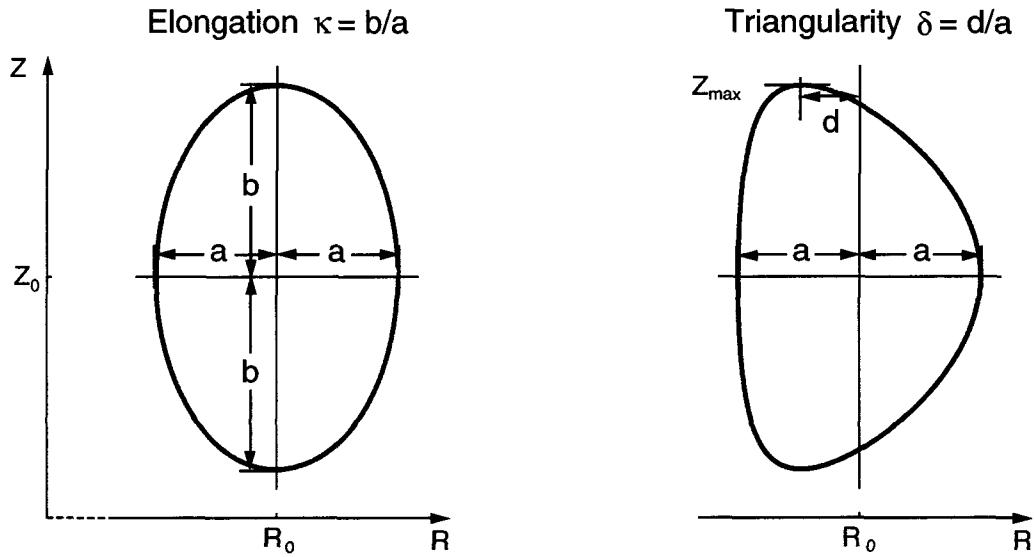


Figure 1.6: Definition of (a) the elongation κ , and (b) the triangularity δ , for a plasma with a minor radius a .

There are two main plasma configurations employed to separate the plasma from the vacuum vessel wall. In the first configuration the outer boundary of the plasma is defined using a material limiter as shown in figure 1.7. In the second configuration the magnetic field structure is modified to form a stagnation point, the so-called X-point and produce

a magnetic divertor (figure 1.7). The last closed flux surface (LCFS) in the limited configuration is in direct contact with the material wall. In the diverted configuration the contact between plasma and wall takes place on the divertor plates which accordingly have to be designed to withstand a large power flux. Since these divertor plates are further away from the hot plasma, diverted plasmas are generally cleaner than limited plasmas.

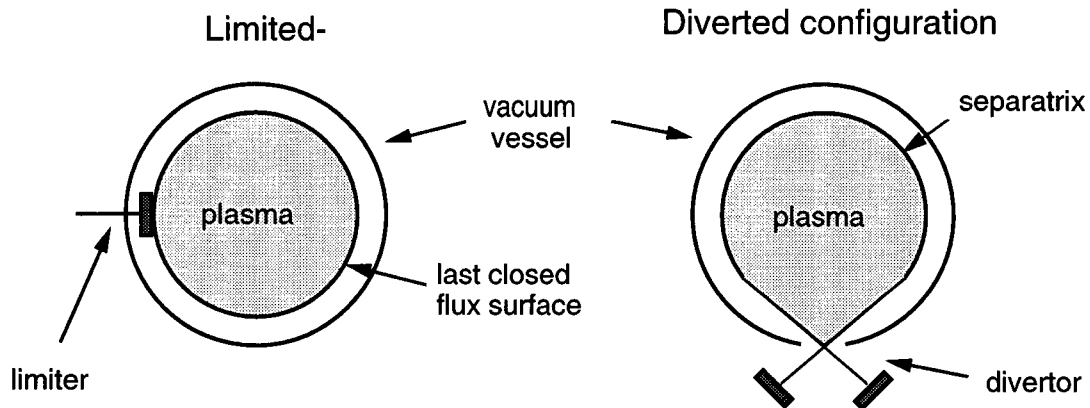


Figure 1.7: Separation of the plasma from the vessel wall in a limiter and a divertor configuration.

1.1.3 Plasma heating

Owing to the resistivity of the plasma the toroidal plasma current also heats the plasma with the Ohmic heating power density being,

$$p_{\Omega} = \eta j^2. \quad (1.12)$$

However, the plasma resistivity η , decreases with increasing temperature as $T_e^{-3/2}$. Since the current density j , is limited by MHD events (see section 2) a temperature can be reached where the efficiency of Ohmic heating becomes too low to be useful for further heating. This temperature increases with the toroidal magnetic field. However, the fields of today's supra-conducting magnets are not sufficient to obtain the temperatures required for fusion with purely Ohmic heating and supplementary heating methods are necessary.

One additional heating method consists of injecting energetic particle beams of neutral hydrogen or deuterium into the plasma. The neutral particles travel unaffected by the magnetic field until they ionise. Once they are ionised the resulting ions and electrons are held by the magnetic field and deposit their energy via collisions to the rest of the plasma. The deposition region depends essentially on the orbits of the created highly energetic ions.

A second heating method introduces electro-magnetic waves into the plasma. In addition to collisional absorption the variety of electro-magnetic wave modes in a magnetised

plasma allows for many different heating schemes. Once the wave has coupled to the plasma, it has to propagate to an absorption zone. The absorption is particularly high at resonant frequencies such as the ion or electron cyclotron frequencies,

$$\omega_{ci} = \frac{q_i B}{m_i} \quad (1.13)$$

$$\omega_{ce} = \frac{e B}{m_e} \quad (1.14)$$

or the lower hybrid frequency,

$$\omega_{LH} \approx (\omega_{ci} \cdot \omega_{ce})^{1/2} \quad (1.15)$$

and at higher harmonics of these frequencies. Ion cyclotron frequencies in tokamaks are typically in the MHz range from 20 MHz upwards, while the electron cyclotron frequencies are approximately 1000 times higher ranging up to 200 GHz. Lower hybrid resonance heating schemes use medium frequencies in the order of a few Giga-Hertz. The B -dependence of these resonances allows for a more or less localised heating depending on the absorption properties of the resonances.

The electron cyclotron heating (ECH) has the advantage that the wave can couple directly to the electro-magnetic field in the vacuum allowing the antenna to be located far from the plasma boundary. The propagation and absorption properties of a high frequency (HF) wave are illustrated in the *Clemmow-Mullaly-Allis* (CMA) diagram for a cold plasma, (figure 1.8). In the CMA diagram the abscissa represents essentially the density and the ordinate the magnetic field. For a wave which propagates perpendicular to the magnetic field ($\vec{k}_{HF} \perp \vec{B}$) one has to distinguish between the ordinary mode (O-mode), where the incident wave's electric field is parallel to the background magnetic field ($\vec{E}_{HF} \parallel \vec{B}$), and the extraordinary mode (X-mode), where it lies in a plane perpendicular to the background magnetic field ($\vec{E}_{HF} \perp \vec{B}$). The propagation of these waves is described by their index of refraction,

$$N_O^2 = 1 - (\omega_p/\omega)^2 \quad (1.16)$$

$$N_X^2 = \left(1 - (\omega_p/\omega)^2 - \omega_{ce}/\omega\right) \frac{1 - (\omega_p/\omega)^2 + \omega_{ce}/\omega}{1 - (\omega_p/\omega)^2 - (\omega_{ce}/\omega)^2}. \quad (1.17)$$

where $\omega_p = (e^2 n_e / \epsilon_0 m_e)^{1/2}$ is the plasma frequency. If the refractive index becomes zero the wave cannot propagate any further and is reflected, which is referred to as a cut-off. For an O-mode wave such a cut-off occurs for $\omega_{HF} = \omega_p$ and limits the accessibility to densities below a critical density, $n_{e, \text{cut-off}}$, corresponding to the area on the left of the O-mode cut-off in the CMA diagram (figure 1.8). The X-mode wave is reflected at the right-hand cutoff, $\omega_R = \omega_{ce}/2 + [(\omega_{ce}/2)^2 + \omega_p^2]^{1/2}$, and the left hand cut-off, $\omega_L = -\omega_{ce}/2 + [(\omega_{ce}/2)^2 + \omega_p^2]^{1/2}$, both indicated in figure 1.8. For heating at the second

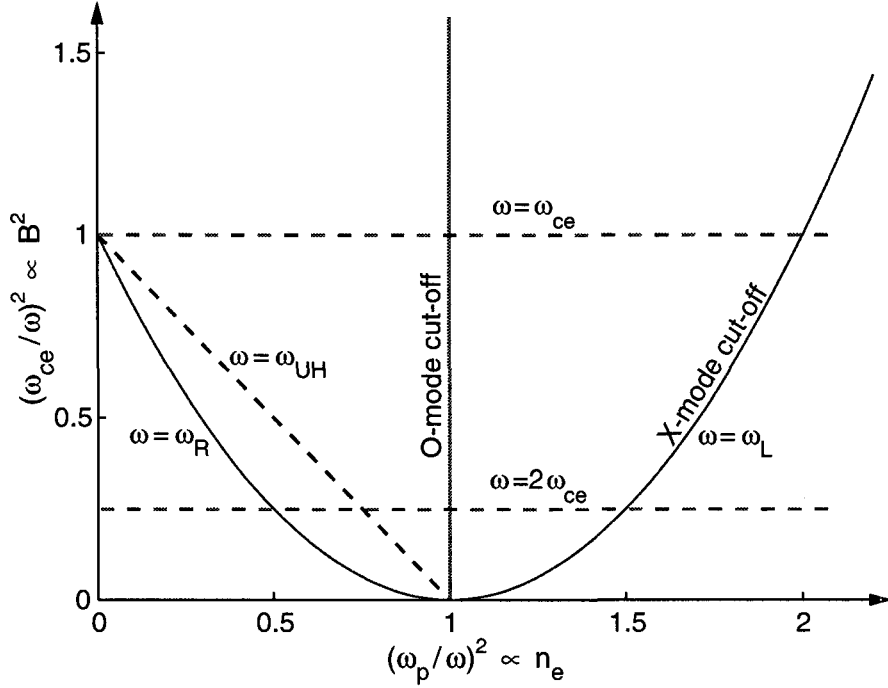


Figure 1.8: CMA diagram for electron cyclotron waves showing cut-offs (solid) and resonances (dashed) of the ordinary and extraordinary mode.

harmonic the X-mode wave is cut-off at $\omega_{\text{HF}} = \sqrt{2}\omega_p$. The corresponding cut-off density is therefore the half of the cut-off density of the same wave in O-mode.

The electro-magnetic wave is absorbed when the refractive index diverges, $N \rightarrow \infty$. In the cold plasma description the O-mode does not possess any resonances, whereas the X-mode has a resonance at the upper hybrid frequency $\omega_{\text{UH}} = (\omega_p^2 + \omega_{\text{ce}}^2)^{1/2}$. However, including hot plasma effects both modes have resonances at the cyclotron frequency and higher harmonics, $l \cdot \omega_{\text{ce}}$, $l = 1, 2, \dots$. The absorption at these resonances depends on the mode, the harmonic, and the plasma parameters. Generally the second harmonic of the extraordinary mode (X2-mode) is absorbed best. The absorption properties of the O1-, X1-, O2- and X3-modes are somewhat weaker.

1.1.4 Power plant concept

In a fusion power plant the temperature of the combustibles D and T should be maintained by the energy transfer of the 3.5 MeV α -particles created by fusion reactions (equation 1.6), rendering additional heating unnecessary. The charged α -particles are confined by the magnetic field and can transfer their energy via collisions. It is important that they are sufficiently well confined to equilibrate their energy with the bulk plasma before leaving the plasma. In contrast to the α -particles the neutrons leave the plasma without further interaction and should be absorbed in a blanket surrounding the reactor vessel.

Such a blanket composed of a compound of lithium can allow the breeding of tritium according to the reactions given in equations 1.8 and 1.9 and fuel the reactor. The heat is carried away by a suitable coolant and provides the power output for the ultimate generation of electricity.

A power balance gives an estimate for the plasma parameters required for a fusion power plant. The reaction rate per unit volume of an optimum 50%-50% deuterium-tritium mixture R_{D-T} , is calculated by averaging the cross section of the D-T reaction σ_{D-T} , over a thermal velocity distribution,

$$R_{D-T} = \frac{1}{4} n^2 \langle \sigma_{D-T} v \rangle_v, \quad (1.18)$$

with n being the total ion density and $\langle \rangle_v$ denoting the average over the velocity distribution. The reaction rate determines the α -particle heating power density $p_\alpha = R_{D-T} \mathcal{E}_\alpha$, where \mathcal{E}_α is the kinetic energy of a generated α -particle. The energy loss can be expressed by an energy confinement time τ_E ,

$$P_{loss} = \frac{W}{\tau_E} = \frac{\int 3nT dV}{\tau_E}. \quad (1.19)$$

In equation 1.19 the total energy W , is expressed by the volume integral over the comprised energy densities of $\frac{1}{2}nT$ per degree of freedom of the ions and of the electrons. The power balance of the entire plasma taking into account an auxiliary heating power P_{aux} , is,

$$\underbrace{\int \frac{1}{4} n^2 \langle \sigma_{D-T} v \rangle_v \mathcal{E}_\alpha dV}_{P_\alpha} + P_{aux} = \underbrace{\frac{\int 3nT dV}{\tau_E}}_{P_{loss}}. \quad (1.20)$$

If the plasma temperature can be sustained by α -particle heating alone, the plasma ignites. Using equation 1.20 and taking constant density and temperature for simplicity, a temperature dependent condition for ignition can be derived,

$$n\tau_E > \frac{12}{\langle \sigma_{D-T} v \rangle_v} \frac{T}{\mathcal{E}_\alpha}. \quad (1.21)$$

The condition for the product of density and confinement time has a broad minimum at 30 keV [1]. The use of this minimum value of $n\tau_E$ leads to the ignition criterion for the triple product,

$$nT\tau_E > 3 \times 10^{21} \text{ m}^{-3} \text{ keV s}. \quad (1.22)$$

The precise requirement depends on the shape of the density and temperature profiles. For parabolic profiles the requirement for the peak values is,

$$\hat{n}\hat{T}\tau_E > 5 \times 10^{21} \text{ m}^{-3} \text{ keV s}. \quad (1.23)$$

The achieved value of this parameter has improved by seven orders of magnitude over the past 45 years and is on the verge of reactor conditions (see figure 1.9).

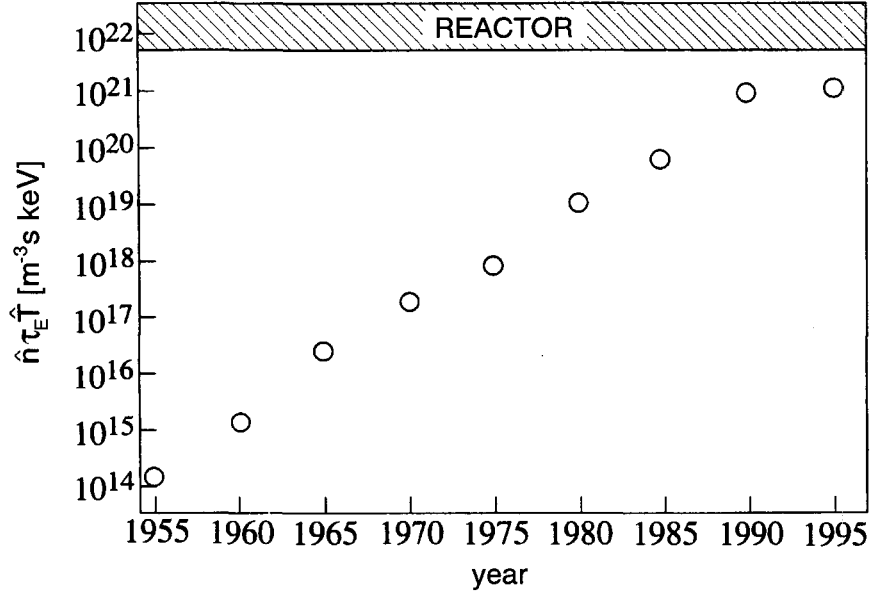


Figure 1.9: Progress in increasing the triple product $\hat{n}\hat{T}\tau_E$, leading towards reactor conditions [1].

1.2 Motivation for the thesis

This thesis addresses the behaviour of mainly pressure driven instabilities in a tokamak. Through an interpretation of measurements, instabilities and the conditions leading to their occurrence should be characterised. A comparison with theory will then lead to a deeper understanding of the physics involved. Pressure driven instabilities are important since they limit the performance of tokamaks in several ways, in particular with regard to a power plant.

- **Efficiency aspect**

The criterion for ignition (equation 1.22) has shown that high densities at high plasma temperatures are essential to meet the condition for a fusion power plant. Increasing the plasma pressure $p = nT$, means advancing towards economical power plant conditions. The dimensionless parameter beta, which is the ratio of plasma and magnetic field pressure,

$$\beta = \frac{\langle p \rangle}{B_0^2 / 2\mu_0} \quad (1.24)$$

with $\langle \rangle$ denoting the volume average, is particularly important since it is used as a figure of merit for the efficiency of a tokamak. The pressure stands for fusion yield and the magnetic field for the price of the machine as higher beta allows for either the use of lower magnetic fields or smaller and therefore cheaper machines.

- **Confinement aspect**

Instabilities not only limit the achievable beta but generally enhance the transport. This decreases the confinement time and consequently, lowers the triple product (equation 1.22). This can be compensated by building a larger machine but leads to higher costs.

It is, therefore, obvious that avoiding instabilities and extending the beta limit is desirable as it may lead to a more economical solution for a fusion reactor. TCV is well suited for MHD analysis since the MHD stability can strongly depend on the geometry. The powerful heating system allows for the attainment of high temperatures. More importantly, it provides a local power deposition which allows to tailor the pressure and the current profiles and test and improve them in order to optimise the stability of the plasma.

1.3 Outline of the thesis

A brief introduction to nuclear fusion and the tokamak as a possible concept to exploit fusion as a future energy source has been given in this chapter. Magnetohydrodynamic theory which gives an accurate description of many aspects of the behaviour of a hot plasma is reviewed in chapter 2. The TCV tokamak on which the work was performed, the ECH heating system and the diagnostics which were used are outlined in chapter 3. In chapter 4 a special emphasis is given to the fast magnetic fluctuation diagnostic which is a key diagnostic for monitoring and identifying instabilities. Chapter 5 describes the analysis tools which were set up in the course of this thesis in order to analyse the fluctuation measurements. In particular, a simulation of magnetic islands proved to be essential for the identification of mode structures in TCV. This thesis focuses on four instabilities which are all an issue for the operation of a future fusion experiment, such as ITER.

- Chapter 6 gives an original systematic analysis of the shape dependence of the **sawtooth instability**. Sawteeth are common to most standard tokamak scenarios and a control of their occurrence and size is desirable, in particular to avoid seeding of neoclassical tearing modes. TCV was perfectly suited for such an analysis allowing a wide range of scanned plasma shapes. The analysis resulted in the identification of an 'ideal' or 'resistive' regime depending on the plasma shape and led to a journal publication:

H. Reimerdes, A. Pochelon, O. Sauter, T.P. Goodman, M.A. Henderson, An. Martynov "Effect of triangular and elongated plasma shape on the sawtooth stability", *Plasma Phys. Control. Fusion* **42** (2000) 629-639.

- Chapter 7 reports observations on precursor oscillations to **edge localised modes** (ELMs). The high resolution of TCV's toroidal array of pick-up coils allowed to resolve hitherto unreported features. ELMs are necessary for the density and impurity control in high confinement modes but can cause critical power loads on target plates. A control of their size and frequency is deemed necessary for a reactor. The results of this work on TCV led to a journal publication:

H. Reimerdes, A. Pochelon, W. Suttrop, "Toroidally asymmetric ELM precursor in TCV", *Nucl. Fusion* **38** (1998) 319-323.

- Chapter 8 describes the MHD activity prior to the **ideal beta limit** in highly elongated plasmas. High elongations promise a better efficiency and improved confinement and could possibly reduce the cost of a reactor. TCV's unique design allows to operate routinely at very high elongation ($\kappa > 2$). The characterisation of instabilities at high elongation contributed to a journal publication:

F. Hofmann, O. Sauter, H. Reimerdes, I. Furno, A. Pochelon, "Experimental and theoretical stability limits of highly elongated tokamak plasmas", *Phys. Rev. Lett.* **81** (1998) 2918-2921.

- Chapter 9 analyses the triggering mechanism of **neoclassical tearing modes** (NTMs) in TCV. In a fusion reactor these modes are likely to impose a pressure limit well below the ideal MHD limit. If their triggering can be avoided, operation in a meta stable state would be possible. The observations in TCV show that conventional tearing modes supply the seed island. Such a trigger mechanism has yet to be reported from other tokamak experiments but is considered to be of importance elsewhere, too. The new findings were reported at several conferences, among them:

H. Reimerdes, T. Goodman, A. Pochelon, O. Sauter, "Neoclassical tearing modes in TCV", *27th EPS Conference on Controlled Fusion and Plasma Physics (Budapest, 2000)* (2000) P.1025.

In chapter 10 conclusions are drawn on the presented work and proposals for future work outlined.

Chapter 2

Magnetohydrodynamic theory

A many body system like a plasma can be described by a set of Boltzmann equations for the distribution functions of each particle species. In a fusion plasma the two forces acting on particles are short-range interactions due to collisions, which are predominantly elastic Coulomb collisions and long-range Lorentz forces originating from macroscopic \vec{E} and \vec{B} fields, which requires a coupling of the Boltzmann equations to Maxwell's equations. The full set of equations then provides a very detailed description of the plasma behaviour ranging from the orbits of individual particles to the macroscopic behaviour of fusion experiments. However, the broadness of information is accompanied by a complexity, which makes even a numerical solution practically impossible. Therefore, a simpler model, like the magnetohydrodynamic (MHD), which leads to a reduction of the dimensionality of the description of the plasma, is necessary.

In this chapter the MHD description of a plasma is introduced, sketching its derivation and listing the underlying assumptions. The ideal MHD equations are used to find equilibrium states and stability limits. Techniques to analyse the stability of the equilibrium states are presented and an overview of various types of instabilities which occur in tokamak plasmas is given. The knowledge summarised in this chapter is well documented in various textbooks, e.g. [3, 4, 5] and forms the basis of the analysis presented in this thesis.

2.1 MHD equations

The MHD equations are derived from the Boltzmann equations by calculating moments and introducing macroscopic physical variables, such as density $n_\alpha(\vec{x}, t)$, or velocity $\vec{v}_\alpha(\vec{x}, t)$, with α denoting the particle species. Each moment equation contains the next higher moment forming an infinite set of fluid equations. For a complete description of the plasma behaviour the fluid equations are coupled to the full set of Maxwell's equations.

The description of a plasma can be substantially simplified by two important assump-

tions. In the first assumption, the low-frequency approximation, the displacement current and net charges are neglected in Maxwell's equations. Displacement currents can be neglected if the phase velocity of the electro-magnetic wave of interest, as well as the ion and electron thermal velocities are much slower than the speed of light, $\omega/k, v_{T_i}, v_{T_e} \ll c$. Net charges can be neglected if the characteristic frequencies are much lower than the electron plasma frequency, $\omega \ll \omega_p$ ($\omega_p = (ne^2/m_e\epsilon_0)^{1/2}$) and if the characteristic lengths are much longer than the Debye length, $\lambda \gg \lambda_d$ ($\lambda_d = (\epsilon_0 k_B T_e / n_e e^2)^{1/2}$). Neglecting net charges implies the quasi-neutrality of the plasma,

$$n_e = n_i = n \quad (2.1)$$

where it has been assumed that ions are singly charged, $Z_i = 1$. The low-frequency Maxwell equations are then,

$$\nabla \times \vec{B} = \mu_0 \vec{j} \quad (2.2)$$

$$\nabla \times \vec{E} = -\frac{\partial \vec{B}}{\partial t} \quad (2.3)$$

$$\nabla \cdot \vec{B} = 0. \quad (2.4)$$

As a second assumption the electron mass is neglected. As with the first assumption this requires that the frequencies of interest are small compared to the response of the electrons, namely to ω_p and characteristic lengths large compared to λ_d .

The single fluid MHD description of a plasma is now obtained by introducing fluid variables, such as the mass density ρ , fluid velocity \vec{v} , and current density \vec{j} , and combining the equations for electrons and ions, assuming $m_e \ll m_i$,

$$\rho = m_i n_i + m_e n_e \approx m_i n_i \quad (2.5)$$

$$\vec{v} = \frac{1}{\rho} (m_i n_i \vec{v}_i + m_e n_e \vec{v}_e) \approx \vec{v}_i \quad (2.6)$$

$$\vec{j} = en(\vec{v}_i - \vec{v}_e) \approx en(\vec{v} - \vec{v}_e). \quad (2.7)$$

The total pressure p , and temperature T , are obtained by summing over the species. The equation of conservation of mass results from the sum over the continuity equations for ions and electrons,

$$\frac{\partial \rho}{\partial t} = -\nabla \cdot (\rho \vec{v}). \quad (2.8)$$

The difference of the continuity equations yields $\nabla \cdot \vec{j} = 0$, which is consistent with the low-frequency form of Ampere's law (equation 2.2). The evolution of the fluid velocity is given by the momentum equation,

$$\rho \left(\frac{\partial \vec{v}}{\partial t} + (\vec{v} \cdot \nabla) \vec{v} \right) = \vec{j} \times \vec{B} - \nabla \cdot P \quad (2.9)$$

where P is the pressure tensor. The force equations for electrons expressed in single fluid quantities yield the generalised Ohm's law,

$$\vec{E} + \vec{v} \times \vec{B} = \eta \vec{j} + \frac{1}{en} (\vec{j} \times \vec{B} - \nabla \cdot P_e) \quad (2.10)$$

where the electric resistivity η , originates from friction between electrons and ions. This set of single-fluid equations (equations 2.8 – 2.10) together with Maxwell equations (equations 2.2 – 2.4) is still incomplete. Closure requires assumptions concerning the next higher moment P .

2.2 Ideal MHD

The ideal MHD model uses further simplifications. It is assumed that electrons and ions are collision dominated, which is the usual assumption to render a fluid description applicable. Collisions equilibrate the distribution functions and give rise to an isotropic pressure tensor. It can be shown that if $\rho_i/a \ll 1$, where a is a macroscopic scale length of the plasma, the terms proportional to $1/n$ on the right-hand side of Ohm's law (equation 2.10) are small compared to $\vec{v} \times \vec{B}$ [4]. The resistivity term in equation 2.10 can also be neglected, if resistive diffusion is sufficiently small. This imposes an upper limit on the collisionality but can also be expressed as a lower limit of the macroscopic length scale, a . The ideal MHD equations are then,

$$\frac{\partial \rho}{\partial t} = -\nabla \cdot (\rho \vec{v}) \quad (2.11)$$

$$\rho \left(\frac{\partial \vec{v}}{\partial t} + (\vec{v} \cdot \nabla) \vec{v} \right) = -\nabla p + \vec{j} \times \vec{B} \quad (2.12)$$

$$\vec{E} = -\vec{v} \times \vec{B}. \quad (2.13)$$

The set of equations can be closed by assuming adiabatic behaviour

$$\frac{\partial p}{\partial t} + \vec{v} \cdot \nabla p = -\gamma p \nabla \cdot \vec{v} \quad (2.14)$$

with $\gamma = 5/3$ being the ratio of the specific heats.

Unfortunately, an analysis of the various assumptions made in the derivation of the ideal MHD equations shows that not all assumptions are valid for plasmas of fusion interest. In particular, the assumed high collisionality is not satisfied. However, as the incorrectly treated parts, namely the transport of parallel momentum and energy, are of little importance in equilibrium and stability calculations, the ideal MHD model has proven to provide an accurate description of macroscopic plasma behaviour.

2.2.1 Frozen flux

The ideal MHD model has an important consequence for the magnetic flux $\Psi = \int \vec{B} d\vec{A}$, which is the amount of magnetic field passing through a given surface. Its temporal evolution depends on the change of the magnetic field and the motion of the surface,

$$\frac{\partial \Psi}{\partial t} = \int \frac{\partial \vec{B}}{\partial t} \cdot d\vec{A} - \oint \vec{u} \times \vec{B} \cdot d\vec{l} \quad (2.15)$$

where \vec{u} is the velocity of the integration boundary. Substituting $\partial \vec{B} / \partial t$ with Faraday's law (equation 2.3) and replacing the electrical field \vec{E} by the ideal MHD approximation of Ohm's law (equation 2.13) yields,

$$\frac{\partial \Psi}{\partial t} = \oint (\vec{v} - \vec{u}) \times \vec{B} \cdot d\vec{l}. \quad (2.16)$$

Thus, the magnetic flux through a loop moving with the plasma ($\vec{v} - \vec{u} = 0$) remains constant. It is said that in ideal MHD the magnetic flux is *frozen* in the plasma fluid.

2.2.2 Tokamak equilibrium

The time independent form of the ideal MHD equations ($\partial / \partial t = 0$) can be used to calculate an equilibrium configuration. According to equation 2.12 a static equilibrium, where the velocities are also set to zero ($\vec{v} = 0$), requires,

$$\nabla p = \vec{j} \times \vec{B}. \quad (2.17)$$

A scalar multiplication of equation 2.17 with \vec{B} yields $\vec{B} \cdot \nabla p = 0$. Thus, there are no pressure gradients along magnetic field lines. The magnetic field lines lie on the nested surfaces of constant pressure, referred to as magnetic flux surfaces. Similarly, a scalar multiplication of equation 2.17 with \vec{j} yields $\vec{j} \cdot \nabla p = 0$, implying that currents only flow tangential to flux surfaces. Owing to $\nabla \cdot \vec{B} = 0$ the poloidal flux defined by,

$$\psi_{\text{pol}} = \int_{A_{\text{tor}}} \vec{B} \cdot d\vec{A} \quad (2.18)$$

and the toroidal flux defined by,

$$\psi_{\text{tor}} = \int_{A_{\text{pol}}} \vec{B} \cdot d\vec{A} \quad (2.19)$$

with A_{tor} and A_{pol} being arbitrary toroidal and poloidal cross sections of a flux surface, are constant on magnetic surfaces. The introduction of ψ_{pol} and ψ_{tor} allows to rewrite the definition of the safety factor (equation 1.11) as,

$$q = \frac{d\psi_{\text{tor}}}{d\psi_{\text{pol}}}. \quad (2.20)$$

The cylindrical coordinates (R, φ, Z) are well suited for the description of a toroidal axisymmetric equilibrium. The toroidal unit vector is $\vec{e}_\varphi = R\nabla\varphi$. The poloidal magnetic field can be expressed using the toroidal component of the vector potential \vec{A} ,

$$\vec{B} = \nabla \times A_\varphi \hat{e}_\varphi + B_\varphi \hat{e}_\varphi. \quad (2.21)$$

However, it is customary to use a stream function, $\psi = RA_\varphi$,

$$\vec{B} = \nabla \times \psi \nabla \varphi + B_\varphi \hat{e}_\varphi. \quad (2.22)$$

Using the stream function the poloidal magnetic field in cylindrical coordinates can be expressed by,

$$B_R = -\frac{1}{R} \frac{\partial \psi}{\partial Z} \quad (2.23)$$

$$B_Z = \frac{1}{R} \frac{\partial \psi}{\partial R}. \quad (2.24)$$

A comparison with equation 2.18 reveals that the stream function is proportional to the poloidal flux, $\psi_{\text{pol}} = 2\pi\psi$.

Substituting \vec{B} according to equation 2.22 in Ampere's law (equation 2.2) yields an expression for the current density,

$$\begin{aligned} \mu_0 \vec{j} &= \nabla \times (\nabla \times \psi \nabla \varphi + RB_\varphi \nabla \varphi) \\ &= -\frac{1}{R} \Delta^* \psi \hat{e}_\varphi + \nabla(RB_\varphi) \times \nabla \varphi \end{aligned} \quad (2.25)$$

where Δ^* is the elliptic operator,

$$\Delta^* = R \frac{\partial}{\partial R} \left(\frac{1}{R} \frac{\partial}{\partial R} \right) + \frac{\partial^2}{\partial Z^2}. \quad (2.26)$$

Using equation 2.22 and equation 2.25 the force equation (equation 2.17) can be rewritten as,

$$\mu_0 p'(\psi) \nabla \psi = -\frac{1}{R^2} \Delta^* \psi \nabla \psi - \frac{RB_\varphi}{R^2} \nabla(RB_\varphi). \quad (2.27)$$

Therefore, $\nabla(RB_\varphi)$ is also orientated in the direction of $\nabla\psi$. Thus, the function,

$$I(\psi) = RB_\varphi \quad (2.28)$$

is constant on a flux surface. Substituting RB_φ in equation 2.27 yields the so-called *Grad-Shafranov* equation,

$$\Delta^* \psi = -\mu_0 R^2 p'(\psi) - I(\psi) I'(\psi). \quad (2.29)$$

The Grad-Shafranov equation is a nonlinear elliptic differential equation and must, in general, be solved numerically. However, the problem is ill posed, since $p'(\psi)$ and $I(\psi)I'(\psi)$

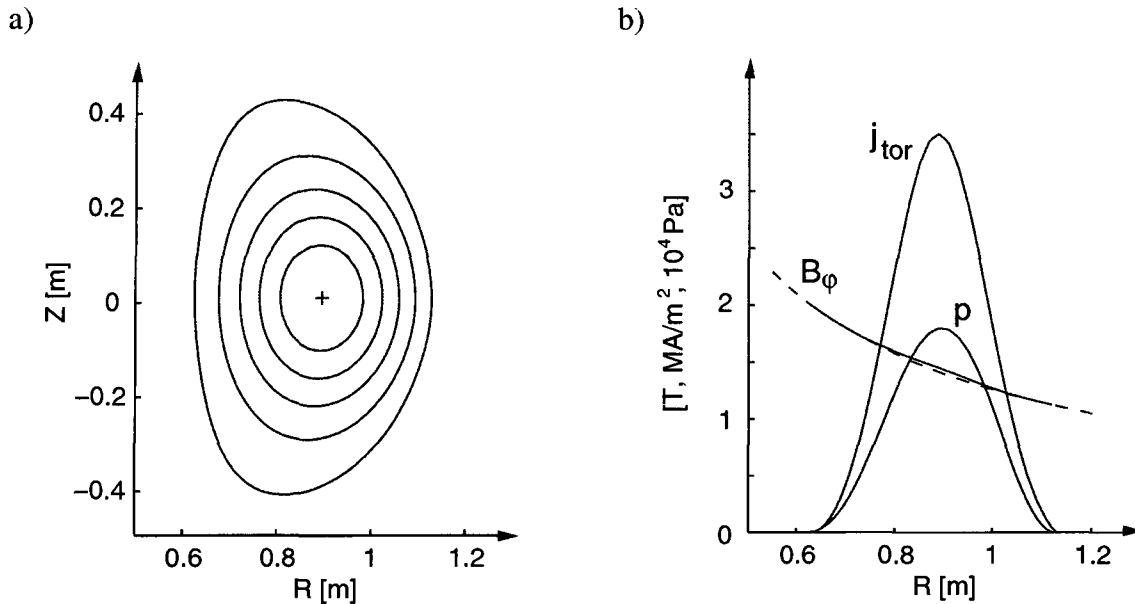


Figure 2.1: (a): A TCV equilibrium, calculated with LIUQE, shows the nested flux surfaces. (b): The corresponding toroidal field B_ϕ , toroidal current density j_{tor} , and plasma pressure p . The toroidal field is compared to the vacuum field (dashed line) showing the small paramagnetism of a low pressure plasma ($\beta_p < 1$).

must be given as functions of ψ , whose spatial dependence is not known until equation 2.29 is solved and consequently, iterative schemes have to be used. The reconstruction method used by the Grad-Shafranov solver LIUQE [6] on TCV plasmas is described in section 3.4. A reconstructed TCV equilibrium is shown in figure 2.1. Common features of tokamak equilibria are the outward shift of the magnetic axis, referred to as *Shafranov shift*, as well as the para- or diamagnetism of the plasma, which depends on the plasma pressure.

2.2.3 Stability analysis

The stability of an equilibrium with ρ_0 , \vec{j}_0 , and \vec{B}_0 satisfying the ideal MHD equilibrium can be determined by its linear response to an arbitrarily small perturbation. Accordingly, a displacement $\vec{\xi}$ of a fluid element with respect to its equilibrium position is introduced. The resulting velocity $\vec{v}_1 = \partial \vec{\xi} / \partial t$, is a first order term in the linearised ideal MHD equations. The linearised and integrated form of the continuity equation (equation 2.8),

$$\rho_1 = -\nabla \cdot (\rho_0 \vec{\xi}) \quad (2.30)$$

describes the change in density due to compression. Using the continuity equation the corresponding change in pressure is obtained from the state equation (equation 2.14),

$$p_1 = -\gamma p_0 \nabla \cdot \vec{\xi} - \vec{\xi} \cdot \nabla p_0. \quad (2.31)$$

The linearised form of Ohm's law (equation 2.10) yields,

$$\vec{B}_1 = \nabla \times (\vec{\xi} \times \vec{B}_0) \quad (2.32)$$

and the perturbed current density is calculated from Ampere's law (equation 2.2),

$$\mu_0 \vec{j}_1 = \nabla \times \vec{B}_1. \quad (2.33)$$

The perturbed quantities on the right hand side of the linearised momentum equation (equation 2.9),

$$\rho_0 \frac{\partial \vec{v}_1}{\partial t} = -\nabla p_1 + \vec{j}_1 \times \vec{B}_0 + \vec{j}_0 \times \vec{B}_1 \quad (2.34)$$

can be replaced using equations 2.31, 2.32, and 2.33 to obtain a single vector equation for the displacement $\vec{\xi}$,

$$\rho_0 \frac{\partial^2 \vec{\xi}}{\partial t^2} = \vec{F}(\vec{\xi}) \quad (2.35)$$

with \vec{F} being the force operator,

$$\begin{aligned} \vec{F}(\vec{\xi}) = & \nabla (\gamma p_0 \nabla \cdot \vec{\xi} + \vec{\xi} \cdot \nabla p_0) \\ & + \frac{1}{\mu_0} [(\nabla \times \nabla \times (\vec{\xi} \times \vec{B}_0)) \times \vec{B}_0 + (\nabla \times \vec{B}_0) \times \nabla \times (\vec{\xi} \times \vec{B}_0)]. \end{aligned} \quad (2.36)$$

With appropriate boundary conditions the problem can be solved as an initial value problem. Since the coefficients in \vec{F} do not depend on time it can also be formulated as a normal mode problem using the Fourier Ansatz $\vec{\xi}(\vec{x}, t) = \hat{\vec{\xi}}(\vec{x}) e^{i\omega t}$, which leads to the eigenvalue equation,

$$-\omega^2 \rho_0 \hat{\vec{\xi}} = \vec{F}(\hat{\vec{\xi}}). \quad (2.37)$$

In the remainder of this section the hat notation will be dropped. It can be shown that the operator \vec{F} is self adjoint and hence its eigenvalues ω^2 , are real [4]. A positive eigenvalue $\omega^2 > 0$ corresponds to a pure oscillation and is hence considered as stable, whereas $\omega^2 < 0$ implies a solution which grows exponentially.

It is also possible to use a variational formulation of the problem. Multiplication of (2.37) with $\vec{\xi}$ and integration over the plasma volume can be interpreted as the conservation of energy,

$$\frac{\omega^2}{2} \int \rho_0 |\xi|^2 dV = -\frac{1}{2} \int \vec{\xi} \cdot \vec{F}(\vec{\xi}) dV = \delta W. \quad (2.38)$$

The sign of δW determines the stability since $\delta W < 0$ implies $\omega^2 < 0$. The *energy principle* states that the existence of any allowable trial function $\vec{\xi}$ that makes δW negative guarantees the existence of an eigenfunction with an even smaller eigenvalue and is, therefore, sufficient for instability. Taking into account appropriate boundary conditions

the potential energy δW can be separated into a plasma (F: fluid), a surface (S), and a vacuum (V) contribution [4],

$$\delta W = \delta W_F + \delta W_S + \delta W_V. \quad (2.39)$$

The usual approach is an expansion of the displacement vector $\vec{\xi}$, in periodic coordinates,

$$\vec{\xi} = \sum_{m,n} \vec{\xi}_{m,n}(r) e^{-i(m\theta - n\varphi)} \quad (2.40)$$

introducing the poloidal and toroidal mode numbers m and n . The helicity of the magnetic field line coincides with the helicity of the dominant (m, n) contribution of the perturbation when $q = m/n$.

2.3 Ideal instabilities

In the frame of ideal MHD, instabilities are usually classified by two characteristics. Firstly, one distinguishes between modes whose mode structure does not require any motion of the plasma-vacuum boundary, referred to as internal modes, and those whose mode structure move the plasma-vacuum interface, referred to as external modes. Secondly, each instability can be characterised by its dominant driving term, which can be the gradient of the pressure or the gradient of the plasma current parallel to the magnetic field lines.

2.3.1 Pressure driven modes

The most unstable pressure driven instabilities are internal modes with short wavelengths perpendicular to the magnetic field. They can be subdivided into interchange and ballooning modes.

Interchange modes

The interchange mode is similar to the Rayleigh-Taylor instability in fluid dynamics. The role of the gravitational force is taken by the radial force resisting the bending of magnetic field lines. This field line tension tends to shorten curved field lines and move them inward. Plasma pressure tends to push the plasma outward. If the pressure gradient and the field line curvature have the same direction, flux tubes at different radii can interchange which leads to a state of lower potential energy. If the pressure gradient opposes the curvature, the system is stable.

The interchange mode can be stabilised by shearing the magnetic field so that neighbouring flux tubes cannot be interchanged without a bending of field lines. The magnetic

shear s , is defined using the safety factor q (equation 1.11),

$$s = \frac{r}{q} \frac{dq}{dr}. \quad (2.41)$$

Another stabilising mechanism is based on the fact that field line curvature on the inside of the torus is anti-parallel to the pressure gradient and consequently, favourable for stability. Therefore, an appropriate averaging over the curvature of field lines has to be used to derive a necessary condition for stability against localised interchange from the energy functional (equation 2.39). The so-called *Mercier criterion* for the stability of localised interchange in a circular plasma in a large-aspect ratio approximation is,

$$-D_I \approx \frac{1}{4} - \frac{2\mu_0 r}{B_0^2 s^2} (-p') (1 - q^2) > 0 \quad (2.42)$$

and represents a necessary condition for ideal MHD stability. Its violation indicates the existence of a localised instability and possibly a large scale instability as well. The Mercier criterion gives an expression for the magnetic shear, which is necessary to suppress ideal interchange. For $q > 1$ the stabilising contribution of the average curvature of the toroidal field, which is represented by the factor $p'q^2$ in equation 2.42, is sufficiently large for pressure gradients to become stabilising.

Since the Mercier criterion is obtained from an averaging over favourable and unfavourable curvature regions it can be largely modified by plasma shaping. In order to correct for shaping effects, the ellipticity $e = (\kappa - 1)/2$ is introduced as a second small parameter in the large aspect ratio expansion. The normally leading pressure contribution of $O(\epsilon^2)$ vanishes on the $q = 1$ surface (equation 2.42) leaving the $O(\epsilon^2 e)$ shaping term as the leading contribution [7],

$$-D_I \approx \frac{1}{4} - \frac{2\mu_0 r_1}{B_0^2 s_1^2} (-p'_1) \frac{3(\kappa_1 - 1)}{2} \left(1 - \frac{2\delta_1}{\epsilon_1}\right) > 0, \quad (2.43)$$

where the index 1 indicates the value on the $q = 1$ surface. Note, that for a $\kappa_1 = 1$ neither triangularity nor pressure affect the stability boundary. Elongation by itself is destabilising, whereas a combination of elongation and sufficient triangularity improves the stability. This improved stability of triangular plasmas reflects the fact that a large fraction of a field line is located in the favourable curvature region on the inside of the torus.

Ballooning modes

For high pressures, the stabilising effect of average curvature and pressure gradients for $q > 1$ against interchange modes can be eluded by allowing perturbations with short wavelengths to concentrate in the unfavourable curvature region on the outer side of the

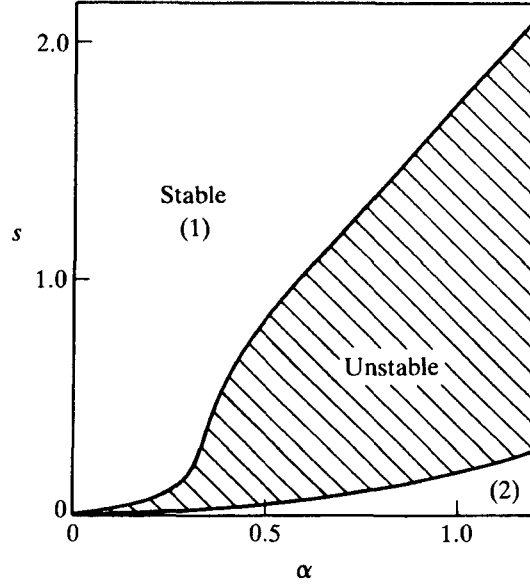


Figure 2.2: Ballooning mode stability for circular flux surfaces showing the first (1) and second (2) stability regions [1].

torus. The potential energy thus released can be greater than the energy required for the line bending inherent in the variation of the perturbation along field lines. Owing to their spatial structure, these high n instabilities are called *ballooning modes*. As with the interchange mode, their stability can be expressed as a condition for the magnetic shear at a given pressure gradient. The pressure gradient is usually replaced by a normalised pressure gradient,

$$\alpha = \frac{2\mu_0 R_0 q^2}{B_0^2} \left(-\frac{dp}{dr} \right). \quad (2.44)$$

The stability calculation starts from the energy functional (equation 2.39) in the limit of large mode numbers. A numerical analysis for a circular plasma leads to the stability boundary in the $s - \alpha$ diagram shown in figure 2.2. In the so-called *first stability region* (figure 2.2(1)), the required shear increases with the pressure gradient. For circular flux surfaces the stability boundary can be approximated by $s \approx 0.6\alpha$. There is also a *second stability region* (figure 2.2(2)), where the pressure is no longer limited. The stabilising effect of pressure gradients at high pressure can be attributed to the Grad-Shafranov shift, which increases the length of the field line in the favourable inner region of the torus. However, in a circular plasma this region is not accessible. Plasma shaping, which alters the ballooning stability, is required to open a passage between the first and second stability regions.

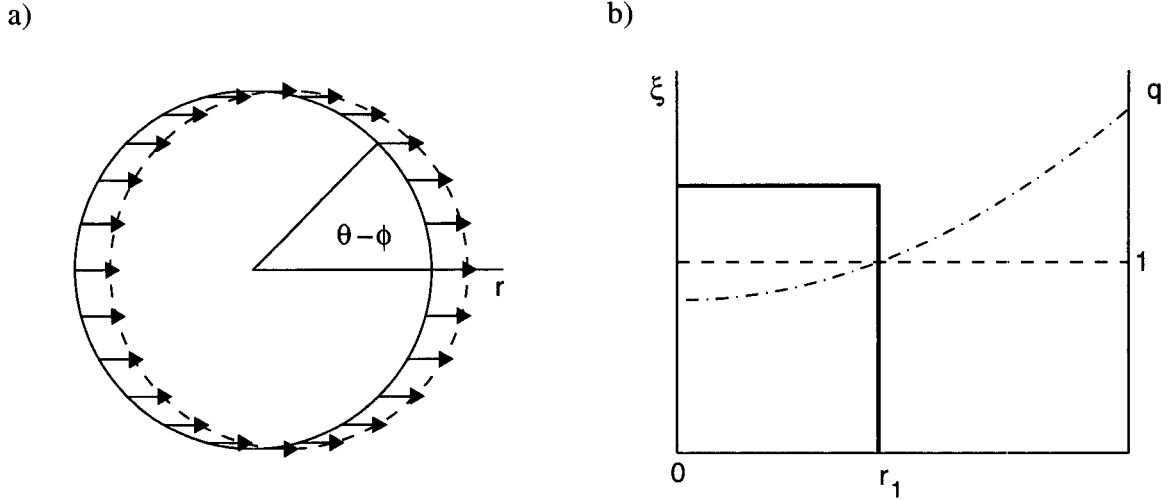


Figure 2.3: (a) Radial displacement of a circular flux surface of an $m = 1$ perturbation and (b) the radial dependence of ξ for an unstable mode.

2.3.2 Current driven modes

For low beta, the main destabilising term is the radial gradient in the parallel current. In order to minimise the field line bending, small mode numbers are the most unstable. They are often referred to as *kink modes*. For a circular, low beta ($\beta \sim \epsilon^2$) plasma in the straight tokamak approximation, without a conducting wall, the potential energy (equation 2.39) for a perturbation with a radial displacement $\xi(r)e^{i(m\theta - n\varphi)}$ is,

$$\begin{aligned} \delta W = & \frac{2\pi B_0^2}{\mu_0 R_0} \left(\int_0^a \left[\left(r \frac{d\xi}{dr} \right)^2 + (m^2 - 1) \xi^2 \right] \left(\frac{n}{m} - \frac{1}{q} \right)^2 r dr \right. \\ & \left. + \left[\frac{2}{q_a} \left(\frac{n}{m} - \frac{1}{q_a} \right) + (1 + m) \left(\frac{n}{m} - \frac{1}{q_a} \right)^2 \right] a^2 \xi_a^2 \right). \end{aligned} \quad (2.45)$$

The role of ξ_a and the sign of $n/m - 1/q_a$ in equation 2.45 lead to the different stability properties of internal and external modes.

Internal kink mode

Since the perturbation of an internal mode does in a first approximation not affect the plasma boundary ξ_a , the second term on the R.H.S. of equation 2.45 can be set to zero. For $m > 1$ the remaining integral is always positive and internal modes generally stable. For $m = 1$ a displacement (figure 2.3(a)), which is rigid inside $q = 1$ and zero outside (figure 2.3(b)), reduces the integrand to its minimum value, that is zero. Thus the $m = 1$ mode on the $q = 1$ surface is marginally stable and the expansion of δW has to be extended to the next order in ϵ , which also includes pressure effects. It was shown by Bussac *et al* [8] that for simple current profiles toroidal effects like the coupling to $m \pm 1$

sidebands stabilise the internal kink mode up to $\beta_{p,1} \approx 0.3$. Here, the poloidal beta is defined by,

$$\beta_{p,1} = \frac{\langle p \rangle_1 - p(r_1)}{B_p^2(r_1)/2\mu_0} \quad (2.46)$$

where $\langle \rangle_1$ denotes a volume average within the $q=1$ surface. However, the shaping of the poloidal plasma cross section can largely modify the critical value of $\beta_{p,1}$. These shaping effects will be discussed in detail in chapter 6.

An estimate for the growth rate of the internal kink can be obtained by balancing the driving force of the instability determined by the potential energy δW (equation 2.45), against the inertia which is dominated by the return flow within a boundary layer at the $q = 1$ surface,

$$\gamma \approx \frac{4\delta W v_A}{s_1 \xi^2 r_1^2 B_0^2} \quad (2.47)$$

with $v_A = B/(\mu_0 n_i m_i)^{1/2}$ being the Alfvén velocity.

The presence of fast particles as well as collisionless thermal trapped ions have a stabilising effect, which can be accounted for by adding further terms to the potential energy derived from ideal MHD theory,

$$\delta W = \delta W_{\text{MHD}} + \delta W_{\text{fast}} + \delta W_{\text{trapped}}. \quad (2.48)$$

The internal kink mode can generally be avoided by maintaining $q_0 > 1$. Although these profiles are MHD stable it is non-trivial to operate Ohmically heated plasmas at $q_0 > 1$, since the temperature dependence of the conductivity $\sigma \propto T_e^{3/2}$, leads to a peaking of the current profile.

For high-beta plasmas the ordering used in equation 2.45 can no longer be applied and pressure terms have to be taken into consideration. For a sufficiently high beta it is possible to destabilise ideal internal kink modes with $m > 1$. These modes are referred to as *infernal modes* [9].

External kink mode

Even if a movement of the plasma boundary is allowed, modes with a resonant surface inside the plasma, $m/n < q_a$, result in the low-beta approximation in a positive energy functional (equation 2.45) and are always stable. Since q increases outside the plasma, modes with resonant surfaces outside the plasma yield $m/n > q_a$ and can, therefore, be unstable. For $m > 1$, current profiles with large current gradients close to the edge, in particular, are unstable. Therefore, the current profile has to be sufficiently peaked in the plasma centre. For example, in the case of so-called *Shafranov profiles* [10],

$$j(r) = \begin{cases} j_0 & \text{for } r < r_0 \\ 0 & \text{for } r_0 < r < a \end{cases} \quad (2.49)$$

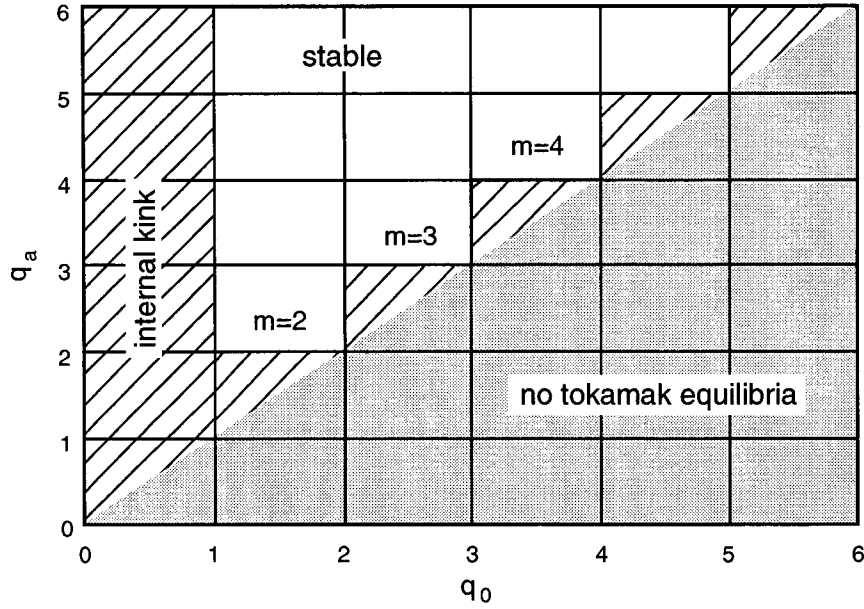


Figure 2.4: Stability of external and internal kink modes in the low beta approximation. The stability limit is most restrictive for $n = 1$ modes. The stability of the external modes is determined using Shafranov current profiles (equation 2.49).

the stability requirement is

$$q_a \geq [q_0] + 1 \quad (2.50)$$

where $[q_0]$ represents the integer part of q_0 . This stability requirement imposes an upper limit to the total current $I_P \propto 1/q_a$ which depends on the central current density $j_0 \propto 1/q_0$, as shown in figure 2.4.

A profile independent current limit is imposed by the external $m = 1$ mode. For a rigid displacement $\xi = \text{const.}$ the integral term on the R.H.S. of equation 2.45 vanishes. The resulting potential energy is,

$$\delta W = \frac{4\pi^2 B_0^2}{\mu_0 R_0} n \left(n - \frac{1}{q_a} \right) a^2 \xi_a^2 \quad (2.51)$$

which depends solely on the total current $\propto q_a$ and not the profiles. The requirement for stability is most restrictive for $n = 1$ and leads to the *Kruskal-Shafranov limit* $q_a > 1$. In practice, the internal kink prevents the central safety factor from decreasing significantly below 1. In agreement with equation 2.50, the appearance of the 2/1 kink-mode imposes the operational current limit,

$$q_a \geq 2. \quad (2.52)$$

In a toroidal geometry pressure effects can become important. For $\beta \sim \epsilon$ the most unstable eigenfunction corresponds to a combination of kinking and ballooning effects and it is no longer possible to distinguish between current and pressure driven modes.

However, it is possible to suppress the external kink mode by moving an ideal conducting wall sufficiently close to the plasma boundary.

2.3.3 Beta limit

Since pressure driven modes can be stabilised by magnetic shear, it is possible to optimise the current and pressure profiles to increase the global beta. Such an optimisation with respect to ballooning and Mercier stability in addition to $n = 1$ external kink modes was carried out by *Troyon et al* [11] and led to the semi-empirical ideal beta limit,

$$\beta[\%] \leq c_T \cdot \frac{I[\text{MA}]}{a[\text{m}]B[\text{T}]} \quad (2.53)$$

with c_T being a constant in the range of $2.8 < c_T < 3.5$. In most regimes the $n = 1$ external ballooning-kink mode was found to set the most severe β -limit. The optimised profiles have a q_0 slightly above unity to satisfy the Mercier criterion and avoid the $m = 1$ internal kink mode. The pressure profile is broad and the q profile is flat over most of the radius and only rises rapidly near the plasma edge. The Troyon limit (equation 2.53) agrees well with the experimental limits found in various tokamaks for a range of shapes and aspect ratios.

2.3.4 Axisymmetric mode

Another instability that needs to be considered is the $n = 0$ external mode. The most unstable perturbation corresponds to a nearly rigid vertical displacement of the plasma, implying a large $m = 1$ component. Substituting $m = 1$ and $n = 0$ into equation 2.45 and assuming a rigid displacement results in $\delta W = 0$, indicating neutral stability of a circular cylindrical plasma. However, if the plasma is elongated it becomes unstable to motion in the direction of elongation. For small elongations the vertical position can be stabilised by a shaping of the external vertical field B_z , requiring a positive magnetic field decay index, $n = -(R/B_z)(\partial B_z/\partial R)$. This mechanism fails at higher elongations and the instability occurs on an inertial time-scale. The stability can be substantially improved by adding a conducting wall. A sufficiently close fitting wall stabilises the axisymmetric mode, while a resistive wall can only slow down its growth rate to one on a resistive time scale. An accurate analysis requires a two-dimensional calculation including toroidicity which adds further stabilising effects.

2.4 Resistive Instabilities

The consideration of the resistivity of the plasma removes constraints from the ideal MHD equation and can thereby make states of lower potential energy accessible to the plasma.

In particular, it allows magnetic field lines to break and reconnect, which can lead to new classes of instabilities such as resistive tearing modes. The relaxation of constraints can also accelerate the growth of existing ideal instabilities. The reconnection of magnetic field lines at a resonant flux surface leads to the formation of magnetic islands.

2.4.1 Magnetic Islands

A non-zero resistivity allows the plasma to diffuse slowly, on a resistive time scale, across magnetic field lines. Rapid reconnection can only occur in the vicinity of a magnetic surface, where the perturbation is resonant and produces a magnetic island configuration. The topology of such a magnetic island located on a rational surface $q = m/n$ is best described in the helical coordinate system $(\hat{e}_\rho, \hat{e}_\zeta, \hat{e}_\eta)$, where \hat{e}_η has the same helicity as field lines on the resonant flux surface, \hat{e}_ρ is perpendicular to the flux surfaces and \hat{e}_ζ perpendicular to both these directions. In a cylindrical approximation the radial flux coordinate ρ , is substituted by r . In the following a $'$ denotes a differentiation with respect to r , an index s the value on the resonant surface and the indices 0 and 1 the equilibrium and perturbed values, respectively. By definition, the ζ -component of the equilibrium field,

$$B_{0\zeta}(r) = B_{0\theta}(r) \left(1 - \frac{q(r)}{q_s}\right) \quad (2.54)$$

vanishes on the resonant surface. If the magnetic shear s (equation 2.41), is approximately constant in the vicinity of the resonant surface, $B_{0\zeta}$ can be written as,

$$B_{0\zeta}(r) \approx - \left(B_{0\theta} \frac{q'}{q} \right) \Big|_s (r - r_s). \quad (2.55)$$

For the case of positive shear, $B_{0\zeta}$ is negative for $r > r_s$ and positive for $r < r_s$. A perturbation current along the field lines causes a radial perturbation of the magnetic field. Considering only one harmonic of the radial magnetic field perturbation,

$$B_{1r} = \hat{B}_{1r}(r) \cos(m\zeta) \quad (2.56)$$

the superposition of the equilibrium field (equation 2.54) and the radial perturbation field (equation 2.56) reveals the new topology as can be seen in figure 2.5. A separatrix is formed between sets of nested flux surfaces, surrounding a local magnetic axis and open flux surfaces. The two parts of the separatrix meet in the so-called x-point and the local magnetic axis is labelled the o-point of the island.

The topology of the magnetic island can also be described in terms of the helical flux (per radian) ψ^* which yields,

$$B_r = \frac{1}{r} \frac{\partial \psi^*}{\partial \zeta} \quad (2.57)$$

$$B_\zeta = - \frac{\partial \psi^*}{\partial r}. \quad (2.58)$$

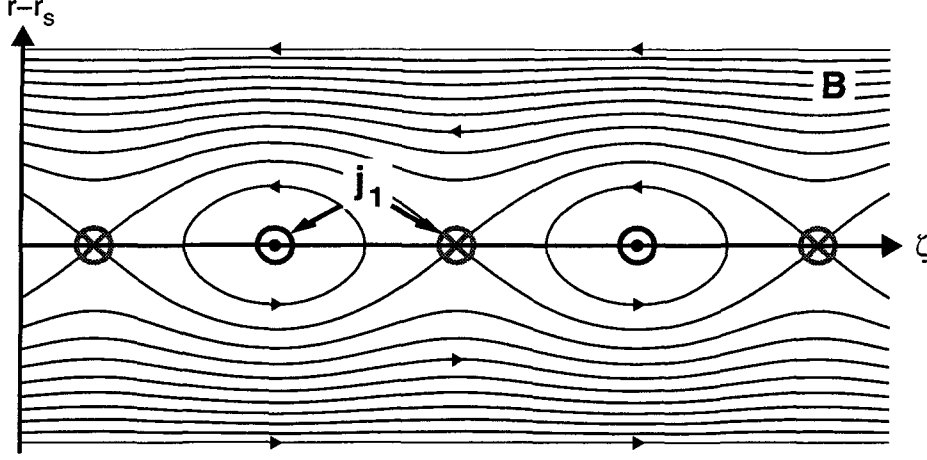


Figure 2.5: Sketch of the island formation resulting from a radial perturbation of the magnetic field. The perturbation is caused by helical perturbation currents j_1 , along the equilibrium field lines on a resonant flux surface at r_s .

The magnetic topology results from the superposition of the equilibrium and the perturbation flux,

$$\psi^*(r, \zeta) = \psi_0^*(r) + \hat{\psi}_1^*(r) \sin(m\zeta). \quad (2.59)$$

In the so-called *constant flux approximation*, radial variations of the perturbed flux ψ_1^* , across the island width are neglected. The equilibrium helical flux is expanded up to the second order of $r - r_s$ with the first order term vanishing due to $\psi_0'^*(r_s) = B_{0\zeta}(r_s) = 0$,

$$\psi^*(r, \zeta) = \psi_0^*|_s + \frac{1}{2}\psi_0^{*''}|_s (r - r_s)^2 + \hat{\psi}_1^*|_s \sin(m\zeta). \quad (2.60)$$

For positive shear, $\psi_0^{*''}|_s$ is positive. Hence, ψ_0^* has a minimum at the resonant flux surface and the separatrix of the island is determined by $\psi^*(r_{\text{sep}}) = \psi_0^*|_s + \hat{\psi}_1^*|_s$. The separatrix is widest at the island's o-point which corresponds to $\zeta = 3\pi/2$. With equation 2.60 the full island width is then given by,

$$w = 4\sqrt{\frac{\hat{\psi}_1^*(r_s)}{|\psi_0^{*''}(r_s)|}}. \quad (2.61)$$

From a diagnostic point of view it is more convenient to express the island width in terms of magnetic fields. Using equation 2.57, $\hat{\psi}_1^*(r_s)$ can be identified as $r_s \hat{B}_{1r}/m$. Substituting equation 2.55 into equation 2.58 and differentiating in the radial direction yields $\psi^{*''} = B_{0\theta}q'/q$. Thus the island width can be written as,

$$w = 4r_s \sqrt{\frac{\hat{B}_{1r}}{mB_{0\theta}s}}|_s = 4r_s \sqrt{\frac{R_0}{r} \frac{\hat{B}_{1r}}{nB_{0\phi}s}}|_s. \quad (2.62)$$

For large islands the radial dependence of the perturbed field and of the magnetic shear have to be taken into account.

2.4.2 Tearing modes

A simple derivation for the growth of magnetic islands will be presented. However, the derivation only applies for modes with $m \geq 2$. The $m = 1$ mode is a special case and will be treated in the section 2.4.3.

Linear growth

In order to describe the growth of magnetic islands, the resistivity of the plasma η , (not to be confused with the index η for the direction along the field line) is accounted for by using Ohm's law (equation 2.10) in the form,

$$\vec{E} + \vec{v} \times \vec{B} = \eta \vec{j}. \quad (2.63)$$

Faraday's equation (equation 2.3) and Ampere's law (equation 2.2) eliminate \vec{E} and \vec{j} and lead to the resistive diffusion equation,

$$\frac{\partial \vec{B}}{\partial t} = \nabla \times (\vec{v} \times \vec{B}) + \frac{\eta}{\mu_0} \nabla^2 \vec{B}. \quad (2.64)$$

The evolution of the perturbed radial field, assuming symmetry along magnetic field lines, is given by,

$$\frac{\partial B_{1r}}{\partial t} = \frac{B_{0\zeta}}{r} \frac{\partial v_{1r}}{\partial \zeta} + \frac{\eta}{\mu_0} \left(\frac{1}{r} \frac{\partial}{\partial r} \left(r \frac{\partial B_{1r}}{\partial r} \right) + \frac{1}{r^2} \frac{\partial^2 B_{1r}}{\partial \zeta^2} \right). \quad (2.65)$$

For a sufficiently small resistivity η , the second term on the R.H.S. of equation 2.65 can be neglected everywhere except in the vicinity of the resonant surface where $B_{0\zeta}$ vanishes. The plasma can be separated into an outer region, where resistive effects are negligible and ideal MHD is valid, and a resistive layer of width d around the resonant surface, where resistive effects are important. In this resistive layer the term which is proportional to $B_{0\zeta}$ in equation 2.65 can be neglected. Furthermore, derivatives in the radial direction dominate over derivatives in the helical direction (long wavelength) and for $r \gg d$, equation 2.65 in the resistive layer yields,

$$\frac{\partial B_{1r}}{\partial t} \approx \frac{\eta}{\mu_0} \frac{\partial^2 B_{1r}}{\partial r^2}. \quad (2.66)$$

Integrating equation 2.66 over the width of the resistive layer d , where B_{1r} is assumed to be approximately constant, gives,

$$d \frac{\partial B_{1r}}{\partial t} \approx \frac{\eta}{\mu_0} \Delta' B_{1r} \quad (2.67)$$

with the tearing parameter Δ' , defined as the jump of the logarithmic derivative of the radial field across the resistive layer,

$$\Delta' = \frac{B'_{1r}(r_s + d/2) - B'_{1r}(r_s - d/2)}{B_{1r}(r_s)}. \quad (2.68)$$

The parameter Δ' is the essential link between the resistive layer and the rest of the plasma and is computed by solving the ideal MHD equation for the radial magnetic field perturbation. The radial field has to be continuous across the resistive layer, while a discontinuity in the first derivative determines Δ' . Finally, the radial perturbation field can be expressed in terms of the island width (equation 2.62) and equation 2.67 becomes the linear growth equation,

$$\frac{\partial w}{\partial t} \approx \frac{\eta}{2\mu_0} \frac{\Delta'}{d} w \quad (2.69)$$

where Δ' determines whether a mode is stable ($\Delta' < 0$) or unstable ($\Delta' > 0$).

Nonlinear growth

However, linear theory is not sufficient to explain the experimental observations, mainly because the island width greatly exceeds the width of the resistive layer. Therefore, nonlinear effects have to be considered. It was shown by *Rutherford* [12] that once the island grows as large as the resistive layer width, second order eddy currents, $j_{2\eta} = v_{1\zeta} B_{1r}/\eta$, cause a new third order force $j_{2\eta} B_{1r}$, which always opposes the $v_{1\zeta}$ flow and reduces the growth rate of the instability. Instead of an exponential growth (equation 2.69), the island width increases linearly in time with a growth velocity,

$$\frac{\partial w}{\partial t} \approx \frac{\eta}{2\mu_0} \Delta'. \quad (2.70)$$

Taking into account modifications of the equilibrium current profile as well as the current profile inside the island, leads to a quasi-linear decrease of the driving term [13]. The island width evolves according to,

$$\frac{\partial w}{\partial t} = 1.66 \frac{\eta}{\mu_0} (\Delta' - \alpha w) \quad (2.71)$$

resulting in a saturated island width, $w_{\text{sat}} = \alpha/\Delta'$. The parameter α is obtained by matching the flux and current density across the island separatrix and depends on local plasma parameters.

Toroidicity and plasma shaping usually have a stabilising effect which can be described by the additional *Glasser-Green-Johnson term* a_{GGJ} [14], resulting in,

$$\frac{\tau_R}{r_s} \frac{dw}{dt} = r_s (\Delta' - \alpha w) - r_s \beta_p \frac{a_{\text{GGJ}}}{w} \quad (2.72)$$

where τ_R is the resistive diffusion time $\mu_0 r_s^2 / 1.66\eta$. Equation 2.72 is usually referred to as the *Rutherford equation*.

In summary, the island evolves in several phases starting with a brief exponential growth (equation 2.69), which is replaced by a linear growth as soon as the island width is comparable to the resistive layer width (equation 2.70). Finally, the island saturates

according to equation 2.71. However, at high beta and low collisionality, neoclassical effects become important, in particular the effect of the bootstrap current. The role played by a perturbation of this current as a further driving term for magnetic islands will be treated in detail in section 9.1.

2.4.3 Resistive internal kink mode

The $m = 1$ mode requires separate treatment as it is also susceptible to be ideally unstable. It was shown in section 2.3.2 that the most unstable perturbation is a step function (figure 2.3(b)), which rapidly changes at the resonant surface. Therefore, the assumption of a constant perturbation field across the resistive layer, which was used in section 2.4.2 for $m \geq 2$ is no longer valid. The steep gradients at the resonant layer drive the reconnection and the mode is unstable to all profiles with $q_0 < 1$. The flow field at the resonant layer, which was determined by inertial effects in the ideal case, is now determined by resistive effects. The growth rate is estimated by,

$$\gamma \approx s^{2/3} \tau_R^{-1/3} \tau_A^{-2/3} \quad (2.73)$$

where $\tau_A = R(\mu_0 n_i m_i)^{1/2} / B_0$ is the Alfvén time. The growth rate for $m = 1$ is generally much larger than that for $m \geq 2$. However, this growth rate depends on whether the ideal mode is unstable, marginal or stable [15].

Chapter 3

The TCV experiment

This work was carried out on the TCV tokamak experiment of the Centre de Recherches en Physique des Plasmas (CRPP) at the Ecole Polytechnique Fédérale de Lausanne. This chapter presents the tokamak, its electron cyclotron heating (ECH) system and the plasma diagnostics which are relevant to this thesis. The reconstruction of equilibria with the LIUQE code, which forms the basis of the interpretation of many measurements and stability calculations, is also introduced.

3.1 Tokamak

The *Tokamak à Configuration Variable* (TCV) is a medium size highly elongated tokamak. It started operation in November 1992 with the main aim to investigate the effect of plasma shape on confinement and stability. TCV was designed to produce a large variety of plasma shapes without requiring hardware modifications. The main machine parameters

Parameter	Symbol	Value (projected)
Major radius	R_0	0.88 m
Minor radius	a	0.25 m
Aspect ratio	$\epsilon = R_0/a$	≈ 3.5
Vacuum vessel elongation	κ_{TCV}	2.9
Toroidal vessel resistance	Ω_{TCV}	45 m Ω
Toroidal field on axis	B_0	≤ 1.54 T
Plasma current	I_P	≤ 1 MA (1.2 MA)
Loop voltage	V_{loop}	≤ 10 V
Additional heating power (ECH)	$P_{\text{ECH}, \text{X2}}$	2.8 MW
	$P_{\text{ECH}, \text{X3}}$	0.48 MW (1.4 MW)
Discharge duration		< 4 s

Table 3.1: Main TCV machine parameters.

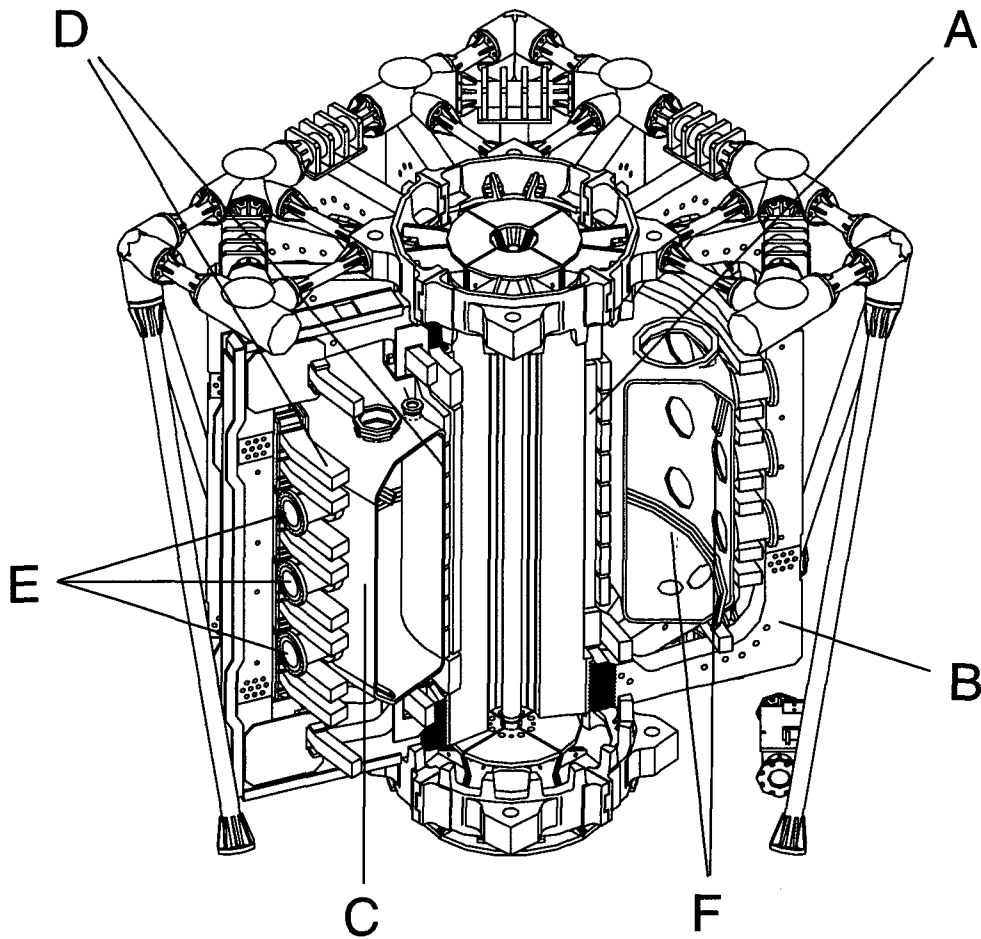


Figure 3.1: Schematic view of TCV showing the OH-transformer coils (A), the toroidal field coils (B), the vacuum vessel (C), the poloidal field coils (D), diagnostic ports (E), and internal control coils (F) .

are listed in table 3.1 and a schematic of the tokamak is shown in figure 3.1.

TCV is equipped with an air core transformer which consists of the coils A1, B1,2, C1,2 and D1,2 as shown in figure 3.2. Their positions and numbers of turns were chosen in order to minimise the perturbation of the magnetic field inside the vacuum vessel. The toroidal field is produced by 16 toroidal field coils which are connected in series. The poloidal field, resulting from the currents in the bus bar which connects adjacent coils, represented by the toroidal conductors T1,2 (see figure 3.2), is mainly compensated for by the current in the return loop T3 (see figure 3.2).

3.1.1 Plasma shaping and control

The flexibility in plasma shaping is achieved by 16 independently controlled poloidal field coils which are mounted in two vertical stacks on both sides of the plasma outside the vac-

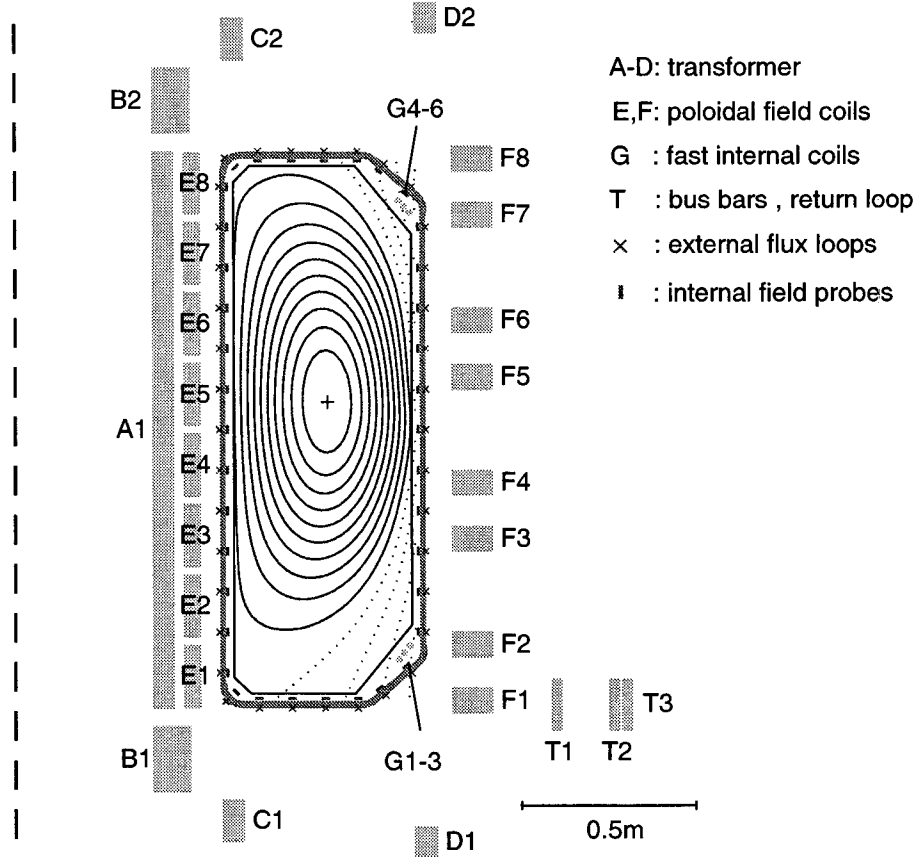


Figure 3.2: Coil configuration showing the transformer windings (A, B, C, D), the poloidal field coils (E, F) and the fast internal coils (G). The bus bars (T1,T2) connecting the toroidal field coils, are partially compensated by the return loop (T3). The magnetic configuration is measured with external flux loops (x) and internal poloidal field coils.

uum vessel (coils E1-8 and F1-8 in figure 3.2). In particular, the operation at high plasma elongation requires a good control of the vertical plasma position (see section 2.3.4), which is achieved by a combination of passive elements and active feedback control. The toroidally continuous, highly conducting vessel wall acts as a passive shell allowing eddy currents which oppose a change of the equilibrium. The low resistance of the vessel leads to long decay times of toroidal vessel currents, for example 8 ms for the $m = 1$ mode. For an active feedback control, the plasma position is observed in real time with flux loops outside and poloidal field probes inside the vacuum vessel. Two toroidally opposed arrays of probes are used to suppress a perturbation from non axis-symmetric $n = 1$ fluctuations. The feedback stabilisation uses the external poloidal field coils together with two further poloidal field coils which are located inside the vacuum vessel near the outer corners (coils G1-6 in figure 3.2). The internal coils allow a shorter response time of 0.1 ms, ten times faster than the external coils. The TCV control system has made it possible to stabilise plasmas with open loop growth rates up to 4400 s^{-1} [16].

3.1.2 Plasmas

TCV has produced a wide range of limited and various diverted configurations, amongst these are the limited, single null diverted (SND) and double null diverted (DND) discharges shown in figure 3.3(a)-(d). To date, Ohmic H-modes (high energy confinement) have been obtained with Edge Localised Modes (ELMy H-mode) and without (ELM-free H-modes) in both limited and diverted configurations. Plasma currents up to 1 MA have been attained (figure 3.3(e)) and purely wave driven currents up to 210 kA achieved (figure 3.3(f)). The plasma shapes span a wide parameter range with elongations from 1 to 2.8 and triangularities from -0.8 to 0.9 (figure 3.3(i)-(k)). Rectangular shapes were also produced (figure 3.3(l)). A list of typical values of various plasma parameters is given in table 3.2.

Parameter	Symbol	TCV values
Central electron density	n_{e0}	$1 - 20 \cdot 10^{19} \text{ m}^{-3}$
Central electron temperature	T_{e0}	$< 1 \text{ keV (Ohmic)}$ $< 15 \text{ keV (ECW)}$
Central ion temperature	T_{i0}	$< 800 \text{ eV (Ohmic)}$ $< 500 \text{ eV (ECW)}$
Alfvén velocity	$v_A = B/(\mu_0 n_i m_i)^{1/2}$	$1.5 - 7 \cdot 10^6 \text{ m/s}$
Alfvén time	$\tau_A = R/v_A$	$0.1 - 0.6 \mu\text{s}$
Plasma frequency	$f_p = (e^2 n_e / (\epsilon_0 m_e))^{1/2} / (2\pi)$	$28 - 120 \text{ GHz}$
Electron cyclotron frequency	$f_{ce} = eB/m_e / (2\pi)$	$\sim 41 \text{ GHz}$
Ion cyclotron frequency	$f_{ci} = ZeB/m_i / (2\pi)$	$\sim 11 \text{ MHz}$
Electron Larmor radius	$\rho_e = (2m_e k_B T_e)^{1/2} / (eB)$	$70 - 250 \mu\text{m}$
Ion Larmor radius	$\rho_i = (2m_i k_B T_i)^{1/2} / (eB)$	$2.5 - 4.0 \text{ mm}$
Elongation	κ	$1 - 2.8$
Triangularity	δ	$-0.8 - 0.9$

Table 3.2: Typical parameters in Ohmically and ECH/ECCD heated TCV plasmas.

3.1.3 First wall

The internal surface of the stainless steel vacuum vessel has to meet the demands of the variety of configurations, with wall components being required to play the role of both limiter and divertor surfaces. Therefore, 90% of the internal surface is covered with 24 mm thick graphite tiles, designed to withstand the large power fluxes during ECH heating and eliminate plasma contamination by metallic impurities. Standard vessel conditioning

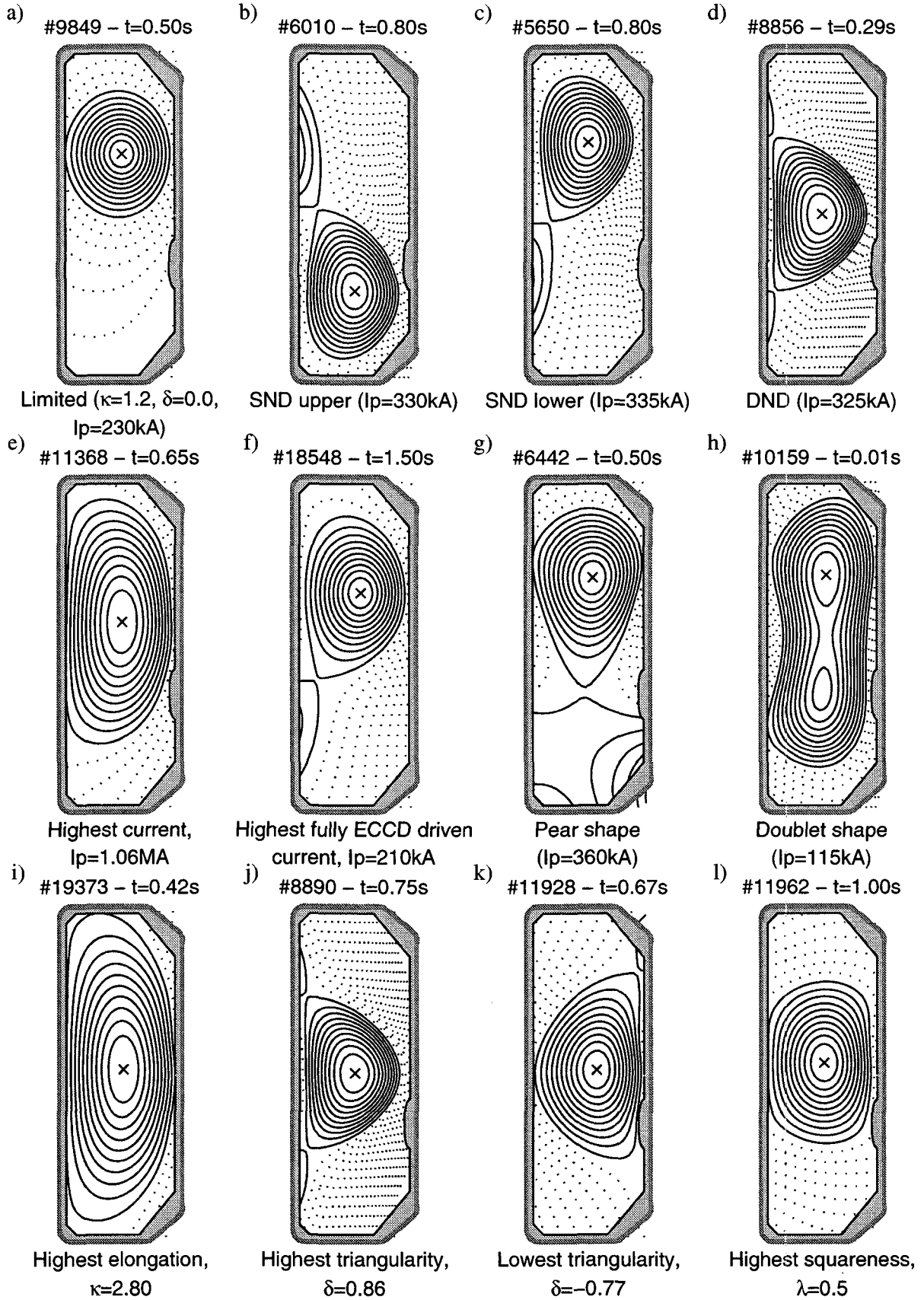


Figure 3.3: Various plasma configurations and shapes achieved in TCV. (a)-(d) show limited, single-null-diverted (SND), and double-null-diverted (DND) configurations, (e)-(h) TCV peculiarities, and (i)-(l) the highest shaping parameters currently achieved.

techniques comprise the bake-out of the vessel at temperatures up to 250° C and boronisation by plasma chemical vapour deposition in a 10%B₂D₂/90%He gas mixture. The boronisation is typically carried out 2-3 times a year, with each treatment depositing a boron layer of 10 nm. During operation the typical base vacuum level resides at a pressure of $1 \cdot 10^{-8}$ mBar. Helium glow discharge cleaning is regularly used between tokamak discharges as a means of controlling the short term surface properties.

3.2 Electron cyclotron heating system

TCV is equipped with a very flexible electron cyclotron heating (ECH) and electron cyclotron current drive (ECCD) system, which was designed to access a wide range of plasma shapes. The system consists of six 82.7 GHz gyrotrons for heating at the second harmonic of the electron cyclotron resonance ω_{2ce} , and three 118 GHz gyrotrons for heating at the third harmonic ω_{3ce} [17]. These frequencies correspond to near central heating for a toroidal field of 1.45 T. The nominal power is 465 kW for each of the 82.7 GHz gyrotrons and 480 kW for each of the 118 GHz gyrotrons, resulting in a total HF power of 4.2 MW for a maximum pulse length of 2 s. The gyrotrons are grouped into three clusters of three units with a separate power supply for each cluster. Each gyrotron couples the HF beam through a matching optics unit to an evacuated transmission line where it propagates to a quasi optical launching antenna installed on the tokamak. The polarisation of each beam can be modified and is usually set for propagation as an extraordinary wave (X2-, X3-mode).

X2 system

For each cluster of X2 gyrotrons, there is one launcher mounted in an equatorial port (L1 and L4 in figure 3.4) and two launchers (L2, L3 and L5, L6 in figure 3.4) mounted in upper lateral ports. Each launcher has two degrees of freedom, one of which provides steering of the microwave beam in a fixed plane during a discharge. The other allows to rotate the sweeping plane between discharges, for example to introduce a toroidal injection angle for current drive experiments. The polarisation of the wave is optimised for the launching geometry of each shot. The X2 system allows to heat and drive current in plasmas with a density up to the cut-off density for the X2-mode propagation, $n_{e,\text{cut-off,X2}} = 4.25 \cdot 10^{19} \text{ m}^{-3}$.

X3 system

The three gyrotrons of the X3 cluster are combined in one launcher at the top of the vessel (figure 3.4). The microwave beam is injected nearly tangentially to the resonant surface to maximise the absorption by increasing the path length through the resonance. The launching mirror can be displaced radially between discharges to inject the beam

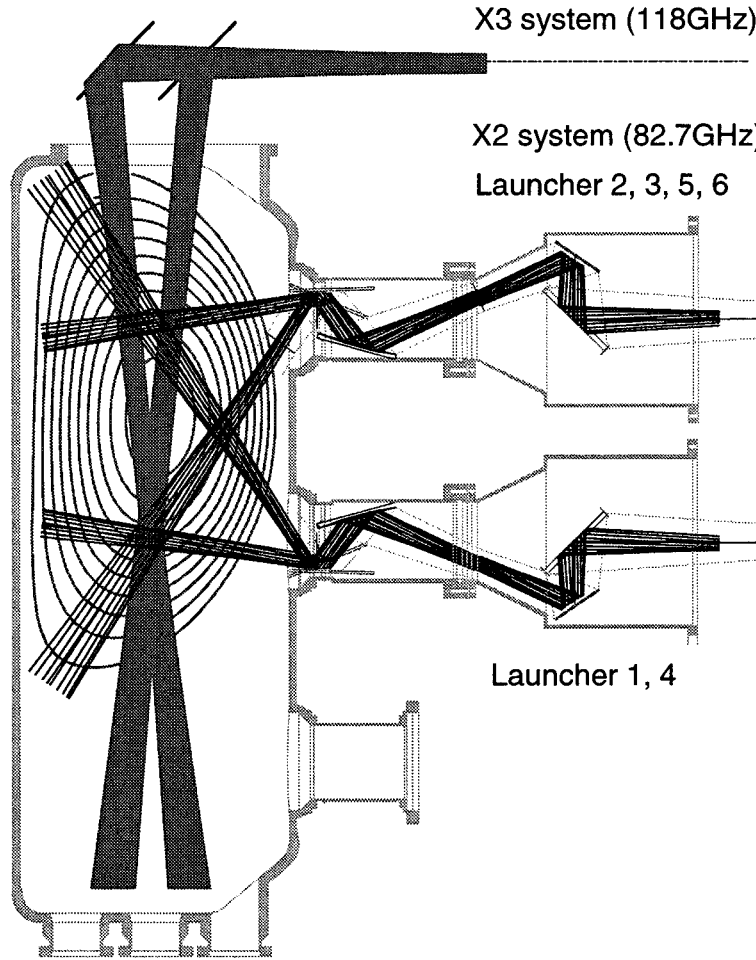


Figure 3.4: Beam lines of the X2 and the X3 ECH system. The X2 launchers are placed on two equatorial (L1, L4) and four upper lateral ports (L2, L3, L5, L6). Two degrees of freedom allow the access of a wide range of heating locations and current drive. The X3 launcher is mounted on the top of the machine and can be radially displaced to view the resonance from the high or low field side.

from either the low (LFS) or high field side (HFS) of the resonance. The mirror can also be rotated during the discharge allowing adjustment of the beam along the resonance surface. The X3-mode injection extends the accessible density domain up to $n_{e,\text{cut-off},X3} = 11.5 \cdot 10^{19} \text{ m}^{-3}$.

3.3 Diagnostics

TCV is equipped with a number of diagnostics measuring many different plasma parameters. Only the diagnostics providing the most important measurements for the presented analysis are described here.

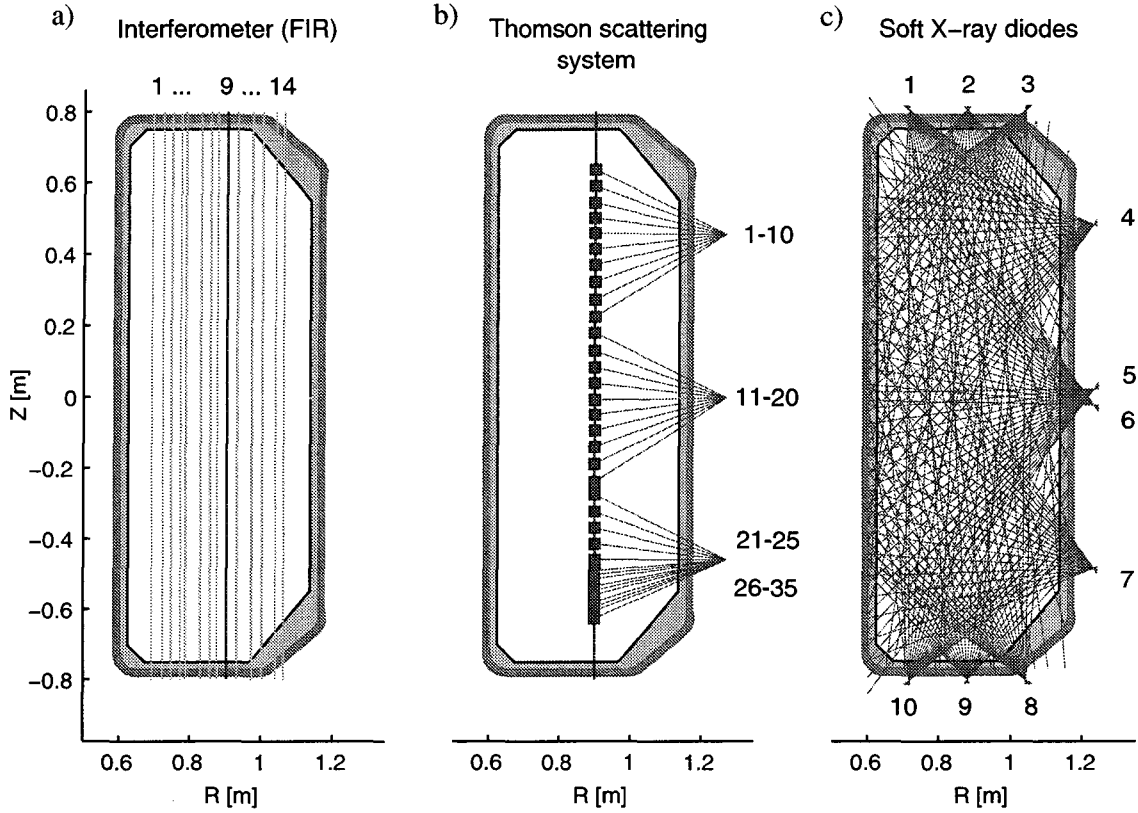


Figure 3.5: Geometry of (a) the 14 diagnostic chords of the FIR interferometer (the central chord is highlighted), (b) the laser and 35 viewing chords of the Thomson scattering diagnostic and (c) the 200 lines of sight of the soft X-ray diodes used for the tomographic reconstruction of the emissivity.

3.3.1 Far-infrared interferometer (FIR)

The line integrated electron density \bar{n}_e , is measured with a Mach-Zehnder interferometer. The interferometer measurement uses the density dependence of the refractive index of an electro-magnetic wave in a plasma. For a frequency much larger than both the plasma frequency and the electron cyclotron frequency, $\omega \gg \omega_p, \omega_{ce}$, the refractive index of the ordinary (equation 1.16) and extraordinary (equation 1.17) waves can be approximated by,

$$N_O \approx N_X \approx 1 - \frac{1}{2} \left(\frac{\omega_p}{\omega} \right)^2. \quad (3.1)$$

The line integrated density is proportional to the phase shift $\Delta\Phi$, between a beam passing through the plasma and a reference beam outside the plasma,

$$\Delta\Phi = \frac{\lambda e^2}{4\pi c^2 \epsilon_0 m_e} \int n_e(l) dl. \quad (3.2)$$

The instrument installed on TCV uses a heterodyne technique to measure this phase shift. In this case, the probing beam is superposed with a reference beam with a well

known phase behaviour, called a local oscillator (LO). The frequency of the LO beam has a slight frequency offset $\Delta\omega$, from the probing beam at ω_0 . Since the beams are coherent the electric field vectors, $E_{\text{probe}} = \hat{E}_{\text{probe}} e^{i(\omega_0 t + \Phi(t) + \phi_{\text{probe}})}$ and $E_{\text{LO}} = \hat{E}_{\text{LO}} e^{i(\omega_0 t + \Delta\omega t + \phi_{\text{LO}})}$ of the probing and LO beam can be summed. The detector measures the intensity I_{plasma} , of the mixed beams,

$$\begin{aligned} I_{\text{plasma}} &\propto (E_{\text{probe}} + E_{\text{LO}})(E_{\text{probe}} + E_{\text{LO}})^* \\ &= \hat{E}_{\text{probe}}^2 + \hat{E}_{\text{LO}}^2 + 2\hat{E}_{\text{probe}}\hat{E}_{\text{LO}} \cos(\Delta\omega t - \Phi(t) + \phi_{\text{LO}} - \phi_{\text{probe}}) \end{aligned} \quad (3.3)$$

whose amplitude oscillates with the beat frequency $\Delta\omega$, of the two beams. After filtering out the DC terms the remaining signal is,

$$S_{\text{plasma}} \propto \hat{E}_{\text{probe}}\hat{E}_{\text{LO}} \cos(\Delta\omega t - \Phi(t) - \phi_{\text{plasma}}) \quad (3.4)$$

with $\phi_{\text{plasma}} = \phi_{\text{probe}} - \phi_{\text{LO}}$ being a constant, which depends only on the optical length of the paths in the experimental setup. The phase shift $\Phi(t)$, due to the plasma can be determined by comparing the phase of the plasma signal S_{plasma} , to that of the reference signal,

$$S_{\text{ref}} \propto \hat{E}_{\text{probe}}\hat{E}_{\text{LO}} \cos(\Delta\omega t - \phi_{\text{ref}}). \quad (3.5)$$

The detected phase shift, $\Phi(t) + \phi_{\text{plasma}} - \phi_{\text{ref}}$, is the plasma induced phase shift with a constant offset due to the different path lengths of the various beams.

The TCV system [18] comprises 14 vertical chords in a single poloidal plane as shown in figure 3.5(a). The interferometer uses an optically pumped CH_2F_2 far-infrared (FIR) laser with a wavelength of $214.6 \mu\text{m}$. The frequency offset of $\Delta\omega/2\pi = 100 \text{ kHz}$ is produced by the Doppler shift caused by diffraction off a rotating grating. The signal detectors (InSb hot electron bolometers) have an extremely low noise equivalent power and their frequency response of up to 750 kHz is sufficient to resolve the 100 kHz beat frequency. The beat frequency sets the limit of the time resolution of the density measurement. At the chosen wavelength and according to equation 3.2 a phase shift of 2π corresponds to a change of the line integrated density of $1.04 \cdot 10^{19} \text{ m}^{-2}$. The accuracy of the phase analysis is about 20 degrees and leads to a resolution limit of approximately $\Delta\bar{n}_e \approx 5 \cdot 10^{17} \text{ m}^{-2}$.

3.3.2 Thomson scattering

TCV is equipped with a multi-point Thomson scattering diagnostic for electron temperature T_e , and density n_e , measurements [19, 20]. The measurement is based on the spectral analysis of light which is scattered by the free electrons in the plasma. If the wave vector k_i of the input wave is sufficiently large, yielding $k_i \lambda_D \gg 1$, particle correlations can be ignored and the scattered power can be obtained as an incoherent sum of powers from

single electrons. The scattered field from a single electron moving with a velocity \vec{v}_e has a frequency,

$$\omega_s = \omega_i + (\vec{k}_s - \vec{k}_i) \cdot \vec{v}_e \quad (3.6)$$

which is the Doppler shifted frequency with respect to the input wave with a frequency ω_i . In the non-relativistic approximation and for a monochromatic incident wave the frequency spectrum for a fixed scattering geometry is directly proportional to the one-dimensional velocity distribution in the direction along $\vec{k} = \vec{k}_s - \vec{k}_i$. Assuming a Maxwellian electron distribution the electron temperature is obtained from the width of the measured spectrum. For $T_e > 5$ keV relativistic effects should be taken into account. The intensity of the scattered light is proportional to the electron density. Thus, density measurements can be obtained by integrating the scattered signal over the width of the spectrum.

The system on TCV uses three Q-switched Nd:YAG lasers which operate at a pulse rate of 20 Hz each. The beams are combined to form a closely spaced fan within a poloidal plane. From the side of the detection optics this fan appears like a single beam (see figure 3.5(b)). Using alternate triggering of the lasers, higher sampling rates (60 Hz average) can be obtained. Thirty-five viewing chords are distributed on three horizontal ports. Each chord views a scattering volume of 4 cm along the laser beam. The scattered radiation is analysed with filter polychromators with three or four spectral channels which have been optimised for temperatures in the range of 50 eV – 20 keV. To determine the electron density the absolute magnitude of the scattered signal is calibrated against Raman scattering from molecular Nitrogen. The electron density measurement is cross-checked by comparing the line integrated data to those obtained from the interferometer (section 3.3.1).

3.3.3 Soft X-ray emissivity measurements

The soft-X-ray emission of a plasma originates from electron-ion and electron-impurity Bremsstrahlung as well as recombination radiation. The Bremsstrahlung spectrum essentially depends on density, temperature and impurity content. For a Maxwellian electron distribution and ions of charge Z the continuous Bremsstrahlung spectrum is,

$$\frac{dN}{dE_X} \propto Z^2 n_e n_Z \frac{g_{ff} e^{-E_X/T_e}}{E_X \sqrt{T_e}} \quad (3.7)$$

with N being the number of emitted photons of an energy E_X . The calculation of the electron-impurity-ion recombination radiation is complicated as a detailed knowledge of the atomic structure of the impurity ion is required.

In TCV, soft X-ray emission of the plasma is measured with photodiodes, which are sensitive up to 10 keV. Energies below 1 keV, which can originate from impurity line radiation, are filtered with a Beryllium absorption foil of 47 μ m thickness. The TCV

system [21] consists of 10 pinhole cameras, each comprising one strip of 20 Silicon pin diodes. The cameras are distributed in 9 ports of a single poloidal sector giving full poloidal coverage (figure 3.5(c)). The resulting 200 lines-of-sight are used to perform a tomographic reconstruction of the local X-ray emissivity for all plasma configurations on TCV. The spatial resolution of the tomographic inversion is 30 – 40 mm. The temporal resolution is limited by the acquisition system allowing sampling rates of up to 80 kHz.

Four further diodes are arranged in an equidistantly spaced toroidal array. They are placed at the top of the vessel viewing the plasma along a vertical chord at $R = 0.84$ m, passing the plasma centre at a distance of about 7 cm. The diodes are equipped with 50 μ m Be filters and the measurements acquired with up to 250 kHz.

Owing to the dependence of E_X on n_e and T_e , which are both approximately constant on magnetic flux surfaces, the soft X-ray measurements are sensitive to the presence of MHD instabilities. The tomographic reconstruction allows to determine the sawtooth inversion radius [22] and identify the poloidal mode structure of modes. The toroidal array adds information about the toroidal mode structure by resolving low toroidal mode numbers $n = 1, 2$. Since the diodes are sensitive to photon energies above 1 keV only electrons above approximately 400 eV contribute to the signal. Thus, the soft X-ray diagnostic mainly measures central phenomena and therefore, provides complementary information to the magnetic measurements, which will be described in detail in chapter 4.

3.4 Equilibrium reconstruction

The problem of the equilibrium reconstruction consists of finding a solution $\psi(R, Z)$, to the Grad Shafranov equation (equation 2.29), repeated here,

$$R \frac{\partial}{\partial R} \left(\frac{1}{R} \frac{\partial \psi}{\partial R} \right) + \frac{\partial^2 \psi}{\partial Z^2} = -\mu_0 R^2 p'(\psi) - I(\psi) I'(\psi) \quad (3.8)$$

where $\psi = \psi_{\text{pol}}/2\pi$ is the poloidal stream function introduced in equation 2.22. The arbitrary source functions $p'(\psi)$ and $I(\psi)I'(\psi)$, with the ' denoting differentiation with respect to ψ and I defined according to equation 2.28 are chosen, such that measurements are reproduced as accurately as possible. However, this problem is ill posed, since $p'(\psi)$ and $I(\psi)I'(\psi)$ must be given as functions of ψ , whose spatial dependence is not known until equation 3.8 is solved. Consequently, an iterative scheme like the one described below has to be employed.

The reconstruction using magnetic measurements only, encounters a fundamental problem which results from the decomposition of the toroidal current density into two parts, one proportional to Rp' and the other to II'/R , as can be seen from equation 2.25. The relative importance of these terms can only be determined due to the difference in their R -dependence and the accuracy of this decomposition rapidly decreases as one moves

from the plasma boundary towards the magnetic axis. Therefore, the inclusion of internal measurements can greatly improve the accuracy of the reconstruction.

The TCV equilibria are reconstructed using the Grad-Shafranov solver LIUQE [6]. The standard reconstruction, calculated immediately after each discharge, uses the magnetic measurements from the flux loops and poloidal field probes shown in figure 3.2. It is optional to include further experimental data, such as pressure measurements from the Thomson scattering diagnostic (section 3.3.2), measurements from a diamagnetic loop, the inversion surface of sawteeth obtained from the tomographic reconstruction of the soft X-ray emissivity [22], and/or Faraday rotation measurements from a polarimeter [18]. The source functions are expanded into a series of pre-defined base functions,

$$p' = \sum_{n=0}^{N_p} a_n U_n(\psi) \quad (3.9)$$

$$II' = \sum_{n=0}^{N_T} b_n U_n(\psi) \quad (3.10)$$

$$(3.11)$$

where a_n and b_n are constants to be determined. The base functions are defined as functions of the normalised poloidal flux $\phi = (\psi - \psi_a) / (\psi_0 - \psi_a)$, yielding $\phi = 0$ at the edge and $\phi = 1$ on axis,

$$U_0 = 1 \quad (3.12)$$

$$U_1 = \phi \quad (3.13)$$

$$U_2 = 1 - (2\phi - 1)^2 \quad (3.14)$$

$$U_3 = [1 - (2\phi - 1)^2] (2\phi - 1). \quad (3.15)$$

The base functions $U_1 - U_3$ are shown in figure 3.6. The optimum number and combination of source functions depends on the properties of the analysed equilibrium and the type of measurements available.

LIUQE solves the reconstruction problem by an iterative procedure, which is as follows:

1. A rough approximation of the plasma current distribution $j_{\text{tor}}(R, Z)$, is found using a fast magneto-static method.
2. The Grad-Shafranov equation, $\Delta^* \psi(R, Z) = j_{\text{tor}}(R, Z)$, is solved using the measured flux as a boundary condition to obtain $\psi(R, Z)$.
3. The profile parameters a_n and b_n are computed so as to obtain the best fit of the measurements, minimising $\chi^2 = \sum_i [(M_i - M_i^*) / \Delta M_i]^2$, where M_i^* is the reconstructed measurement and ΔM_i the typical RMS error of the measurement, M_i . The flux $\psi(R, Z)$ is assumed fixed.

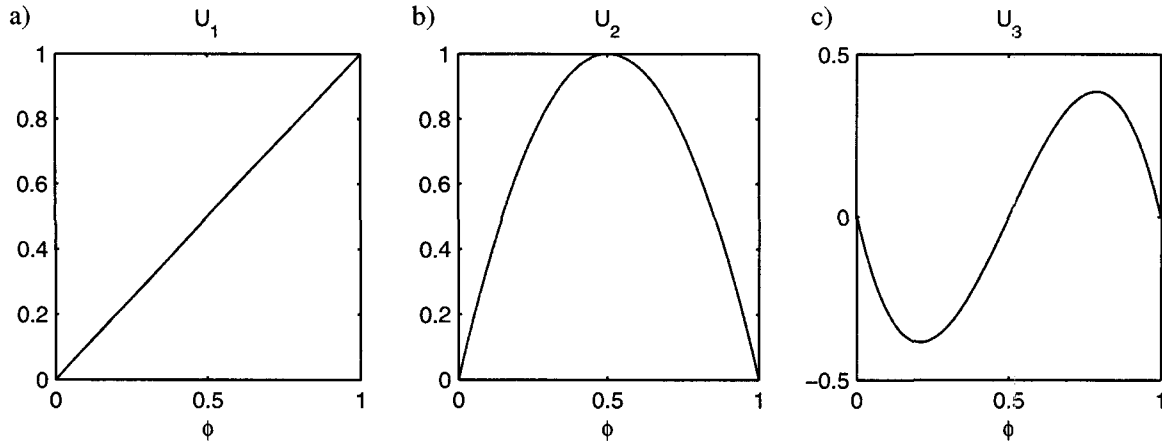


Figure 3.6: LIUQE base functions U_n , with $n = 1 - 3$, used for the reconstruction of the p' and II' profiles.

4. The toroidal current density $j_{\text{tor}} = Rp' + (\mu_0 R)^{-1}II'$, is computed as a function of R and Z using the profiles $p'(\psi)$ and $II'(\psi)$ fitted in the previous step as well as $\psi(R, Z)$ obtained in step 2.
5. The steps 2-4 are repeated until a suitable convergence criterion is satisfied.

The accuracy of the LIUQE reconstruction depends on the plasma size and the magnitude of the plasma current, which determine the number of useful measurements and the signal amplitude, respectively. It is also important that the chosen polynomial base functions have sufficient degrees of freedom to describe the actual profiles. An estimate of the accuracy can be obtained by comparing flux surfaces with measured plasma parameters, which are assumed to be constant on flux surfaces, such as the soft X-ray emissivity, temperature or density. The existence of sawteeth and their inversion radius also allow a cross-check of the reconstructed safety factor on axis q_0 , and the location of the $q = 1$ surface.

3.5 Concluding remarks

The unique shaping capabilities make the TCV tokamak particularly attractive for MHD analysis. It not only allows the exploration of extreme parameter ranges and the monitoring of the MHD behaviour, but will also prove to be a powerful tool for the probing of the behaviour of MHD instabilities which can strongly depend on the geometry. The powerful and flexible heating system allows the attainment of high temperatures in various shaped plasmas. More importantly, it provides a local power deposition which allows to tailor pressure and also current profiles, which are crucial for the stability of the plasma.

The analysis of instabilities requires diagnostics which detect them, resolve their structure and their temporal evolution. For central modes this is performed by the soft X-ray

diagnostic, which will be complemented by fast magnetic fluctuation measurements mainly monitoring the plasma edge (see chapter 4). In addition to the characterisation of the instabilities, relevant plasma parameters have to be measured. The main parameters are electron temperature and density measured with the Thomson scattering diagnostic and the FIR-interferometer.

Chapter 4

Fast magnetic fluctuation diagnostic

On TCV magnetic measurements are used for real time control of the plasma shape, off-line reconstruction of the magnetic topology, and monitoring of fast magnetic fluctuations. Various sensors include poloidal flux loops, saddle loops and poloidal field probes. However, only the magnetic probes installed inside the vacuum vessel provide measurements whose time resolution is not limited by the magnetic diffusion time of the conducting vacuum vessel. Since the typical time scales of MHD instabilities are much shorter than the magnetic diffusion time, for example 8 ms for the $m = 1$ mode, only the magnetic probes are well suited to monitor fast magnetic fluctuations.

This chapter describes the magnetic probes with regard to their use as a fast fluctuation diagnostic. It includes the arrangement in arrays and the design of the probes. The characteristics of the probes were determined by an absolute calibration. The described calibration setup allowed to determine each probes response over a wide frequency range which is of particular importance for fast fluctuation measurements. A description of the signal processing up to the data acquisition is also given.

4.1 Probe arrangement

The wide range of plasma shapes requires a dense set of magnetic measurements. Currently 203 poloidal pick-up coils are installed inside the TCV vessel. These probes are arranged in toroidal and poloidal arrays. There are four complete poloidal arrays of 38 probes each, located in the sectors 3, 7, 11 and 15, which are toroidally separated by 90° . These probes are evenly distributed around the poloidal circumference as shown in figure 4.1(a). The poloidal position is numbered clockwise starting on the equatorial mid-plane on the high-field side of the vessel. Currently only one poloidal array is used for fast measurements. TCV was originally equipped with two complete toroidal arrays of probes located in the equatorial mid-plane on the low- (LFS) and high-field side (HFS). These arrays consisted of 16 and 8 equidistant probes, respectively. In 1997 two further

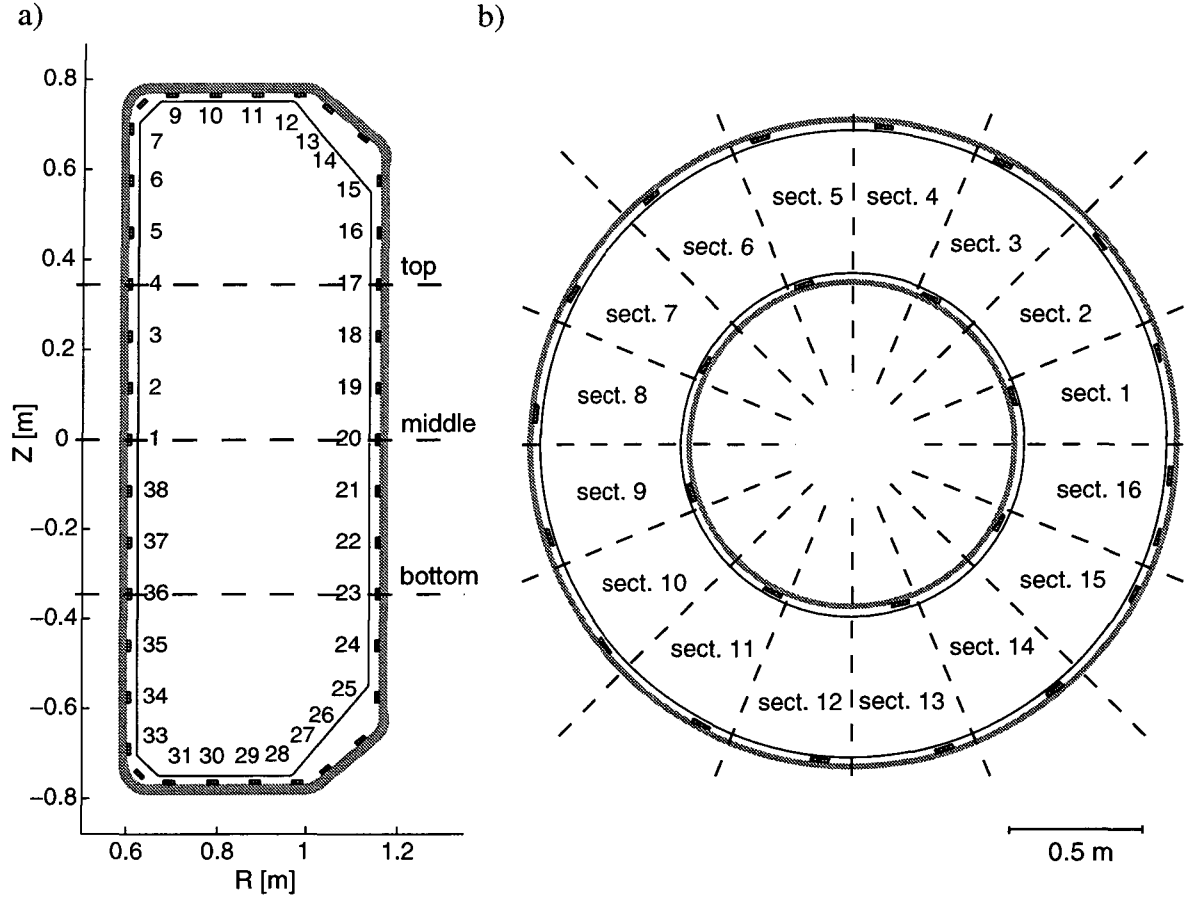


Figure 4.1: Arrangement of the TCV magnetic probes in poloidal and toroidal arrays. (a): The 38 probes of each poloidal array are numbered clockwise starting on the equatorial mid-plane on the high field side of the vessel. The poloidal locations of the six toroidal arrays are indicated (dashed lines). (b): Full toroidal arrays are located on the low- and high-field side consisting of 17 and 8 probes, respectively.

arrays were added on each side, 35 cm above and below the mid-plane, allowing for a larger signal amplitude for plasmas shifted towards the bottom or top of the vessel. The poloidal locations of the toroidal arrays are indicated in figure 4.1(a). Furthermore, the arrays on the LFS were complemented by a 17th probe in sector 16A, thus increasing the resolution of toroidal mode numbers up to $n = 16$. The location of the probes forming the toroidal arrays are shown in figure 4.1(b).

The magnetic probes are mounted directly on the inside of the vacuum vessel, where they are protected from the plasma by graphite tiles. The probes measure the component of the poloidal magnetic field parallel to the vessel wall. They are spring loaded against rails as can be seen in figure 4.2.

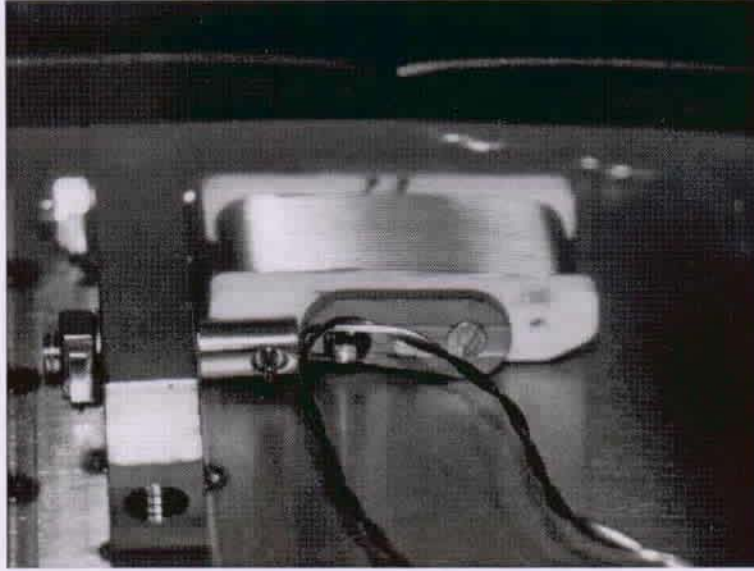


Figure 4.2: Magnetic probe mounted inside TCV close to the vessel wall.

4.2 Magnetic probe

Magnetic pick-up coils measure the time derivative of the magnetic flux which induces the voltage,

$$U_p = -\frac{\partial}{\partial t} \int_{\text{probe}} \vec{B} d\vec{A}. \quad (4.1)$$

Assuming that the variations of the magnetic field within the probe volume are small, the measurement determines the time derivative of the magnetic field along the axis of the probe. Owing to $(\vec{\nabla} \times \delta\vec{B})_r = 0$ in the absence of a current density, the poloidal perturbation field outside the plasma δB_θ , is larger than the toroidal perturbation field δB_φ , typically exceeding it by one order of magnitude [23]. An alignment of the probe along the poloidal direction is, therefore, well suited for the analysis of magnetic fluctuations.

4.2.1 Construction

The probes presently installed in TCV have an improved design and replaced the first generation of TCV probes [24] in 1997. The probes consist of a 1 mm *THERMOCOAX*® mineral insulated coaxial wire which is wound in one layer around a ceramic body. The windings were designed to minimise the effective areas perpendicular to the main probe axis. Further design constraints were the 400° C baking capability of the vacuum vessel, a maximum 12 mm gap between the wall and the graphite tiles and an appropriate signal level avoiding large voltage spikes, which could cause short circuits between the central conductor and the shield. A schematic of a probe is shown in figure 4.3.

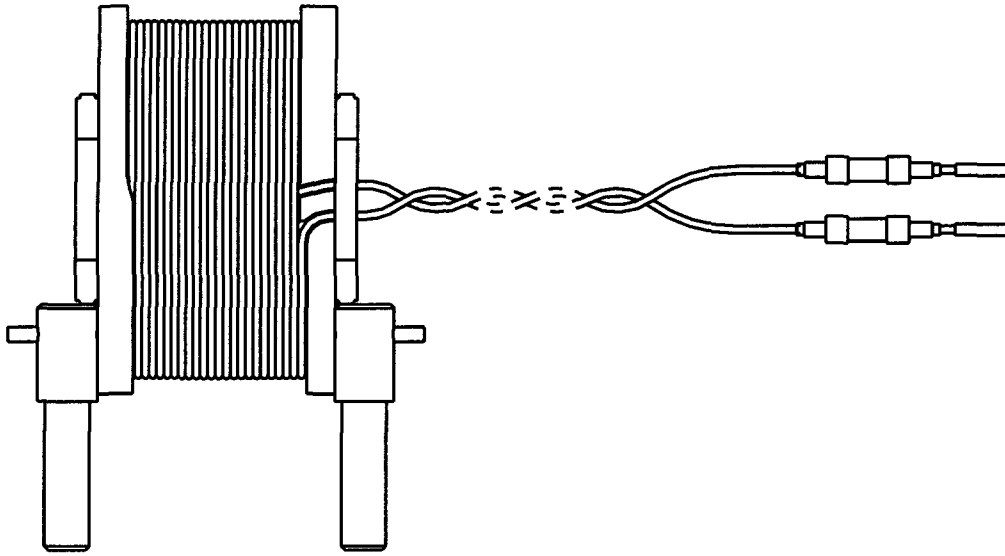


Figure 4.3: Schematic of a magnetic probe. The size in the figure corresponds to the actual size.

4.2.2 Calibration

The use of the poloidal field measurements for the real time control requires an absolute calibration with an uncertainty of less than 1%. Since the exact geometry of the probe windings varies more than the required precision, the probes were calibrated using a well known magnetic field. The calibration setup allowed to determine the effective area as well as the frequency response for frequencies ranging from 100 Hz to 100 kHz. The magnetic field was produced by the configuration of a pair of Helmholtz coils for the major axis and two pairs of coils for the two minor axes. Each coil had 49 windings which were arranged in 7 equal layers. The major axis of the calibration setup corresponded to the poloidal axis, when mounted in the vessel and required the highest precision. The Helmholtz coils were used because of their easily accessible chamber of a highly homogeneous field. The geometry of the coil set is well known (figure 4.4) and the magnetic field can be calculated by Biot-Savart integration. For the main axis the magnetic field per unit current and averaged over the probe volume is $b_p = 0.2944 \text{ mT/A}$. The calibration required the measurement of the transfer function between the probe signal and the current in the coils.

The transfer functions were measured with an HP 3589A Spectrum Analyser. It can be operated as a single-channel network analyser, where the source frequency and the local-oscillator frequency are synthesised from a common reference frequency. The measurement of a transfer function H consists of a reference measurement U_R , and a

transmission measurement U_T ,

$$H = \frac{U_T}{U_R}. \quad (4.2)$$

The spectrum analyser was swept from 100 Hz to 1 MHz. The source was fed into a power amplifier ($U-I$ converter) which drove the current in the calibration coils. The duration of the frequency sweep and the bandwidth of the receiver were chosen in order to minimise noise, spectral smearing and measurement time, while satisfying the required precision.

The calibration setup is shown in figure 4.5. The current measurements were performed by two independent methods, namely by the voltage drop over a known impedance Z , and by a transformer. The signal over the shunt had to be amplified. The transfer functions between the signals of both current measurements U_r and U_t and the actual current,

$$G_x = \frac{U_x}{I}, \quad x = r, t \quad (4.3)$$

take into account the impedance of the shunt, source and receiver, as well as the transfer function of the differential amplifier. The network measurements consisted of the current measurements as references and the signal of the probe as the transmission measurement giving,

$$G_{px} = \frac{U_p}{U_x}, \quad x = r, t. \quad (4.4)$$

The response of the probe could then be obtained from the network measurements (equation 4.4) and the transfer functions for both current measurements (equation 4.3) by,

$$H_{px} = -\frac{U_p}{sB} \quad (4.5)$$

$$= -\frac{G_{px}U_x}{sb_p I} = -\frac{G_{px}}{sb_p} G_x \quad (4.6)$$

where $s = i\omega$. An example of the measured transfer functions is shown in figure 4.6. The two measurements show good agreement over a wide range of frequencies. There are, however, discrepancies at very low, $f < 10^3$ Hz, and very high frequencies, $f > 10^5$ Hz.

4.2.3 Frequency response

The probe response at high frequencies is influenced by non-ideal effects, such as the capacity of its cable and coupling to its shielding. An equivalent circuit including the resistivity, capacity and self inductance of the probe and its cable (R_p , C_p , L_p) as well as the shielding (R_s, L_s) is shown in figure 4.7 [24]. Assuming an ideal coupling between the probe and its shielding the circuit can be described by the coupled equations,

$$R_p I_p + sL_p I_p + \frac{I_p}{sC_p} + s\sqrt{L_p L_s} I_s = s\Psi \quad (4.7)$$

$$R_s I_s + sL_s I_s + s\sqrt{L_p L_s} I_p = s\sqrt{L_s/L_p} \Psi, \quad (4.8)$$

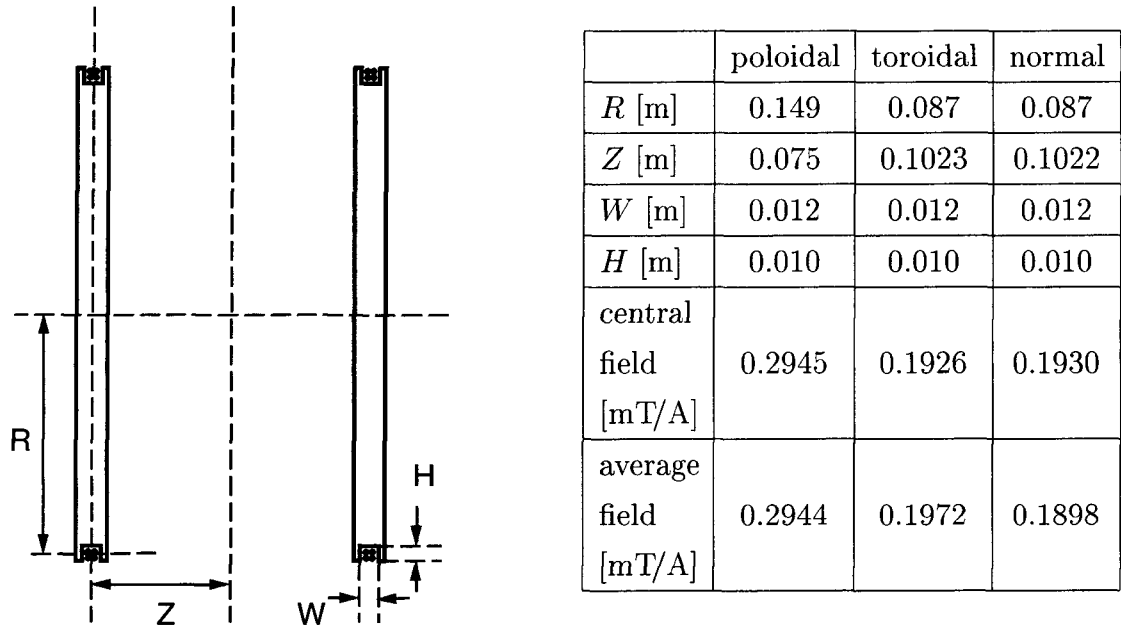


Figure 4.4: Geometry of the calibration coils for the poloidal, toroidal and normal direction. Each coil has 49 windings arranged in 7 equal layers. The resulting field is calculated in the centre as well as averaged over the volume of the magnetic probe.

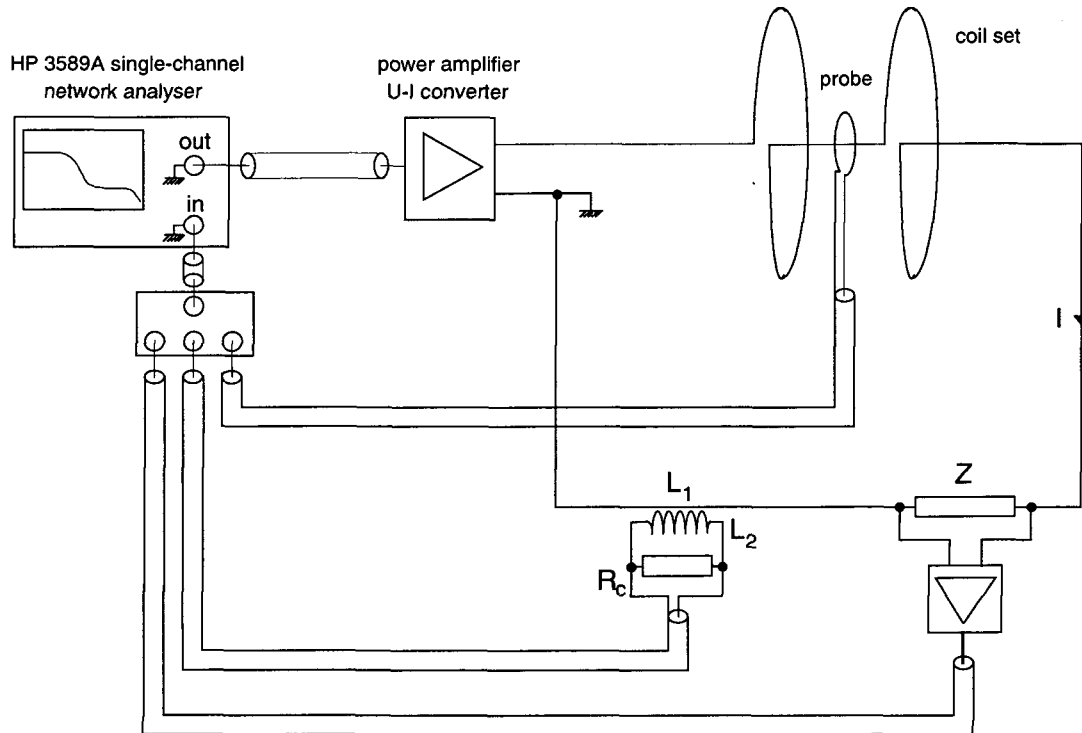


Figure 4.5: Magnetic probe calibration setup using a single-channel network analyser. Two independent measurements of the current in the coil set are used as references for the transmission measurement on the probe, while the source is fed into a $U-I$ converter driving the current.

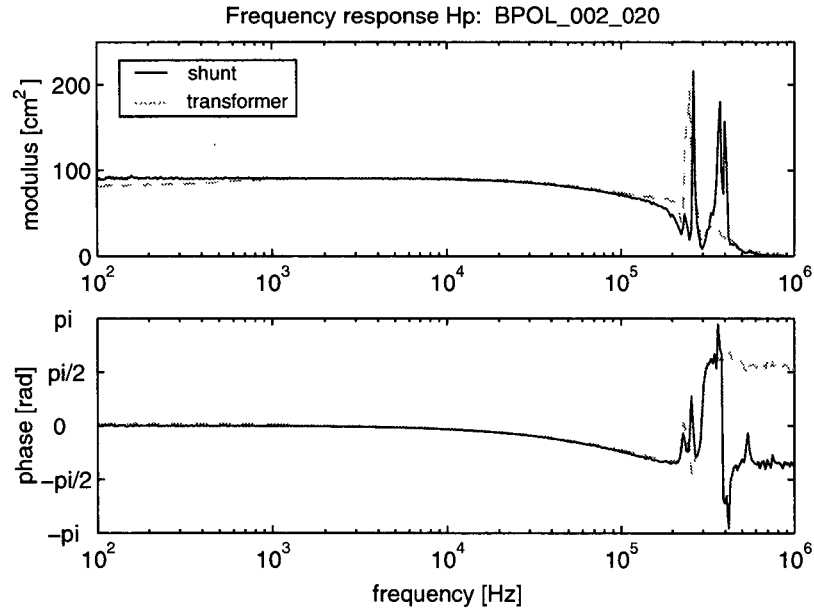


Figure 4.6: Frequency response of a magnetic probe determined by a current measurement using a shunt (full) and one using a transformer (dashed line). The frequency response above 100 kHz is masked by the response of the current measurements.

where $\Psi = BA_p$ is the measured flux. The frequency response of the probe is then given by,

$$H_p = -\frac{U_p}{sB} = \frac{A_p}{1 + s[(L_s/R_s) + R_p C_p] + s^2 R_p C_p [(L_p/R_p) + (L_s/R_s)]}. \quad (4.9)$$

Consequently, the measured transfer functions H_p are fitted to a transfer function with two cut-off frequencies, $1/(2\pi\tau_1)$ and $1/(2\pi\tau_2)$,

$$H_p = \frac{A_p}{(1 + s\tau_1)(1 + s\tau_2)}. \quad (4.10)$$

In order to use the measurements over the whole frequency range, an instrumentation

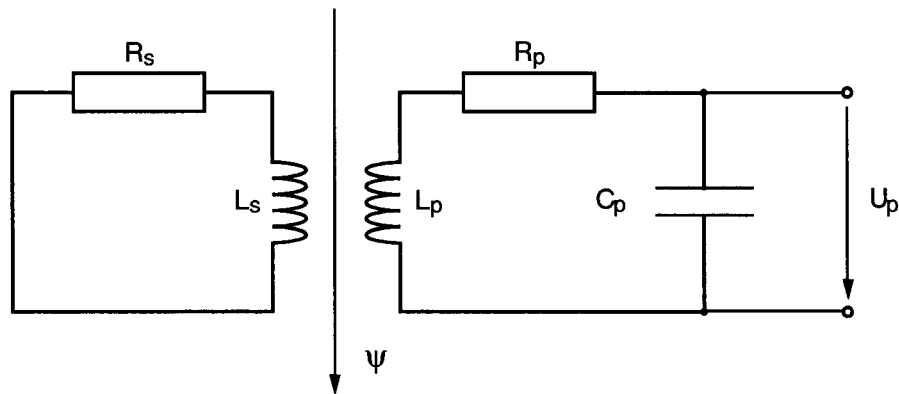


Figure 4.7: Schematic circuit of a magnetic probe (p) including its shielding (s).

specific contribution H_x is separated from the measurements $H_{px} = H_p H_x$ $x = r, t$ [25]. The probe response H_p is different for each probe, whereas H_x has a unit DC gain and one frequency response for each of the two methods. The so determined DC response of the probe, corresponding to the effective area and the first pole, are shown in figure 4.8(a) and (b). Typical values are 91 cm^2 and 95 kHz . The minor axes, corresponding to the toroidal and normal directions when mounted on the TCV vessel wall, are fitted assuming the same poles. The distributions of their effective areas are shown in figure 4.8(c) and (d). The optimised design of the windings led to a peak in the distribution of the normal area around zero. The effective toroidal area cannot be eliminated and varies around an average of 1.4 cm^2 . Although the toroidal field is much larger than typical perturbations, it has only low frequency components and does not induce a large signal. It can easily be separated from the fluctuation measurement.

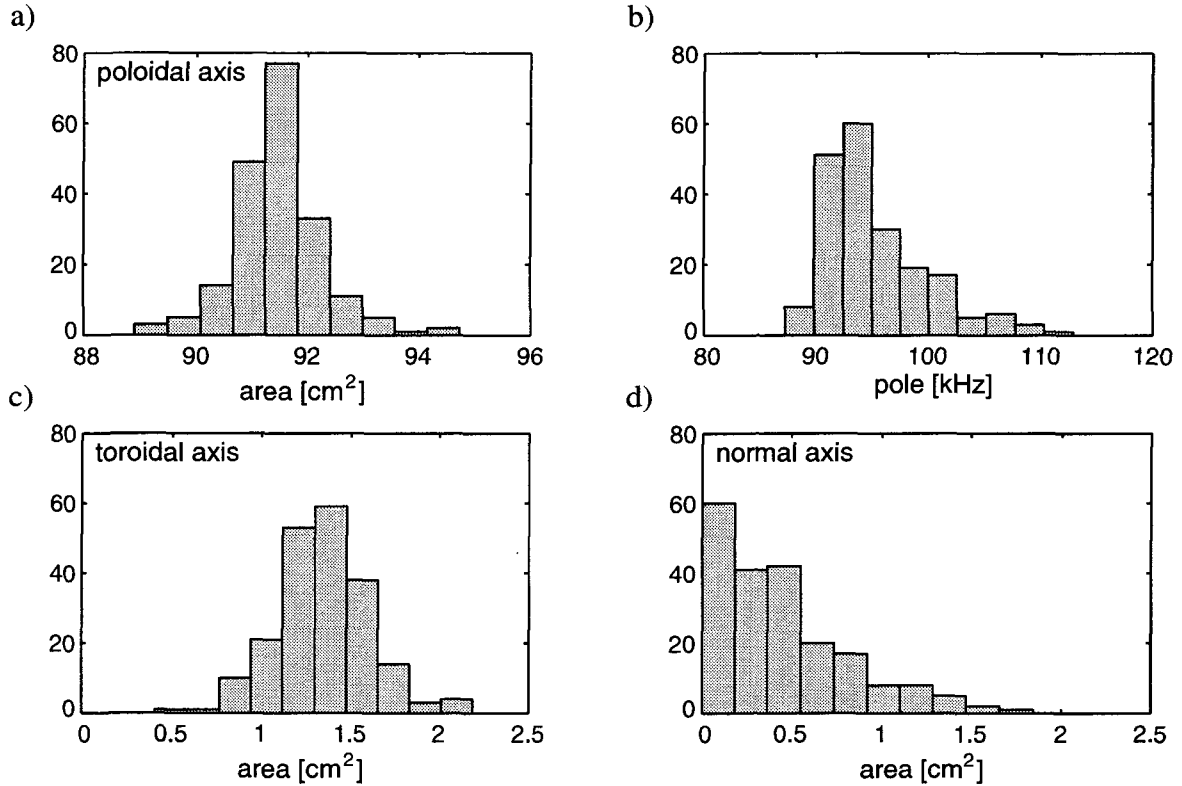


Figure 4.8: Distribution of the main characteristics of the 203 magnetic probes in TCV. The effective area of the main axis (a) and the first pole (b) are obtained by a fit. Assuming the same frequency response as the poloidal axis the effective areas in the toroidal (c) and normal directions (d) are also obtained.

4.3 Signal processing

During the processing of the signal, an adequate amplitude has to be maintained for a variety of events in the plasma over a wide frequency range. Low frequency signals from changes in the equilibrium configuration lead to signals of a few millivolts, MHD modes typically at 5–10 kHz result in signals of several volts and fast events like disruptions can lead to voltage spikes of up to 100 V. These signals in their entirety should be digitised and stored for post-shot analysis.

4.3.1 Amplifying chain

The low amplitude of the frequency signals requires an amplification of the detected signal. The amplifying chain is sketched in figure 4.9. In order to prevent a saturation of the amplifiers, they are preceded by a filter with a first-order pole at 100 Hz and a zero at 3.5 kHz, attenuating high frequency signals by a factor of 35. The amplification is set up in two stages. A pre-amplifier, located close to the tokamak, amplifies the signals before the long transmission line to the acquisition room. The pre-amplifier is programmable with gains of 4, 8, 16 or 32 and has a cut-off frequency of 200 kHz. Before the signals enter the rack in the data acquisition room, they are galvanically separated from the tokamak. The main amplifier is also programmable with gains ranging from $\frac{1}{4}$ to 32. The cut-off of this amplifier is also at 200 kHz.

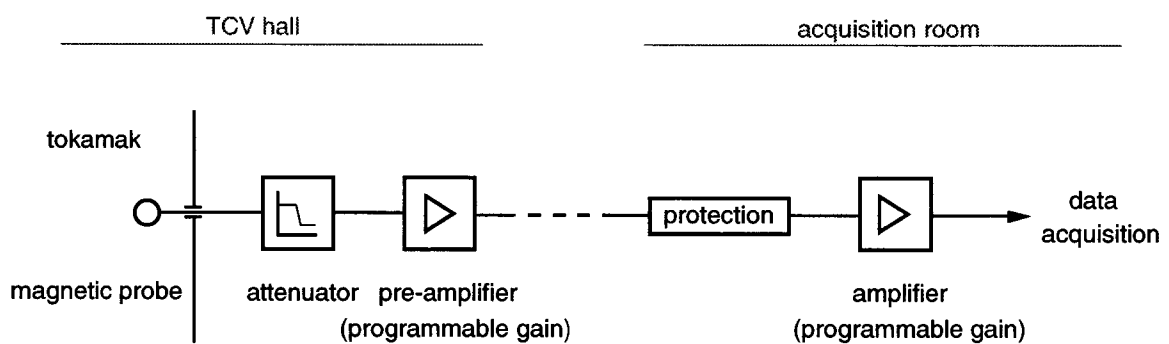


Figure 4.9: Sketch of the amplifying chain of the magnetic fluctuation measurements.

The frequency response of each element of the amplifying chain, assuming a unit DC gain, is shown in figure 4.10. The multiple poles of amplifiers and probe lead to a strong attenuation of the signal for frequencies above 100 kHz.

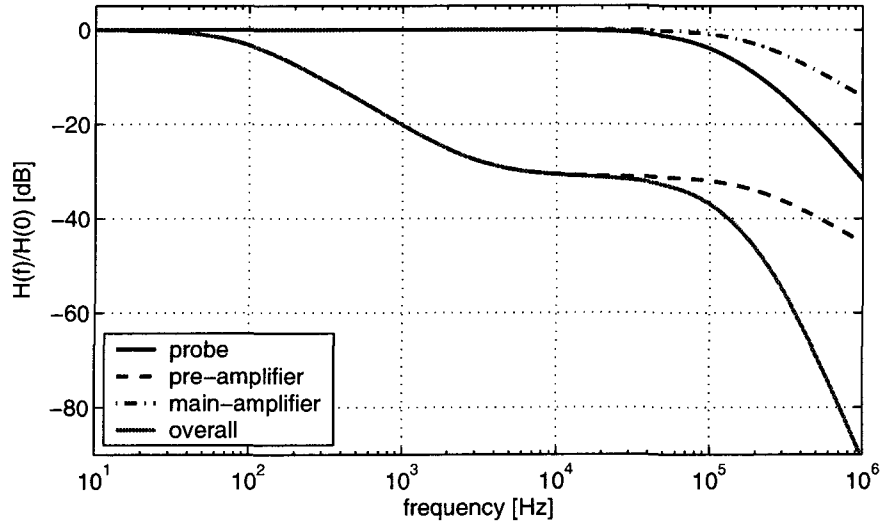


Figure 4.10: Frequency response of each element of the amplifying chain, namely the magnetic probe, the pre-amplifier including the attenuator, and the main amplifiers, as well as the overall transfer function. All transfer functions are normalised on the DC gain.

4.3.2 Acquisition

The signal acquisition is performed by 12-bit ADCs. The signals can be digitised with a sampling rate up to 1 MHz. Each channel can store 0.5 Mega samples. Usually, the signals are sampled with 50 to 125 kHz. Since the current diagnostic setup is limited to 60 channels, not all of the probe signals can be acquired simultaneously. However, owing to the toroidal symmetry and the plasma rotation, it is sufficient to record only one poloidal and one toroidal array. The variety of plasma shapes leads to large variations in the distance between the probes and the plasma. The acquisition optimises the information in the probe signals by choosing different subsets of probes depending on the vertical plasma position. A TCV discharge can accumulate up to 50 MByte of magnetic data. This data is archived in a compressed format, typically reducing the data size by a factor of 3-4, by the MDS+ data acquisition system [26]. The process of reading the data out of the ADC modules and storing it on hard disk can take up to 5 minutes.

4.4 Concluding remarks

The fast magnetic fluctuation diagnostic uses a dense set of poloidal pick-up coils inside the TCV vessel. The design of the probes was optimised for TCV signals up to 100 kHz. The arrangement of the probes result in full toroidal and poloidal coverage of the plasma in order to reveal the complete structure of MHD instabilities. An absolute calibration over a wide frequency range allows a quantitative analysis of instabilities. The dual use of the probes for control and fluctuation measurement does not lead to any conflicts. The

flexible data acquisition optimises between the gathered temporal and spatial information and the size of the stored data and the duration of the acquisition process.

Chapter 5

Magnetic fluctuation analysis

MHD instabilities perturb the equilibrium magnetic field. These perturbations usually extend to the plasma edge, where they can be detected with magnetic pick-up coils. Owing to the rotation of the plasma they are usually observed as fluctuations. The perturbation of the magnetic surfaces also affects flux surface quantities, such as the temperature, density or soft X-ray emissivity and can therefore, be observed with corresponding diagnostics which provide a sufficient temporal and spatial resolution.

This chapter presents the analysis of the magnetic fluctuations measured with pick-up coils inside the TCV vessel (chapter 4). In the course of this thesis several numerical methods to extract the temporal and spatial behaviour of MHD modes have been implemented on TCV. These methods, which are also applicable to other fluctuation measurements, are described and their advantages and restrictions discussed. An interpretation of the measured mode structure at the edge can require an inversion of the structure within the plasma. Such an inversion is performed for magnetic islands [27]. For a quantitative analysis of magnetic islands, independent estimates of their width are used.

5.1 Perturbation of the magnetic field

The magnetic probes measure temporal variations of the poloidal magnetic field, δB . Since the typical frequencies of MHD instabilities are in the kHz range and higher, they can easily be separated from the slower changes of the equilibrium magnetic field.

5.1.1 Decomposition into modes

In order to extract coherent modes, the fluctuation measurements can be decomposed into spatial Fourier components. In analogy with the calculation of eigenmodes (section 2.2.3) the measurements are expanded in a toroidal angle φ , and a poloidal angle θ . While the toroidal symmetry justifies the expansion in φ , toroidicity and plasma shaping break the poloidal symmetry and introduce higher harmonics to the expansion in θ . Asymmetries in

the poloidal setup of the diagnostics can lead to further structures in the measurements. Also, the eigenfunction of the instability itself can consist of several harmonics. Therefore, the measured perturbation generally consists of a combination of several Fourier components,

$$\delta B(\vec{x}, t) = \sum_{m,n} \delta \hat{B}_{m,n} \cos(\vec{k}_{m,n} \vec{x} - \Phi_{m,n}(t)) \quad (5.1)$$

$$= \sum_{m,n} \delta \hat{B}_{m,n} \cos(m\theta - n\varphi - \Phi_{m,n}(t)). \quad (5.2)$$

Although $\delta \hat{B}_{m,n}$ is strictly just the amplitude of a Fourier component, it is often referred to as the amplitude of an m/n mode, labelling an instability by its dominant Fourier component. The phase $\Phi_{m,n}$ of the m/n component generally varies with time,

$$\begin{aligned} \Phi_{m,n}(t) &= \omega_{m,n}t + \chi_{m,n} = \vec{k}_{m,n} \vec{v}t + \chi_{m,n0} \\ &= \left(\frac{m}{r} v_\theta - \frac{n}{R} v_\varphi \right) t + \chi_{m,n} \end{aligned} \quad (5.3)$$

where \vec{v} is the phase velocity of the magnetic perturbation with respect to the probes and $\chi_{m,n}$ a constant phase angle. It is impossible to distinguish between a poloidal and a toroidal rotation by magnetic measurements alone.

5.1.2 Plasma rotation

In the ideal MHD model the magnetic flux through any surface moving with the plasma is conserved (see section 2.2.1). In return, it can be concluded that a magnetic structure moves with the plasma which then gives rise to the observed fluctuation frequency. However, the absence of any external momentum source for TCV plasmas result only in small plasma velocities. Consequently, the Hall term in the generalised Ohm's law (equation 2.10) cannot be neglected in the derivation of equation 2.16 for the evolution of magnetic flux. Taking into account the Hall term results in,

$$\frac{\partial \Psi}{\partial t} = \oint \left(\vec{v} - \frac{1}{en_e} \vec{j} - \vec{v}_A \right) \times \vec{B} \cdot d\vec{l}. \quad (5.4)$$

Therefore, assuming ideal conductivity the magnetic field perturbation moves with the electron fluid [28],

$$\vec{v}_e = \vec{v} - \frac{\vec{j}}{en_e}. \quad (5.5)$$

Since magnetic field lines are also lines of equal phase of a perturbation, only the components normal to \vec{B} , namely the normal plasma velocity, \vec{v}_\perp and the diamagnetic current,

$$\vec{v}_{e\perp} = \vec{v}_\perp + \frac{\vec{\nabla} p \times \vec{B}}{en_e B^2} \quad (5.6)$$

are relevant. The rotation is also influenced by viscosity damping the poloidal rotation and drag effects leading to mode coupling or even to mode locking to the vessel wall.

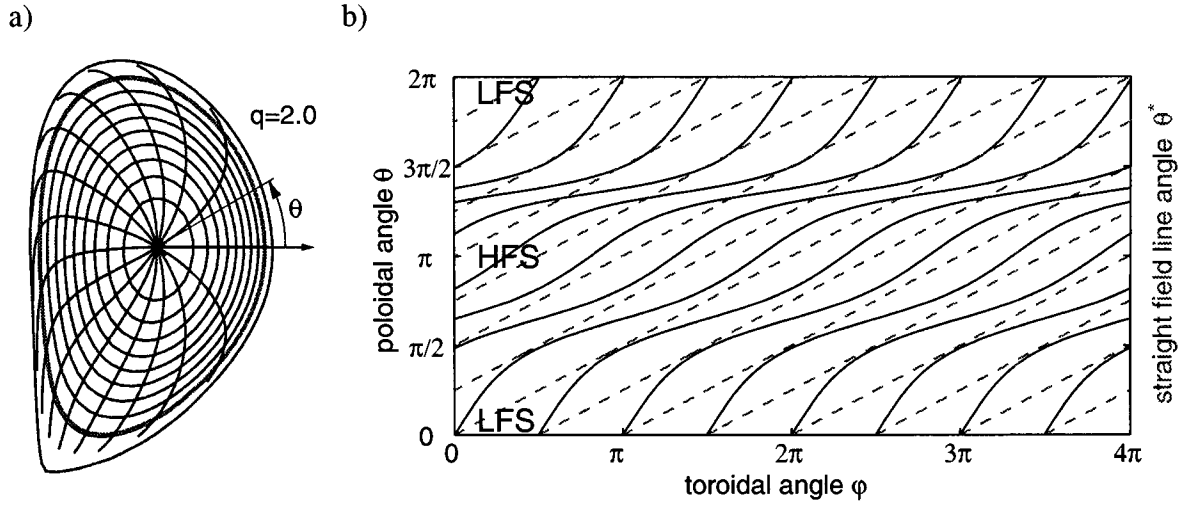


Figure 5.1: Magnetic field line geometry of the diverted discharge #15542 at $t = 0.5$ s. (a): The flux contours in the poloidal plane show the plasma shape. The geometry of the field lines on the flux surfaces is represented by the contours of the straight field line angle θ^* , indicating the advance of field lines in the poloidal directions for equal toroidal arc lengths. (b): The field lines of the $q = 2$ surface are shown in the unfold $\theta - \varphi$ plane (solid). Replacing the polar angle θ by θ^* results in straight magnetic field lines (dashed).

5.1.3 Geometry of magnetic field lines

Instabilities are usually resonant on rational q surfaces and consequently, have the same helicity as the magnetic field lines. The field lines of the equilibrium field lie on nested flux surfaces (section 2.2.2), which are usually described by the coordinates φ and θ . Owing to the $1/R$ decay of the toroidal field, the angle of a field line with respect to the toroidal direction is generally lower on the high-field-side (HFS) than on the low-field-side (LFS). Consequently, the poloidal wavelengths are shorter on the HFS than on the LFS. The pitch angle of the field line also decreases at the top and bottom of elongated plasmas as well as in the vicinity of an X-point, where it approaches zero. The field line geometry of a diverted plasma is shown in figure 5.1(a),(b). In order to exclude the effects of toroidicity and shaping, a poloidal variable $\theta^*(\theta)$ is introduced, so that the magnetic field follows straight lines in the $\theta^* - \varphi$ plane. The so-called *straight field line angle* θ^* , yields,

$$\frac{\vec{B} \cdot \vec{\nabla} \theta^*}{\vec{B} \cdot \vec{\nabla} \varphi} = \text{const.} \quad (5.7)$$

The multiplication of the representation for an axisymmetric field, $\vec{B} = I(\Psi)\vec{\nabla}\varphi + \vec{\nabla}\Psi \times \vec{\nabla}\varphi$, obtained from equation 2.22 and equation 2.28, with $\vec{\nabla}\theta^*$ and substituting into equation 5.7 results in,

$$\underbrace{\vec{\nabla}\Psi \times \vec{\nabla}\varphi \cdot \vec{\nabla}\theta^*}_J \cdot \frac{\partial \theta^*}{\partial \theta} = \text{const.} \cdot \frac{I(\Psi)}{R^2}. \quad (5.8)$$

The mixed product of $\vec{\nabla}\Psi$, $\vec{\nabla}\varphi$, and $\vec{\nabla}\theta$ on the left hand side of equation 5.8 can be identified as the Jacobian J , of the coordinate transformation of the flux coordinates (Ψ, φ, θ) into cylindrical coordinates (R, φ, Z) . It can be simplified by using the toroidal symmetry and the identity of the toroidal coordinate,

$$J = \begin{vmatrix} \partial\Psi/\partial R & 0 & \partial\Psi/\partial Z \\ \partial\varphi/\partial R & 1/R & \partial\varphi/\partial Z \\ \partial\theta/\partial R & 0 & \partial\theta/\partial Z \end{vmatrix} = \frac{1}{R} \left(\frac{\partial\Psi}{\partial R} \frac{\partial\theta}{\partial Z} - \frac{\partial\Psi}{\partial Z} \frac{\partial\theta}{\partial R} \right) \quad (5.9)$$

Equation 5.8 can be integrated over θ ,

$$\theta^*(\theta) = \text{const.} \cdot I(\Psi) \int_0^\theta \frac{d\theta}{R^2 J}. \quad (5.10)$$

The constant is determined by normalising $\theta^*(2\pi)$ to 2π ,

$$\theta^*(\theta) = 2\pi \frac{\int_0^\theta (R^2 J)^{-1} d\theta}{\int_0^{2\pi} (R^2 J)^{-1} d\theta} \quad (5.11)$$

where the Jacobian can be computed from $\Psi(R, Z)$ which is available from the equilibrium reconstruction.

5.2 Numerical techniques for the mode analysis

Various techniques are used to extract information concerning the temporal evolution and spatial structure of coherent modes. These methods can also be applied to other fluctuation measurements. In the following an arbitrary fluctuation signal $y(\vec{x}, t)$, is analysed.

5.2.1 Temporal analysis

Fourier transform

The standard approach to the analysis of an oscillating signal is the Fourier transform, which links the representation of a function in the time and frequency domains,

$$Y(\omega) = \int_{-\infty}^{\infty} y(t) e^{i\omega t} dt. \quad (5.12)$$

In an experiment a function $y(t)$ is usually recorded over a finite time interval and at a finite sampling rate $f_s = 1/\Delta t$, leading to N discrete samples $x(t_k)$. The discrete form of the Fourier transform (equation 5.12) is,

$$Y(f_n) = \Delta t \sum_{k=0}^{N-1} y(t_k) e^{2\pi i k n / N} \quad (5.13)$$

with $f_n = n/(N\Delta t)$. Equation 5.13 is periodic in n which is usually varied from $-N/2$ to $N/2$ and corresponds to a spectral resolution up to the Nyquist frequency, $f_c = 1/(2\Delta t)$.

If the signal $y(t_k)$ consists of purely real values, the Fourier coefficients of positive and corresponding negative frequencies are complex conjugates, $Y(-f_n) = Y(f_n)^*$. The original data set can be reconstructed from the Fourier coefficients using the discrete form of the inverse Fourier transform,

$$y(t_k) = \frac{1}{N\Delta t} \sum_{n=0}^{N-1} Y(f_n) e^{-2\pi i k n / N}. \quad (5.14)$$

Power spectral density

An estimate of the continuous power spectrum $P(f)$, can be obtained from the Fourier coefficients $Y(f_n) = Y_n$ and is defined at $N/2 + 1$ positive frequencies as,

$$\begin{aligned} P(0) &= \frac{1}{(N\Delta t)^2} |Y_0|^2 \\ P(f_n) &= \frac{1}{(N\Delta t)^2} \left[|Y_n|^2 + |Y_{N-n}|^2 \right] \quad n = 1, \dots, \frac{N}{2} - 1 \\ P(f_c) &= \frac{1}{(N\Delta t)^2} |Y_{N/2}|^2. \end{aligned} \quad (5.15)$$

The normalisation used in equation 5.15 ensures that the sum over all $N/2 + 1$ values of $P(f_n)$ is equal to the mean squared amplitude of the function $y(t)$. The value $P(f_n)$ is an estimate of the average power over a narrow window centred on f_n . However, this window extends beyond the mid-distance from the preceding discrete frequency and the mid-distance to the next and leads to significant leakage of signal power into adjacent frequency bins. The reason for this leakage is the finite length of the sampled time interval, which can be seen as the product of an infinite run of sampled data and a box function. The Fourier transform of the product is then given by the convolution of the Fourier transform of the data set and that of the box function, which leads to a broadening of the power spectrum. This can be reduced by replacing the box window with a window function $w(t_k)$, which changes gradually from zero to a maximum and then back to zero. In this case equations 5.13 and 5.15 become,

$$Y^w(f_n) = \Delta t \sum_{k=0}^{N-1} x(t_k) w(t_k) e^{2\pi i k n / N} \quad \text{with } n = 0, \dots, N-1 \quad (5.16)$$

and

$$\begin{aligned} P(0) &= \frac{1}{(N\Delta t)^2 W_{\text{ms}}} |Y_0^w|^2 \\ P(f_n) &= \frac{1}{(N\Delta t)^2 W_{\text{ms}}} \left[|Y_n^w|^2 + |Y_{N-n}^w|^2 \right] \quad n = 1, \dots, \frac{N}{2} - 1 \\ P(f_c) &= \frac{1}{(N\Delta t)^2 W_{\text{ms}}} |Y_{N/2}^w|^2 \end{aligned} \quad (5.17)$$

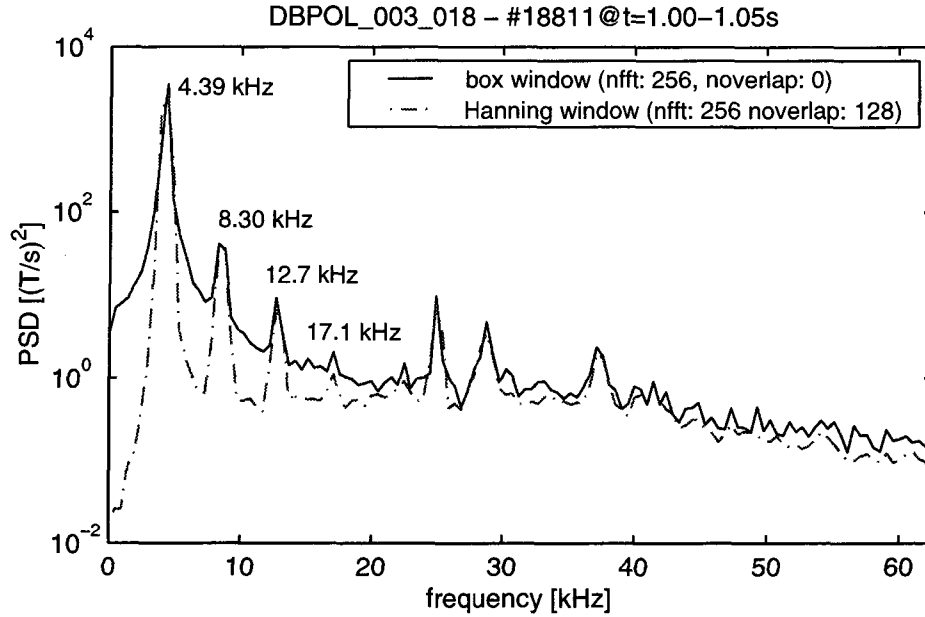


Figure 5.2: Estimates of the power spectral density for a discharge where a strong mode at 4.4 kHz was present. The estimate using a Hanning window and overlapping data segments shows significantly sharper peaks at the mode frequency and higher harmonics than the box window.

where $W_{\text{ms}} = \sum_k w_k^2 / N$ is the mean square of the window coefficients. The power estimation also suffers from a large variance. A method used to reduce this variance is the partitioning of the original sampled data into K segments each of $M = N/K$ consecutive data points. An averaging of the power estimates at $M/2 + 1$ discrete frequencies over the segments reduces the variance of the estimate by a factor K . It is easy to combine the data windowing and the segmentation of the original data set. The spectral variance can be further minimised by overlapping consecutive segments.

In figure 5.2 the comparison between a power estimate using a box window and no overlapping segments (solid line) and an estimate using a Hanning window, which is defined by $w_k = \frac{1}{2}[1 - \cos(2\pi k/(N - 1))]$ with $k = 0, \dots, N - 1$, and overlapping (dashed line), illustrates the improvement. The estimate using the Hanning window has a narrower peak at 4.4 kHz, corresponding to the frequency of a mode, and three higher harmonics, while the box window leads to a significant leakage to neighbouring frequencies.

The use of an estimate of the power spectral density allows the identification of the frequency of a mode. The Fourier coefficients (equation 5.16) at this frequency can then be used to determine the mode structure, as is described in section 5.2.2.

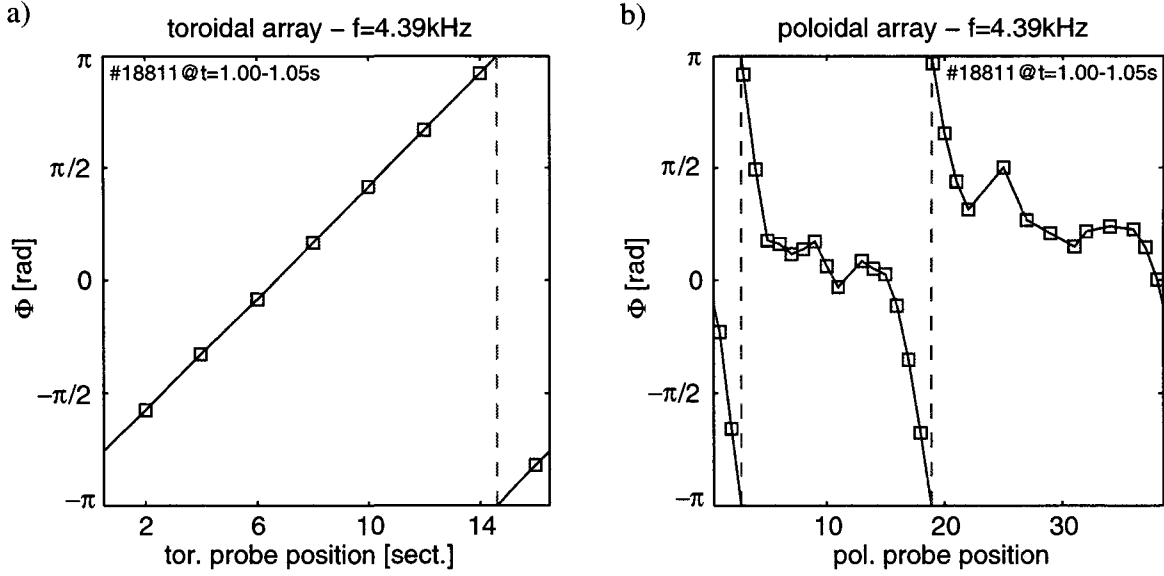


Figure 5.3: The phase of the Fourier coefficient at 4.4 kHz of measurements with the toroidal (a) and poloidal (b) array of pick-up coils is shown as a function of the probe position. Following the phase along the toroidal and poloidal directions reveal the toroidal and poloidal mode numbers $n = 1$ and $m = 2$.

5.2.2 Spatial analysis

The identification of the toroidal structure is simplified by the toroidal symmetry of a tokamak plasma, which allows a straightforward decomposition into toroidal mode components. The poloidal mode identification is more complex with toroidicity and poloidal shaping affecting the structure of the perturbation. Variations among the setup of the detectors, such as the varying orientation and distance of the magnetic probes with respect to the plasma, can also affect the measured poloidal structure of a mode.

Spectral analysis

The spectral analysis is based on the Fourier transform of the measurements. As it was shown in section 5.2.1, the amplitude of the complex Fourier coefficient allows to estimate the spectral density revealing the frequency f_* , of a distinct mode. In addition to the measurement of the signal power, the Fourier coefficient at the mode frequency Y_* , also yields a phase angle $\Phi_* = \arctan(\Im(Y_*)/\Re(Y_*))$. A comparison of the real part of the inverse Fourier transform (equation 5.14) with the mode expansion (equation 5.1) easily identifies the phase angle of the Fourier coefficient Φ_* , as the phase of the mode $\vec{k}\vec{x}$.

Figure 5.3 shows the phases of magnetic fluctuation measurements at $f_* = 4.4 \text{ kHz}$ as they were recorded with the toroidal array on the LFS (a) and the poloidal array in sector 3 (b). Owing to the toroidal symmetry of the plasma and the toroidal probe array, the phase difference $\Delta\Phi$, between probes of the toroidal array increases linearly with the

toroidal spacing of the probes $\Delta\varphi$, allowing to determine the toroidal mode number from only two toroidally spaced probes,

$$n(f_*) = \frac{\Delta\Phi(n^*)}{\Delta\varphi}. \quad (5.18)$$

For the complete toroidal arrays of TCV it is usually sufficient to count the multiples of 2π of the phase shift along the entire toroidal circumference. In figure 5.3(a) an $n = 1$ structure is easily identified. The identification of the poloidal mode structure is more complicated. As can be seen in figure 5.3(b), the slope of the phase changes strongly with poloidal position. Eddy currents in the wall and the change of probe orientation close to the vessel corners even allow a reversal of the phase change. Without a detailed calculation, which takes into account the internal structure of the mode as well as the response of the conducting vessel and the poloidal geometry, as will be described in section 5.3, it is necessary to count the multiples of 2π of the phase shift along the entire poloidal circumference. However, this can be complicated by a fast changing phase which occurs in the vicinity of x-points or by low signal amplitudes caused by large distances between the resonant surface and the magnetic probes.

The advantage of the spectral mode analysis is its close relation to the decomposition of the signals into modes. To do so, it uses standard routines such as the Fast Fourier Transform (FFT). However, its application is restricted to modes whose oscillation frequencies remain constant over the analysed time interval. This time interval, however, needs to be of a certain length to allow for a sufficient frequency resolution.

Toroidal mode amplitude

Signals which are measured with complete and equidistant toroidal arrays of detectors, such as the toroidal arrays of magnetic probes on the HFS and LFS (section 4.1), as well as a toroidal array of soft X-ray diodes (section 3.3.3), can be directly decomposed into toroidal Fourier components. The measurements $y(t_k, \varphi_l)$, taken at N toroidal locations, can be decomposed for any sampled time t_k yielding cosine and sine components for toroidal mode numbers $n = 0, 1, \dots, N/2$,

$$c_n(t_k) = \frac{2}{N} \sum_{l=1}^N y(t_k, \varphi_l) \cos(n\varphi_l) \quad (5.19)$$

$$s_n(t_k) = \frac{2}{N} \sum_{l=1}^N y(t_k, \varphi_l) \sin(n\varphi_l). \quad (5.20)$$

The Fourier components of the measurements can also be expressed by mode amplitudes $A_n(t_k) = \sqrt{c_n(t_k)^2 + s_n(t_k)^2}$ and corresponding phases $\Phi_n(t_k) = \arctan(s_n(t_k)/c_n(t_k))$,

$$y(t_k, \varphi_l) = \frac{A_0(t_k)}{2} + \sum_{n=1}^{N/2} A_n(t_k) \cos(n\varphi_l - \Phi_n(t_k)). \quad (5.21)$$

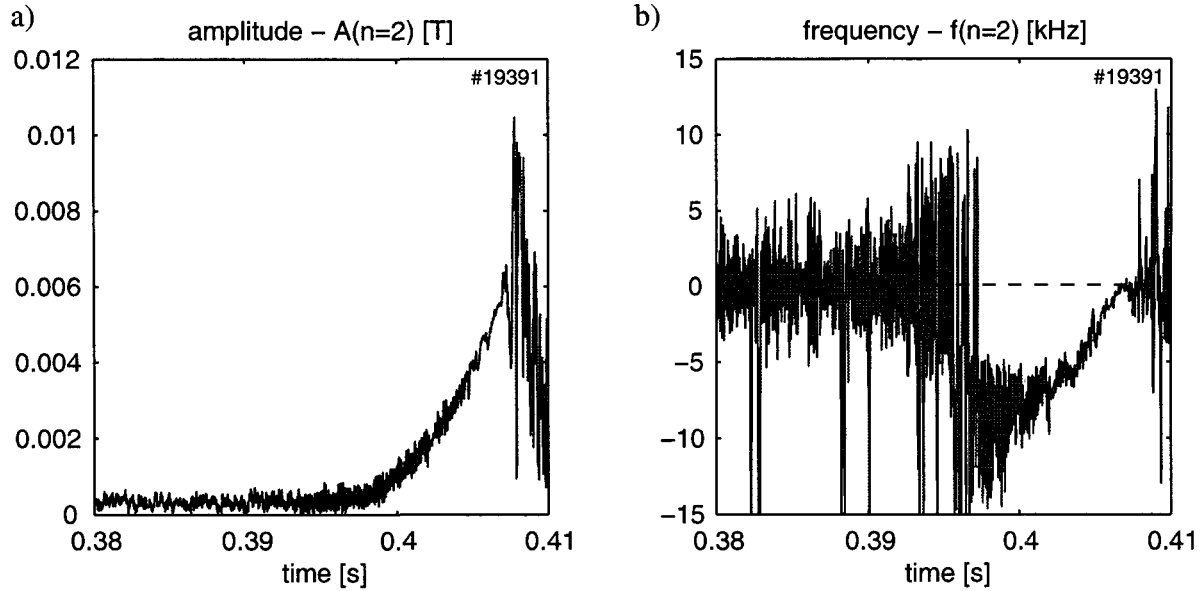


Figure 5.4: The toroidal mode analysis shows an $n = 2$ disruption precursor mode, which starts to grow at $t = 0.396$ s (a) while its initial frequency of 8 kHz continuously slows down and eventually locks to the vessel (b).

This decomposition is equivalent to a Fourier transform (equation 5.12) between φ and $k = n/R$ space. However, the periodic boundary conditions are strictly true leading to discrete modes characterised by their mode numbers n . Therefore, their representation as a Fourier series is more appropriate. Spectral leakage which was seen in the time spectra does not occur. The amplitude A_n , yields information about the mode growth, whereas the phase Φ_n , can be derived in time yielding a frequency. Figure 5.4 shows an $n = 2$ mode which starts to grow at $t = 0.395$ s. While its initial frequency of 8 kHz decreases until it locks to the vessel, the mode amplitude continuously grows until the discharge is terminated by a disruption at $t = 0.409$ s.

In contrast to the spectral analysis the toroidal mode analysis does not impose any time behaviour and allows to resolve instabilities with varying frequencies. Since MHD instabilities usually have a single toroidal mode number, A_n comprises the total signal power of this instability independent of the number and importance of its poloidal harmonics. It does not, however, reveal any information concerning the poloidal mode structure.

5.2.3 Spatiotemporal analysis

Bi-orthogonal decomposition

Another method for the analysis of spatiotemporal signals is the bi-orthogonal decomposition (BD), which is formally identical to the singular value decomposition (SVD) in numerical linear algebra. Unlike Fourier techniques, it is a multivariate analysis handling

several dimensions at the same time. The bi-orthogonal decomposition separates synchronised signals into coherent modes and their corresponding temporal evolutions. Measurements $y(t_i, x_j)$ taken at M locations x_j and sampled at N times t_i can be constructed from $K = \min(N, M)$ pairs of spatial eigenvectors $\phi_k(x_j)$ and temporal eigenvectors $\psi_k(t_i)$,

$$y(t_i, x_j) = \sum_{k=1}^K A_k \phi_k(x_j) \psi_k(t_i). \quad (5.22)$$

The spatial eigenvectors ϕ_k , are also called *topos* and the temporal eigenvectors ψ_k , *chronos*. *Topos* and *chronos* are mutually orthonormal. The eigenvalues or weights A_k , are positive or equal to zero and it is conventional to sort the pairs of bi-orthogonal components in order of decreasing weights. The total signal energy $E = \sum_i \sum_j x^2(t_i, x_j)$, is equal to the sum of the squared weights,

$$E = \sum_k^K A_k^2. \quad (5.23)$$

The relative energy stored in each pair of eigenvectors (ϕ_k, ψ_k) can be expressed with the dimensionless energy,

$$p_k = A_k^2 / E \quad (5.24)$$

which quantifies the importance of an eigenvector. The space-time complexity of the signal is measured by a normalised entropy defined by,

$$H = \frac{-\sum_{k=1}^K p_k \log p_k}{\log K} \quad (5.25)$$

which is zero if $y(t_i, x_j)$ is separable and one if all eigenvectors have equal weights.

The presence of noise limits the number of significant components. Random fluctuations add a constant contribution to the square of the eigenvalues which should converge towards a constant value. However, the experiment usually shows a transition from a steep weight distribution to a flat tail of slowly decreasing weights which leaves some ambiguity in the determination of the significant components. A physical interpretation of the bi-orthogonal decomposition is the projection of the data on an orthonormal basis which de-correlates both the time and space series. In this new basis, coherent structures become more evident. The BD has the property that the truncated sum over ordered eigenvectors is the best approximation of the original data y , in a least-square sense.

An interesting case is the presence of two similar, non-negligible weights $A_{k_1} = A_{k_2}$. This degeneracy can usually be ascribed to the existence of a spatiotemporal symmetry, $y(t+t_0, x) = y(t, x-x_0)$, such as a rotating mode. In this case the phase of ϕ_{k_1} and ϕ_{k_2} as well as of ψ_{k_1} and ψ_{k_2} are shifted by $\pi/2$. A variation of the mode's frequency only shows up in the *chrono* and not in the *topo*. Coupled modes, which have identical frequencies

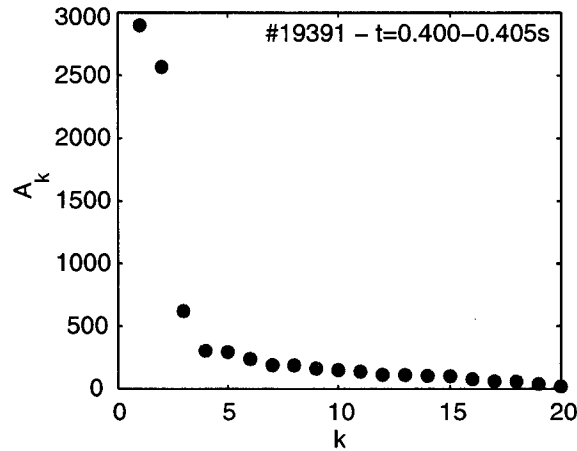


Figure 5.5: Eigenvalues of the bi-orthogonal decomposition of magnetic measurements of the disruption precursor in #19391. The two main eigenvectors are degenerated and the corresponding topes and chronos shown in figure 5.6.

but different wave vectors, are not separated and appear in one pair of bi-orthogonal components.

In figure 5.6 the possibilities of the bi-orthogonal decomposition are illustrated for the magnetic measurements of a disruption precursor with a toroidal and a poloidal array. The two principal eigenvectors, which comprise 95% of the total signal power, are degenerated and describe a rotating mode. The toroidal and poloidal parts of the two main topes, which are shown separately in (a) and (b), respectively, as well as the corresponding chronos (c), show the typical phase shift of $\pi/2$. The toroidal part of the topes reveals an $n = 2$ structure whereas the poloidal part indicates an $m = 3$ periodicity. The chronos show a decreasing frequency and an increasing amplitude.

The example in figure 5.6 illustrates the advantages of the bi-orthogonal decomposition over standard Fourier techniques. In contrast to the spectral analysis described in section 5.2.2, the BD does not assume a constant frequency throughout the analysed time interval and allows to identify an arbitrary time evolution. Neither does it make any assumptions concerning the spatial structure like the toroidal mode analysis (section 5.2.2), which requires pure spatial Fourier components. It can, therefore, be used to analyse the poloidal structure. The properties of the bi-orthogonal decomposition as well as its applications have been discussed in detail by *Dudok de Wit et al* [29] and *Kim et al* [30].

5.3 Modelling of magnetic islands

In order to interpret the poloidal structure of the magnetic measurements from the edge, magnetic islands are modelled and the corresponding response of the magnetic probes computed [31]. This calculation is simplified by the assumption that the perturbation

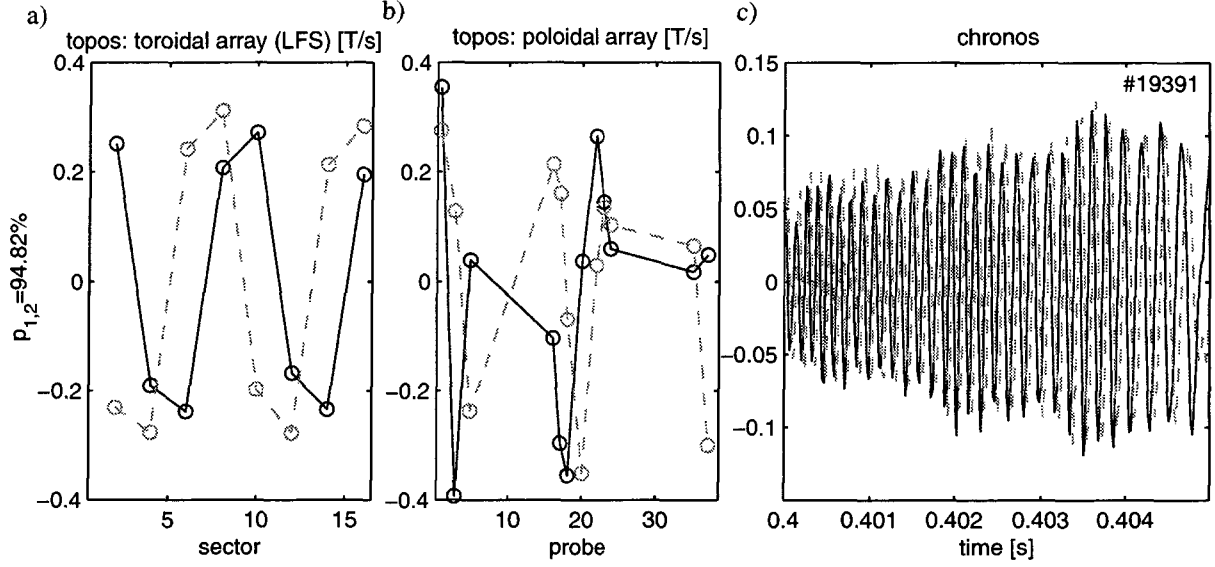


Figure 5.6: Two main bi-orthogonal components of magnetic measurements of a disruption precursor (weight distribution in figure 5.5). The topos are separated into the contributions of the toroidal (a) and poloidal (b) arrays. The corresponding chronos are shown in (c). The degenerated eigenvectors are interpreted as a rotating 3/2 mode.

currents only flow along the magnetic field lines and that they are concentrated on the corresponding resonant flux surface neglecting the response of the remaining plasma. These currents are force-free and do not change the equilibrium. The calculation of the magnetic field at the probe includes the induced toroidal eddy currents in the vacuum vessel.

5.3.1 Perturbation current density

Using the straight field line angle θ^* (equation 5.7), the perturbation current in the direction of the magnetic field can be decomposed into Fourier components with poloidal and toroidal mode numbers m and n ,

$$\delta \vec{j}(\varphi, \theta^*, \Psi) = c(\Psi) \cdot \sin(m\theta^* - n\varphi) \cdot \vec{B}. \quad (5.26)$$

Since the perturbation current density is divergence free, $\vec{\nabla} \cdot \vec{j} = 0$, the Ansatz in equation 5.26 leads to,

$$0 = \vec{B} \cdot \vec{\nabla} (c(\Psi) \sin(m\theta^*(\theta) - n\varphi)) \quad (5.27)$$

which can be simplified by using the derivatives of the flux function $\partial\Psi/\partial Z = -RB_R$ (equation 2.23) and $\partial\Psi/\partial R = RB_Z$ (equation 2.24) and assuming toroidal symmetry, $\partial C(\Psi)/\partial\varphi = 0$,

$$\begin{aligned} 0 &= m \left(B_R \frac{\partial\theta^*}{\partial R} + B_Z \frac{\partial\theta^*}{\partial Z} \right) - \frac{nB_\varphi}{R} \\ &= m\vec{B} \cdot \vec{\nabla}\theta^* - n\vec{B} \cdot \vec{\nabla}\varphi. \end{aligned} \quad (5.28)$$

Equation 5.28 is a resonance condition which is only fulfilled at a the $q = m/n$ flux surface.

In the limit of the model the perturbation current is a sheet current on this resonant surface. In order to transform the current density $j(\Psi)$ into a sheet current density j_A it is assumed that current flows in a infinitesimally narrow flux tube of width $d\Psi$ which corresponds to a radial width dr ,

$$j_A d\Psi = j(\Psi) dr. \quad (5.29)$$

With $d\Psi = RB_\theta dr$ the sheet current density can be identified as,

$$j_A = \frac{j(\Psi)}{RB_\theta}. \quad (5.30)$$

Even though the current, which flows in a flux tube, is constant on a flux surface, the surface current density varies like $1/RB_\theta$ and it follows that,

$$\vec{j}_A \propto \frac{1}{RB_\theta} \cdot \sin(m\theta^* - n\varphi) \cdot \vec{B}. \quad (5.31)$$

In order to reconstruct the poloidal component of the perturbation field only the toroidal component of the perturbation current density needs to be taken into account. With $I = RB_\varphi \approx \text{const.}$ the toroidal perturbation current density is proportional to,

$$j_{A,\varphi} \propto \frac{1}{R^2 B_\theta} \cdot \sin(m\theta^* - n\varphi). \quad (5.32)$$

5.3.2 Reconstruction of the magnetic perturbation

For a numerical reconstruction of the magnetic perturbation field at the location of the probes, it is necessary to discretise the model. The resonant flux surface and the conducting vacuum vessel are divided into toroidal filaments. In the following the flux surface filaments will be labelled with s , the vessel filaments with v and the 38 magnetic probes of the poloidal array with m . The poloidal magnetic perturbation field at the probe location B_m , depends linearly on the toroidal component of the perturbation current $I_s = j_{A,\varphi} \Delta l_\theta$, where Δl_θ is the length of the filament in the poloidal plane, and also on toroidal eddy currents in the vessel I_v ,

$$B_m = b_{ms} I_s + b_{mv} I_v. \quad (5.33)$$

The coefficients b_{ms} and b_{mv} are obtained from a Biot-Savart integration along the current filament k ,

$$B_m = \underbrace{\frac{\mu_0}{4\pi} \oint_k \frac{d\vec{l}_k \times (\vec{r}_m - \vec{r}_k)}{|\vec{r}_m - \vec{r}_k|^3} \cdot \hat{e}_m}_{b_{mk}} I_k, \quad k = s, v \quad (5.34)$$

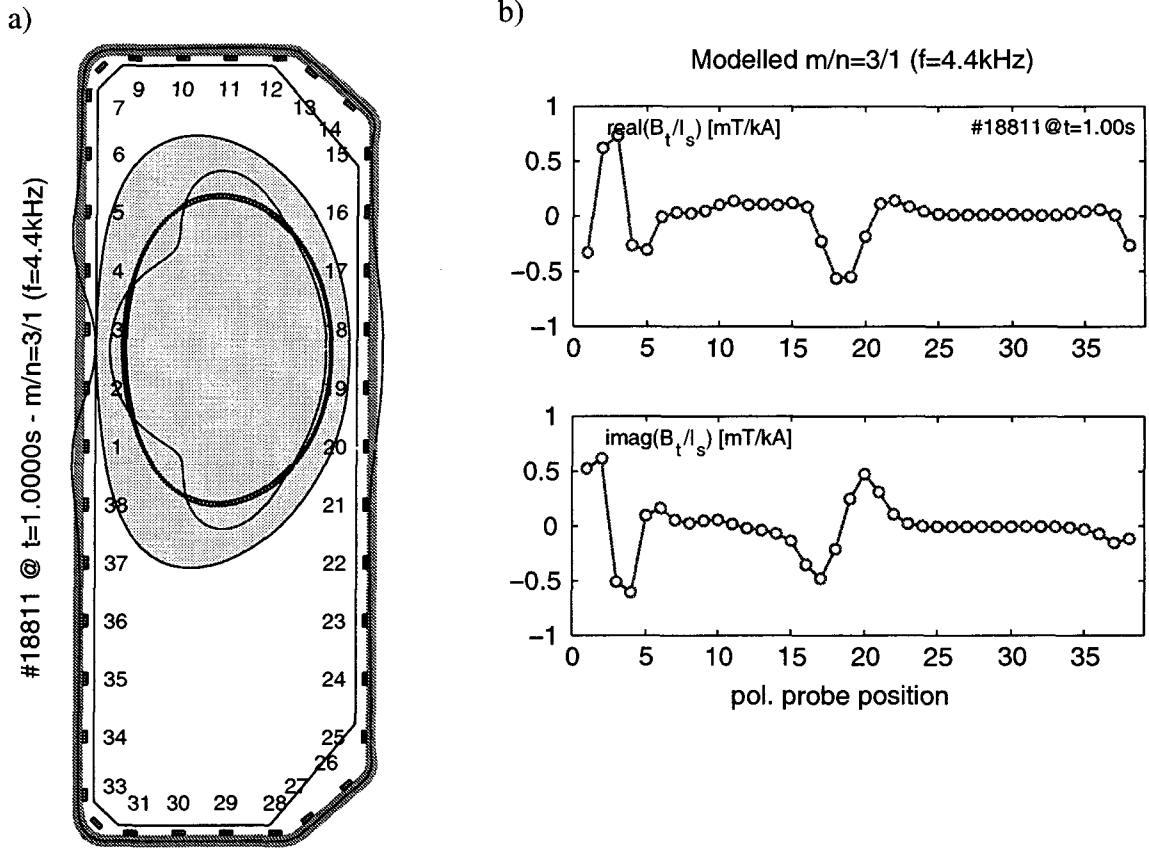


Figure 5.7: (a): The time varying perturbation current of a modelled 3/1 island located on the $q = 3$ surface leads to eddy currents in the vessel. The current in each of the 256 toroidal filaments in the plasma and in the vessel are indicated. (b): The magnetic field at the location of the probes is calculated from the modelled perturbation currents.

with \hat{e}_m being a unit vector along the axis of the probe m . The currents in the vessel filaments are caused by time-varying currents in the plasma and in the vessel itself. Kirchshoff's loop law applied to a vessel filament states,

$$0 = R\delta_{vv'}I_{v'} + M_{vv'}\dot{I}_{v'} + M_{vs}\dot{I}_s \quad (5.35)$$

where R is the resistance of a vessel filament and $M_{vv'}$ and M_{vs} mutual inductances. The latter are obtained by integration over the toroidal filaments,

$$M_{kk'} = \left(\frac{\mu_0}{4\pi}\right)^2 \oint_k \oint_{k'} \frac{d\vec{l}_k \cdot d\vec{l}_{k'}}{|\vec{r}_k - \vec{r}_{k'}|}, \quad k, k' = s, v. \quad (5.36)$$

Owing to dissipation, a time-varying electric field does not uniformly penetrate the conducting vessel wall. It decays exponentially to $1/e$ of its initial amplitude in a distance,

$$d_{\text{skin}} = \sqrt{\frac{2}{\mu\omega\sigma}} \quad (5.37)$$

which is called skin depth [32]. For a typical mode frequency of 5 kHz the skin depth of the TCV vessel is 6 mm. The current in the vessel concentrates on the surface. The

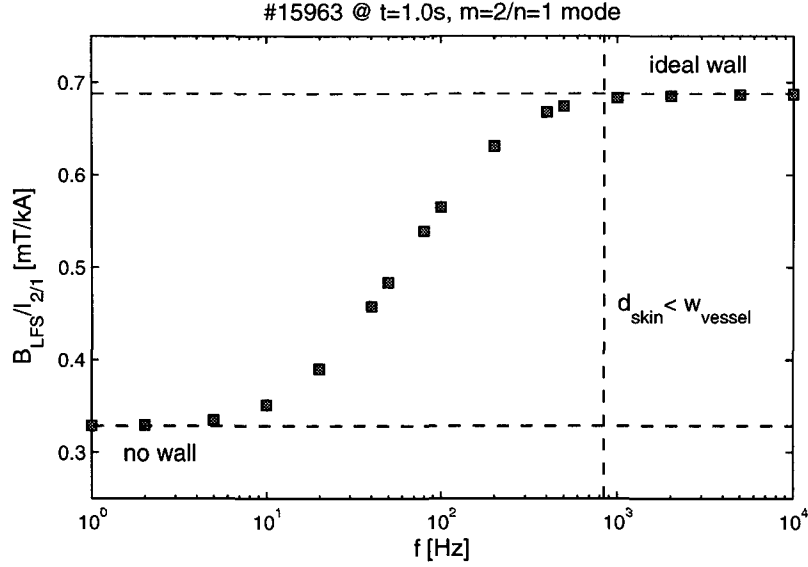


Figure 5.8: The modelled amplitude of a 2/1 mode at the location of a magnetic probe on the LFS is shown as a function of the mode frequency. The limits of an ideal wall ($R_v = 0$) and of no wall are included. For frequencies above 880 Hz the skin depth d_{skin} becomes smaller than the width of the TCV vacuum vessel w_{vessel} .

reduction of resistivity is taken into account by assuming only a conducting layer with a maximum width of $d_{\text{skin}}(\omega)$. For a perturbation with a frequency ω , equation 5.35 results in an expression for the induced eddy currents,

$$\begin{aligned}
 0 &= R(\omega) \delta_{vv'} I_{v'} + i\omega M_{vv'} I_{v'} + i\omega M_{vs} I_s \\
 \Leftrightarrow I_{v'} &= \underbrace{\left(i \frac{R(\omega)}{\omega} \delta_{vv'} - M_{vv'} \right)^{-1} M_{vs}}_{c_{v's}(\omega)} I_s.
 \end{aligned} \tag{5.38}$$

Since $R \propto \sqrt{\omega}$ it can be seen from equation 5.38, that for sufficiently high frequencies the vessel behaves like an ideal conductor. The magnetic perturbation at the probes can now be computed by,

$$B_m(\omega) = (b_{ms} + b_{mv} c_{vs}(\omega)) I_s. \tag{5.39}$$

The modelled perturbation currents for a 3/1 island located on the $q = 3$ surface in discharge #18811 are sketched in figure 5.7(a). The eddy currents in the wall are calculated according to equation 5.38 assuming a rotation of 4.4 kHz. The magnetic field at the location of the magnetic probes which results from the currents in the plasma and in the wall filaments, is shown in figure 5.7(b).

The frequency dependence of the magnetic perturbation at the location of the probes is illustrated in figure 5.8. The magnetic perturbation field due to a 2/1 mode at a probe on the LFS is computed for various rotation frequencies. For very low frequencies, $f < 10$ Hz, eddy currents in the wall can be neglected. As the frequency increases the effect of eddy

currents in the vessel becomes important. For $f > 1$ kHz the resistivity of the wall can be neglected and the field amplitude approximately doubles with respect to the no-wall case. The effect of the finite penetration length of electrical fields is small, since the skin depth is large compared to the vessel width for all frequencies where the resistivity of the vessel is important.

5.3.3 Identification of the experimental mode structure

The observed mode is identified by comparing the experimental structure $b_j = b(x_j)$, to the modelled structure of an m/n -mode $B_{m,n}(x_j)$, or the linear combination of several modes $\sum_{k=1}^K a_k B_{m_k, n_k}(x_j)$. The data is fitted in a least square-sense, choosing the K coefficients a_k to minimise,

$$\chi^2 = \sum_{j=1}^N \left(\frac{b_j - \sum_{k=1}^K a_k B_k(x_j)}{\sigma_j} \right)^2. \quad (5.40)$$

The uncertainty σ_j , of the measurement taken at the location x_j , is usually assumed to be constant. The quality of the fit $B = \sum_k a_k B_k$, can be evaluated by calculating the probability Q , that, taking the model to be true and the measurements to be normally distributed with a standard deviation of σ , χ^2 exceeds the minimum value obtained in the fit [33]. However, if the uncertainty of the measured mode structure is unknown, some kind of error for the fit can be derived by minimising χ^2 using an arbitrary σ . If it is assumed that all measurements have the same standard deviation and that the model is true, the standard deviation of the measurements can be calculated,

$$\sigma^2 = \sum_{j=1}^N (b_j - B(x_j))^2 / N \quad (5.41)$$

and an error bar assigned to each data point.

The identification of the poloidal structure of the mode observed in #18881 (figure 5.3) is shown as an example. The experimental structure was extracted using a spectral analysis (see section 5.2.2). Since the toroidal structure is easily obtained from the spectral analysis of the toroidal array, the poloidal structure is only compared to modelled $n = 1$ modes, namely a 2/1 (figure 5.9(a)) and a 4/1 island (b). The fit of the 2/1 mode results in significantly lower standard deviation of $\sigma_{2/1} = 0.37$ mT than the fit of the 4/1 mode which yields $\sigma_{4/1} = 0.58$ mT, and confirms the previous identification (figure 5.3). The fits to odd poloidal mode numbers result in much higher standard deviations and can immediately be excluded.

The example shown in figure 5.9 illustrates one of the difficulties of the poloidal mode analysis. Both the 2/1 and the 4/1 modes lead to similar perturbation structures at probes on the LFS. This results from the pitch angle of the field line which increases towards the

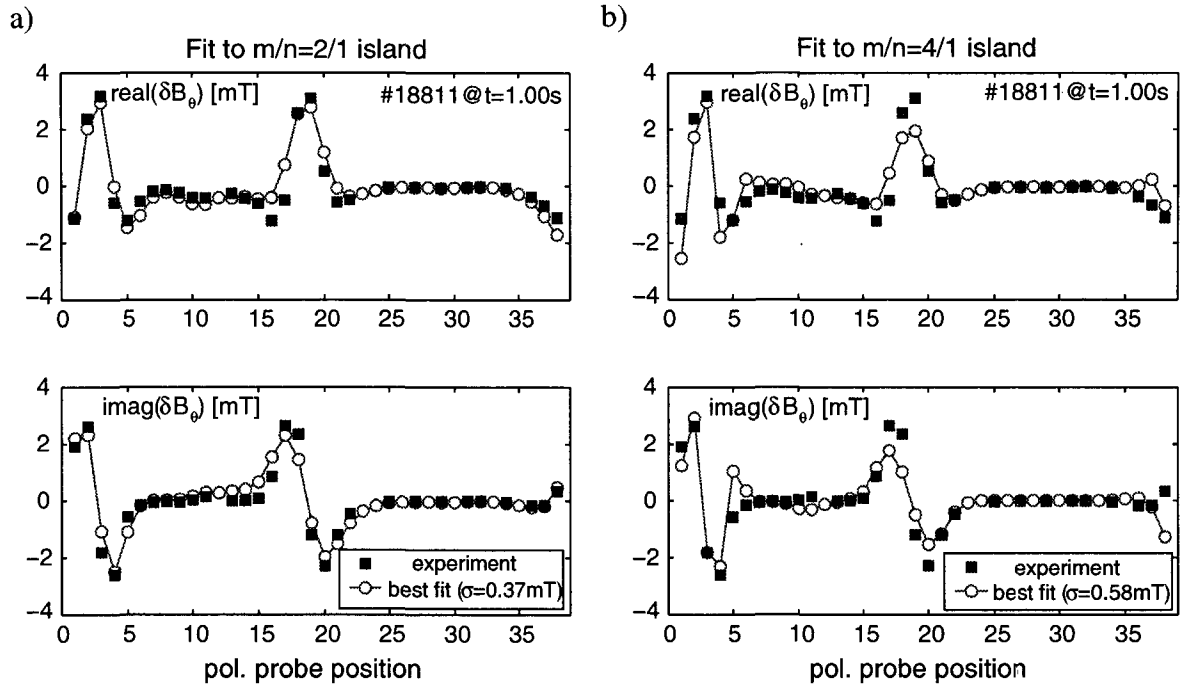


Figure 5.9: Least-square fit of modelled 2/1 (a) and 4/1 islands (b) to the experimental mode structure obtained by the spectral analysis of magnetic measurements in the discharge #18811 (see figure 5.3(b)). The fit of the 2/1 island results in significantly lower $\sigma_{2/1} = 0.37 \text{ mT}$ than the fit of the 4/1 mode, yielding $\sigma_{4/1} = 0.58 \text{ mT}$ and identifies the mode as a 2/1 island.

plasma edge. Therefore, the identification of the poloidal mode structure requires a close spacing of probes over a wide poloidal range and an accurate treatment of the field line geometry, in particular in highly shaped plasmas. In spite of the complete poloidal array of TCV, the wide poloidal coverage is hampered by the great distance between many of the probes and the plasma.

A reduced poloidal coverage due to a low signal amplitude as well as toroidicity and shaping effects, results in the non-orthogonal response of different modes. The angle α between the responses of two modelled modes $Y_{m,n}$ and Y_{m^*,n^*} , can be defined by $\cos \alpha = \langle Y_{m,n}, Y_{m^*,n^*} \rangle / (\|Y_{m,n}\| \|Y_{m^*,n^*}\|)$, where $\langle \rangle$ denotes the scalar product. The angles between various $n = 1$ and $n = 2$ modes of the discharge #18811 shown in figure 5.9 are listed in table 5.1(a) and (b), respectively. It can be seen that even and odd poloidal mode numbers are well separated, though not orthogonal, whereas modes with the same parity are almost parallel. In particular, the angle of $\cos \alpha \approx 0.83$ between the response of a 2/1 and 4/1 mode explains the relatively good fit of the 4/1 response to the 2/1 mode structure in figure 5.9(b).

a)

Angles between modelled $n = 1$ modes

mode	2/1	3/1	4/1	5/1
2/1	1	0.09	0.83	0.10
3/1		1	0.28	0.89
4/1			1	0.43
5/1				1

b)

Angles between modelled $n = 2$ modes

mode	3/2	4/2	5/2	6/2
3/2	1	0.52	0.92	0.49
4/2		1	0.45	0.93
5/2			1	0.34
6/2				1

Table 5.1: The angle define by $\cos \alpha = \langle Y_{m,n}, Y_{m^*,n^*} \rangle / (\|Y_{m,n}\| \|Y_{m^*,n^*}\|)$ between modelled island responses of various $n = 1$ (a) and $n = 2$ islands (b) calculated for the discharge #18811 at $t = 1.0$ s.

5.4 Island width

A quantitative analysis of magnetic islands requires the calculation of their widths, w (see section 2.4.1). In order to interpret the magnetic measurements taken at the plasma edge as a perturbation inside the plasma, the signals have to be inverted.

5.4.1 Cylindrical approximation

The simplest model assumes a cylindrical geometry (r, θ, z) with the periodic boundary condition $f(z) = f(z + 2\pi R_0)$. The vacuum vessel wall at a distance $r = b$ is considered to be an ideal conductor. Furthermore, it is assumed that the plasma outside the resonant flux surface at a radius $r = r_s$ can be ignored. Thus, the perturbed flux ψ_1 , defined by $B_{1r} = (-1/r)(\partial\psi_1/\partial\theta)$ and $B_{1\theta} = \partial\psi_1/\partial r$, is a solution of the Laplace equation,

$$\Delta\psi_1(r, \theta, z) = 0 \quad \text{for } r > r_s. \quad (5.42)$$

A decomposition into Fourier components serves as an Ansatz,

$$\psi_1(r, \theta, z) = \hat{\psi}_1(r) e^{i(m\theta - nz/R_0)} \quad (5.43)$$

and leads to the equation,

$$\frac{1}{r} \frac{\partial}{\partial r} \left(r \frac{\partial \hat{\psi}_1(r)}{\partial r} \right) - \left(\frac{m^2}{r^2} + \frac{n^2}{R_0^2} \right) \hat{\psi}_1(r) = 0. \quad (5.44)$$

Assuming a large toroidal wavelength ($R_0/n \gg r/m$) the general solution of (5.44) is,

$$\hat{\psi}_1(r) = c_1 r^m + c_2 r^{-m}. \quad (5.45)$$

The two free parameters c_1 and c_2 can be determined by the boundary conditions $\hat{\psi}_1(r_s) = \hat{\psi}_{1,s}$ and $\hat{\psi}_1(b) = 0$ resulting in,

$$\hat{\psi}_1(r) = \frac{\hat{\psi}_{1,s}}{(r_s/b)^{-m} - (r_s/b)^m} \left[\left(\frac{r}{b} \right)^{-m} - \left(\frac{r}{b} \right)^m \right]. \quad (5.46)$$

The magnetic field can be calculated from the flux function $\psi_1(r, \theta, z)$,

$$B_{1r} = -\frac{im}{r} \frac{\hat{\psi}_{1,s}}{(r_s/b)^{-m} - (r_s/b)^m} \left[\left(\frac{r}{b}\right)^{-m} - \left(\frac{r}{b}\right)^m \right] e^{i(m\theta - nz/R_0)} \quad (5.47)$$

$$\text{and } B_{1\theta} = -\frac{m}{r} \frac{\hat{\psi}_{1,s}}{(r_s/b)^{-m} - (r_s/b)^m} \left[\left(\frac{r}{b}\right)^{-m} + \left(\frac{r}{b}\right)^m \right] e^{i(m\theta - nz/R_0)}. \quad (5.48)$$

In the following the amplitude of the Fourier components of B_1 including a possible phase shift will be denoted with a hat. Using equation 5.47 to calculate $B_{1,s}$ identifies $\hat{\psi}_{1,s} = ir_s \hat{B}_{1r,s}/m$. Then equation 5.47 and 5.48 can be written as,

$$\hat{B}_{1r} = \frac{r_s}{r} \frac{\hat{B}_{1r,s}}{(r_s/b)^{-m} - (r_s/b)^m} \left[\left(\frac{r}{b}\right)^{-m} - \left(\frac{r}{b}\right)^m \right] \quad (5.49)$$

$$\text{and } \hat{B}_{1\theta} = -\frac{ir_r}{r} \frac{\hat{B}_{1r,s}}{(r_s/b)^{-m} - (r_s/b)^m} \left[\left(\frac{r}{b}\right)^{-m} + \left(\frac{r}{b}\right)^m \right]. \quad (5.50)$$

For $r_s/b \ll 1$ it follows that $|\hat{B}_{1r,s}| \approx |\hat{B}_{1\theta,s}|$. In the same approximation the magnetic field decays radially with $1/r^{m+1}$, which is referred to as multipole field decay. Equations 5.49 and 5.50 allow an inversion of the magnetic measurements outside the plasma. For $r_s/b \ll 1$ the components of the magnetic field measured just in front of the ideal conducting wall $r = b$, are,

$$\hat{B}_{1r}(b) = 0 \quad (5.51)$$

$$\text{and } \hat{B}_{1\theta}(b) = -i \frac{2\hat{B}_{1r,s}}{(b/r_s)^{m+1}}. \quad (5.52)$$

It is now possible to derive an island width from the mode amplitude measurements at the plasma edge $B_{\theta,m,n}$ using equation 2.62 and equation 5.52,

$$w = \sqrt{\frac{8(b/r_s)^{m+1} B_{\theta,m,n}(b)}{\epsilon_s n B_{0,\varphi} s_s}} \cdot r_s. \quad (5.53)$$

The uncertainty of this estimate of the island width is mainly caused by the simplifications in the underlying model. The assumed cylindrical geometry and the neglect of the plasma, both, lead to systematic errors. The uncertainty of the equilibrium reconstruction also contributes to the uncertainty of w . In particular the shear on the resonant surface s_s , has a large error bar.

5.4.2 Reconstruction of the island geometry

The determination of the island size can be improved over the cylindrical estimation (equation 5.53) by using the island model developed in section 5.3 to reconstruct the perturbation in the whole plasma. The superposition of the helical perturbation flux ψ_1^* and the equilibrium flux ψ_0^* then reveals the full geometry of the magnetic island [31].

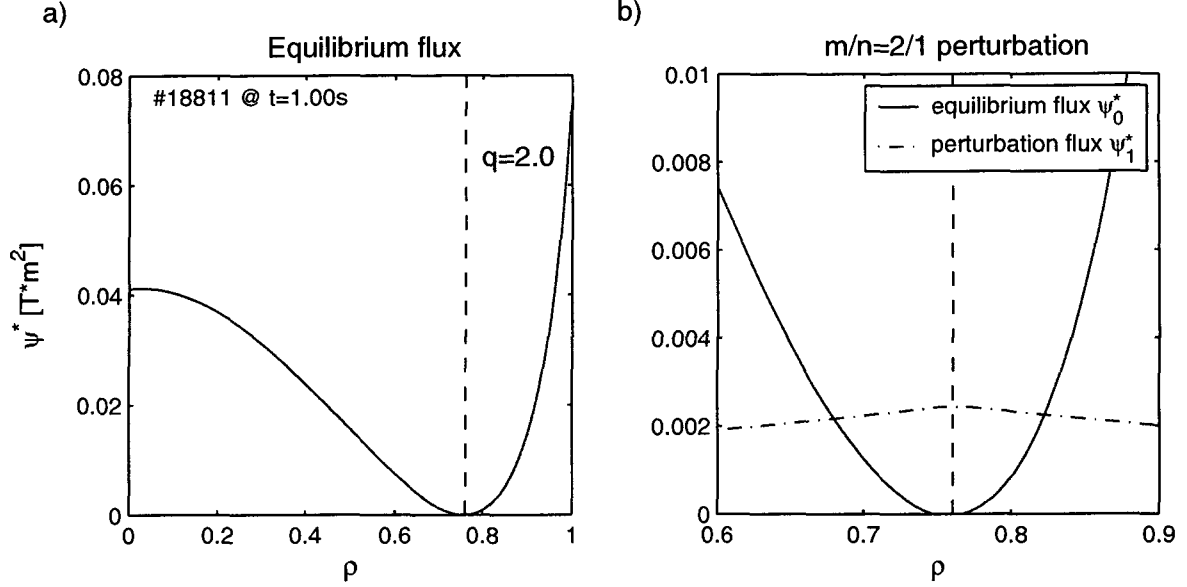


Figure 5.10: Helical equilibrium flux ψ_0^* of the $q = 2$ surface in the whole plasma (a) and together with the perturbation flux ψ_1^* in the vicinity of the $q = 2$ surface (b). The perturbation flux is reconstructed using the least-square fit of an $m/n = 2/1$ island to the experimental mode structure (figure 5.9).

The helical equilibrium flux across the whole plasma can be calculated from the poloidal flux ψ_{pol} (equation 2.18) and the toroidal flux ψ_{tor} (equation 2.19), thereby, replacing the previously used parabolic expansion of ψ^* in the vicinity of the resonant flux surface (equation 2.60). In order to calculate the helical equilibrium field, an artificial zero shear field with the safety factor of the resonant surface q_s is subtracted from the equilibrium field. According to the definition of q (equation 2.20) the poloidal flux of a zero shear field is $\psi_{\text{pol}, q=q_s} = \psi_{\text{tor}}/q_s$. Thus, the helical equilibrium flux is given by,

$$\psi_0^* = \psi_{\text{pol},0} - \frac{1}{q_s} \psi_{\text{tor},0}. \quad (5.54)$$

For positive shear, ψ_0^* has a minimum at the resonant flux surface. Figure 5.10(a) shows ψ_0^* for $q_s = 2$ of discharge #18811, where magnetic measurements revealed an $m/n = 2/1$ mode (figure 5.9).

The reconstruction of the helical perturbation flux can replace the constant flux assumption which was introduced in section 2.4.1 and has been used to derive equation 5.53. The comparison between the measured mode structure and a modelled m_k/n_k island (section 5.3.3) results in a coefficient a_k which determines the amplitude of the toroidal component of the perturbation current in the filaments on the resonant flux surface,

$$I_s = a_k I_{m_k, n_k}(x_s). \quad (5.55)$$

The perturbation of the helical flux at an arbitrary location in the plasma x_p , is calculated from the mutual inductance M_{ps} , between the toroidal current filaments located at x_p and

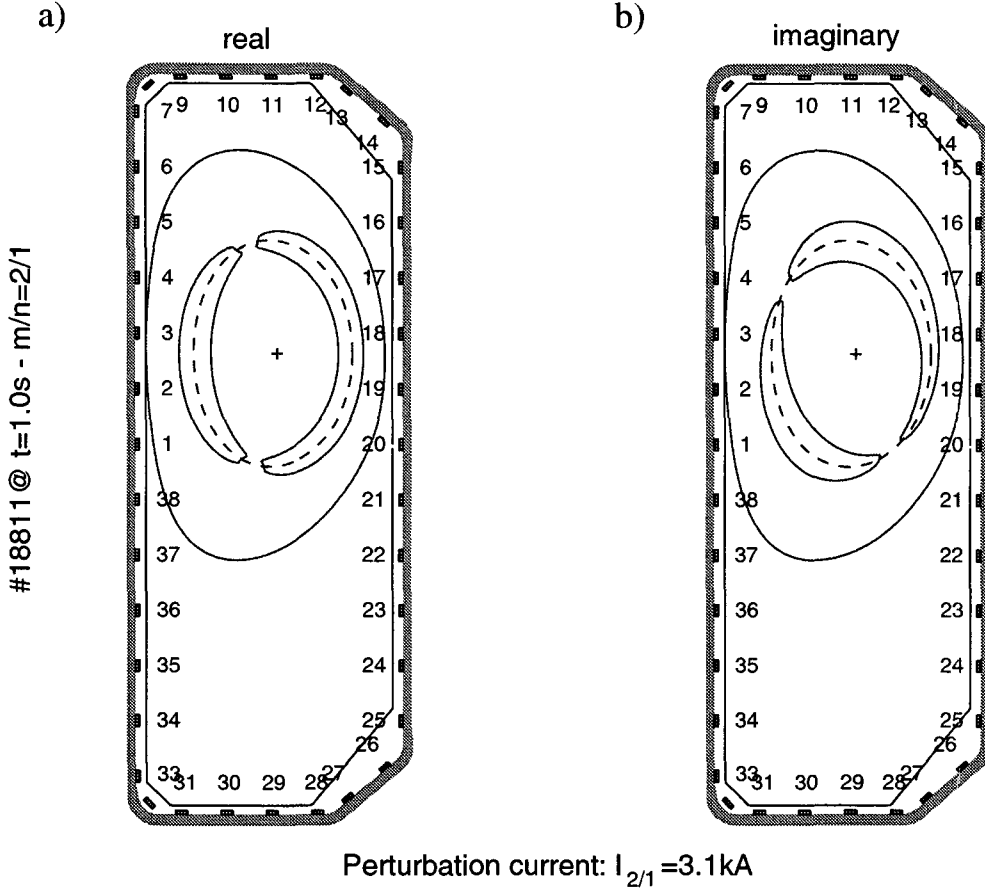


Figure 5.11: Island geometry of the 2/1 mode in discharge #18811 resulting from the real (a) and imaginary (b) part of the reconstructed perturbation current (figure 5.9). The contour line of the helical flux of the island's separatrix $\psi^*(\rho_{\text{sep}})$ reveals an island width corresponding to 20% of the minor radius and shows the typical “croissant” shape.

x_s (equation 5.36) and the current along the magnetic field lines,

$$\psi_1^*(x_p) = M_{ps} I_s \cdot \frac{\sqrt{B_\varphi^2 + B_\theta^2}}{B_\varphi}. \quad (5.56)$$

The reconstructed perturbation flux of the 2/1 mode in discharge #18811 is shown in figure 5.10(b).

When superposing ψ_0^* and ψ_1^* , the extremum of the equilibrium flux at the resonant surface is modulated by the perturbation flux. The x-points of the resulting islands are located at the maxima of ψ_1^* , the o-points at the minima. Figures 5.11 (a) and (b) show the typical “croissant” shaped contours of the helical flux of the island's separatrix of the 2/1 mode in #18811 for two different phase angles. The helical perturbation flux, however, is usually modified by the presence of the plasma, thereby, altering the geometry of the island. The presented model also neglects the influence of the plasma on the decay of the radial perturbation. In [31], *Schittenhelm et al* estimated that this effect leads to an overestimation of the island width of the order of 15%.

5.4.3 Confinement degradation

An independent estimate of w can be obtained from the confinement degradation due to the island. The separatrix of an island connects the plasma on both sides of the island, increasing the effective radial heat diffusivity. In the Chang and Callen belt model [34] the parallel heat diffusivity is assumed to be infinite leading to a flat pressure profile across the island, which is then approximated by a cylindrical belt of width $h = w/\sqrt{2}$. Assuming a constant heat diffusivity and heating power deposition profile, a confinement degradation $\Delta W/W$, can be caused by an island with a width,

$$w = \frac{\sqrt{2}}{4} \frac{(-\Delta W)}{W} \frac{a^4}{r_s^3} \quad (5.57)$$

where r_s is the radius of the resonant surface. The confinement degradation is altered if all of the heat were deposited in the plasma centre,

$$w = \frac{\sqrt{2}}{2} \frac{(-\Delta W)}{W} \frac{a^2}{r_s}. \quad (5.58)$$

The island width resulting from the confinement degradation has a large uncertainty, which originates in the global energy measurement, the uncertainty of the position of the resonant flux surface and most importantly from the simplifications in the model itself. Nevertheless, it allows an independent cross check and agrees with the magnetic measurements within approximately 20%.

5.5 Concluding remarks

Several numerical methods have been presented to extract coherent mode structures from fluctuation measurements, separating their temporal and spatial behaviour. These methods were implemented in the standard data analysis of magnetic fluctuation measurements on TCV. Many features of these methods are complementary to each other and are applied accordingly, allowing to detect many types of coherent fluctuations. While the toroidal arrays provide a very sensitive means to identify the toroidal structure, the interpretation of the poloidal mode structure is complicated by the flexibility of the TCV vessel and the variety of possible plasma shapes. The modelling of magnetic islands and their responses at the magnetic probes has allowed to separate between geometry or diagnostic induced, and intrinsic mode structure and has, therefore, been very useful in the interpretation of the poloidal measurements. However, the tight spacing of the probes in the poloidal array and a complete acquisition in the vicinity of the plasma is necessary rather than supplementary for a basic poloidal mode analysis.

Chapter 6

Sawtooth oscillations

Sawtooth oscillations, named after the characteristic shape of their soft X-ray signal, were first observed on the ST tokamak [35] and are present in most standard tokamak scenarios. Although they have been the subject of many studies, the underlying mechanisms are not yet fully understood.

After a brief introduction into the phenomenology and the present understanding of sawteeth, a link between the two most obvious sawtooth characteristics, namely their period and amplitude, is made. This chapter then presents an original analysis of the shape dependence of sawtooth characteristics using TCV's unique shaping capability together with its flexible ECH system. In particular, the response of sawteeth to an increase of central heating power is observed to depend strongly on the plasma shape. The experimental observation is then related to the role of the ideal or resistive internal kink mode in triggering the sawtooth crash [36, 37].

6.1 Introduction into sawteeth

Sawtooth oscillations are periodic oscillations of central temperature, density and other plasma parameters. A slow rise principally of temperature, during the sawtooth ramp is followed by the onset of the $m/n=1/1$ internal kink mode (see chapter 2) causing a rapid drop, the so-called sawtooth crash. During this crash a reconnection process results in the flattening of the central temperature and density profiles. The corresponding outward transport of energy defines an inversion radius ρ_{inv} , which separates the central region where energy is lost, from an outer region where energy is deposited. The inversion radius is closely related to the $q=1$ surface. The investigation of sawteeth has concentrated on three separate aspects: firstly, on the transport of particles and energy as well as current diffusion during the sawtooth ramp, secondly, on the instability triggering the sawtooth crash, and finally, on the relaxation process leading to the rapid outward transport.

The interest in sawteeth originated in their impact on central plasma parameters and

the resulting degradation of confinement. TCV discharges, where sawteeth were stabilised using ECCD techniques, showed a significant improvement in energy confinement [38]. In a fusion reactor the repetitive flattening of the central temperature profile would also greatly influence the fusion yield. In recent years, a main concern has arisen from the observation that sawteeth can generate seed islands on outer resonant flux surfaces which trigger neoclassical tearing modes, which again limit the achievable beta. The description of the underlying physics of neoclassical tearing modes and an analysis of their occurrence in TCV is given in chapter 9. Nevertheless, sawteeth are also beneficial since they can prevent the accumulation of impurities in the plasma centre.

A comprehensive understanding of the underlying instability leading to the sawtooth crash is necessary in order to predict the sawtooth behaviour in a future fusion reactor and to find ways to control their occurrence and amplitude.

6.2 Sawtooth period and crash amplitude

Sawteeth are commonly observed with the soft X-ray diagnostic (see section 3.3.3). Characteristic parameters, such as the sawtooth period τ_{saw} , and the sawtooth amplitude A_{saw} , are obtained from a soft X-ray emission measurement I_x , along a chord passing through the plasma centre. The amplitude of the sawtooth crash is normalised to the total chord intensity ($A_{\text{saw}} = \Delta I_x / I_x$). The crash amplitude can be corrected for the temperature dependence of the X-ray emissivity (equation 3.7),

$$\alpha = d(\ln I_x) / d(\ln T_e). \quad (6.1)$$

Assuming carbon as the dominant impurity, α decreases from 1 at 900 eV, typical for T_{e0} in ohmic plasmas, down to 0.6 at 2.5 keV [39]. With density variations assumed negligible, $\alpha^{-1} A_{\text{saw}}$ then provides an estimate for the relative core electron pressure loss due to the sawtooth, $\Delta W_{e,c} / W_{e,c}$.

The evolution of the central plasma pressure during the sawtooth ramp phase can be obtained by analysing the one-dimensional electron heat balance equation [40],

$$\frac{\partial w_e}{\partial t} = p_{\text{in}} - p_{\text{ei}} - p_{\text{rad}} - \frac{1}{r} \frac{\partial (r q_c)}{\partial r}. \quad (6.2)$$

Here, p_{in} is the heating power density, p_{ei} the electron-ion heat transfer, p_{rad} the radiated power density and q_c the convection and conduction losses. It has been shown that for Ohmic TCV plasmas the re-heat rate in the sawtooth ramp phase is mainly determined by the heating power density [41],

$$\frac{\partial w_e}{\partial t} \approx p_{\text{in}}. \quad (6.3)$$

In the core region, radiation losses are small due to high temperatures and conduction losses small due to small gradients. Therefore, it is thought that the main discrepancy between re-heat rate and heating power density arises from electron-ion equipartition.

For the standard triangular shaped sawteeth, equation 6.3 allows to link the observables τ_{saw} and A_{saw} ,

$$\frac{\alpha^{-1} A_{\text{saw}}}{\tau_{\text{saw}}} \approx \frac{\partial w_e / \partial t}{w_e} = \frac{p_{\text{in}}}{\frac{3}{2} n k_B T_e}. \quad (6.4)$$

In the same approximation an integration of equation 6.3 over the sawtooth period and averaging over the core volume yields,

$$\frac{\Delta W_{e,c}}{V_c} \approx \langle p_{\text{in}} \rangle \tau_{\text{saw}}. \quad (6.5)$$

Therefore, τ_{saw} is an estimate for the energy which is lost during the sawtooth crash. If it is assumed that the relaxed profiles are flat within $q=1$, the lost energy can also be expressed as $\Delta W_{e,c}/V_c = \frac{3}{2} (\langle p_e \rangle_1 - p_{e1})|_{t_{\text{saw}} - \epsilon}$. Thus, the sawtooth period can also be seen as an estimate for the central poloidal beta $\beta_{p,1}$, defined according to Bussac (equation 2.46), which is attained prior to the sawtooth crash.

6.3 Density dependence of sawtooth instability

A linear increase of the sawtooth period with density was initially seen on TFR [42] and has since been observed on many other experiments, for example JET [43]. In order to verify this behaviour for sawteeth in Ohmic TCV plasmas, discharges with the same plasma shape ($\kappa = 1.50 \pm 0.03$ and $\delta = 0.23 \pm 0.02$) and the same plasma current, $I_P = 265 \pm 0.05$ kA, corresponding to an edge safety factor of $q_a = 4.5 \pm 0.2$, but varying densities have been analysed. Figure 6.1 shows the dependence of the sawtooth period on the line-averaged density $\langle n_e \rangle_{\text{FIR}}$, which is obtained from a central chord of the FIR interferometer (section 3.3.1). The line-averaged density varied from 0.5 to $6.5 \times 10^{19} \text{ m}^{-3}$. Over a large part of this density range, the sawtooth period is found to be proportional to the density (figure 6.1(a)). However, for $\langle n_e \rangle_{\text{FIR}} < 2 \times 10^{19} \text{ m}^{-3}$ the sawtooth period deviates from the linear dependence to a much weaker dependence.

Throughout the scanned densities the sawtooth amplitude remained approximately constant. This is consistent with $\tau_{\text{saw}} \propto \langle n_e \rangle$ and equation 6.4. In the linear Ohmic confinement regime, the temperature and consequently, the resistivity η , do not vary with density. At constant current the Ohmic heating power density, $p_{\text{Ohm}} = \eta \langle j \rangle^2$, also remains constant, leading to the observed inverse proportionality of re-heat slope and density.

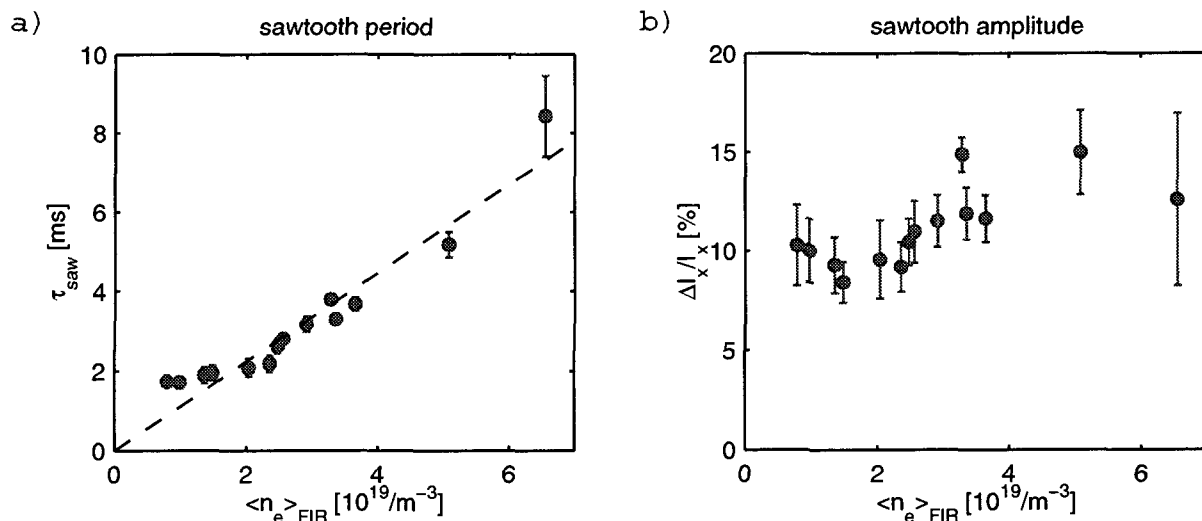


Figure 6.1: Dependence of sawtooth period (a) and amplitude (b) on the line averaged density, $\langle n_e \rangle$, in Ohmically heated and moderately shaped plasmas ($\kappa = 1.50 \pm 0.03$ and $\delta = 0.23 \pm 0.02$). The edge safety factor was kept constant ($q_a = 4.5 \pm 0.2$).

6.4 Shape dependence of sawtooth instability

There are various means by which the shaping of the poloidal plasma cross section can influence the sawtooth characteristics. On the one hand shaping can modify the time scale of the evolution of the relaxed profiles to an unstable state. The heating power density p_{in} , as well as the local energy confinement time τ_{E1} , depend on the plasma shape. Moreover, changes in the global energy confinement result in different central temperatures and hence different current diffusion times, τ_{R} . On the other hand, shaping can modify the stability criterion of the internal kink. In particular, the critical pressure gradient of the ideal internal kink mode is predicted to depend on shape. Early analytic calculations have already pointed out the destabilising effect of elongation while higher order distortions of the poloidal plasma cross section were found to be stabilising [44].

6.4.1 Experiment

A systematic scan of the shape of Ohmically and ECH heated plasmas has been performed. During these experiments the elongation was varied from 1.1 to 2.1 (2.4 in ohmic only) and the triangularity from -0.25 to $+0.45$ (figure 6.2). The flux contours of a typical discharge together with the ECH beam location and the vacuum vessel are shown in figure 6.3(a). The sawtooth period τ_{saw} and its amplitude A_{saw} were determined and then averaged over stationary intervals of typically 100 ms, corresponding to 20 to 200 sawtooth periods (figure 6.3(b)).

In order to separate the shape dependence, other plasma parameters such as the

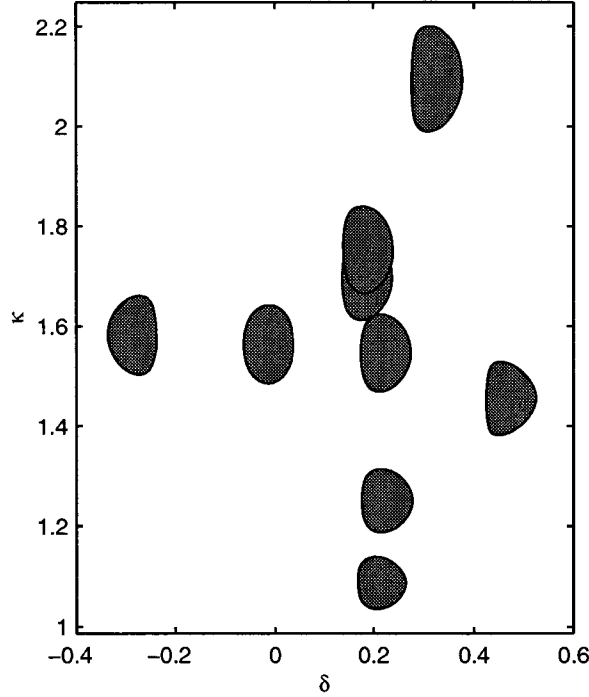


Figure 6.2: Systematic scan of plasma elongation κ , and triangularity δ .

temperature, density, and current profiles, which could influence the sawtooth behaviour, were kept similar. It has been seen that over a wide range of plasma shapes the profile broadness is related to the position of the $q=1$ surface or the sawtooth inversion radius ρ_{inv} [45], accordingly,

$$\langle p_e \rangle / p_{e0} \approx \rho_{\text{inv}} \approx \langle j \rangle / (q_0 j_0) \quad (6.6)$$

where $\langle \rangle$ denotes volume averages and ρ is a normalised plasma radius defined by $\rho = (V(\rho)/V_{\text{total}})^{1/2}$. The inversion radius has also been observed to scale according to,

$$\rho_{\text{inv}} \approx \frac{1}{q_{\text{eng}}} \cdot \frac{2}{\kappa_0 + 1/\kappa_0} \quad (6.7)$$

where $q_{\text{eng}} = 2B_0\pi a^2\kappa/(\mu_0 R_0 I_P)$ is the engineering safety factor which depends only on global parameters. Experimentally, ρ_{inv} and consequently the profile broadness were kept constant by carefully adjusting I_P , while the edge safety factor q_a , increased with elongation from 2.5 to 3.5 and with triangularity from 2.5 to 3.0. The sawtooth inversion contour was determined from the tomographic inversion of soft X-ray emission measurements (section 3.3.3) and then mapped onto a flux coordinate using the reconstructed flux from the equilibrium code LIUQE (section 3.4). For all explored shapes the inversion radius was found to be $\rho_{\text{inv}} = 0.45 \pm 0.05$. The remaining variations were neither correlated with variations in shape nor heating power and were of the order of the uncertainties of the tomographic inversion and of the equilibrium reconstruction.

The electron temperature and density measurements were obtained from the Thomson scattering diagnostic (section 3.3.2). There are 10 to 25 measurement locations inside the plasma, depending on the plasma elongation. Since the measurements were not synchronised with sawteeth, the profiles had to be averaged over the stationary intervals. In these experiments typically 6 profiles could be used for averaging. Throughout the scanned plasma shapes, the broadness of the ohmic electron temperature profile $\langle T_e \rangle / T_{e0} = 0.57 \pm 0.05$ and electron density profile $\langle n_e \rangle / n_{e0} = 0.74 \pm 0.03$ remained constant. The values determined for the inversion radius and the profile broadness are consistent with previous work [45].

In order to exclude the influence of density (section 6.3), the shape scan was performed at similar densities with n_{e0} ranging from 2.2 to $3.1 \times 10^{19} \text{m}^{-3}$. Within this density range the period of Ohmic sawteeth in a moderately shaped plasma ($\kappa = 1.5$, $\delta = 0.2$) at constant q_a varied only from 1.9 to 2.2 ms, or less than 15% (figure 6.1(a)).

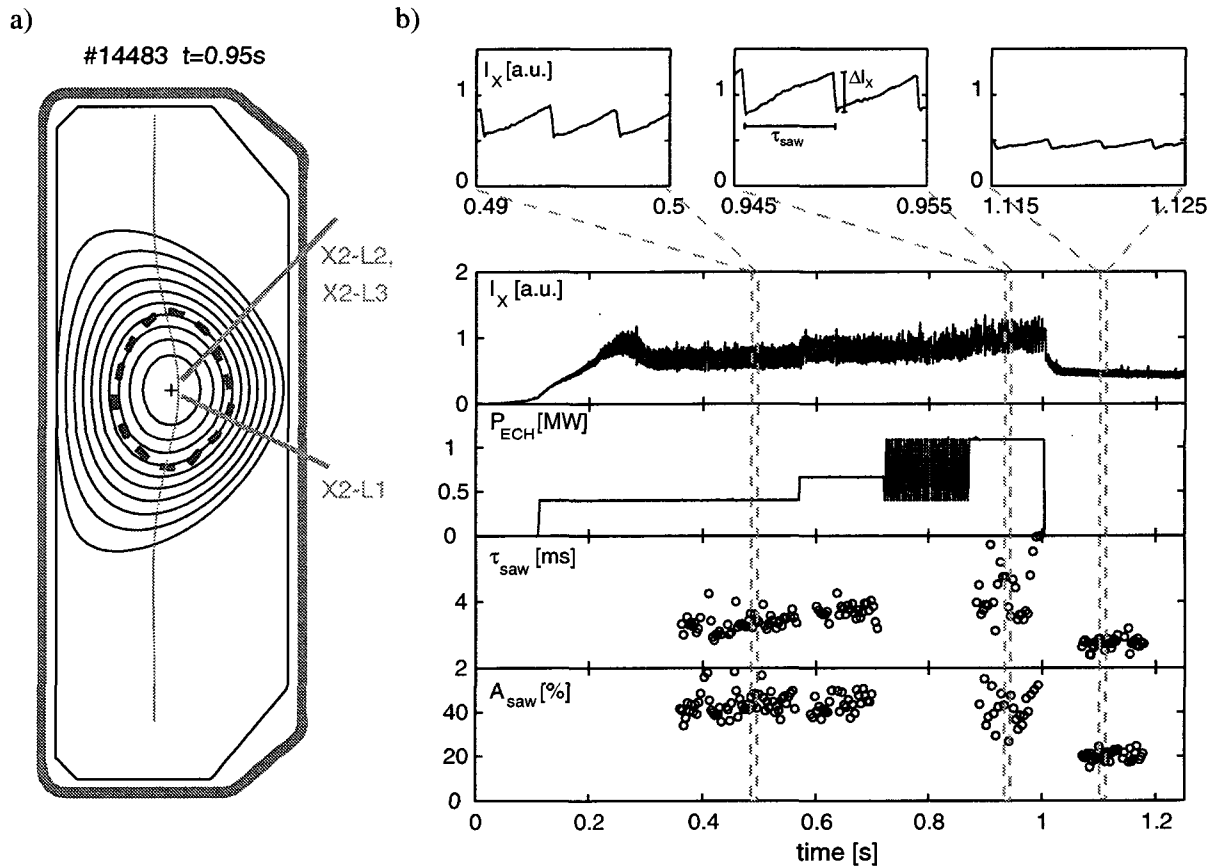


Figure 6.3: (a): Poloidal cross section of a plasma ($I_P = 400 \text{ kA}$, $\kappa = 1.45$, $\delta = 0.45$) and ECH launching geometry for central power deposition. The absorption layer for the X2-mode and the sawtooth inversion radius are indicated. (b): Soft X-ray emission measurements I_X along a central chord show the variations of sawteeth during the stepping up of the ECH power. The sawtooth period τ_{saw} , and their crash amplitude A_{saw} , are determined in intervals with constant plasma parameters.

Additional ECH heating at the second harmonic extraordinary mode (X2-mode) was applied to increase the plasma pressure. At the time of these experiments only three 82.7 GHz gyrotrons with a total of 1.4 MW of additional heating power were operational (section 3.2). The chosen density range is well below the cut-off density of the X2-mode thereby avoiding any significant refraction of the beams. The heating power was increased in three steps and included an interval where the power was modulated. A central power deposition was chosen so as to guarantee similar effects on current and pressure profiles and increase the global pressure rather than induce local changes in the vicinity of the $q=1$ surface. In particular, non-standard sawtooth behaviour such as *saturated*, *inverse*, or *humpback* sawteeth [46], which usually result from localised off-axis heating [47, 48], were avoided. Figure 6.3(a) shows the X2-mode launching geometry and the resonance position for a vacuum field of 1.43 T which is locally increased by the paramagnetism of the plasma. Some ordinary mode (O-mode) component of the injected ECH beam, which is weakly absorbed at first path, leads to a more distributed absorption after multiple reflections on the wall. The deposition profile is obtained from the response of the soft X-ray emissivity to the switch-off of the ECH power [49]. The resulting deposition agrees well with ray-tracing results obtained from the TORAY code [50]. Both methods confirm a peaked power absorption in a region well inside the $q=1$ surface.

6.4.2 Variations of sawtooth characteristics

In a moderately shaped ($\kappa = 1.5$, $\delta = 0.2$) Ohmically heated TCV plasma with $n_{e0} \approx 2.5 \times 10^{19} \text{m}^{-3}$, sawteeth typically have periods of 2 ms and crash amplitudes of 10%. Triangularity and elongation scans were performed around this shape, keeping either $\kappa \approx 1.5$ or $\delta \approx 0.2$ constant.

In Ohmic plasmas the modification of the triangularity introduces significant changes of sawtooth characteristics (figure 6.4(a) and (c)). Increasing δ from 0 to 0.45 almost doubles the sawtooth period and increases the amplitude of the crash by a factor of four. The modification of τ_{saw} and A_{saw} saturates for negative triangularities. As already noted by *Weisen et al* [41] the longer sawtooth period at higher triangularity is not sufficient to explain the increase in amplitude. In addition, poorer confinement at higher triangularity as observed in Ohmic TCV plasmas [51] leads to lower temperatures which result in a higher resistivity, η . Consequently, the Ohmic heating power density $p_{\text{Ohm}} = \eta \langle j \rangle^2$, is higher, which also contributes to the increase in amplitude (equation 6.4).

The dependence of the sawtooth period on elongation is somewhat weaker (figure 6.4(b)), with shorter sawtooth periods at higher elongations. Despite the weak trend in the behaviour of τ_{saw} the crash amplitude decreases drastically with elongation (figure 6.4(d)). For $\kappa = 2.3$ the crash amplitude measures only a fourth of that in an almost circular

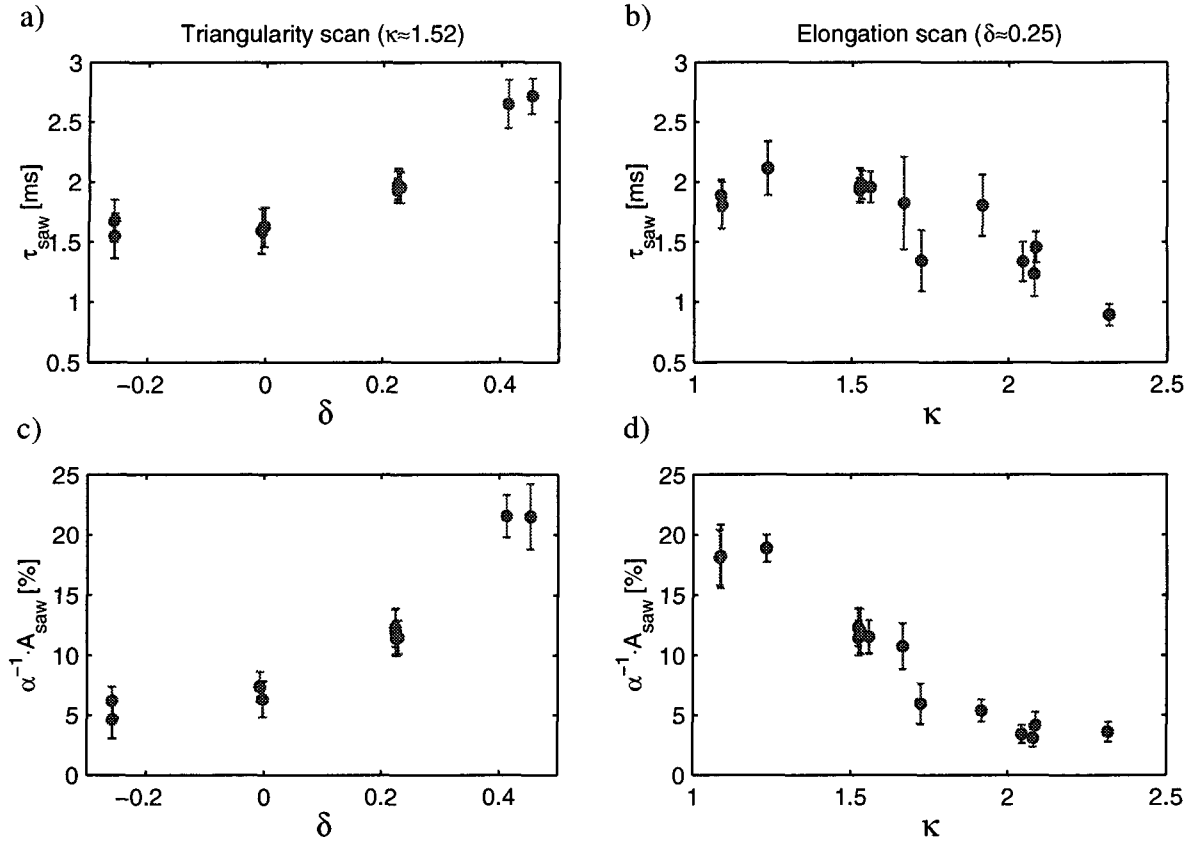


Figure 6.4: Sawtooth characteristics in Ohmic plasmas as a function of triangularity (a), (c) and elongation (b), (d), while density and inversion radius are kept constant. The values of the sawtooth period (a), (b) and the sawtooth crash amplitude (c), (d) are averaged over stationary phases. The error bars indicate the standard deviation within these phases.

plasma although the inversion radius was kept constant throughout these experiments. Again, the variation of τ_{saw} is not sufficient to explain the variation of $\alpha^{-1} A_{\text{saw}}$. As for decreasing δ , the Ohmic heating power density decreases with increasing κ (while ρ_{inv} is kept constant), which results in the observed drop in crash amplitude.

Central ECH deposition strongly enhances the effect of shape, previously observed in Ohmic plasmas. For high positive triangularity auxiliary heating increases τ_{saw} even further up to 4 ms and $\alpha^{-1} A_{\text{saw}}$ up to 65%, where it saturates. Small and negative δ results in even shorter and smaller sawteeth (figure 6.5(a) and (c)). We further note that the assumption of constant density throughout the sawtooth cycle is no longer valid in ECH heated plasmas [52] and therefore $\alpha^{-1} A_{\text{saw}}$ fails as an estimate for the central pressure loss. With additional heating a distinct dependence of the sawtooth period on elongation also becomes apparent (figure 6.5(b) and (d)). For nearly circular plasmas additional heating further increases τ_{saw} and A_{saw} while at high elongations τ_{saw} and A_{saw} are decreased further below Ohmic values.

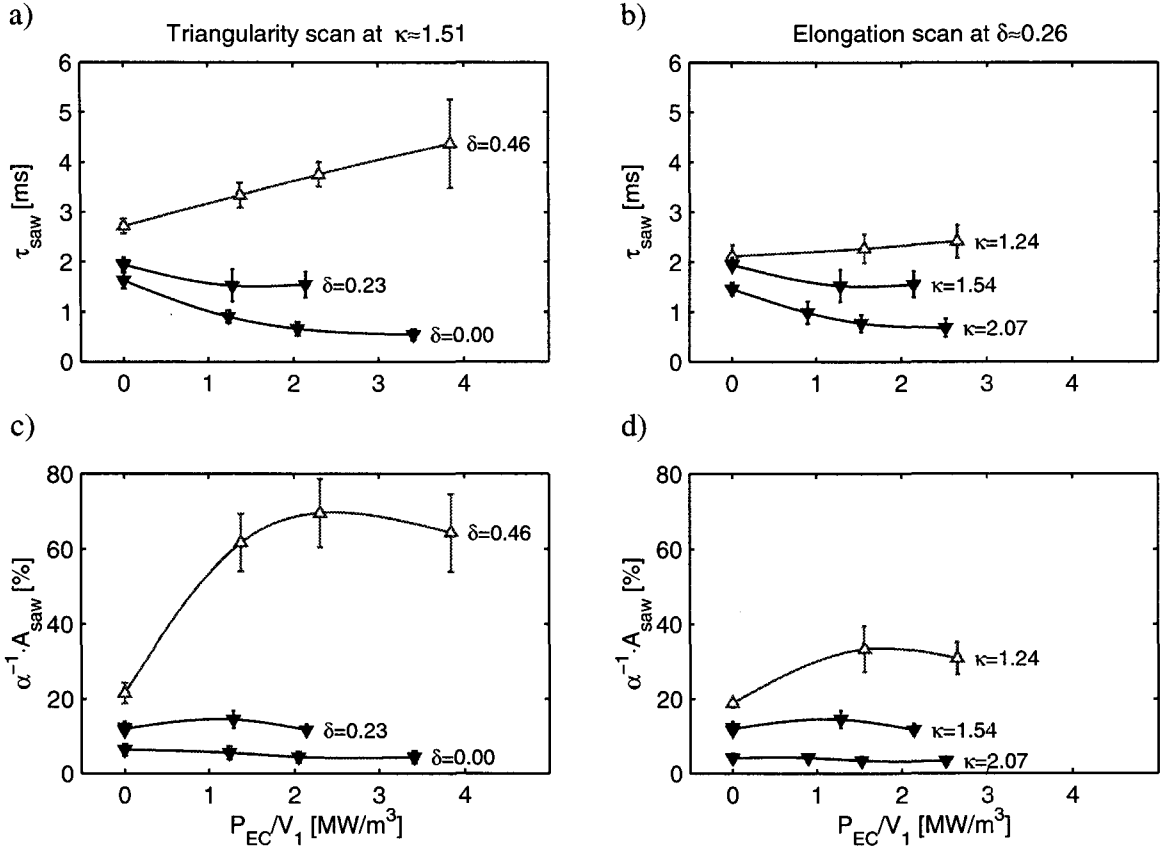


Figure 6.5: Sawtooth characteristics as a function of auxiliary heating power density within the $q=1$ surface for various triangularities (a), (c) and elongations (b), (d). Electron density and sawtooth inversion radius were kept constant. Shown is the dependence of sawtooth period (a), (b) and the relative sawtooth crash amplitude (c), (d) on ECH power. The values are averaged over a stationary phase with the bars indicating the standard deviation within these phases.

Thus, the enhancement of the effect of shape on sawtooth behaviour is due to the shape dependent response to ECH. The shaping parameters for which the increase of P_{ECH} results in a decrease of τ_{saw} , i.e. auxiliary heating is destabilising, and the shaping parameters for which an increase of P_{ECH} is stabilising, are shown in figure 6.6, clearly indicating this shape dependence.

6.4.3 Comparison with a sawtooth model

The observed response of sawteeth to heating is investigated in the frame of a model which was developed to predict the sawtooth period in JET and ITER [53] and which had already been successfully applied to Ohmic TCV plasmas [54].

According to this model an ideal internal kink triggers the sawtooth crash if its growth cannot be stabilised by plasma rotation, i.e. if,

$$\gamma_{ideal} > c_h w_{i,dia} \quad (6.8)$$

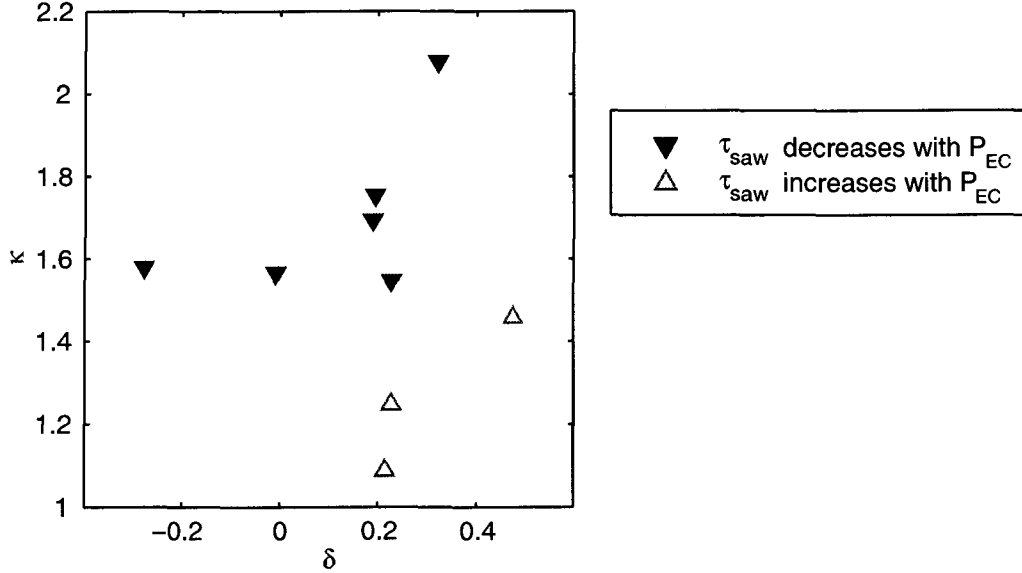


Figure 6.6: The discharges where τ_{saw} decreases (full triangles) or increases (open triangles) with P_{ECH} are shown as a function of shaping parameters at the plasma edge.

where γ_{ideal} is the growth rate of the ideal internal kink (equation 2.47), $c_h \approx 0.5$ a constant and $\omega_{i,\text{dia}} = kT_i/(L_p e B_0 r_1)$ the ion diamagnetic drift frequency with L_p being a pressure scale length. In a low density TCV plasma, the amplitude of the term which can stabilise the internal kink mode is typically $c_h \omega_{i,\text{dia}} \approx 5 \times 10^3 \text{ s}^{-1}$, a value which is observed to decrease with the auxiliary electron heating power.

The growth rate of the ideal internal kink (equation 2.47) can be expressed in terms of a normalised potential energy $\delta \hat{W} = -4\delta W/s_1 \xi^2 \epsilon_1 R B^2$,

$$\gamma_{\text{ideal}} = \frac{-\delta \hat{W}}{\tau_A} \quad (6.9)$$

with $\tau_A = R/v_A$ being the Alfvén time.

In addition to the ideal MHD potential energy, fast particle and trapped ion effects can also contribute to the potential energy (equation 2.48). However, in these TCV experiments, the stabilising effect of fast particles on sawteeth can be neglected. Also, the stabilising effect of collisionless thermal trapped ions in the present low density plasmas is small, with $\delta \hat{W}_{\text{trapped}}/\tau_A$ of the order of $5 \times 10^2 \text{ s}^{-1}$. Therefore, the internal kink can be destabilised by $\delta \hat{W}_{\text{MHD}}$ becoming negative once the plasma pressure sufficiently exceeds a critical value. This critical value depends strongly on plasma shape [7, 44, 55, 56]. Thus, the additional heating increases the plasma pressure which increases the drive of the ideal mode and results in a decrease of the sawtooth period.

If the plasma is stable with respect to the ideal mode, resistivity becomes important (see section 2.4.3). In ECH heated TCV plasmas the ion-gyro radius $\rho_i \approx 0.2 - 0.3 \text{ cm}$

is larger than the resistive layer width $\delta_\eta \approx 0.03 - 0.12 \text{ cm}$ and the growth rate γ_ρ of the resistive internal kink in the so-called *ion-kinetic* regime has to be considered [46]. A typical value is $\gamma_\rho \approx 10^4 \text{ s}^{-1}$. This mode can be stabilised by different diamagnetic effects leading to a condition for the onset of the resistive internal kink mode proposed by *Sauter et al* [54],

$$\gamma_\rho > c_\star (\omega_{\text{e,dia}} \omega_{\text{i,dia}})^{1/2} \quad (6.10)$$

with c_\star being of the order of unity. Since $\omega_{\text{e,dia}} \approx 10^4 \text{ s}^{-1}$ both sides of equation 6.10 are of similar amplitude. The resistive growth rate $\gamma_\rho \propto s_1^{6/7}$ essentially depends on the magnetic shear on the $q=1$ surface $s_1 = \rho_1 (dq/d\rho_1)$, whereas the stabilising electron diamagnetic rotation increases with pressure. Higher temperatures also lead to larger conductivity and slow down the diffusion of the current profile. Additional ECH increases p_e and influences the evolution of s , leading to different dynamics with respect to the ideal mode. In particular, the stabilisation of a resistive mode by electron diamagnetic rotation, $\omega_{\text{e,dia}} \propto T_e$, and a larger resistive diffusion time, $\tau_R \propto T_e^{3/2}$, offer possible explanations for an increase of the sawtooth period with additional electron heating.

Therefore, the response of sawteeth to auxiliary heating is expected to depend on whether ideal or resistive MHD determines the mode dynamics. As discussed above, this essentially depends on the potential energy of the ideal mode $\delta \hat{W}_{\text{MHD}}$, which contains the shape dependence. A necessary condition for ideal MHD stability is the Mercier criterion (see section 2.3.1). Numerical simulations by *Lütjens et al* [7] have shown that in elongated plasmas with weak central shear, the minimum $\beta_{\text{p},1}$ is set by a violation of the Mercier criterion leading to an $n = 1$ mode with large growth rates. More importantly, these simulations have also shown that the shape dependence of $\delta \hat{W}_{\text{MHD}}$ is similar to the shape dependence of the Mercier criterion. In cases where the Mercier criterion was violated within the whole $q < 1$ region, the eigenfunction of the unstable mode resembles the standard step function of the internal kink. The expansion of the Mercier criterion up to $O(\epsilon^2 e)$ (equation 2.43) illustrates the effect of elongation and triangularity. Assuming parabolic pressure profiles which gives $\beta_{\text{p},1} \approx -2\mu_0 p'_1 R_0^2 / (B_0^2 2r_1)$, equation 2.43 yields

$$\frac{1}{4} - \frac{3\epsilon_1^2}{s_1^2} (\kappa_1 - 1) \beta_{\text{p},1} \left(1 - \frac{2\delta_1}{\epsilon_1} \right) > 0 \quad (6.11)$$

for stability.

In figure 6.7, marginal stability according to the Mercier criterion (equation 6.11) is shown for two values of $\beta_{\text{p},1}$, with $s_1 = 0.1$ and $\rho_1 = 0.5$ assumed constant as a function of the local shaping. The discharges in figure 6.6 are shown in figure 6.7 as a function of the local shaping parameters at $q = 1$ which are obtained from the equilibrium reconstruction. A comparison of the sawtooth response to ECH with the Mercier stability boundary shows that the critical $\beta_{\text{p},1}$ is particularly low for discharges where additional heating could not

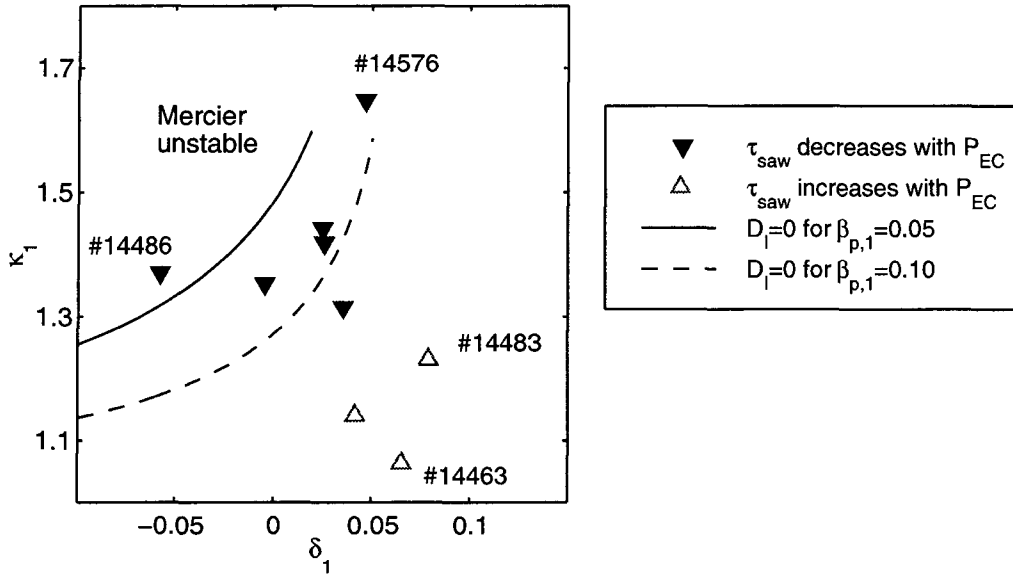


Figure 6.7: The discharges of figure 6.6 are shown as a function of shaping parameters on the $q=1$ surface. The plasma shapes are compared to the shapes corresponding to marginal stability according to the Mercier criterion (equation 6.11) for two different values of $\beta_{p,1}$ and assuming constant shear $s_1 = 0.1$ and inversion radius $\rho_{\text{inv}} = 0.5$.

improve sawtooth stability (full triangles in figure 6.7). For these plasma shapes the potential energy of the ideal mode can be sufficiently negative to determine the sawtooth trigger which is consistent with the interpretation of the decrease of the sawtooth period presented above.

The stability of the internal kink in four discharges, labelled by their shot numbers in figure 6.7, has been analysed by the linear full ideal MHD code KINX [57, 58]. The equilibria were reconstructed by LIUQE using the experimental pressure profiles from Thomson scattering measurements and the inversion radius. An ideal conducting wall was assumed at 1.15 times the minor radius, corresponding to the TCV plasma-wall distance on the low field side. The growth rate of the ideal internal kink mode was computed for different values of $\beta_{p,1}$ by scaling the original pressure profiles. The resulting growth rates are shown in figure 6.8. From the experimental values of $\beta_{p,1}$ the discharges at low triangularity (#14486) and high elongation (#14576) are unstable, whereas the discharges at high triangularity (#14483) and low elongation (#14463) are clearly stable. This confirms that the two classes of shapes obtained from the experimental sawtooth behaviour (open and closed symbols in figures 6.5–6.9), which were linked to ideal MHD stability or instability using the Mercier criterion, are indeed stable or unstable with respect to the ideal internal kink mode.

The shape dependent response of sawteeth to heating power can also be seen in the electron pressure profiles. In figure 6.9, the time averaged pressure profiles of a plasma

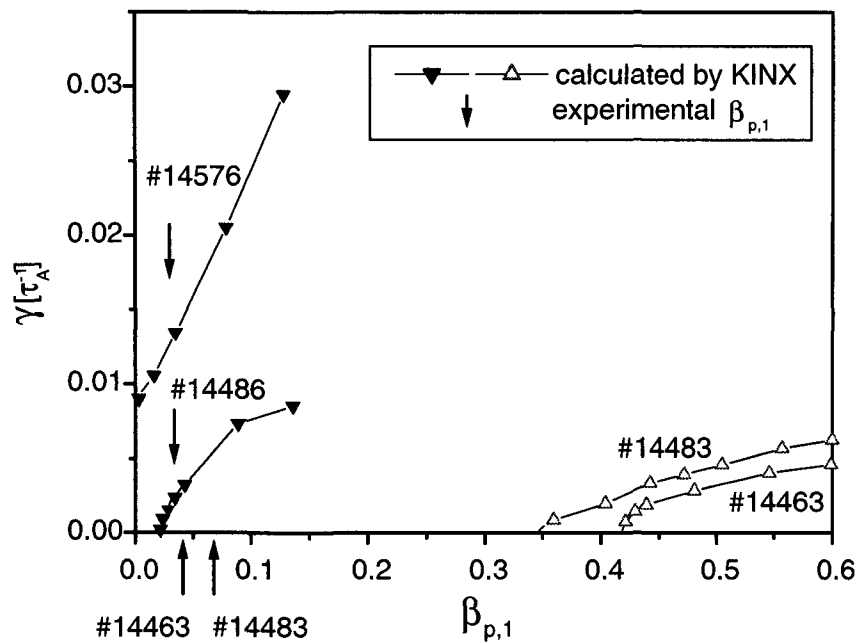


Figure 6.8: Growth rate of the ideal internal kink mode calculated by KINX for experimental equilibria with scaled pressure profiles. An ideal conducting wall has been assumed at 1.15 times the minor radius. From the experimental values of $\beta_{p,1}$, which are indicated by arrows, the discharges #14486 and #14576 are unstable, whereas #14483 and #14463 are stable.

where τ_{saw} increased with P_{ECH} (a) are compared with the profiles of a plasma where τ_{saw} decreased with P_{ECH} (b). In the first case (a) the increase of the central heating from Ohmic to 1 MW of auxiliary heating power leads to a peaking of the pressure profile, whereas in case (b) the central pressure profile remains essentially flat. The variation of the pressure profiles with heating can be summarised in the variation of $\beta_{p,1}$, which increases with P_{ECH} in case (a) whereas it remains constant in case (b) (see inserts in figure 6.9). Thus, case (b) is consistent with an imposed $\beta_{p,1}$ limit, independent of heating power, leading to the observed decrease of τ_{saw} for this plasma shape. This supports the idea of ideal MHD being responsible for the triggering of the sawtooth. However, the measured betas are time averages of measurements, which were not synchronised with sawteeth and are, therefore, lower than the critical beta obtained directly before the crash.

6.4.4 Shape dependence of ideal central beta limit

For all plasma shapes, where τ_{saw} decreased with P_{ECH} , the limiting $\beta_{p,1}$ was independent of heating power (e.g. figure 6.9(b)), whereas for the other plasma shapes $\beta_{p,1}$ increased with power (e.g. figure 6.9(a)). For the shapes where $\beta_{p,1}$ reaches a limit, this limit is shown as a function of the triangularity and elongation (figure 6.10(a) and (b)). Despite a

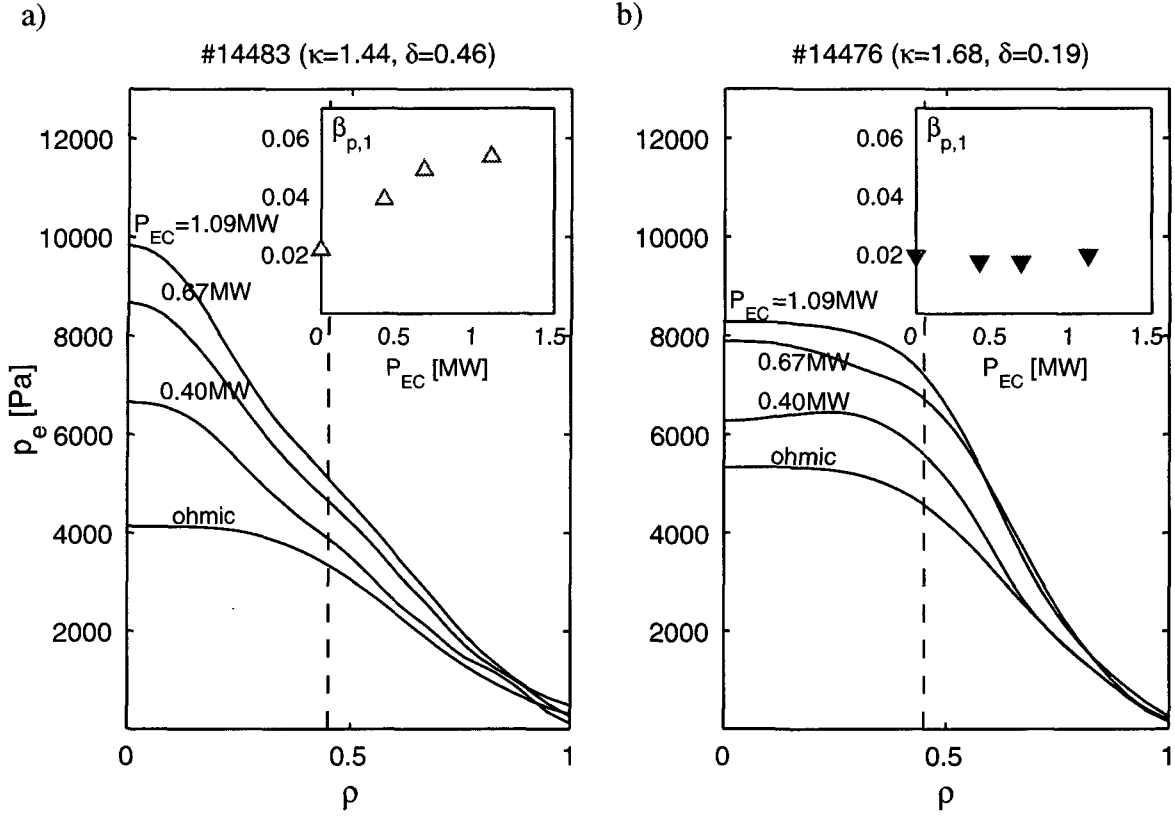


Figure 6.9: Electron pressure profiles (averaged over typically six time slices) for different ECH powers for a shape ($\kappa = 1.44$, $\delta = 0.46$) where τ_{saw} increases with heating power (a) and a shape ($\kappa = 1.68$, $\delta = 0.19$) where τ_{saw} decreases with heating power (b). The inserts show the power dependence of β_p at $\rho = 0.45$, corresponding to the inversion radius (dashed line).

large scattering of the data, a stabilizing trend with increasing triangularity and decreasing elongation is observed. The dependence on κ_1 can be compared to an expansion of the energy functional of the ideal internal kink [55],

$$\delta \hat{W}_{\text{MHD}} = -\frac{3}{4}(\kappa_1 - 1)\beta_{p,1} + \Delta q \left[\frac{13}{48} - 3\beta_{p,1}^2 + \frac{\kappa_1 - 1}{2} \left(13\beta_{p,1}^2 - \frac{1}{4}\beta_{p,1} - 1 \right) \right]. \quad (6.12)$$

The expansion (equation 6.12) contains terms up to the second order in ϵ and first order in e , including $O(\epsilon^2 e)$ and is given for a parabolic current profile. The value of beta for marginal stability $\beta_{p,1,\text{crit}}$, calculated from equation 6.12 assuming $\Delta q = 0.25$, is shown in figure 6.10(b). The experimental limiting $\beta_{p,1}$ shows the same trend as the analytic $\beta_{p,1,\text{crit}}$, albeit with a weaker dependence. Note that both the analytic formula (see figure 6.10(b)) and the ideal MHD calculation (figure 6.8), predict the highly elongated plasma (#14576) to be unstable even at zero $\beta_{p,1}$.

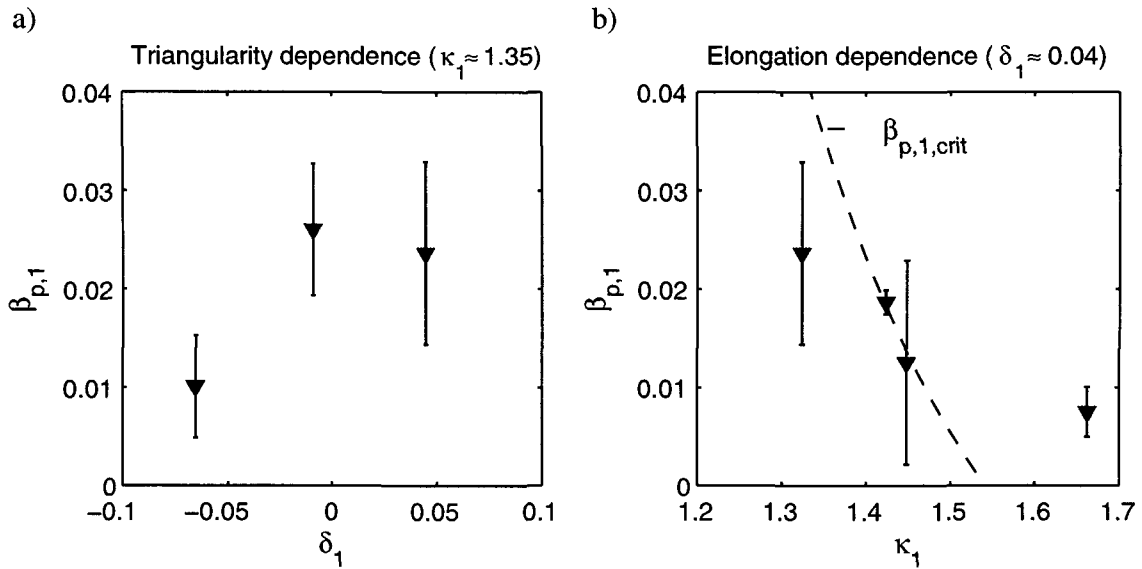


Figure 6.10: The poloidal beta on $q=1$ in discharges, where it could not be increased with additional heating, is shown as a function of triangularity (a) and elongation (b) on the $q=1$ surface. The measurements are averaged over typically 6 times and the error bars indicate the standard deviation among different power levels. It is compared with the poloidal beta for marginal stability of the ideal internal kink according to equation 6.12, assuming $\Delta q = 0.1$ (dashed line in (b)).

6.5 Concluding remarks

High triangularities and low elongation are seen to improve the stability of sawteeth in TCV plasmas, but also lead to large sawtooth crashes. Low triangularity and high elongation reduce the sawtooth amplitude, which can both reduce sawtooth related heat pulses and decrease the risk of possible seed island generation resulting from large sawtooth crashes. However, the core confinement remains at a low level.

In addition to their period and amplitude, the response of sawteeth to an increase of central heating power also depends strongly on the plasma shape. For the plasma shapes for which full ideal MHD calculations as well as analytic expressions predict a low critical $\beta_{p,1}$ (defined according to equation 2.46), the experiment also shows a low pressure limit which cannot be increased with additional heating and consequently leads to shorter sawteeth. In the frame of the presented model of the sawtooth trigger [53], this is consistent with an ideal internal kink mode triggering the sawtooth crash. In particular, the observed κ_1 -dependence of the limiting beta is in qualitative agreement with an analytic prediction [55]. For shapes where the ideal MHD mode is expected to be marginal or stable, in particular at high positive triangularity, the core pressure can be significantly increased with additional heating. This can be explained by an increase of the electron diamagnetic rotation which is expected to increase with the electron pressure

and has a stabilizing effect on the resistive mode.

The experiments have shown that in low density ECH heated TCV plasmas at low triangularity and sufficient elongation, ideal MHD significantly contributes to the triggering of the sawtooth crash. In this regime, the observed shape dependence supports theoretical predictions of the shape dependence of the ideal internal kink mode [55].

A prediction of the sawtooth period has to take into account the evolution of the current profile which has been successfully performed for various Ohmic [54] and some ECH heated [59] TCV plasmas, however, without leaving the resistive regime. The presented results point out that the simulations of sawteeth in ECH heated TCV plasmas in general, require an accurate description of the shape dependence of the ideal MHD stability.

Chapter 7

Edge localised modes

High confinement mode (H-mode) discharges are usually accompanied by a mainly pressure driven instability, called edge localised mode (ELM) (reviews in [60, 61, 62]). While ELMs are beneficial for the control of the particle content of the plasma, they can also lead to high peak power loads on divertor plates, which is a serious concern for a fusion reactor. ELMs are deemed necessary for the operation of a fusion reactor in an H-mode regime, but a control of their behaviour and in particular their size is required.

After an introduction into ELMs outlining their phenomenology and the current understanding, this chapter analyses the structure of coherent magnetic oscillations which are observed prior to ELMs in TCV. The high spatial resolution of the toroidal array of magnetic probes allowed the observation of a previously unobserved toroidal asymmetry of these precursor oscillations [63, 64]. Unlike conventional MHD modes this instability starts toroidally localised. The asymmetry must be intrinsic to the plasma and a link to a central mode is suggested.

7.1 Introduction into ELMs

7.1.1 Phenomenology

H-mode discharges are usually perturbed by periodic bursts of MHD activity and D_α emission. These so-called edge localised modes (ELMs) lead to a loss of energy and particles from a region near the plasma boundary. The ELM-related energy loss has usually only a small effect on the energy confinement time. However, the loss of energy can occur fast enough to cause high peak power loads on the divertor target plates. Nevertheless, ELMs are beneficial in avoiding the accumulation of impurities and can control the particle content of the plasma. ELM-free H-modes usually terminate in high density disruptions. Therefore, ELMs are necessary for a stationary H-mode operation. A control of the level and the repetition frequency of these edge fluctuations would be desirable in order to meet these various conflicting conditions.

Classification of ELMs

The classification of ELMs into several types according to their characteristics was originally introduced for ELMs observed in DIII-D [65]. *Type I* or “giant” ELMs are associated with the largest ELM energy and particle losses and are marked by large D_α spikes. Their repetition frequency increases with increasing heating power. *Type II* and “grassy” ELMs are irregular, high frequency, low-amplitude fluctuations. *Type III* ELMs are of medium amplitude and, unlike type I ELMs, their repetition rate decreases with increasing heating power until they disappear completely. This scheme has allowed a classification of most of the ELMs observed on other tokamaks.

The magnetic fluctuations during the phase of enhanced transport have a broad turbulent spectrum. Often coherent precursor oscillations, which are localised on the torus outboard side, are observed. The precursors have low to medium mode numbers with n typically ranging from 4 to 10. Typical growth times range from $50\ \mu\text{s}$ in TCV (section 7.2) to 1 ms prior to certain type I ELMs in ASDEX-Upgrade [61].

7.1.2 Current understanding

ELMs are only observed in H-mode plasmas, where the formation of an edge transport barrier results in a steepening of the edge pressure gradient. The pressure gradients obtained prior to type I ELMs are close to the ideal ballooning limit (see section 2.3.1). The smaller type II ELMs occur at similar pressure gradients but only in highly shaped plasmas and are associated with the second stability region (see figure 2.2). Type III ELMs occur at lower pressures and are found below a critical edge temperature.

The existence and magnitude of a pressure limit prior to type I ELMs and the localisation of the precursor on the side of unfavourable curvature led to the linking of ELMs to ideal ballooning [66]. In order to obtain large discrete collapse events which are separated by quiescent periods, a coupling to low n kink modes (section 2.3.2), partially driven by the large bootstrap current in the steep pressure gradient region, could be important. However, the expected sensitivity of ELMs to the distance between resonant surfaces and the plasma edge, has not been established.

Therefore, a model based on a coupling of current-driven peeling and ballooning modes has been developed [67]. Numerical analysis has shown that the gradient of the parallel current density j_\parallel , at the plasma vacuum interface can be sufficient to drive medium n modes. An increase of the edge pressure gradients further destabilise these modes. In this framework the ELM cycle is determined by the resistive time-scale on which the edge current density rises before the edge becomes peeling unstable. The size of the ELM is determined by the radial width of the unstable eigenfunction and allows for large type I as well as smaller type II ELMs.

The suppression of type III ELMs at higher temperatures points at a possible role of resistivity in the underlying instability mechanism. Models based on a form of resistive interchange are currently being discussed.

7.1.3 ELMs in TCV

Ohmic H-modes have been obtained in various diverted and limited plasma configurations in TCV. In ELM-free H-modes the particle density rises continuously until the discharge usually terminates with a high density disruption. Quasi-stationary H-modes have only been obtained in the presence of ELMs. The characteristics of the observed ELMs are continuous, ranging from small ELMs, typically causing a loss of 5% of the plasma energy content and considered to be of type III, to low frequency ELMs referred to as large ELMs causing a loss of up to 12% of the plasma energy [68]. An unambiguous classification in the usual scheme (section 7.1.1), for example by performing a scan of auxiliary heating power, has of yet not been possible.

7.2 Observation of precursor oscillations

Coherent magnetic oscillations have often been observed to precede ELMs in TCV. Dedicated experiments were carried out to analyse the temporal evolution and the spatial structure of these precursor oscillations.

7.2.1 Experiments

The ELM precursor oscillations have only been detected with the fast magnetic fluctuation diagnostic (chapter 4). In order to maximise the signal amplitude, in spite of the multipole field decay of the perturbation (equation 5.50), the distance between the plasma and the magnetic probes was minimised. Therefore, toroidal and poloidal measurements were performed on two different plasma configurations. For toroidal measurements a single null upper divertor (SNU) plasma on the midplane ($z=0$), allowing a minimal distance of down to 5 cm on the high-field side (HFS) and 7.5 cm on the low-field side (LFS) between the plasma edge and the probes of the toroidal array, was investigated (figure 7.1(a)). In order to allow maximum poloidal phase information the poloidal measurements have been performed on SNU plasmas, which were moved as close to the bottom as was possible during H-mode operation. A minimum distance of 10 cm to the probes at the bottom of the vessel has been achieved (figure 7.1(b)). For these experiments the magnetic probes were acquired with the maximum sampling frequency of 1 MHz.

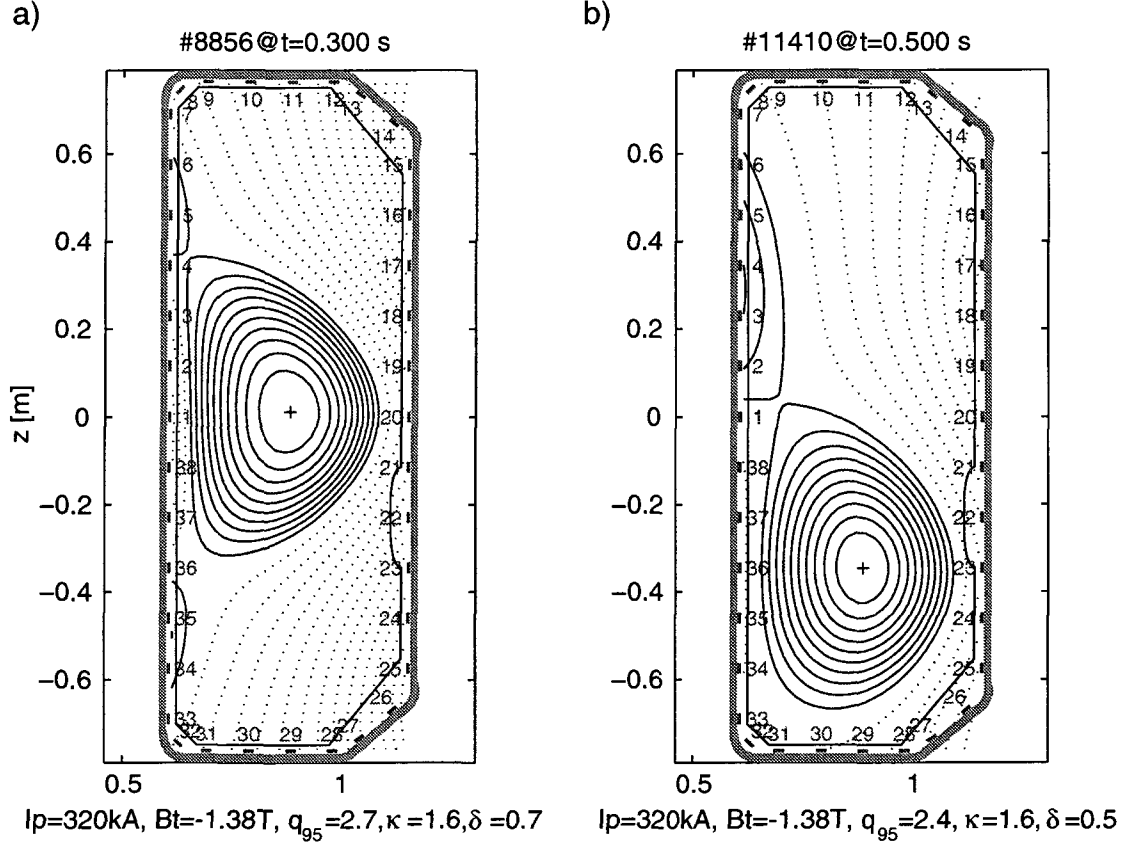


Figure 7.1: Poloidal cross section showing the position of the magnetic probes and the plasma configurations used. (a): SNU configuration for toroidal mode number analysis. The toroidal arrays are located in the equatorial plane corresponding to positions 1 (HFS) and 20 (LFS). (b): SNU configuration for poloidal mode number analysis.

7.2.2 Toroidal measurements

The ELMs obtained in the discharges, which were optimised for measurements with the toroidal arrays of magnetic probes, caused a moderate particle loss of 2 – 4% and an energy loss of 2 – 6% of the total plasma content. These are typical figures for type III ELMs in TCV. Their repetition frequency ranges from 120 to 300 Hz.

For many ELMs a coherent precursor oscillation has been detected several $100\ \mu\text{s}$ before the onset of the enhanced particle transport phase, corresponding to the rise of the D_α -signal. The precursor is only detected on the LFS (figure 7.2), even though the distance between probes and plasma there is greater than on the HFS.

The measurements with the full toroidal array on the LFS reveal a toroidal asymmetry of the initial growth of the ELM precursor. The precursor first develops at a toroidally localised position (figure 7.3(b), A). This instability then grows both in amplitude and toroidal extent with a typical growth time of $\tau_{\text{prec}} = 50\ \mu\text{s}$ (figure 7.3(b), B). At the same time the precursor frequency f_{prec} , decreases from typically 120 to 70 kHz. The toroidal

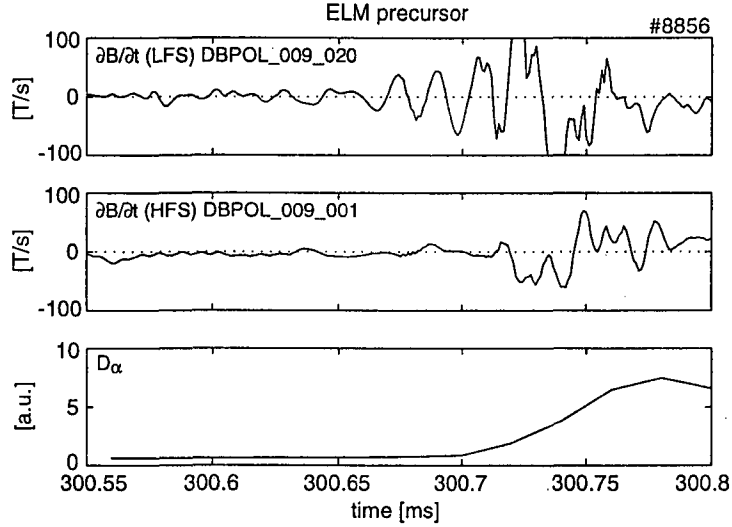


Figure 7.2: Magnetic fluctuations $\partial B_\theta / \partial t$, measured on both sides of the plasma prior to an ELM. The ELM precursor is only detected on the LFS even though the distance there between separatrix and probe is greater. The D_α signal indicates the phase of enhanced radial transport.

location of the instability rotates in the electron diamagnetic drift direction. When the precursor encompasses the entire toroidal circumference, the increased transport of energy and particles, as indicated by the increase of the D_α signal, begins. The magnetic oscillations then lose their coherence while the fluctuation amplitude rises strongly (figure 7.3(b), C). Due to the rotation of the toroidally localised precursor, measurements taken at one toroidal location show apparent characteristics of beating, as have been observed on other experiments [69, 70].

The toroidal position, where the precursor is first detected, differs from ELM to ELM (compare figure 7.3(b), A and figure 7.4(a), A). Occasionally, a simultaneous onset of the precursor at two toroidal positions is observed (figure 7.4(b), B₁ and B₂). In this case the two positions are always 180° apart toroidally and both positions also rotate in the electron diamagnetic drift direction.

Toroidal mode spectrum

The measurements of magnetic fluctuations, B_θ , on the LFS at 16 toroidal positions have been decomposed into spatial Fourier coefficients yielding amplitudes A_n , for toroidal mode numbers $n = 0, 1, \dots, 8$ (section 5.2.2). The toroidal mode spectrum of the precursor in #8856 at $t = 0.3$ s (figure 7.3) is shown in figure 7.5. The precursor consists of medium $n = 6 - 8$, predominantly 7 and 8, components, but spatial aliasing could possibly mask higher mode numbers such as 9 or 10. The $n = 6 - 8$ components grow with a typical growth time of 50 μ s. Immediately before the enhanced transport phase the $n = 5$

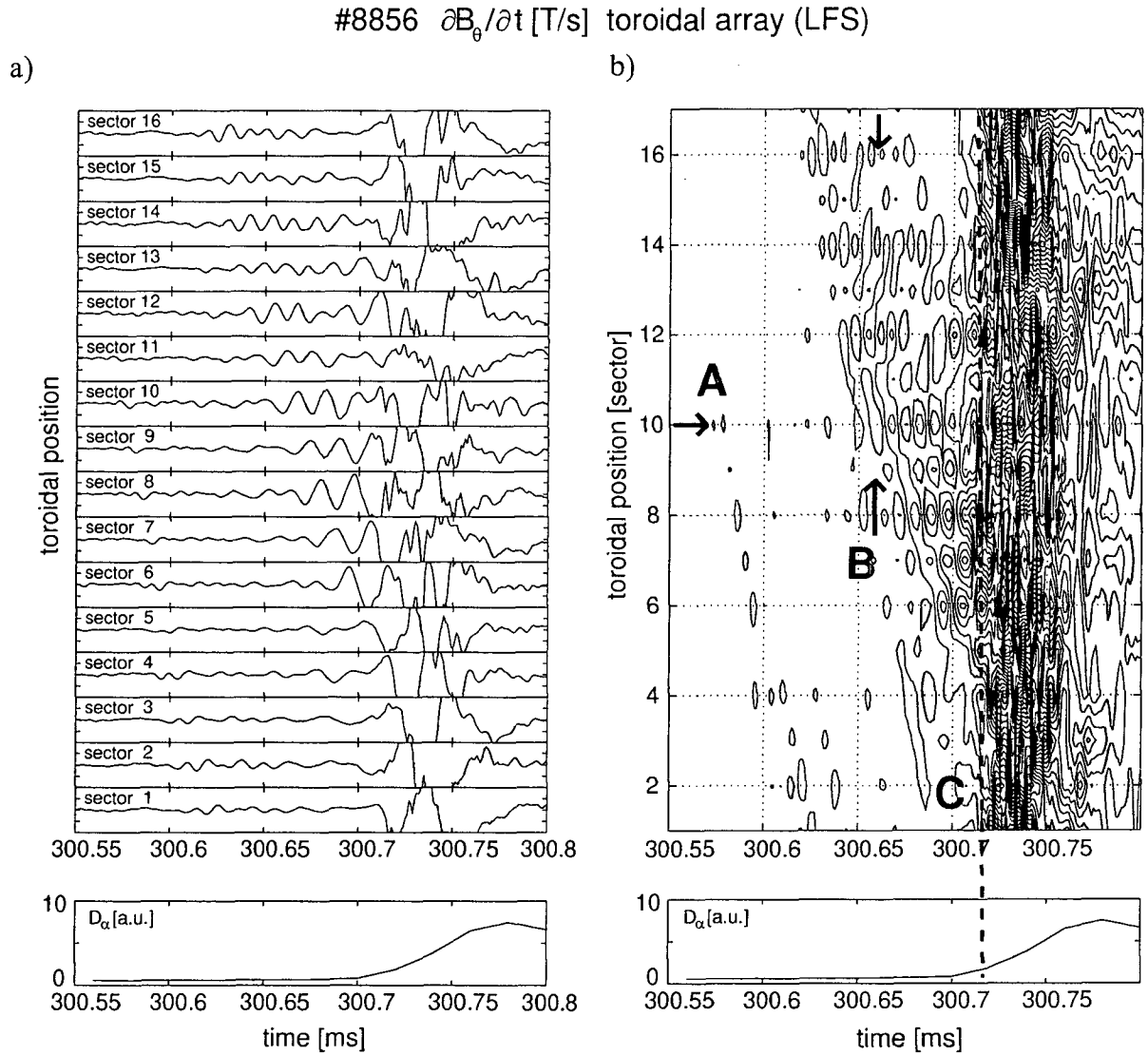


Figure 7.3: (a): Measurements of $\partial B_\theta / \partial t$ with the toroidal array on the LFS show coherent ELM precursor oscillations. The D_α signal indicates the onset of the enhanced radial transport phase. (b): Contour lines of the same measurements of $\partial B_\theta / \partial t$ show the toroidally localised onset (A). The precursor grows in amplitude and toroidal extent (B). When it encompasses the whole toroidal circumference the increased transport phase begins (C).

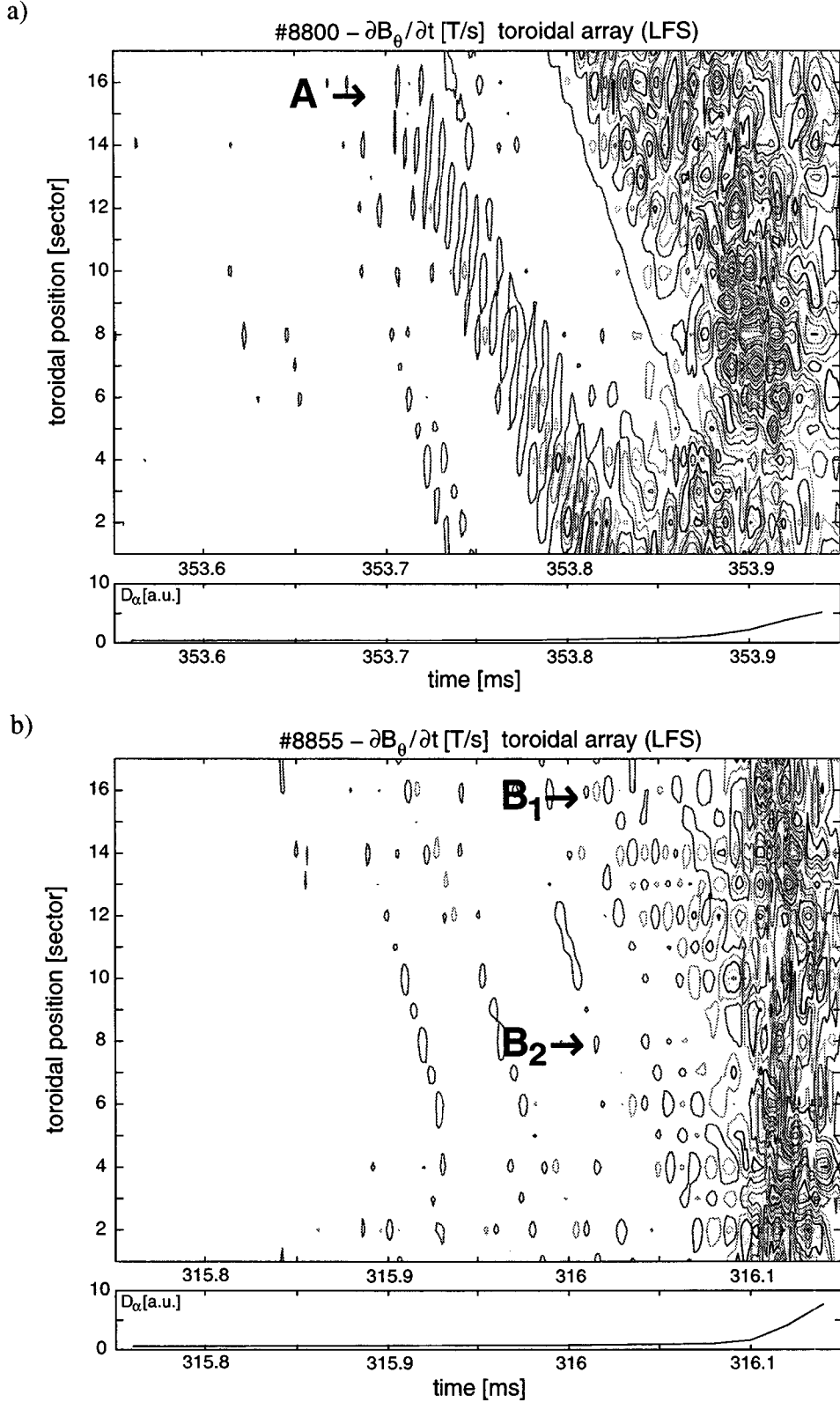


Figure 7.4: Measurements of $\partial B_\theta / \partial t$ with the toroidal array on the LFS show ELM precursors. (a): The onset of the precursor is detected at different toroidal locations (compare A to figure 7.3(b) A). (b): Occasionally, a simultaneous onset at two toroidally opposed locations is observed (B_1 , B_2).

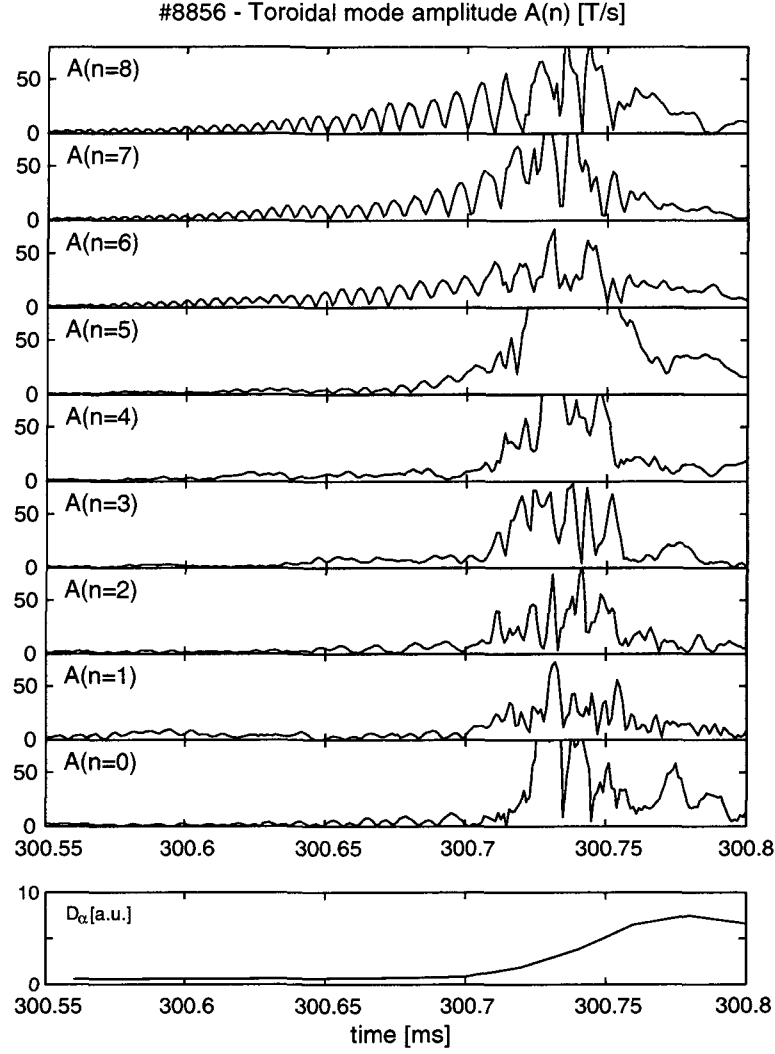


Figure 7.5: Toroidal mode amplitudes of the ELM precursor measured with the LFS array (figure 7.3). The amplitude of the $n = 6 - 8$ components grow over several $100 \mu\text{s}$. The beginning of the enhanced transport phase indicated by the increase of the D_α signal is accompanied by a fast growth of lower, in particular the $n = 5$, mode components.

component also starts to grow on an even faster time scale of $\sim 10 \mu\text{s}$. The toroidal phase velocity increases with increasing mode number. During the enhanced transport phase the mode spectrum broadens.

The amplitude of the $n = 8$ component shows an oscillation with twice the precursor frequency. Since the $n = 8$ is the spatial correspondence of the Nyquist frequency, the zeros in its amplitude are caused by the passing of the zeros of the $n = 8$ component by the position of the probes. However, oscillations are also observed on lower n mode amplitudes. They have the same frequency as the $n = 8$ amplitude but their minima are not necessarily at zero amplitude.

7.2.3 Poloidal measurements

The measurements of the poloidal mode structure of the ELM precursor oscillations were performed on a plasma with a similar shape to that used during the toroidal measurements but with the plasma shifted towards the bottom of the vessel. The ELMs obtained during these discharges caused particle losses of 4 – 7% and energy losses of 8 – 11%, typical for TCV large ELMs. The ELM repetition frequency is also slightly lower than in the configuration used for the toroidal measurements and ranges from 80 to 200 Hz.

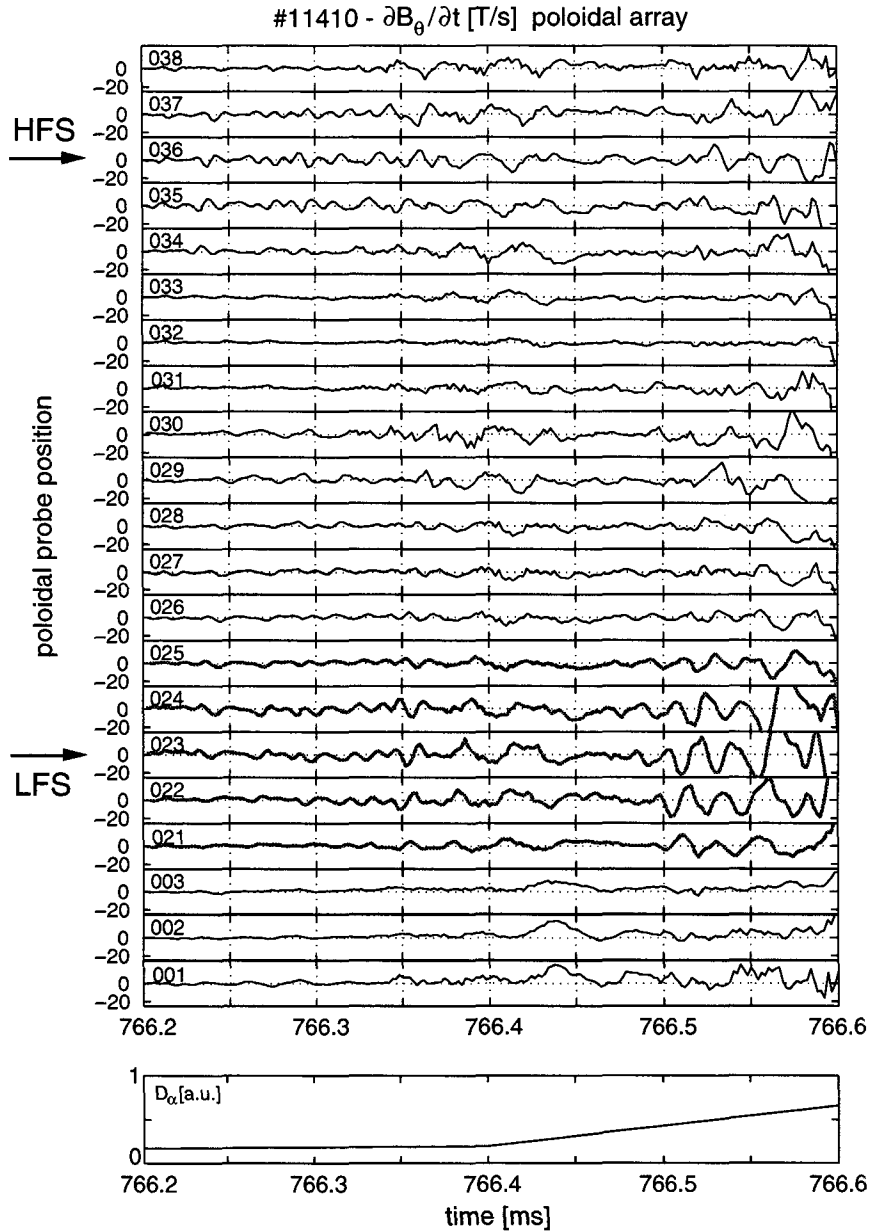


Figure 7.6: Measurements of $\partial B_\theta / \partial t$ with the poloidal array show ELM precursor oscillations on probes located on the outboard side of the plasma. The D_α signal indicates the onset of the enhanced radial transport phase.

These ELMs show coherent precursor oscillations with frequencies and growth rates similar to the type III precursors described in section 7.2.2. Although three quarters of the plasma circumference was surrounded by magnetic probes, the magnetic fluctuation measurements (figure 7.6) mainly show the precursor on the LFS probes 21-25 located closest to the plasma (figure 7.7(a)). As with the toroidal measurements the precursor rotates in the direction of the electron diamagnetic drift.

The poloidal mode structure is identified by measuring the phase differences $\Delta\Phi$ between the signals and comparing them with the poloidal spacing of the probes $\Delta\theta$. Since it is assumed that the perturbation follows the geometry of the field line and that it is resonant close to the plasma edge, the straight field line angle θ^* , (see section 5.1.3) of the surface containing 95% of the poloidal flux is used as the poloidal coordinate of the measurements. The phase, which could be averaged over three precursor oscillation periods, increases linearly with the poloidal position of the probes and yields a poloidal mode number, $m = \Delta\Phi/\Delta\theta^* = 12$ (figure 7.7(b)). An error in the determination of the poloidal mode structure can be introduced by the uncertainty of the resonant surface and by the varying angle between the axis of the probes and the resonant surface. A poloidal mode number $m \approx 12$, is consistent with the low safety factor $q_{95} = 2.4$ in this discharge, the medium toroidal mode numbers n obtained from the previous toroidal measurements and a resonant flux surface close to the plasma edge.

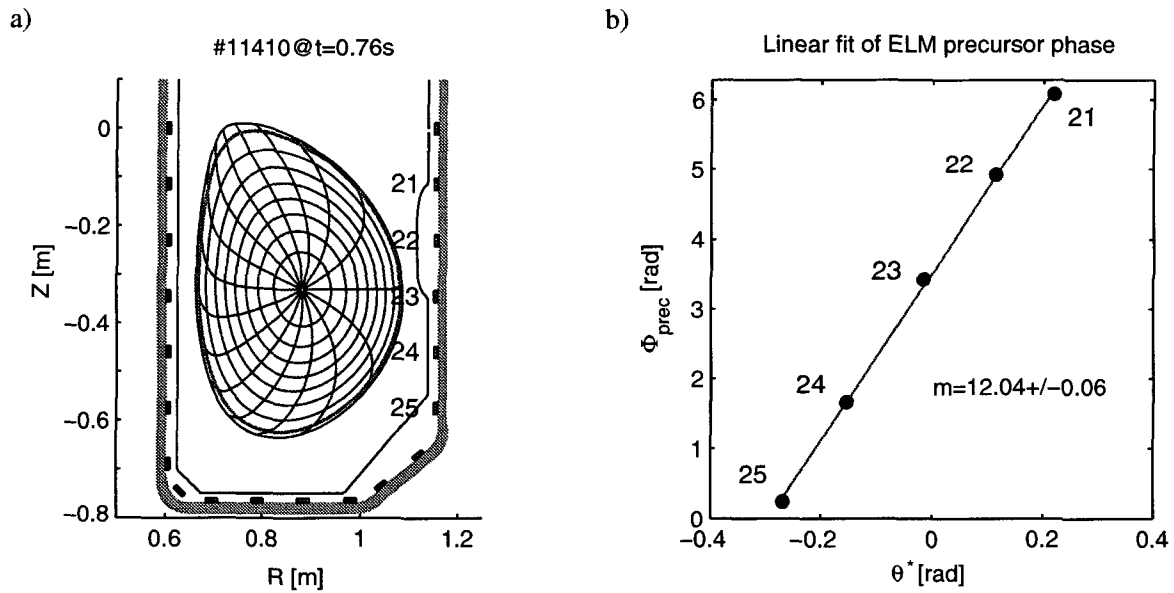


Figure 7.7: (a): The magnetic fluctuation measurements prior to an ELM show a precursor on the LFS probes 21-25 located closest to the plasma (figure 7.6). (b): The phase of the precursor oscillation averaged over three periods is proportional to the poloidal position of the probe measured in the straight field line angle of a resonant surface close to the edge (comprising 95% of the poloidal flux). The fit yields a poloidal mode number $m = 12$.

7.3 Toroidal asymmetry of the precursor

The observed toroidal asymmetry of the ELM precursor oscillation differs from the usually assumed toroidal symmetry in tokamak plasmas. The observed mode structure and possible causes are analysed in detail.

7.3.1 Toroidal mode structure

A toroidal envelope of the oscillation amplitude can be caused by a spatial beating of two superposed modes or by a toroidal localisation of a mode. Since the measured toroidal mode number is close to the resolution limit, the effects of discretisation were studied by numerical simulations. For both mode structures the signals at the 16 toroidal locations, φ_i , with $i = 1, \dots, 16$, have been modelled and resulting spectra compared with the measurements.

Beating modes

A superposition of two modes with $\Delta n = 1$ which have a linear dispersion relation $\omega_n = n\omega_0$,

$$\delta B(\varphi_i, t) = \sum_{n=n', n'+1} A_n(t) \cos(n\varphi_i - \omega_n t + \chi_{0k}), \quad (7.1)$$

shows a spatial beating which corresponds to a toroidal envelope of $n = 1$ that rotates with ω_0 . The corresponding mode spectrum,

$$A_n(t) = A_{n'}(t)\delta_{n',n} + A_{n'+1}(t)\delta_{n'+1,n} \quad (7.2)$$

is not as broad as the measured spectrum (figure 7.5) as it contains only two components. The magnetic signal of two simultaneous, exponentially growing modes with $n = 7$, $n = 8$ has been modelled for the TCV toroidal array and the calculated mode amplitudes are shown in figure 7.8(a). The $n = 7$ component does not show the oscillating amplitude revealed in the experimental data (figure 7.5). Therefore, the model of beating modes does not describe all the characteristics of the observations.

Localised mode

The observed spectrum can be explained by a toroidal localisation of a perturbation with toroidal mode numbers close to the resolution limit. Assuming a Gaussian toroidal weight of the amplitude of the perturbation field,

$$\begin{aligned} \delta B(\varphi_i, t) = & A_{n'}^*(t) \cdot \exp[-\tfrac{1}{2}(\varphi_i - \phi_{\max})^2/\sigma_\phi(t)^2] \\ & \cdot \cos(n'\varphi_i - \omega_{n'}t + \chi_{0n'}) \end{aligned} \quad (7.3)$$

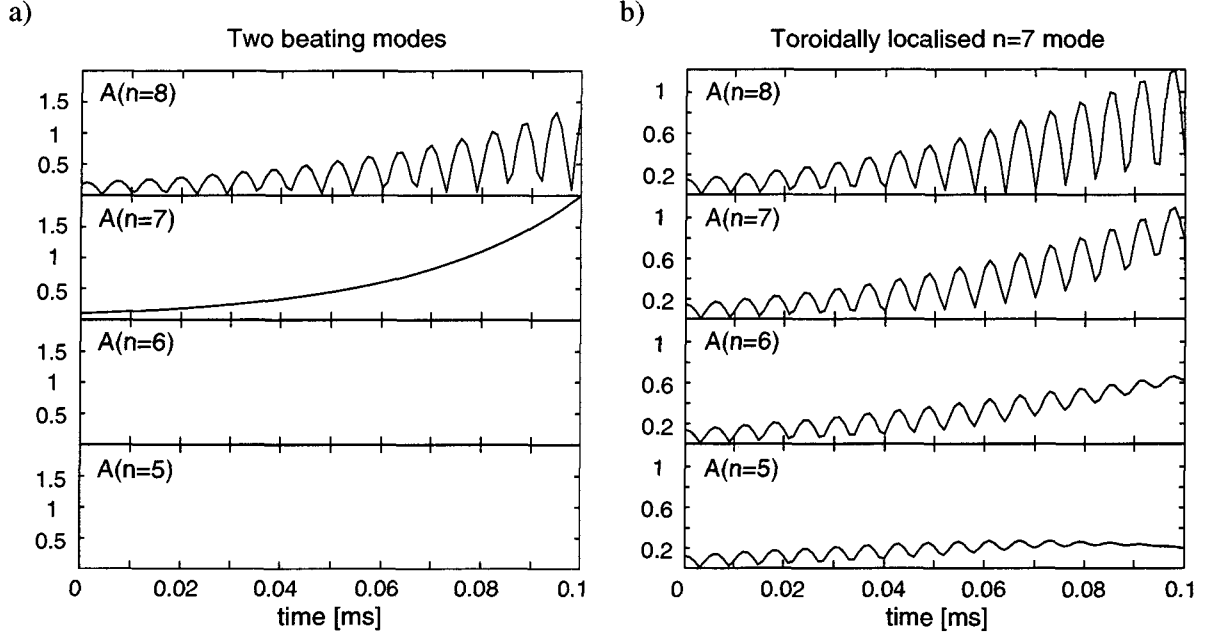


Figure 7.8: Modelled mode spectra of two growing beating modes $n = 7$ and $n = 8$ (a) and a toroidally localised $n = 7$ mode that grows in amplitude and toroidal extent (b) measured with an array of 16 equally spaced probes and treated with the standard mode analysis. The mode spectrum of the toroidally localised $n = 7$ mode shows the same characteristics as the measured mode spectrum in figure 7.5, in particular an oscillation of the amplitude of several mode components.

with an exponentially growing toroidal half width $\sigma_\phi(t)$, the expected mode spectra for $n, n' \gg \sigma_n$ is approximately,

$$A_n(t) \propto \exp[-\frac{1}{2}(n - n')^2 / \sigma_{n'}(t)^2]. \quad (7.4)$$

Since the half width of the spectrum σ_n depends inversely on the toroidal extend ($\sigma_n = 1/\sigma_\phi$), a sufficiently localised mode results in a broad mode spectrum. The mode spectrum for a modelled localised mode (equation 7.3, figure 7.8(b) for $n = 7$) shows the oscillating amplitude even for $n \neq 8$, as in the observed mode spectrum (figure 7.5). Similar oscillations of the spectral amplitudes could also be retrieved for localised $n = 8$ and 9 modes.

7.3.2 Toroidal asymmetry

The toroidally localised onset of the precursor differs from ELM to ELM. In addition, the position of the instability rotates toroidally. Therefore, a localisation due to errors in the measurements, such as probe misalignment or gains, and a triggering of the ELM due to an asymmetry of the TCV assembly can be excluded. The asymmetry causing and maintaining the precursor oscillation must be intrinsic to the plasma.

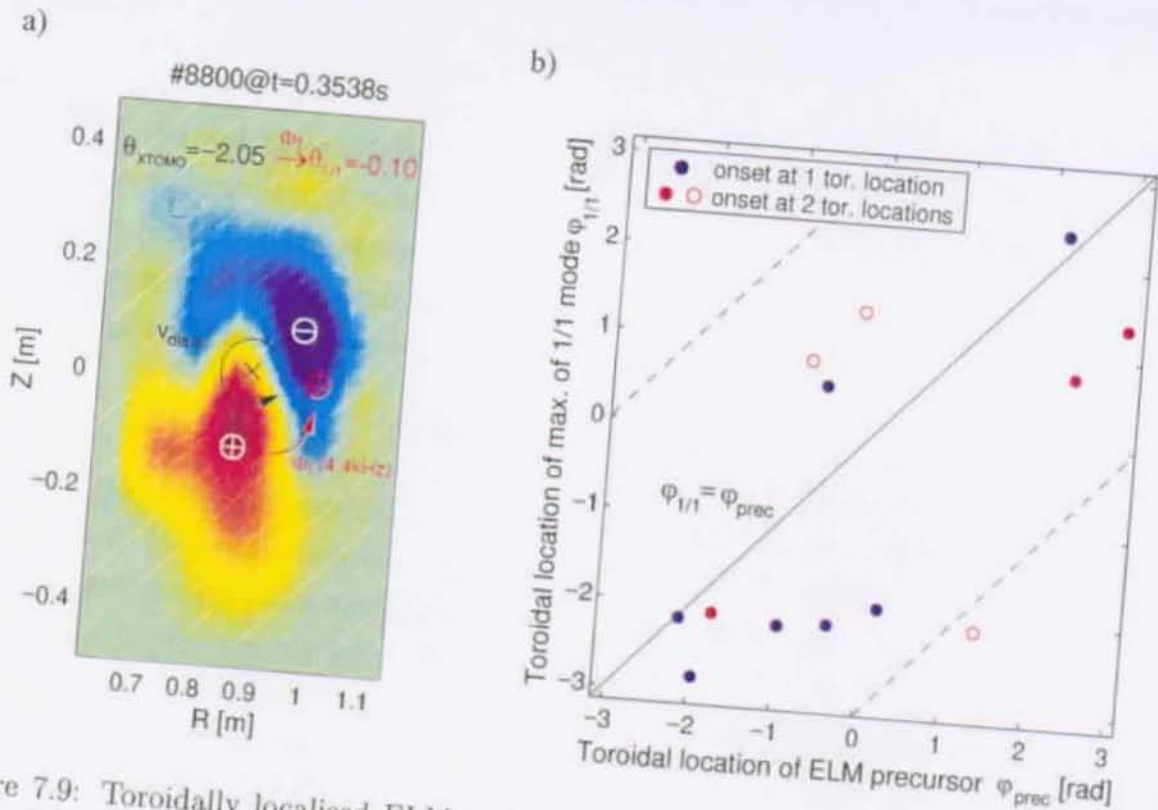


Figure 7.9: Toroidally localised ELM precursors are accompanied by a central $m = 1$ mode. (a): The phase of this mode is retrieved from the two degenerated eigenvectors of the bi-orthogonal decomposition of the soft X-ray emissivity taking into account the phase shift $\delta\Phi_i$, introduced by an anti-aliasing filter. (b): The phase of the mode is mapped on the toroidal plane of the magnetic measurements and its maximum, $\varphi_{1/1}$ compared to the toroidal location of the onset of the ELM precursor, φ_{prec} .

An asymmetry can be caused by an underlying low- n mode located in the high pressure gradient region close to the plasma edge. It has been shown that the stability of ideal ballooning modes is altered in the vicinity of a magnetic island [71]. The magnetic oscillation measurements show some $n = 1$ activity, but with such a small amplitude that neither its structure nor a possible correlation with the localisation of the ELM precursor could be retrieved.

However, the occurrence of asymmetric ELM precursor oscillations is always accompanied by central $m = 1$ mode activity. This mode is seen in the tomographic reconstruction of the soft X-ray emissivity and can usually be associated with the $m/n = 1/1$ sawtooth pre- or post-cursor mode. Occasionally, the $m = 1$ mode is observed during the sawtooth ramp.

The toroidal localisation of the ELM precursor is compared to the phase of the $m/n = 1/1$ mode,

$$\xi_{m/n} \propto \cos(m\theta^* - n\varphi - \Phi(t)) \quad \text{with } m, n = \pm 1 \quad (7.5)$$

where the signs of m and n are determined by the directions of the poloidal and toroidal magnetic fields, respectively. Since the soft X-ray measurements were sampled with

10 kHz, typically one reconstruction can be retrieved per ELM precursor. The phase $\Phi(t)$ of the 1/1 mode is determined from the corresponding degenerated eigenvectors (k_1, k_2) of the bi-orthogonal decomposition of the soft X-ray emissivity, $E_{1/1}(\vec{x}, t) = \sum_{k_1, k_2} A_k \phi_k(\vec{x}) \psi_k(t)$. The $m = 1$ component of the emissivity measured during an ELM precursor in #8800 at $t = 0.3538$ s (figure 7.4(a)) is shown in figure 7.9(a). In order to determine the angle of the maximum of the $m = 1$ mode $\theta_{1/1}^*$, the frequency dependent phase shift $\Phi_f(f)$, introduced by an anti-aliasing filter, must be taken into account,

$$\theta_{1/1}^* = \theta_{\text{XTOMO}}^* - \Phi_f(f) \quad (7.6)$$

where θ_{XTOMO}^* is the observed angle. For these measurements a third order Bessel filter with a cut-off frequency of 5 kHz was used. Since the mode frequency is close to the Nyquist frequency, a rotation in the direction of the electron diamagnetic drift is assumed. In the presented example the mode rotates with 4.4 kHz in the positive poloidal direction and the observed angle of the mode's maximum $\theta_{\text{XTOMO}}^* = -2.054$, corresponds to an actual angle $\theta_{1/1}^* = -0.10$. The measured and reconstructed location of the maximum are indicated in figure 7.9(a). A significant error of the phase shift can be introduced by an uncertainty in the frequency, which is close to the cut-off frequency of the filter. The maximum is mapped to the toroidal plane of the magnetic measurements, $\varphi_{1/1} = (m\theta_{\text{LFS}}^* - \Phi(t))/n$, where θ_{LFS}^* is the poloidal location of the magnetic measurements, and compared to the toroidal location of the onset of the toroidal envelope of the ELM precursor, φ_{prec} (figure 7.9(b)). A simultaneous onset at a second toroidal location is marked by open symbols. It is found that the maximum displacement of the 1/1 mode often precedes the onset of the precursor suggesting a correlation between the central 1/1 mode and the ELM localised at the plasma edge.

7.4 Concluding remarks

In TCV, magnetic oscillations are observed to precede ELMs, believed to be type III ELMs, as well as TCV large ELMs. For both observed types of ELMs, these precursors are strongly localised on the LFS of the torus and have growth rates in the range of 10 to 50 μ s and frequencies in the range of 60 to 120 kHz. These values are in the range of values found for type III precursors on ASDEX-Upgrade [70]. The similar characteristics of their precursors identify both types of ELMs observed in TCV, as type III ELMs. As a result, all TCV ELMs can now be classified in the usual scheme, consisting only of three classes, thereby, reducing the “zoology” of ELMs which exists at different machines.

The high spatial resolution of TCV's toroidal array of magnetic pick-up coils allowed to reveal a toroidal asymmetry in the ELM precursor oscillation, which is very unusual for conventional MHD modes in tokamaks. The precursor has a toroidally localised on-

set. The magnetic oscillation and particularly its mode spectrum is best described by a toroidally localised mode with a medium toroidal mode number $n = 7 - 9$ which grows in toroidal extent and amplitude, while rotating in the electron diamagnetic drift direction. Following the toroidal extension of the instability, the encompassing of the entire toroidal circumference coincides with the onset of the enhanced radial transport of particles and energy. Simultaneously, an $n = 5$ component rapidly grows to a large amplitude. The poloidal mode number of the ELM precursor is approximately $m = 12$ and therefore, consistent with the low safety factor of the analysed discharges and a resonant flux surface close to the plasma edge.

The asymmetry causing and supporting this unusual toroidal localisation of the ELM precursor oscillation, must be intrinsic to the plasma, since errors in the measurements or an asymmetry of the TCV assembly could be excluded. The rotation of the toroidal location of the precursor in the electron drift direction with rotation velocities typical for low- n modes in TCV suggests an instability being the origin of the observed asymmetry. However, a low- n island located close to the edge, which could locally alter the stability with respect to ballooning modes, has not been observed. Nevertheless, a central 1/1 mode always coincides with a localised precursor. A mapping of the phase of the $m = 1$ mode on the outboard midplane suggests a correlation with the ELM precursor with the maximum of the 1/1 mode preceding the ELM precursor. The 1/1 mode is usually associated with the sawtooth pre- or postcursor. A coupling between the 1/1 mode related to the sawtooth and the ELM has hitherto not been observed, but could provide a new explanation for a correlation between sawteeth and ELMs, in particular an observed triggering of an ELM prior to the sawtooth crash.

Chapter 8

Stability limits in highly elongated plasmas

The evolution from circular to elongated plasma shapes has contributed significantly to the improvement of tokamak performance, measured by the achieved triple product shown in figure 1.9. All modern tokamaks have elongated plasmas and the ITER-FEAT design foresees an elongation of $\kappa = 1.85$ [72]. However, there are only a few relevant experiments at higher elongation. TCV, which is one of them, can routinely operate above $\kappa = 2$ and has achieved a record elongation of $\kappa = 2.8$ [73] at a conventional aspect ratio.

This chapter gives an overview of MHD activities observed in highly elongated TCV plasmas. Several MHD instabilities are identified by their mode structure and temporal evolution [74]. The observations are found to be consistent with predictions. In particular, a newly found disruptive current limit, which is preceded by kink-type modes, is encountered for $\kappa > 2.3$. The experiments provide the first confirmation [75] of a previously predicted deviation from the linear Troyon-scaling of the ideal beta limit with normalised current (equation 2.53) at high elongation [76].

8.1 Introduction into elongated plasmas

8.1.1 Properties of elongated plasmas

A main feature of an elongated plasma shape is its capability of carrying a higher plasma current. In a tokamak the current is usually limited by ideal MHD requiring an edge safety factor, $q_a > 2$, for stability (equation 2.50). In a large aspect ratio approximation the edge safety factor is given by,

$$q_a \approx \frac{2\pi a^2 B_0}{R_0 \mu_0 I_P} \cdot \frac{1 + \kappa^2}{2}. \quad (8.1)$$

Consequently, the maximum plasma current scales as $I_P \propto 1 + \kappa^2$. The plasma current and an elongated plasma cross section, both, have favourable confinement and stability properties:

- **Energy confinement**

The beneficial effect of plasma current and elongation on the energy confinement can be seen in various empirical scaling laws, such as the IPB98(y) scaling for ELMy H-modes [77],

$$\tau_{E,th}^{ELMy} \propto I_P^{0.97} \cdot \kappa^{0.67}. \quad (8.2)$$

According to equation 8.2 the energy confinement time increases almost proportionally with I_P and elongation is also found to be beneficial.

The positive effect of elongation is supported by purely geometric arguments. Assuming a shape independent heat diffusivity χ , the reduction of flux surface averaged gradients in elongated plasmas leads to an increased global energy confinement. This improvement in energy confinement can be expressed by a so-called shape enhancement factor [51]. For example, a plasma with $\kappa = 2.4$ and $\delta = 0.4$ has twice the energy confinement time of a circular plasma with the same χ profile and the same input heat flux.

- **Beta limit**

A higher plasma current and therefore, a greater elongation allows a higher value of beta. The β limit determined by ideal MHD theory is seen to scale proportionally with the normalised plasma current $I_N = I_P[\text{MA}] / (a[\text{m}]B[\text{T}])$ (see equation 2.53 in section 2.3.3). This dependence has been experimentally verified up to $\kappa = 2.35$ [78]. However, calculations have predicted a departure from the linear scaling for higher elongations [76].

The beneficial effects of an elongated plasma shape have to outweigh the demands arising from the intrinsic instability of their vertical position (see section 2.3.4). The growth rate of the axisymmetric mode increases with elongation and requires sufficient active and passive control mechanisms, such as a fast feedback control and a close fitting conducting shell.

8.1.2 High elongation in TCV

The TCV tokamak has been especially designed to produce highly elongated plasmas (see section 3.1.1). The combination of an efficient passive stabilisation by the highly conducting vacuum vessel and an active feedback control also using internal coils has allowed the stabilisation of open-loop growth rates up to 4400 s^{-1} [16]. The control of the vertical position also depends on the current profile, with higher currents and broader profiles leading to a better coupling to the vessel and the control coils.

The analysis presented here has been carried out on medium to high density Ohmic discharges which attained a maximum elongation of $\kappa = 2.58$. Recent experiments using optimised current ramp-up scenarios allowed to operate at lower densities and lower internal inductances resulting in the record elongation of $\kappa = 2.80$ [73].

8.2 MHD activity in highly elongated plasmas

Various types of MHD events were observed in highly elongated TCV plasmas. Figure 8.1 shows the characteristic traces of the line-integrated soft X-ray emissivity I_X , the plasma current I_P , magnetic fluctuations measured on the LFS of the plasma $\partial B/\partial t$, and the vertical position observer of the plasma control system $z \cdot I_P$, for three different events.

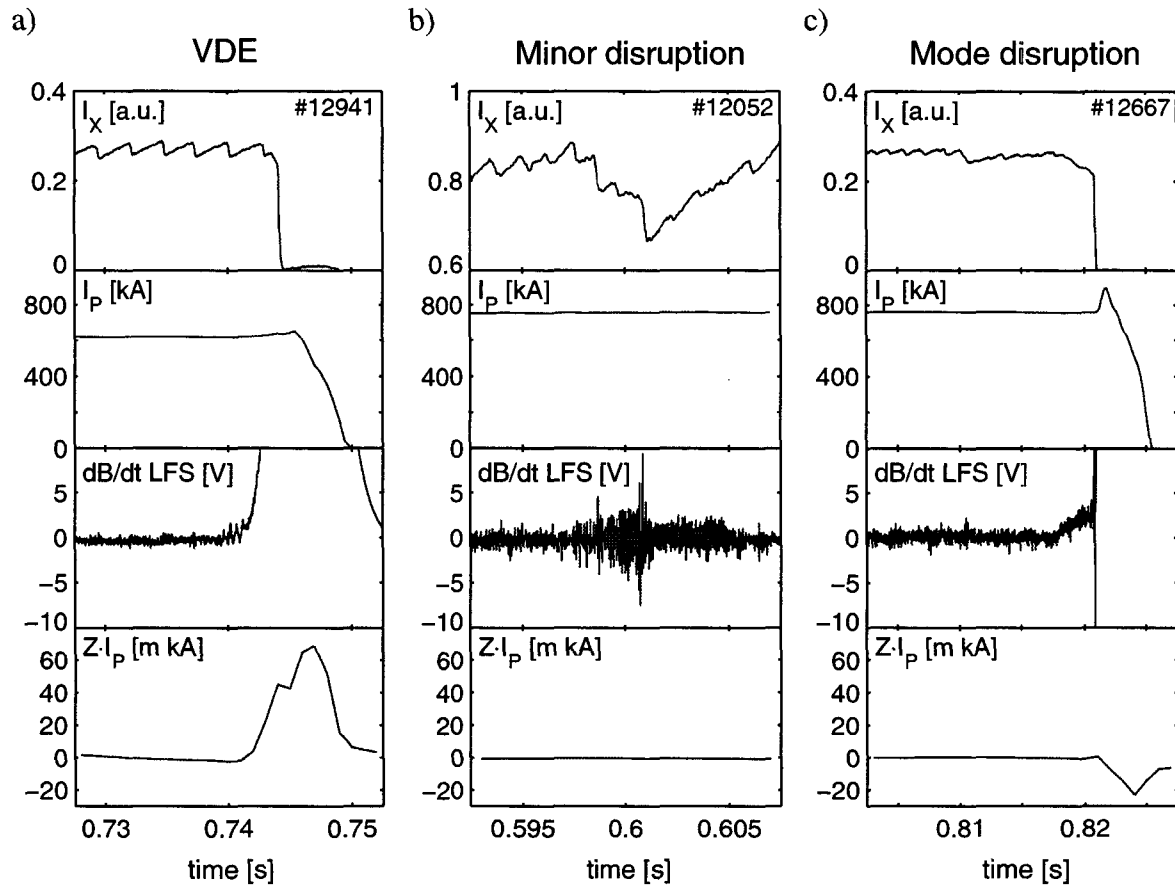


Figure 8.1: Various MHD events observed in highly elongated plasmas. (a): The disruption of discharge #12941 ($\kappa = 2.40$) is caused by a vertical displacement event. (b): A minor disruption in discharge #12052 ($\kappa = 2.40$) is caused by a burst of MHD activity. (c): The disruption of discharge #12667 ($\kappa = 2.53$) is preceded by a locked growing mode.

8.2.1 Vertical displacement events

The discharge #12941, shown in figure 8.1(a), disrupts at a plasma current, $I_P = 620$ kA ($I_N = 2.5$ MA/Tm) and an elongation, $\kappa = 2.40$. The disruption is preceded by an axisymmetric mode causing a so-called vertical displacement event (VDE). The plasma moves towards the top of the vacuum vessel and eventually makes contact with the vessel wall before disrupting. The vertical motion of the plasma column can easily be seen in the real time zI_P -observer used for the position control (bottom trace in figure 8.1(a)).

The bi-orthogonal decomposition of the magnetic perturbation measurements at the edge, which precedes the disruption, reveals a dominant eigenvector comprising 95% of the total signal power. Its topo and chrono are shown in figure 8.2. The part of the topo corresponding to the poloidal array shows a dominant $m = 1$ structure. The magnetic axis is located at $z = +0.10$ m corresponding approximately to the poloidal probe position 2 on the HFS and 19 on the LFS. The contribution of the toroidal array clearly identifies the axisymmetry ($n = 0$) of the perturbation. The chrono reveals some vertical oscillations which grow in amplitude, before the plasma moves in the vertical direction. The $n = 0$ component of the toroidal measurements A_0 , is well fitted by an exponential growth with $\gamma^{-1} \approx 0.5$ ms. The oscillations are caused by the action of the feed-back control system encountering its limit.

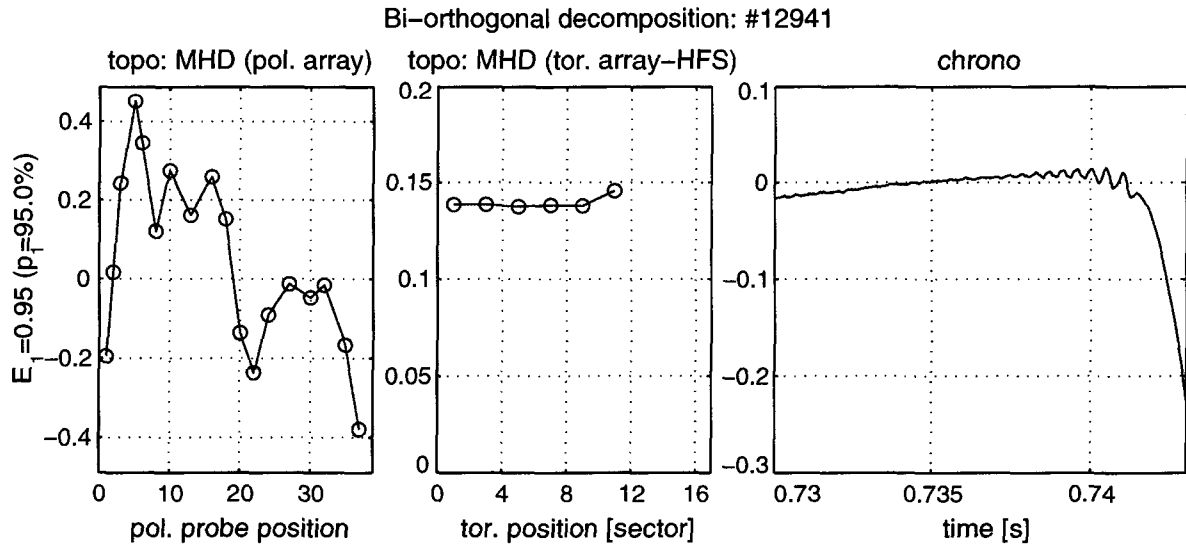


Figure 8.2: Dominant eigenvector of the bi-orthogonal decomposition of the magnetic measurements B , of the poloidal and toroidal (HFS) arrays. The topo, separated into the poloidal and toroidal array, shows a dominant $m = 1/n = 0$ component of the magnetic perturbation which precedes the disruption.

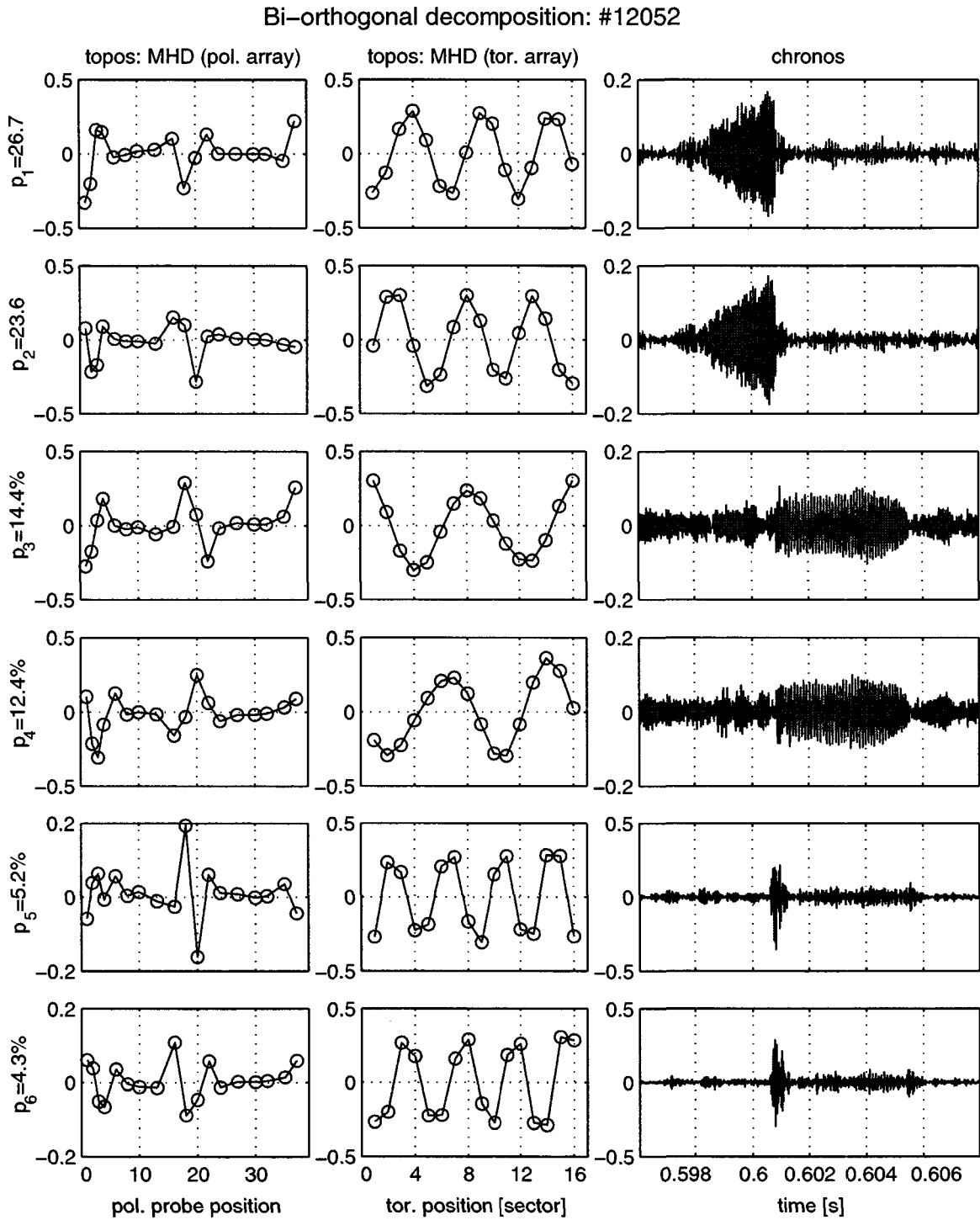


Figure 8.3: Bi-orthogonal decomposition of the magnetic fluctuation measurements, $\partial B / \partial t$, of the poloidal and toroidal (LFS) array during the burst of MHD activity shown in figure 8.1(b). The pairs of first and second (row 1 and 2), third and fourth (row 3 and 4), as well as the fifth and sixth (row 5 and 6) eigenvectors are degenerated and reveal three rotating modes. The poloidal and toroidal mode structures are seen in the corresponding parts of the topos (first and second columns). The time evolution is revealed by the chronos (third column).

8.2.2 Minor disruptions

The discharge #12052 ($I_P = 760$ kA, $I_N = 3$ MA/Tm), shown in figure 8.1(b), is perturbed by a minor disruption at 0.601 ms, clearly seen by the crash in the soft X-ray signal. This event is accompanied by bursts of MHD activity. The discharge can usually recover from these bursts and maintain the plasma current.

The MHD activity is recorded with the arrays of magnetic probes. Figure 8.3 shows the six principal eigenvectors of the bi-orthogonal decomposition of the magnetic measurements. The first and second columns show the poloidal and toroidal (LFS) part of each topo. The third column contains the corresponding chrono. The six eigenvectors form three pairs of degenerated eigenvalues representing three rotating modes. The toroidal components of the topos clearly identify the $n = 3$, $n = 2$ and $n = 4$ mode structures. A comparison between the poloidal components of the topos and modelled island structures, shown in figure 8.4(a)-(c), reveal the corresponding poloidal mode numbers $m = 4$, $m = 3$ and $m = 5$. The $4/3$ mode grows continuously up to the crash in the soft X-ray signal. After the minor disruption it is replaced by a $3/2$ and a $5/4$ mode. The latter disappears in less than a millisecond while the former initially saturates and eventually disappears after 5 ms.

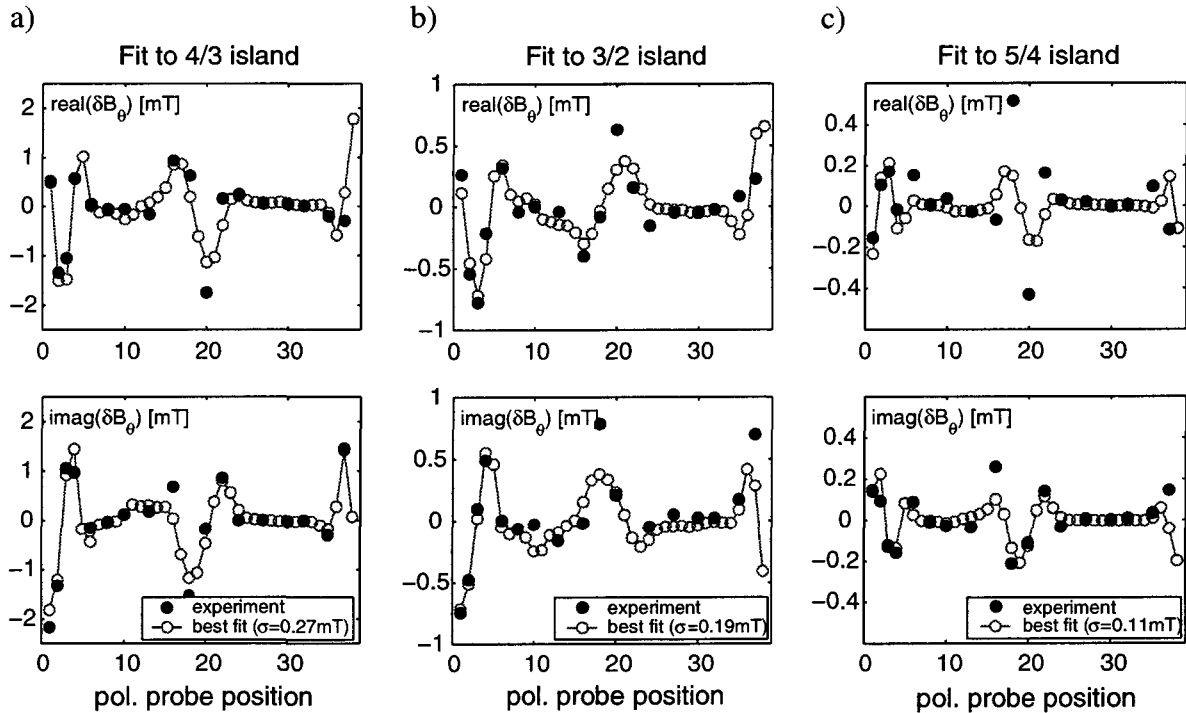


Figure 8.4: The structure of three rotating modes, which were observed in discharge #12052 at $t = 0.6$ s (figure 8.3), are compared with the modelled structure of magnetic islands identifying a (a): $4/3$, (b): $3/2$ and (c): $5/4$ mode structure.

All the modes are rotating in the direction of the electron diamagnetic drift. The 4/3 mode starts at 15 kHz and slows down to 12 kHz while growing in amplitude. The succeeding 5/4 mode rotates with approximately 20 kHz and the 3/2 mode with 10 kHz.

8.2.3 Mode disruptions

The disruption of discharge #12667 ($I_P = 760$ kA, $I_N = 3$ MA/Tm), shown in figure 8.1(c) is preceded by an MHD mode. The bi-orthogonal decomposition of the magnetic measurements (figure 8.5) reveals its mode structure. The toroidal structure is easily identified as an $n = 1$ mode, while the poloidal structure has a predominant $m = 2$ component. However, no good agreement between the experiment and the island model could be obtained, which suggest that the mode is more global than a single island chain and/or of a different nature, such as a kink mode. The mode grows with a characteristic growth time of $\gamma^{-1} \approx 1$ ms and is immediately locked to the TCV wall.

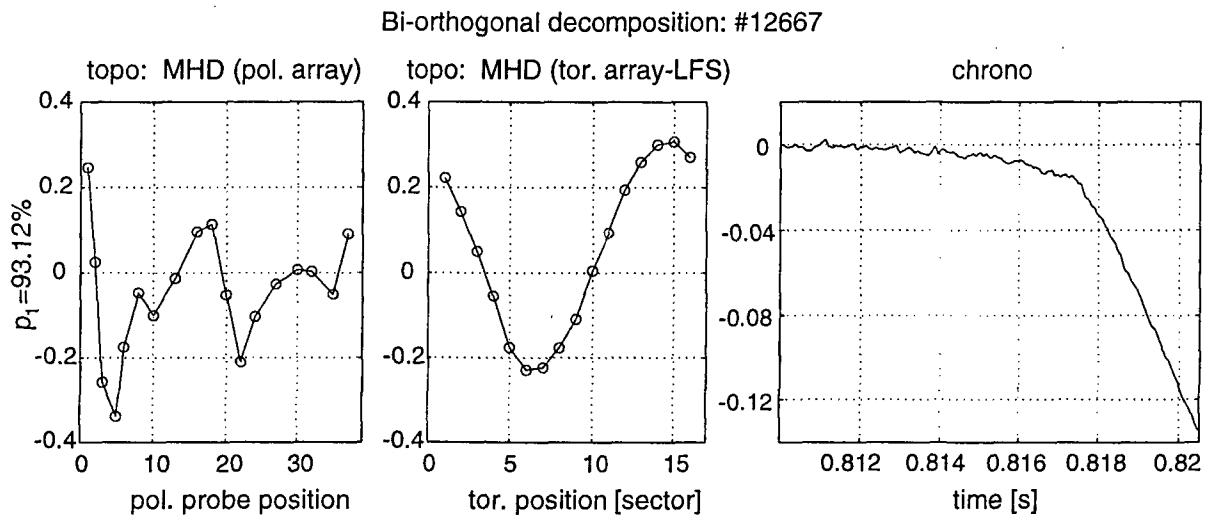


Figure 8.5: The topo corresponding to the largest eigenvalue of the bi-orthogonal decomposition of the integrated magnetic measurements, B , of the poloidal and toroidal (LFS) array reveals a dominant $m/n = 2/1$ structure of the disruption precursor. The chrono shows that the mode grows locked to the vessel wall.

The mode disruption can easily be distinguished from a VDE by the characteristic spike in I_P prior to the disruption. The amplitude of the zI_P -observer signal is also significantly lower (compare figure 8.1(a) and (c)).

8.3 MHD stability in highly elongated plasmas

In order to understand the stability of highly elongated plasmas, the occurrence of the three MHD events described in section 8.2, is linked to plasma parameters. The observed

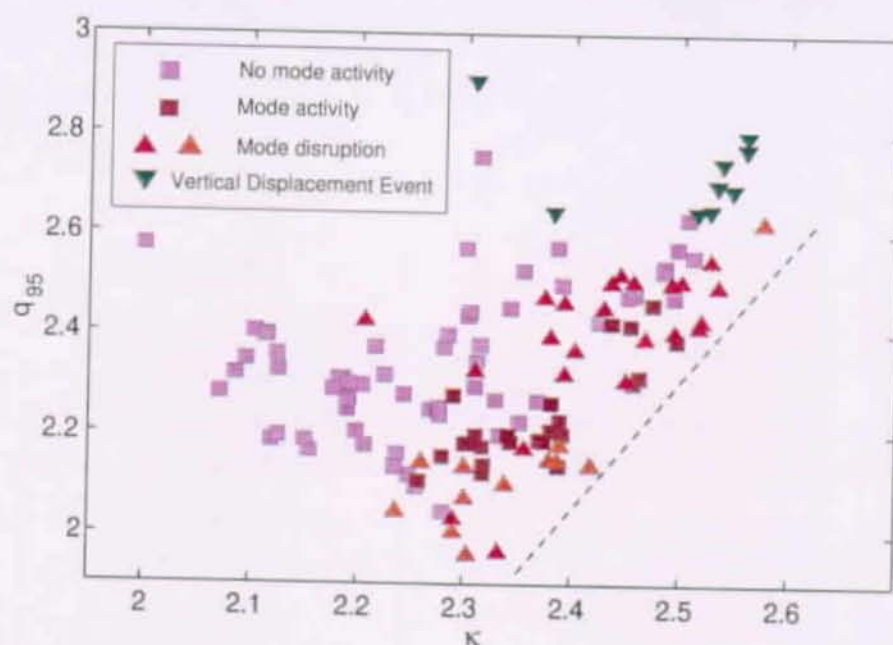


Figure 8.6: The occurrence of MHD activity in highly elongated ohmic plasmas depends on the safety factor taken at the surface containing 95% of the poloidal flux q_{95} , and elongation, κ . Disruptions are marked by triangles while non-disruptive discharges are shown as squares.

stability limits are then compared with theory.

8.3.1 Operational diagram

An extensive database of Ohmic TCV discharges with an elongation greater than 2 has been created. The analysed discharges mainly vary in elongation, and current, but also in triangularity and density. In addition to the MHD events mentioned above (section 8.2), it also contains discharges without any increased MHD activity.

In figure 8.6 the occurrence of MHD activity is marked in the q_{95} - κ plane, where q_{95} is the safety factor on the surface containing 95% of the poloidal flux. Vertical displacement events are indicated by downward triangles, minor disruption by brown squares, mode disruptions by upward triangles and discharges without an increased MHD activity by blue squares. The most obvious experimental observation is a departure from the conventional ideal MHD current limit, $q_a \geq 2$, for elongations greater than 2.3. At these high elongations attempts to increase the current led to disruptions at q_{95} well above 2. The minimum safety factor attained, increased with elongation.

This limit can also be interpreted as a limit to the normalised current I_N . In figure 8.7 the occurrence of MHD events, marked by the same symbols than in figure 8.6, is shown as a function of κ and I_N , revealing the disruptive limit $I_N < 3 \text{ MA/Tm}$. In addition to

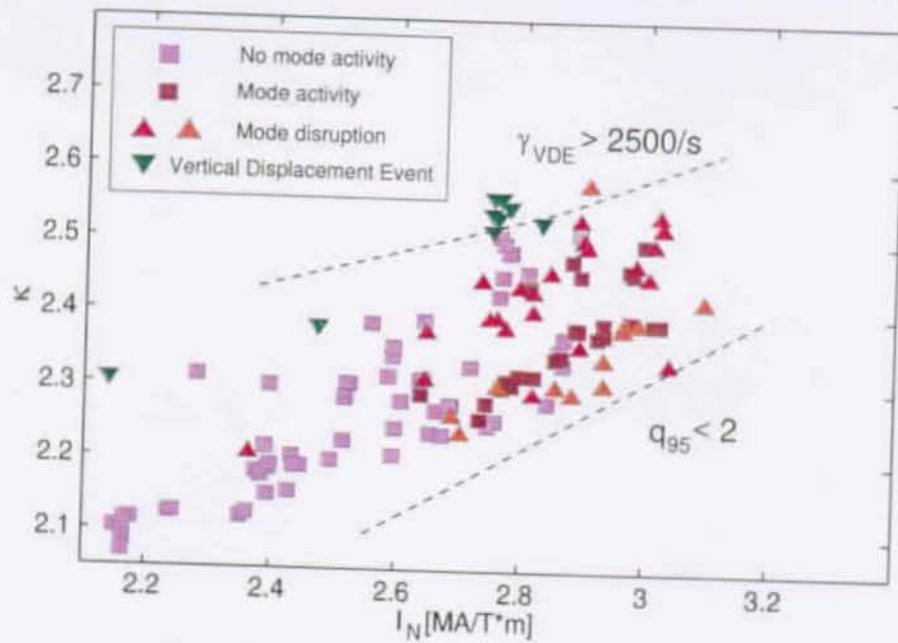


Figure 8.7: MHD activity in highly elongated ohmic plasmas depends on elongation κ , and normalised plasma current $I_N = I_P/(aB_0)$. The dependence of the growth rate of the axisymmetric mode γ_{VDE} [16] and of the safety factor on the surface including 95% of the flux q_{95} , on κ and I_N are indicated by the dashed lines.

this limit of the normalised current, VDEs and mode disruptions impose lower and upper current limits, respectively, with both limits depending on elongation.

8.3.2 Axisymmetric mode

Vertical displacement events are observed to impose an upper limit on the safety factor (figure 8.6), which is equivalent to a lower limit on the current (figure 8.7), for a plasma with a given elongation. This is consistent with the occurrence of the axisymmetric mode, whose growth rate is predicted to increase with decreasing current while the maximum growth rate which the feedback control system is able to stabilise, stays approximately constant. Consequently, the axisymmetric mode imposes a lower current limit. Its growth rate has been computed for highly elongated D-shaped plasmas [16]. The contour for a computed growth rate of $\gamma^{-1} = 2500 \text{ s}^{-1}$ is indicated in the $\kappa - I_N$ plane in figure 8.7 and coincides with the observed disruptive limit. Note, that the value of $\gamma^{-1} = 2500 \text{ s}^{-1}$ is well below the maximum growth rate of 4400 s^{-1} stabilised in TCV (see section 3.1.1). However, the latter was obtained at a much lower plasma current. Owing to limits of the current in the feedback control, the capability of the control system decreases with higher plasma currents.

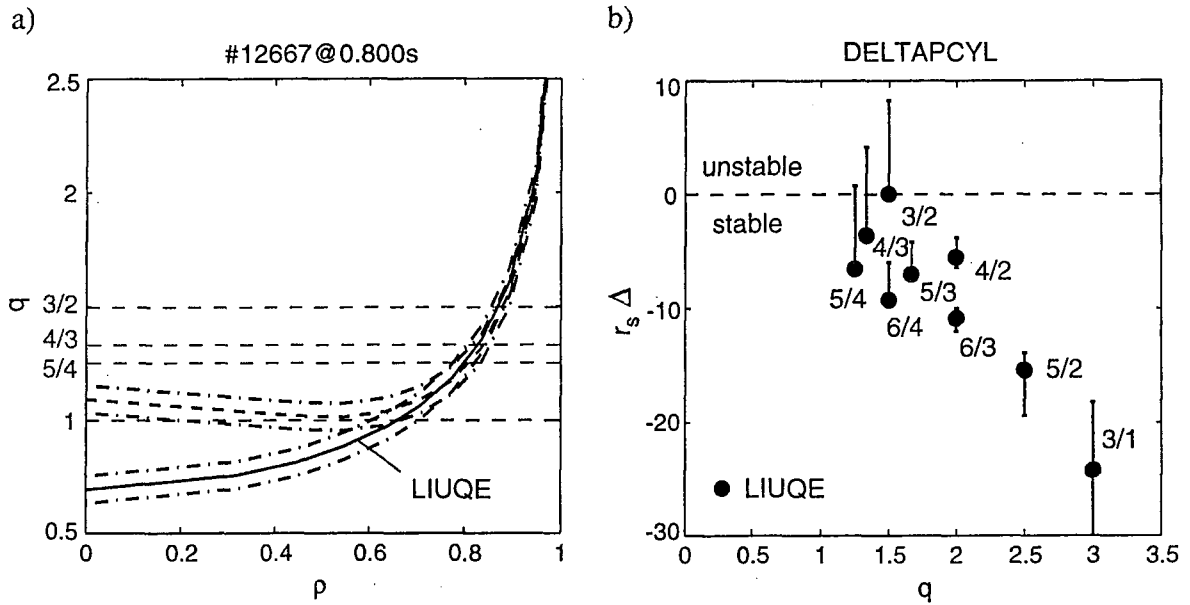


Figure 8.8: Analysis of the tearing mode stability of #12667 ($\kappa = 2.5$, $I_N = 3.0$ MA/Tm). (a): The q -profile is taken from the LIUQE reconstruction (solid line). A second reconstruction is constraint to $q_0 > 1$ (dashed) and the offset of the q -profiles varied (dash-dotted). (b): The tearing parameter Δ' is calculated in a cylindrical approximation. The symbols mark the value found for various modes using the original q -profile and the error-bar indicates the range resulting from the introduced profile variations.

8.3.3 Tearing modes

Rotating modes with $m = n + 1$ were frequently observed in plasmas with $I_N > 2.6$. They rotate in the direction of the electrons with a rotation frequency which is approximately proportional to the toroidal mode number, $\omega_{m/n} \approx n \cdot \omega_0$, with ω_0 typically being in the range from 3 – 6 kHz. This is consistent with modes which move with a toroidally rotating electron fluid (see section 5.1.2). These modes grow on a resistive time scale with characteristic times ranging from 0.5 to 3 ms and either saturate and eventually disappear or cause minor disruptions.

An analysis of the tearing stability of a highly elongated plasma has been carried out. Figure 8.8(a) shows the reconstructed q -profile of a plasmas with $\kappa = 2.5$ (solid line). In order to test its sensitivity with respect to uncertainties of the equilibrium reconstruction q_0 was constrained to a value above one resulting in an even flatter current profile (dashed line). The offset of the whole profile was also varied (dash-dotted line) probing the sensitivity with respect to the distance between a resonant flux surface and the plasma boundary. The tearing parameter Δ' , has been calculated for several modes in a cylindrical approximation ($m \gg 1$) using the code DELTAPCYL [79] and is shown in figure 8.8(b). The values resulting from the original q -profile, indicated by the markers, reveal the 3/2 mode to be the least stable. A flattening of the current profile, indicated

by the errorbars in figure 8.8(b), leads to a decrease of the stability of the 3/2, 4/3 and 5/4 modes up to instability, while the other modes are less affected and remain stable.

This is consistent with the experimental observation of mainly 3/2 and 4/3 as well as occasional 5/4 modes as described in section 8.2.2. In particular, the trend for instability with higher q_0 is consistent with the experiment, where higher elongations lead to flatter current profiles and also the appearance of the modes. Furthermore, the growth of the island width, estimated from magnetic measurements according to equation 5.53, is several m/s and corresponds to expected growth rates of tearing modes (equation 2.72) in the order of $r_s/\tau_R \approx 1$ m/s.

8.3.4 Ideal MHD stability limit

The disruptive limit close to $q_a = 2$ is always preceded by a locked growing mode. This is consistent with the ideal MHD current limit and a kink mode (see section 2.3.2). This limit is well known and is usually avoided. Modes with the same characteristics are seen also to precede the newly found limit, $I_N < 3$ MA/Tm, although q_a was significantly higher than 2. Therefore, calculations predicting the ideal β limit to be altered at high elongation [76] were recently repeated using the plasma shape and profiles of actual TCV discharges [80, 75]. The profiles were scaled to vary β and I_N . The existence of a resistive wall was neglected. The ideal stability limit, which is imposed by an $n = 1$ kink-type mode, is indicated in figure 8.9 for two different elongations with a band representing the effect of small variations of the profiles within the experimental uncertainties. The ideal β limit deviates for $I_N > 2$ from the linear Troyon scaling with I_N . While the deviations from the classical scaling are only small for $\kappa = 2.20$ (#11835), the decrease of the β limit for currents below the zero-beta current limit is significant for $\kappa = 2.5$ (#12413/12414).

TCV discharges with κ ranging from 2.20 to 2.58 are shown in the same β - κ plane with triangle and square markers distinguishing between disruptive and non-disruptive discharges. The experiments are in good agreement with the ideal MHD beta limit. In particular, it is seen that the discharge #12414 terminates in a disruption, whereas the discharge #12413 with identical κ and I_N but lower beta is non-disruptive. However, disruptions also occurred at an I_N and a β far below the ideal limit. These disruptions were usually preceded by cascades of 3/2, 4/3, and occasionally 5/4 modes. It is suggested that the islands modify the current and pressure profiles, such that an ideal mode can even be destabilised at a lower value of beta.

The characteristic growth times of the disruption precursor range from 0.1 to 1.5 ms and, therefore, are too slow for an ideal mode. It is suggested that the finite resistivity of the plasma as well as of the wall are also important, in particular since the disruptions systematically occur at the low β end of the band of uncertainty.

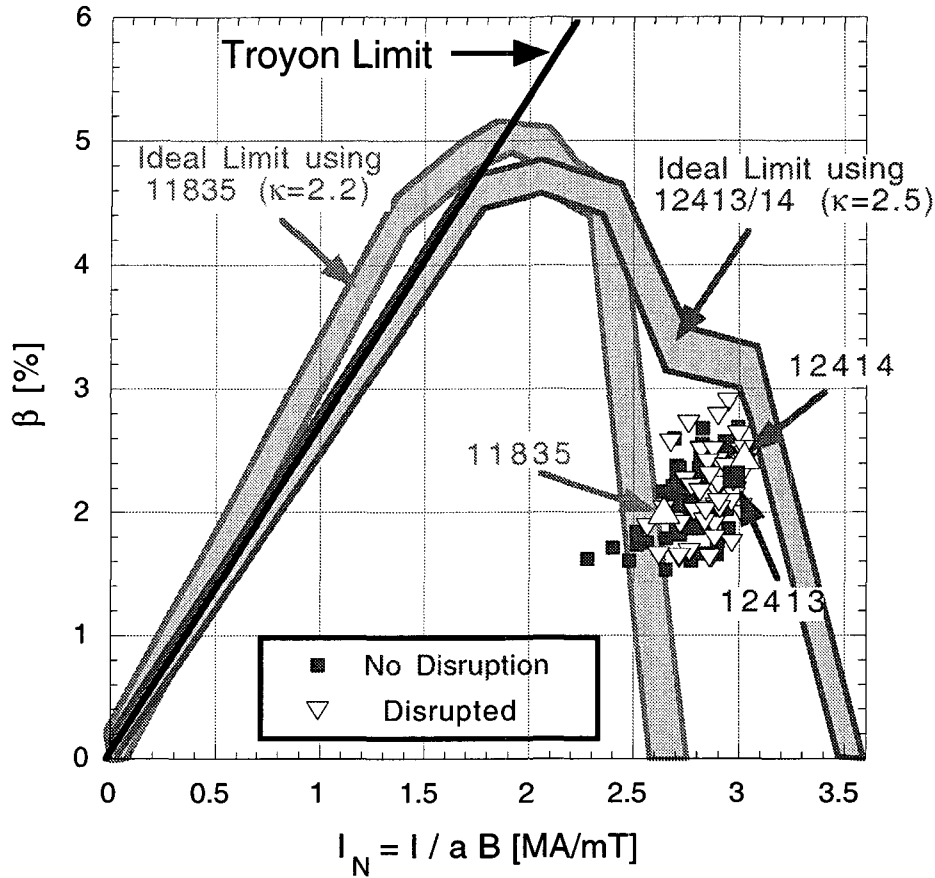


Figure 8.9: Ideal β limit as a function of normalised current, I_N [75]. The limit is calculated using two TCV plasma shapes and scaling the actual profiles. The band indicates experimental uncertainties. Disruptive (triangles) and non-disruptive (square) discharges with κ ranging from 2.20 to 2.58 are marked.

8.4 Concluding remarks

Several MHD events, observed in highly elongated TCV plasmas, were identified. The occurrence of these instabilities was found consistent with stability predictions.

Vertical displacement events, which are caused by axisymmetric modes, impose a lower limit to the plasma current. This limit depends on the plasma shape, the current profile and the passive and active stabilisation capabilities of the tokamak. The experimentally found limit is in good agreement with predicted growth rates of the axisymmetric mode [16].

Observed bursts of MHD activity are caused by tearing modes. These islands have an $m = n + 1$ structure and are located close to the $q = 1$ surface. Calculations of the stability parameters Δ' , suggest that their occurrence is linked to the broad current profiles which are typical for highly elongated plasmas.

For elongations $\kappa > 2.3$, a new disruptive limit of the plasma current, $I_N \leq 3 \text{ MA/Tm}$ is encountered. This limit is found to be consistent with ideal MHD calculations. The TCV observations, therefore, provide the first experimental confirmation of a deviation of the linear Troyon-scaling of the ideal beta limit with normalised current (equation 2.53) at high elongation, which was predicted over 10 years ago [76]. This deviation results in the existence of an optimum elongation and a corresponding normalised current which maximise the attainable beta. The TCV results suggest that this optimum elongation is in the range of $\kappa = 2 - 2.2$.

Chapter 9

Neoclassical tearing modes

Neoclassical tearing modes (NTMs) were first identified in TFTR [81] and have since been observed in high β and low-collisionality discharges in a number of tokamaks, where they often limit the achievable beta [82]. The conditions for their appearance is reactor-relevant and NTMs could impose the most restrictive β -limit in a fusion reactor. A detailed understanding of their destabilisation process is of great importance in order to find methods to avoid them.

This chapter reports the observation of NTMs in TCV. The mode is identified, its structure revealed and the range of relevant plasma parameters given. Special interest is dedicated to the onset of the neoclassical mode. A new trigger mechanism is found showing the need to reconcile conventional and neoclassical tearing for an accurate description [83]. An observed dependence of the mode onset on density is compared to predictions. The TCV results are also interpreted in the context of the observations on other experiments.

9.1 Introduction into neoclassical tearing modes

Neoclassical theory takes into account the effects of modified particle orbits in a toroidal geometry and has important consequences for the transport and stability of tokamak experiments. One of the most prominent effects is the bootstrap current which can add a driving term for magnetic islands.

9.1.1 Bootstrap current

Owing to the $1/R$ decay of the toroidal field, particles with $v_{\parallel}/v_{\perp} < (\Delta B/B)^{1/2}$, where ΔB is the difference between the magnetic field on the HFS and LFS of a flux surface, are trapped in a magnetic mirror on the LFS of the torus. If these trapped particles are sufficiently collisionless their orbits have a radial excursion,

$$w_{bs} = \frac{\rho_s q}{2\sqrt{\epsilon}} \quad (9.1)$$

where $s = i, e$ denotes the particle species and ω_s the corresponding Larmor radius (equation 1.10). Due to the shape of their poloidal projection these orbits are called banana orbits. In the presence of a gradient of the particle collisionality, which can be caused by density and temperature gradients, a net toroidal current arises. For positive shear this current amplifies the Ohmic current. This so-called *bootstrap current* can be written as [84],

$$j_{bs} = \frac{p}{B_{pol}} \left(L_{31} \frac{n'_e}{n_e} + R_{pe} (L_{31} + L_{32}) \frac{T'_e}{T_e} + L_{31} (1 + \alpha_i) (1 - R_{pe}) \frac{T'_i}{T_i} \right) \quad (9.2)$$

where $R_{pe} = p_e/p$ is the electron contribution to the total pressure and the prime denotes a radial derivative. The bootstrap current coefficients L_{31} , L_{32} and α_i depend on the trapped particle fraction which increases with decreasing collisionality ν_e . In general, neoclassical effects are only important if the collisionality is small compared to the banana bounce frequency w_b , leading to the normalisation $\nu_{e^*} = \nu_e/\omega_b \approx n_e q R / (\epsilon^{3/2} T_e^2)$.

9.1.2 Neoclassical effects on the island growth

The neoclassical bootstrap current adds a driving term to the evolution of magnetic islands. A helical perturbation of the bootstrap current generated by the flattening of the pressure profile across an existing island further destabilises the island. The evolution of such *neoclassical tearing modes* is described by the generalised Rutherford equation [82],

$$\frac{\tau_R}{r_s} \frac{dw}{dt} = r_s \Delta'(w) + r_s \beta_p \left((a_{bs}(\nu_{e^*}) - \hat{a}_{GGJ}) \frac{w}{w^2 + w_d^2(\nu_{e^*})} - a_{pol}(w, g) \frac{1}{w^3} \right) \quad (9.3)$$

where τ_R is the resistive time on the resonant flux surface with a radius r_s . The first term on the right hand side of equation 9.3 is the driving term of a conventional tearing mode arising from the free energy of an unstable current profile (see section 2.4.2). The destabilising effect of the perturbed bootstrap current is described in the second term with $a_{bs} = a_2 L_q j_{bs} B_{pol} / p$, where $L_q = q/q'$ is the scale length of the safety factor profile. Since the bootstrap current j_{bs} (equation 9.2), increases with decreasing collisionality, so too does the resulting neoclassical driving term. The stabilising effect of toroidicity and shaping is represented by the modified Glasser-Greene-Johnson term, \hat{a}_{GGJ} .

There are two further effects whose relevance for the evolution of the island width is currently being discussed. The finite ratio of perpendicular and parallel heat conductivity $\chi_\perp/\chi_\parallel$, leads only to an incomplete flattening of the pressure profile across the island and therefore, reduces the perturbation of the bootstrap current. The effect of an incomplete flattening is large for small islands and gives rise to a threshold island width,

$$w_d \approx 5.1 r_s \left(\frac{q}{\epsilon s m} \right)^{1/2} \left(\frac{\chi_\perp}{\chi_\parallel} \right)^{1/4}. \quad (9.4)$$

An incomplete flattening of the pressure profile likewise reduces the stabilising GGJ-term [85] leading to the same w dependence of a_{bs} and \hat{a}_{GGJ} . Ion inertia effects also influence the island evolution. The island propagation through the plasma rest frame induces a time-varying electric field which leads to an ion-polarisation current along the axis of the island. The polarisation current depends on the propagation frequency of the island in the plasma rest frame which is usually assumed to be the electron diamagnetic drift frequency ω_{e*} (equation 5.6), as well as on the number of particles which are affected by the time varying electric field. For low collisionality only trapped particles build up the polarisation current. This effect decays rapidly with increasing island width. While several authors have found that this term is large and stabilising, e.g. [86, 87], recent work indicates that this term is in fact destabilising [88, 89]. The ion polarisation effect is accounted for in the fourth term in equation 9.3 with,

$$\hat{a}_{pol}(w, g) \approx a_3 (L_q / (-L_p))^2 \rho_p^2 g(\epsilon, \nu_i) h_3(w) \quad (9.5)$$

where $\rho_p = (2m_i k_B T_i)^{1/2} / (e B_{pol})$ is the poloidal ion Larmor radius and $\nu_i = \ln \Lambda / (12 \epsilon_0^2 \pi^{3/2}) \cdot (Z^4 e^4 n_i) / (m_i^{1/2} (k_B T_i)^{3/2})$ the ion collision frequency. The uncertainty of the sign of the ion polarisation effect is included in $h_3(w)$ and its reduction at low collisionality described by the function,

$$g(\epsilon, \nu_i) = \begin{cases} \epsilon^{3/2}, & \nu_i / (\epsilon m \omega_{e*}) \leq C \approx 0.3 \\ 1, & \nu_i / (\epsilon m \omega_{e*}) > C \approx 0.3. \end{cases} \quad (9.6)$$

For large islands the main effect arises from the magnetic energy required for the island formation, expressed by a negative Δ' . Then equation 9.3 yields a saturated island width,

$$w_{sat} = r_s \beta_p \cdot \frac{a_{bs} - a_{GGJ}}{-r_s \Delta' (w_{sat})} \quad (9.7)$$

showing the characteristic β_p -dependence.

9.1.3 Triggering mechanisms

For $\Delta' < 0$ stabilising effects at small island width lead to a critical island width w_{crit} . Neoclassical modes require a seed island with $w > w_{crit}$, before the growth described by the modified Rutherford equation (equation 9.3) becomes positive and the island evolves to the full saturated width (equation 9.7). These seed islands are most commonly generated by sawteeth or fishbones which couple to the resonant surface [90, 91]. ELMs are also observed to trigger neoclassical modes [92] and in some cases no measurable seed island was detected prior to these modes [90, 93]. A detailed analysis of the triggering mechanism is difficult since the coupling to the resonant surface is usually masked by the trigger instability itself. In order to discriminate between the models the parametric dependencies of the value of β at the onset of the mode is used. An alternative method is the controlled triggering of neoclassical modes using error-field induced islands [94].

9.2 Observation of neoclassical tearing modes

In TCV neoclassical tearing modes have been observed in discharges using up to 2.7 MW of central ECH power. All these discharges used a launching geometry which included a current drive component in the direction of the Ohmic plasma current (co-ECCD). The NTMs were destabilised from a few 10 ms up to more than 1 s after the onset of the additional heating power.

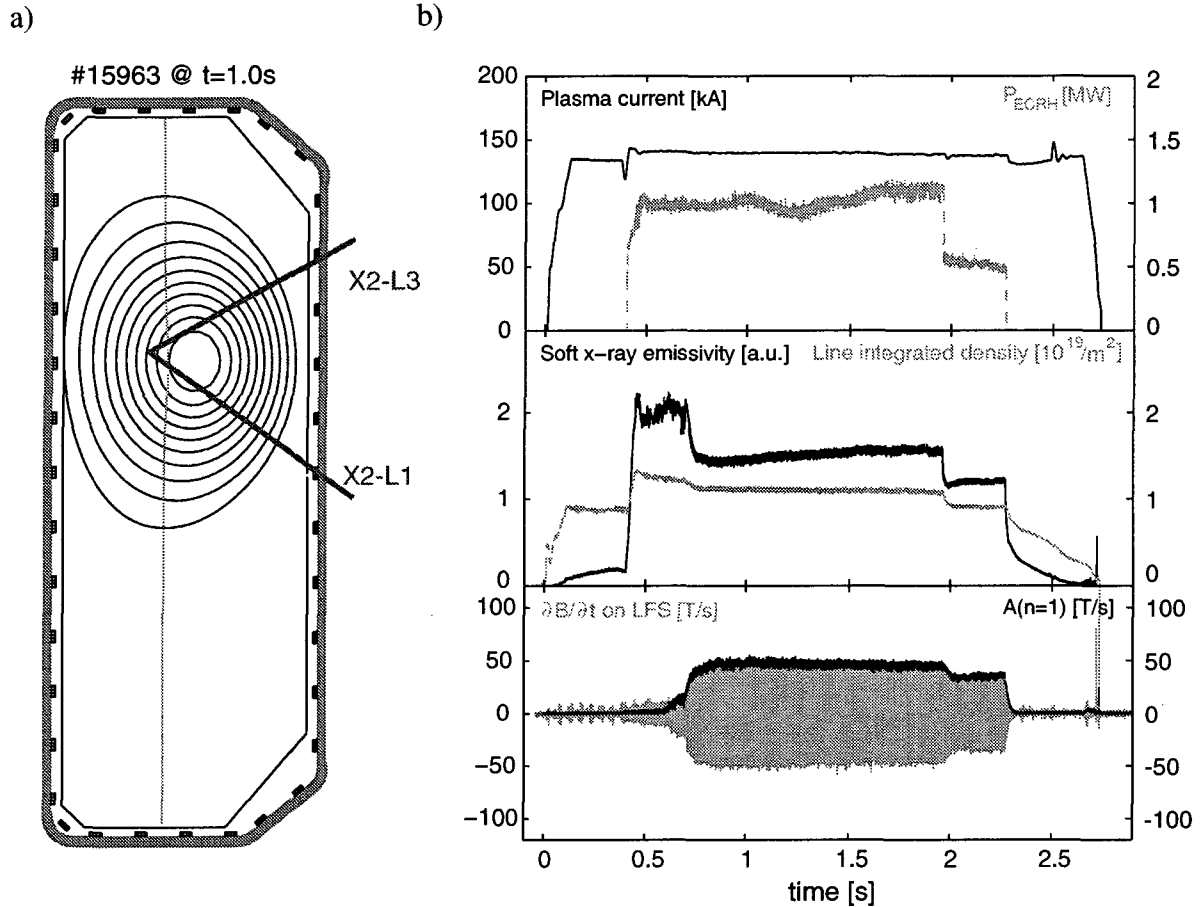


Figure 9.1: (a): The poloidal plasma cross section and the ECH launching geometry indicate a central power deposition at the second harmonic X-mode absorption layer. (b): During ECH heating (top) a drop in the central line integrated soft X-ray intensity (middle) is caused by a large amplitude mode seen in the magnetic fluctuation measurements (bottom). The toroidal array of pick-up coils clearly identifies the $n = 1$ structure.

Figure 9.1(a) shows a typical launching geometry using two gyrotrons. Both beams include a tangential component and drive current in the direction of the ohmic current. About 300 ms after the switch on of the ECH ($t = 0.4$ s) an MHD mode starts to grow and saturates at a high level (figure 9.1(b)). The degradation of energy confinement is clearly visible on a soft X-ray measurement along a central chord. At $t = 1.95$ s one gyrotron is

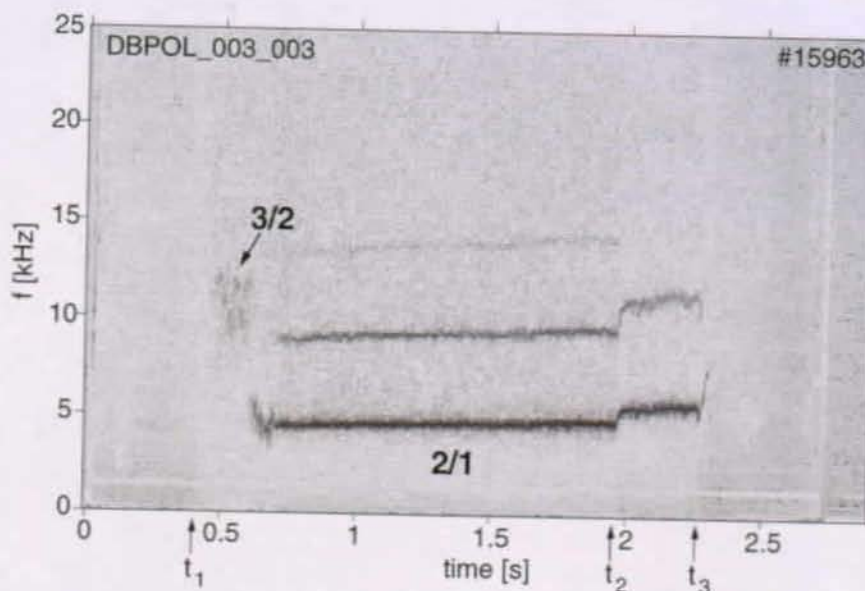


Figure 9.2: Spectrogram of magnetic fluctuation measurements on the high field side. After the switch-on of the two gyrotrons at t_1 an initial 3/2 mode is followed by a large amplitude 2/1 mode. The gyrotrons are switched-off at t_2 and t_3 .

switched off which leads to a decrease in beta. The decrease of the mode amplitude with decreasing beta is consistent with equation 9.7 and suggests its neoclassical origin. At the switch off of the last gyrotron at $t = 2.27$ s, the amplitude quickly decreases to zero.

9.2.1 Mode structure

The mode is seen in magnetic fluctuation measurements at the plasma edge as well as in the tomography of the soft X-ray emissivity. Figure 9.2 shows the power spectral density of magnetic fluctuations measured on the high-field side as a function of time. After the switch-on of the two gyrotrons (t_1) and an initial coherent fluctuation in the range from 10 to 12 kHz, a mode starts with 6 kHz but quickly slows down to 4.5 kHz as it grows in amplitude. At its largest amplitude higher harmonics at 9 and 13.5 kHz are also detected. With the reduction of the heating power (t_2) the frequency increases to 5.5 kHz. The mode disappears after the ECH power is switched off (t_3).

The toroidal array of magnetic probes clearly identifies an $n = 1$ structure (figure 9.1(b)), which rotates in the direction of the electron diamagnetic drift. The poloidal mode structure is measured with the poloidal array of magnetic probes. The bi-orthogonal decomposition of the poloidal measurements in the interval from 0.8 to 1.0 s results in two degenerated eigenvectors comprising 99% of the total signal power which represent the rotating mode. The corresponding topologies are shown in figure 9.3(a). The experimental perturbation structure is compared against the modelled structure of an $m/n = 2/1$ island calculated as described in section 5.3. A fit of phase and amplitude of the modelled

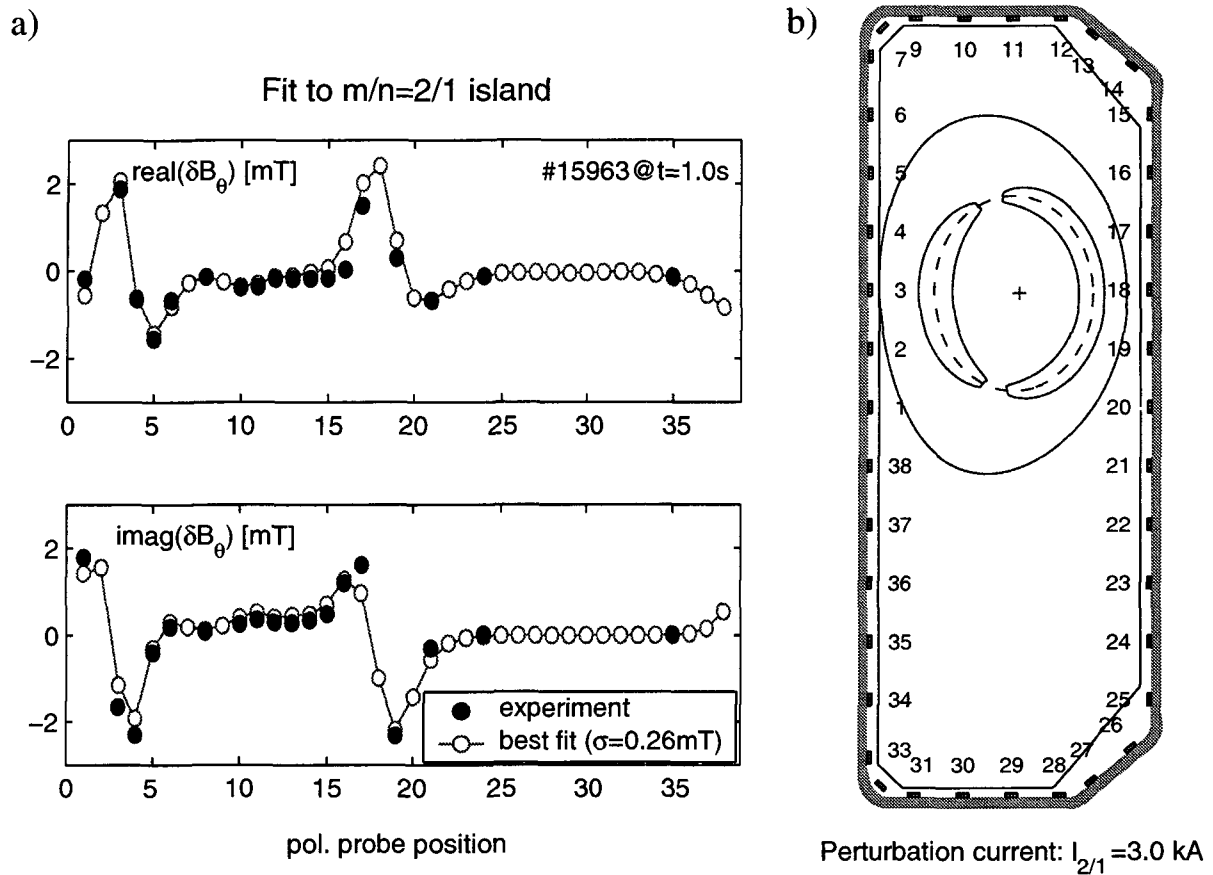


Figure 9.3: (a): The poloidal mode structure, obtained from a bi-orthogonal decomposition of magnetic measurements (full) and the reconstructed magnetic perturbation due to an $m/n = 2/1$ island (open) are in good agreement. (b): The reconstruction of the geometry of the island reveals an island width which corresponds to 20% of the minor radius.

mode leads to good agreement. A standard deviation between modelled and measured values of $\sigma = 0.26$ mT is in the order of the experimental uncertainty and identifies the $2/1$ island (figure 9.3(a)). The superposition of the helical equilibrium and perturbation flux (see section 5.4.2) results in a large island whose width corresponds to 20% of the minor radius (figure 9.3(b)). The coherent fluctuations at 10 to 12 kHz, which follow the onset of the ECH heating, could likewise be identified as a $3/2$ island, however, with a smaller amplitude.

The $2/1$ mode is also seen in the tomographic reconstruction of soft X-ray emission measurements. Figure 9.4 shows the three largest eigenvectors of a bi-orthogonal decomposition of the emissivity in a short time window at $t = 0.8$ s. While the principal eigenvector (a) contains the average profile, the second and third (b,c) are degenerate and show a rotating $m = 2$ mode. The corresponding chronos reveal a rotation frequency of about 5 kHz, which is consistent with the magnetic observations.

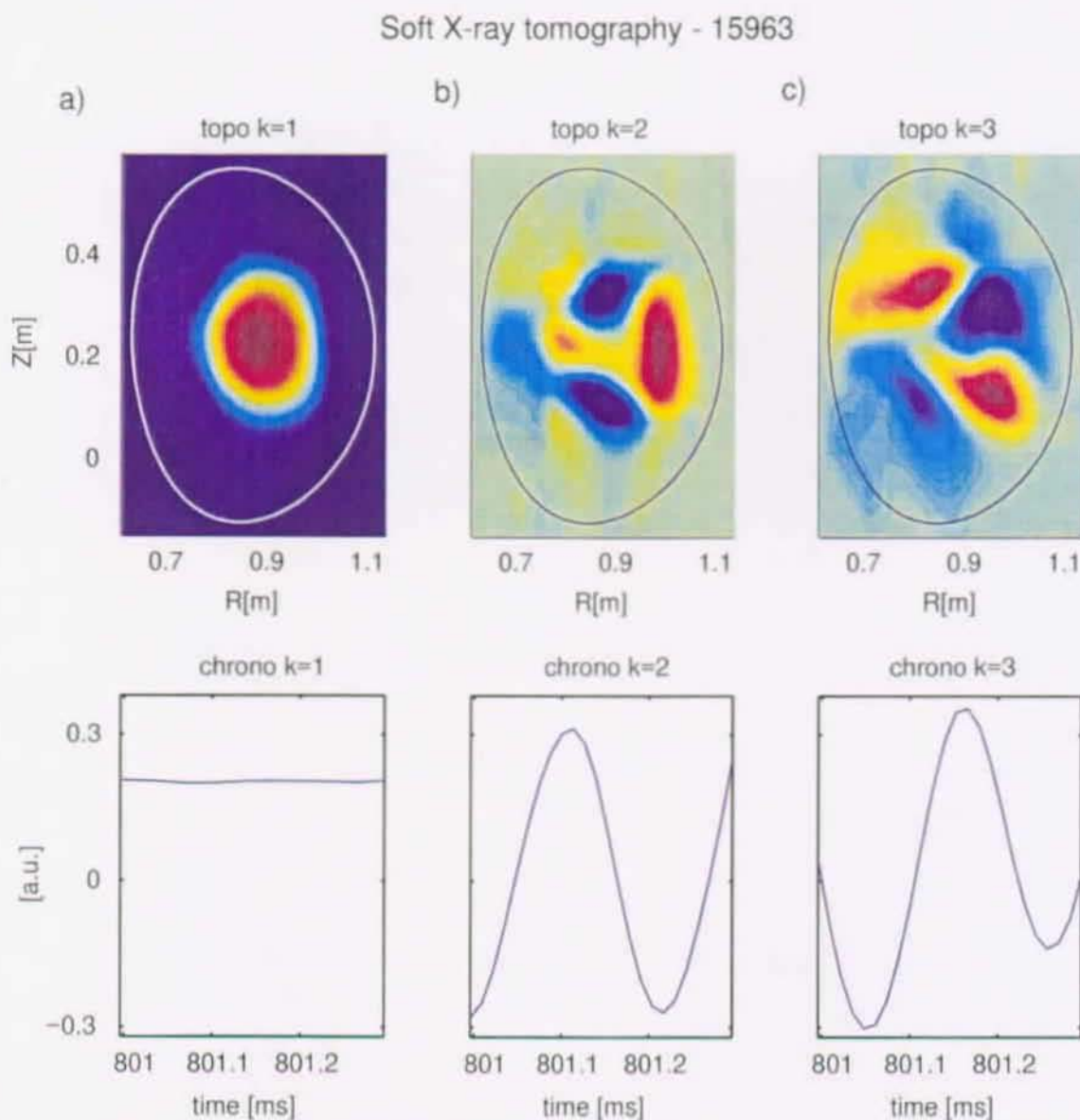


Figure 9.4: Bi-orthogonal decomposition of the reconstructed soft X-ray emissivity of discharge #15963 at $t = 0.8$ s. The principal eigenvector (a) contains the average profile. The second and third eigenvectors (b,c) have degenerated eigenvalues and show a rotating $m = 2$ mode. The corresponding chronos reveal a rotation frequency of about 5 kHz.

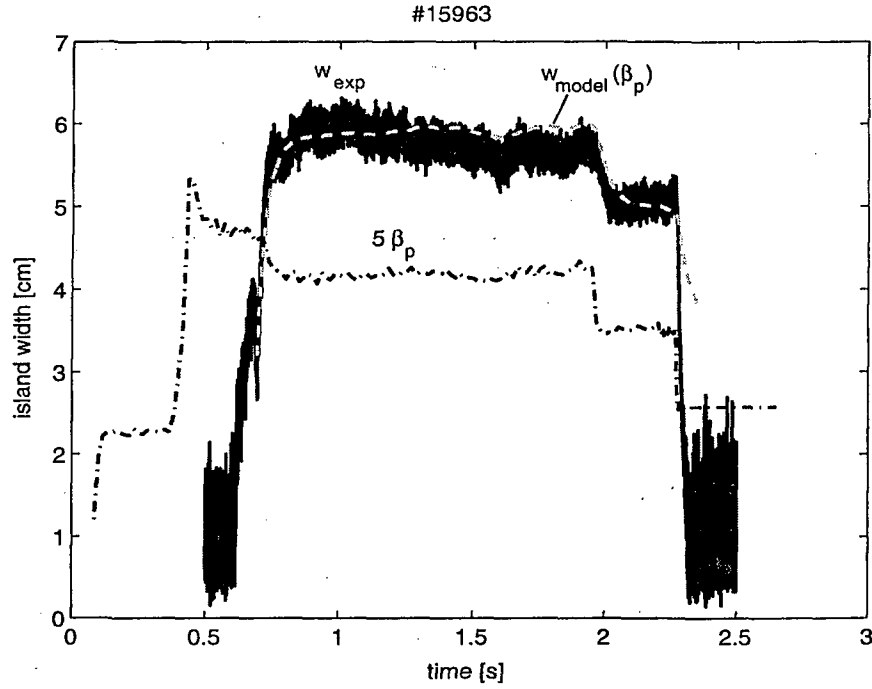


Figure 9.5: The neoclassical evolution of the island width w_{model} , modelled according to equation 9.3 using constant coefficients and the experimental value of β_p , is in good agreement with the experimental island width w_{exp} , derived from magnetic measurements. Stabilising effects for a small island width are neglected ($a_{\text{pol}}, w_d = 0$).

9.2.2 Identification as a neoclassical tearing mode

In order to identify the driving term of the mode, the evolution of w is tested against an island evolution described by the modified Rutherford equation (equation 9.3).

The island width is calculated from the magnetic perturbation field measured at the plasma edge, using the cylindrical constant flux approximation described in section 5.4.1 and given by equation 5.53. The calculated island width, shown in figure 9.5, indicates that the mode saturates at $w \approx 5.8$ cm. Taking into account the full geometry results in a smaller island width of 20% of the minor radius (figure 9.3(b)) which corresponds to 4.9 cm on the equatorial midplane. An independent estimate of w is obtained from the confinement degradation (see section 5.4.3). The energy drop is obtained from the equilibrium reconstruction and results in an island width of 4.5 cm, which is $\sim 20\%$ smaller than the value determined according to equation 5.53 and $\sim 10\%$ smaller than the reconstructed island using the full geometry. This comparison confirms that the cylindrical approximation systematically overestimates w by 10–20%.

The comparison between the experimental island evolution and an evolution according to the Rutherford equation is shown in figure 9.5. Starting with the rapid growth at $t = 0.69$ s, which already corresponds to $w = 3$ cm, the evolution of the experimental

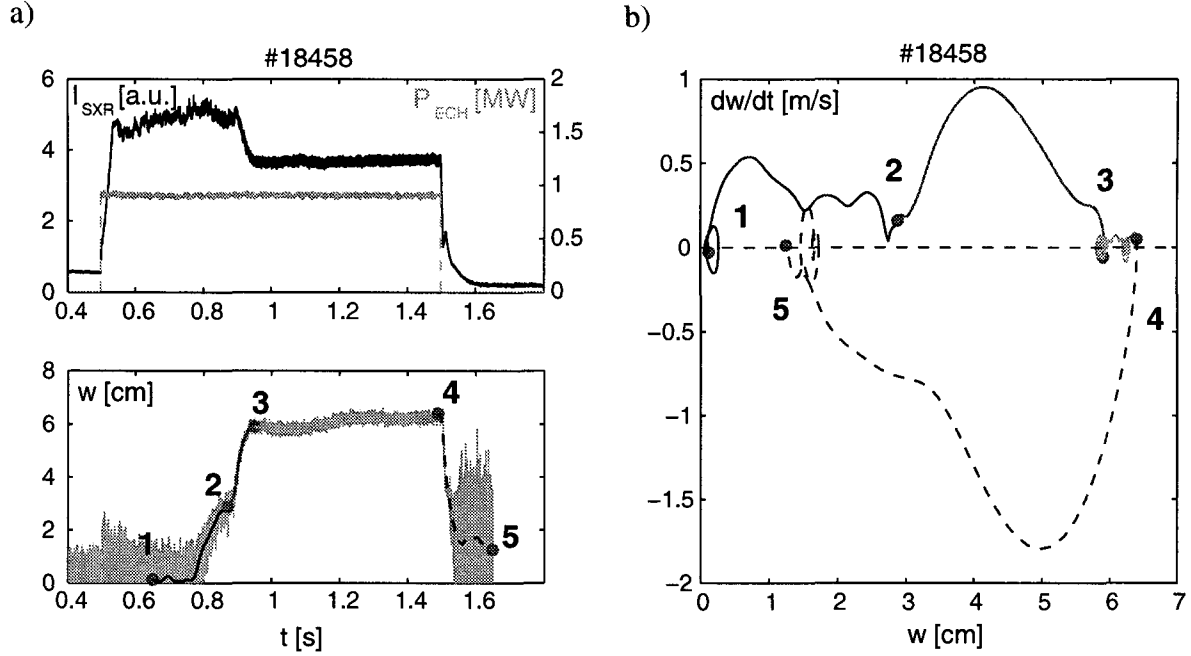


Figure 9.6: The NTM is triggered by a conventional mode which grows on a slow time scale and approaches saturation (2: $t \sim 0.87$ s). Once the critical island width is attained the mode grows on a faster time scale to its full width. After the ECH is switched off (4: $t \sim 1.49$ s) the island width drops quickly (dashed line).

island width agrees well with the prediction. Since the stabilising effects of perpendicular transport and polarisation currents decrease rapidly with increasing w , the parameters w_d and a_{pol} were set to zero. Furthermore, Δ' was assumed to be stabilising ($\Delta' < 0$). Since the classical ($\propto \Delta'$), and the neoclassical ($\propto a_{\text{bs}}$) driving term differ in their β_p and w dependence, the observed mode clearly shows the characteristics of a neoclassical mode. The rapid change of the saturated island width after the switch-off of one gyrotron at $t = 1.95$ s is also characteristic, since β_p changes on a confinement time scale ($\tau_E \sim 5$ ms) whereas Δ' changes on a longer current diffusion time scale ($\tau_{\text{res}} \sim 100$ ms). Nevertheless, the simplifying assumptions did not allow a satisfying description of the island evolution for the small values of w . The evolution for small w , in particular the seeding process, is analysed in detail below.

9.3 Seeding by conventional tearing modes

In TCV, neoclassical modes are observed in L-mode and consequently, ELM-free discharges. The plasmas usually show no or only small sawteeth and they are also stable with respect to the fishbone instability and none of the common trigger mechanisms, described in section 9.1.3, apply.

The onset of neoclassical tearing modes in TCV is investigated in detail by analysing

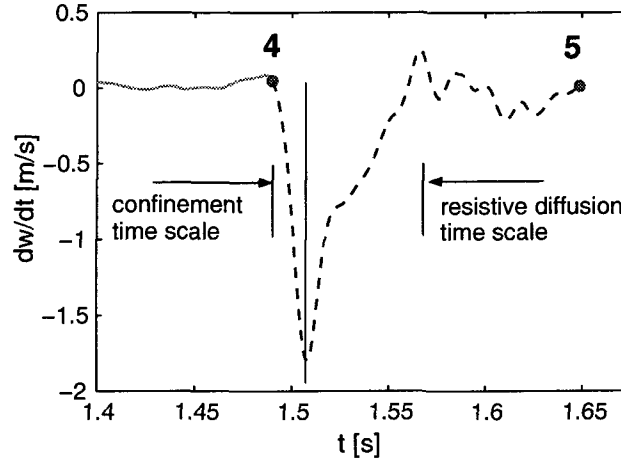


Figure 9.7: At the switch-off of the ECH power in the discharge shown in figure 9.6 the neoclassical driving term decays on a fast confinement time scale ($\tau_E \sim 5$ ms), whereas the conventional tearing mode stability changes on a slower current diffusion time scale ($\tau_{\text{res}} \sim 100$ ms).

the evolution of the island width of the $m/n = 2/1$ NTM seen in #18458 (figure 9.6(a)). The measured growth of the island, shown as a function of the island width in figure 9.6(b), clearly reveals two distinct growth phases. The faster growth at larger mode amplitude corresponds to the neoclassical island evolution previously modelled for #15963 before (see figure 9.5). The critical island width is approximately 2.8 cm. It is suggested that a conventional tearing mode provides the seed island. The 2/1 mode structure of the magnetic perturbation measurements does not show any significant differences between the two growth phases. The initial growth of 0.4 m/s, which corresponds to $r_s \Delta' = 0.4$, decreases as the conventional driving term decreases with w (equation 2.71),

$$\Delta'(w) = \Delta'(0) - \alpha w. \quad (9.8)$$

The effect of Δ' is also visible at the switch-off of ECH (figure 9.7), when dw/dt drops with β on an energy confinement time scale ($\tau_E \sim 5$ ms) to the value determined by Δ' . At such large values of w , Δ' is strongly stabilising, but slowly increases with decreasing w on a current diffusion time scale, $\tau_{\text{res}} \sim 100$ ms. At $t = 1.6$ s it is close to its value prior to the onset of the mode.

In order to demonstrate that the observed growth can be qualitatively described with a conventional tearing mode being the trigger for a neoclassical tearing mode the right-hand-side of the modified Rutherford equation (equation 9.3) has been modelled to reproduce the distinctive features of figure 9.6(b). The w dependence of the conventional tearing stability is assumed to be linear according to equation 9.8. The threshold island width w_d , in addition to the polarisation term, have been taken into account. The polarisation

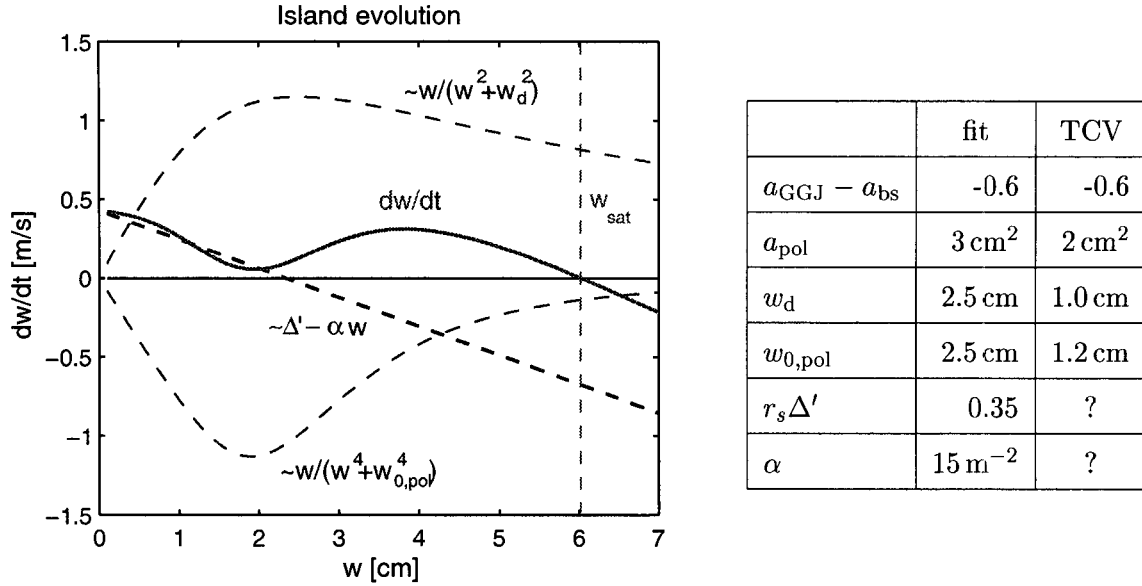


Figure 9.8: The modified Rutherford equation can describe the island width evolution observed in TCV. The coefficients of the four terms on the r.h.s. of equation 9.3 assuming the same w dependence for bootstrap drive and GGJ-stabilisation (dashed) are fitted to reproduce figure 9.6(b) (full). The fitted parameters are similar to the values derived from the measured TCV profiles [82].

term is taken to be stabilising and a threshold width,

$$w_{0,\text{pol}} \approx \sqrt{\epsilon} \rho_p \quad (9.9)$$

is introduced solely to mark the limit of validity of the ion polarisation model, once the island becomes smaller than the ion banana width $w_b = \sqrt{\epsilon} \rho_p$. The result shown in figure 9.8 do indeed reproduce the features of the observed island growth in figure 9.6. The fitted coefficients used in figure 9.8 are compared to the expected value according to the expressions given in [82] using experimental profiles and show good agreement. Only the fitted values for the threshold island width w_{d} and $w_{0,\text{pol}}$ exceed the predicted values by a factor of two. The tearing parameter $r_s \Delta'$, could not be determined as the current profiles of these discharges were not reconstructed with the required precision.

The triggering by a conventional tearing mode explains the peculiar conditions under which NTMs were observed in TCV. Since the discharges have also to be unstable with respect to classical tearing, NTMs are only triggered in discharges where on-axis current drive generates peaked current profiles. A sawtooth induced seed island such as have been observed on other experiments seems unlikely in TCV. The perturbation on the $q = 2$ surface triggered by a sawtooth *gong* [95] would have to exceed the observed w_{crit} , which corresponds to approximately 10% of the minor radius.

9.4 Onset of neoclassical tearing modes in TCV

9.4.1 Discharge parameters and profiles

Neoclassical modes have been observed in plasmas which were heated with 0.8 to 2.8 MW of central ECH and which always included on-axis co-current drive. The central electron density at the onset of the mode ranges from 1.2 to $3.0 \cdot 10^{19} \text{ m}^{-3}$ and is limited by runaway-electrons at low densities and by refraction of the microwave beam at high densities. At the onset of the NTM the electron collisionality normalised to the banana bounce frequency $\nu_{e*} = \nu_e/\omega_b$, is low ranging from 0.01 to 0.06. Since the ECH heating only heats the electrons, the ion temperature remains low. Consequently, the ion collisionality normalised to the electron diamagnetic drift frequency $\nu_* = \nu_i/m\epsilon\omega_{e*}$, which is important for the ion polarisation current (equation 9.6), is high with values typically ranging from 0.1 to 0.5. The poloidal Larmor radius, $\rho_p = 2.6 \text{ cm}$, stays approximately constant. The normalised beta β_N , ranges from 0.4 to 1.0. These values of β_N are well below the values observed in other experiments [82]. However, the strongly localised power deposition of ECH has been seen to generate large pressure gradients. Electron temperature and density measurements by Thomson scattering are shown in figure 9.9(a) and (b), respectively. These pressure gradients can locally generate large bootstrap currents. If the resonant surface is located within this high gradient region, the bootstrap fraction can be sufficient to destabilise a neoclassical island. A broadening of the deposition profile resulted in the avoidance of NTMs and allowed experiments where the plasma current was completely wave-driven [96].

9.4.2 Critical island width

The seed island has to exceed a critical width to trigger the neoclassical tearing mode. Otherwise, the discharge stays meta-stable to NTMs. This is demonstrated in two similar discharges, with the plasma parameters, $I_P = 300 \text{ kA}$, $n_e = 1.3 \cdot 10^{19} \text{ m}^{-3}$, $\kappa = 1.5$, $\delta = 0.08$ being virtually identically. Both discharges were heated with $P_{ECH} = 910 \text{ kW}$. In discharge #18458, shown in figure 9.10(a), a 2/1 island starts to grow at $t = 0.78 \text{ s}$ and approaches saturation. It exceeds a critical width, $w_{crit} = 3.1 \text{ cm}$ just prior to saturation and quickly grows further to its full neoclassical saturated width. In the discharge #18853, shown in figure 9.10(b), the 2/1 island develops at $t = 1.67 \text{ s}$ but saturates well below the critical island width observed in #18458 and consequently, no neoclassical growth is observed.

The slowly growing conventional seed island allows an accurate measure of w_{crit} , where the main uncertainties, arising from the cylindrical approximation and the equilibrium reconstruction, are expected to be systematic. For most of the discharges w_{crit} ranged from 2.8 to 4 cm with a trend to increase with increasing density, shown in figure 9.11.

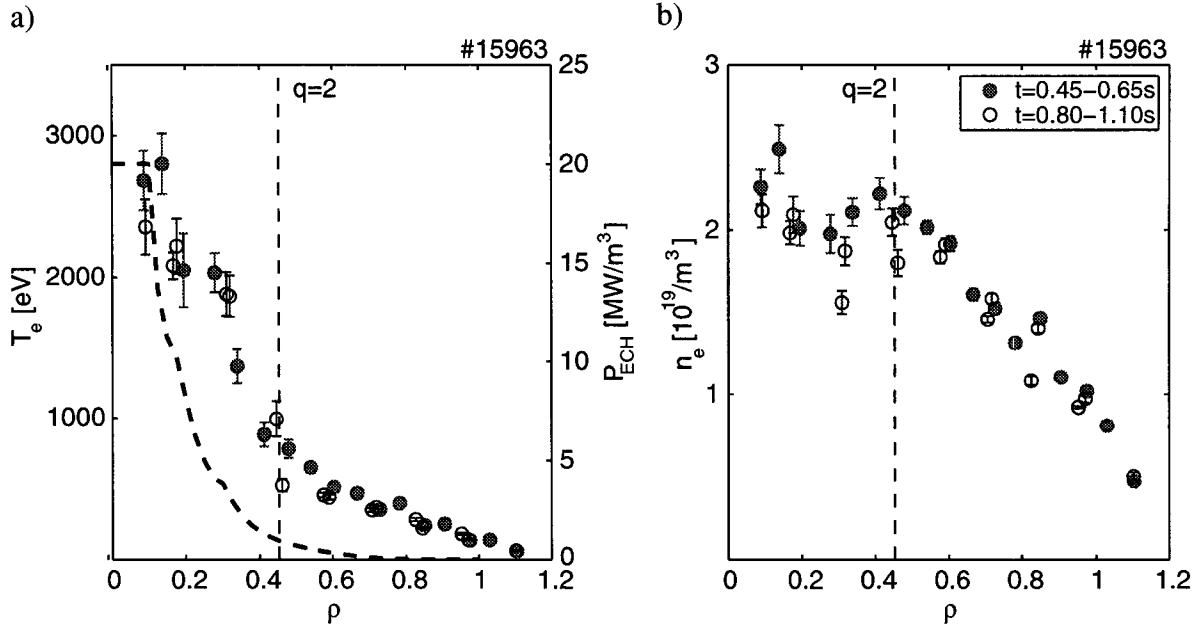


Figure 9.9: Electron temperature (a) and density (b) measurements taken with the Thomson scattering diagnostic prior to the onset (filled) and during (open) a neoclassical tearing mode. The measurements are averaged over a stationary interval with 13 and 19 time points, respectively. The ECH power deposition profile determined by the ray tracing code TORAY and the position of the $q = 2$ resonant surface are indicated (dashed).

A much smaller critical island width was only observed for the discharges at the lowest densities. All these discharges had a similar ion Larmor radius. Neither is there any evidence for a correlation between the normalised beta at the onset of the mode and w_{crit} .

The observed density dependence of the critical island width is compared to the predictions of the finite heat transport and of the polarisation current model. If one assumes that solely the incomplete flattening of the pressure profile across the island gives rise to a threshold island width, equation 9.3 yields,

$$w_{crit,\chi_{\perp}} \approx \frac{-r_s \Delta'}{a_{bs} - a_{GGJ}} w_d^2 \quad (9.10)$$

where w_{crit} was assumed to be small compared to the saturated island width, w_{sat} (equation 9.7). While the bootstrap term a_{bs} decreases with increasing collisionality and hence, density, w_d (equation 9.4) is expected to increase with density. Therefore, the finite heat transport model predicts a continuous increase of w_{crit} with density, which is clearly consistent with the experiment. Similarly, neglecting the incomplete flattening of the pressure profile and assuming only the polarisation current effect to be important, results in a threshold island width,

$$w_{crit,pol} \propto \sqrt{g} \rho_p. \quad (9.11)$$

Here, the collisionality term g (equation 9.6) contains the density dependence, when

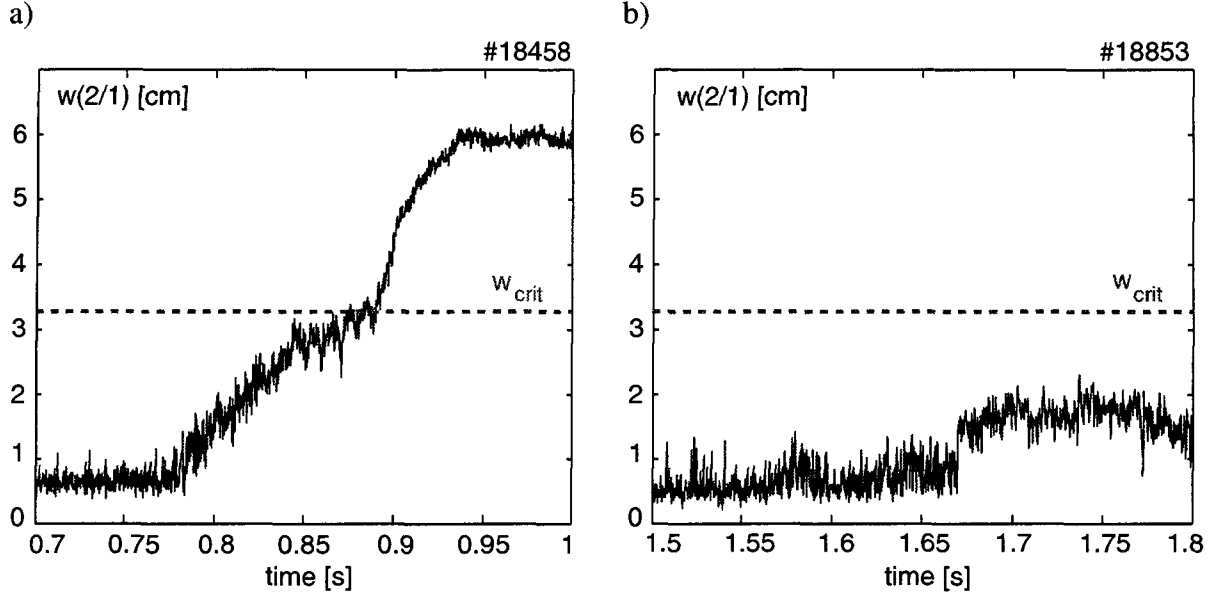


Figure 9.10: Two discharges with nearly identical plasma parameters ($I_P = 300$ kA, $n_e = 1.3 \cdot 10^{19} \text{ m}^{-3}$, $\kappa = 1.5$, $\delta = 0.08$) show the onset of a 2/1 mode whose structure and size are determined by magnetic measurements. For the discharge #18458 (a) the initial island size is large enough to trigger the neoclassical growth, while the mode in #18853 saturates below the critical island width, w_{crit} .

passing from the collisionless regime at low density to the collisional regime at high density. Since this transition, predicted for $\nu_* \approx 0.3$, is expected to occur in the range of $\nu_* = 0.1 - 0.5$, spanned by the TCV experiments, the polarisation current also predicts an increase of w_{crit} with density.

The experimental observations are, therefore, found to be consistent with both models. A discrimination between the two models is, however, difficult, in particular since a possible density dependence of the tearing parameter Δ' could also influence the dependencies of the critical island width.

9.5 Concluding remarks

In TCV, neoclassical $m/n = 2/1$ tearing modes have been identified in low density discharges with central co-ECCD. The plasmas are characterised by a low electron collisionality ν_{e*} , and a medium ion collisionality ν_* , a medium value of beta and particularly peaked pressure and current profiles. The 2/1 mode structure, a large saturated island width corresponding to approximately 20% of the minor radius, and an onset at relatively low values of $\beta_N \approx 0.5$ are similar to the observations in other dominantly electron heated tokamaks, such as COMPASS-D [94] and T-10 [93]. While the onset of NTMs in COMPASS-D was observed at lower density ($\bar{n}_e \sim 5 - 10 \cdot 10^{18} \text{ m}^{-3}$) and lower edge safety

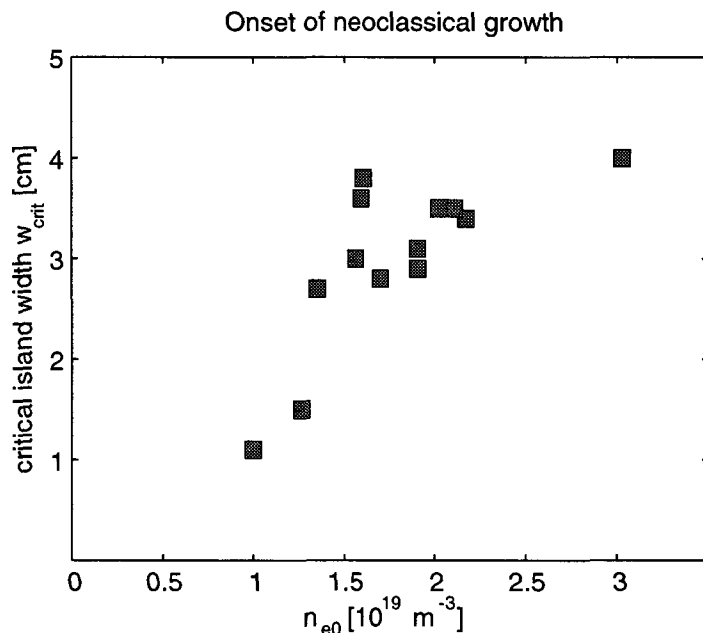


Figure 9.11: Island width at onset of neoclassical growth w_{crit} , determined from magnetic measurements as a function of central density n_{e0} .

factor ($q_a \sim 3 - 4$), the values of β_N and ν_e at the onset of the mode in T-10 were in the same range of the values observed in TCV.

In contrast to other tokamak experiments, where sawteeth, fishbones or ELMs generate the seed island, the trigger in TCV has been identified as a conventional tearing mode. The island clearly shows a conventional and a neoclassical growth phase. These two phases can be distinguished since the saturated width of the conventional island is slightly larger than the critical island width. The TCV results provide the first observations of such a trigger mechanism which could also explain the occurrence of “triggerless” NTMs observed in other experiments.

The slowly growing seed island of such a trigger has allowed for a measurement of the critical island width w_{crit} , which is observed to increase with increasing density. While w_{crit} varies by a factor of four, the poloidal Larmor radius remains constant and no correlation with β_N can be established. This density dependence is consistent with both, the finite heat transport and the polarisation current model for island stability at small island width.

The TCV results show the need to reconcile conventional and neoclassical tearing theory in order to describe the experiments. Means to control the current profile and consequently, the free energy available for the formation of magnetic island, can offer schemes to prevent or, once established, stabilise NTMs. For instance, the stabilisation of NTMs by current profile modification using lower hybrid current drive (LHCD) was successfully demonstrated on COMPASS-D [97]. In these experiments, only modest LHCD power,

corresponding to 10% of the total heating power, was necessary to modify the current profile in the vicinity of the resonant surface of a 2/1 NTM and completely stabilise the mode.

Chapter 10

Conclusion and outlook

The analysis of the magnetohydrodynamic stability of hot deuterium plasmas in the TCV tokamak has revealed new features of several instabilities which are all relevant for the operation of a future fusion reactor, such as ITER, and thereby, of great interest for the community of experimental and theoretical nuclear fusion physicists.

This analysis was made possible using the unique shaping capability of TCV. This capability has allowed the exploration of extreme parameter ranges, in particular high elongation, but was also used as a tool to probe the behaviour of MHD instabilities which can strongly depend on the shape of the poloidal plasma cross section. Similarly, the powerful electron cyclotron heating and current drive system allowed for the attainment of high electron temperatures and pressures in a collisionless regime, but was also used to test the response of instabilities to an increased local heating power density. The presented analysis required a highly resolved monitoring of instabilities. Magnetic fluctuation measurements using a spatially dense set of absolutely calibrated magnetic pick-up coils installed inside the vacuum vessel, were complemented by the tomographic reconstruction of the soft X-ray emission which mainly originates from the central plasma region. For an interpretation of the magnetic fluctuation measurements, several numerical methods to extract the structure and temporal evolution of coherent modes, have been implemented. In particular, the bi-orthogonal decomposition of the complete set of magnetic measurements, comprising poloidal and toroidal arrays, has proven to be an efficient technique for extracting the full mode structure. The identification of a measured poloidal mode structure was found to be complicated by the variable plasma shape and the large distance between a number of the probes and the plasma. This difficulty has been overcome by modelling the probe response to magnetic islands taking into account the exact toroidal geometry of the magnetic field and eddy currents in the vessel wall, which allows an identification of the poloidal mode numbers.

In the future, the diagnostic capabilities of detecting and analysing MHD instabilities will be improved by a recently installed electron cyclotron emission diagnostic provid-

ing local temperature measurements. These internal and local measurements provide additional information about the location and radial structure of the instabilities. A correlation analysis between local temperature and magnetic fluctuation measurements will allow for a direct distinction between magnetic islands and kink-type instabilities.

Sawteeth

The first instability considered was the sawtooth crash, where systematic shape scans revealed a strong dependence of the sawtooth behaviour on the plasma shape. In addition to this dependence of the sawtooth period and amplitude on the plasma shape, a further dependence on central heating power density was demonstrated. This heating power dependence was again observed to depend on shape. The complex sawtooth behaviour in TCV can be interpreted in the frame of an existing model for the sawtooth trigger which was developed in order to predict the sawtooth behaviour in ITER [53]. The interpretation of the TCV observations admits ideal or resistive MHD as being important for triggering a sawtooth depending on the plasma shape. Such a transition between sawtooth regimes has been confirmed by ideal MHD stability calculations predicting a particularly low central pressure limit for plasma shapes when the ideal trigger was deemed important. The TCV experiments, thereby, have confirmed the relevance of ideal and resistive MHD for the sawtooth stability and underline the importance of an accurate description of the shape dependence. In particular, a lowering of the central pressure limit at high elongation leads, in the absence of further stabilising effects, to smaller sawteeth and consequently, smaller cyclic heat pulses and a reduced probability of seed island generation for neoclassical tearing modes.

Nevertheless, an accurate description of the sawteeth has to take into account the evolution of the current profile which has been successfully performed for various Ohmic [54] and some ECH heated TCV plasmas [59], however, without leaving the resistive regime. When including the elongation and triangularity dependence of the ideal MHD stability limit [56], these transport simulations should confirm the presented results.

Edge localised modes

A second instability of interest were edge localised modes (ELMs), which are observed to be preceded by coherent magnetic oscillations. These precursors are detected prior to ELMs, believed to be type III ELMs, as well as TCV large ELMs. For both types of ELMs the precursors have similar characteristics which has allowed an identification of both types of ELMs, as type III ELMs. As a result, all TCV ELMs can now be classified in the usual scheme, consisting of only three classes, thereby, reducing the “zoology” of ELMs which exists at different machines.

The high spatial resolution of TCV’s toroidal array of magnetic pick-up coils has al-

lowed for the observation of a toroidal asymmetry in the ELM precursor oscillations, which is very unusual for conventional MHD modes in tokamaks. Such an asymmetry has yet to be reported from other machines. The random onset and its rotation in the electron diamagnetic drift direction indicate an intrinsic asymmetry causing and supporting the toroidal localisation of the ELM precursor. Surprisingly, the localised precursor has been observed to coincide with a central mode associated with the sawtooth pre- or postcursor, rather than a mode in the edge region of the plasma. A comparison of the phases has suggested a correlation with the maximum of the central mode preceding the toroidal location of the ELM precursor and therefore, a hitherto unobserved coupling between central modes and ELMs. Such a coupling could provide a new explanation for a correlation between sawteeth and ELMs, in particular an observed triggering of an ELM prior to a sawtooth crash.

Unfortunately, the correlation analysis was hampered by the slow sampling rate of the soft X-ray measurements. Since the system is now upgraded to acquire at 80 kHz, new measurements will avoid the uncertainty introduced by the phase shift of the anti-aliasing filter. This work should be also included in an ongoing statistical analysis about the correlation of sawteeth and ELMs [98].

Ideal beta limit at high elongation

The stability of highly elongated plasmas is of great interest at TCV, since it was especially designed to achieve high elongations and for a future fusion reactor, since high elongation promises a higher beta limit. For $\kappa > 2.3$ however, a new disruptive current limit was encountered well below the conventional current limit, which corresponds to $q_a > 2$. This limit, which is preceded by a kink-type mode, was found to be consistent with ideal MHD stability calculations. The TCV observations have, therefore, provided the first experimental confirmation of a deviation of the linear Troyon-scaling of the ideal beta limit with normalised current at high elongation, which had been predicted for over 10 years [76]. This deviation of the linear Troyon limit results in the existence of an optimum elongation and a corresponding normalised current which maximise the attainable beta. The TCV results have shown that this optimum elongation is in the range of $\kappa = 2 - 2.4$.

Several other MHD events were encountered during TCV's operation at high κ . Axisymmetric modes causing vertical displacement events impose a lower current limit which increases with elongation. This operational limit depends on the capability of the feedback control system and the growth rate of the mode. The experimentally found limit is in good agreement with predicted growth rates of the axisymmetric mode. Furthermore, bursts of tearing modes causing minor disruptions were frequently observed. The islands are located close to the $q = 1$ surface and resistive stability calculations suggest that they are destabilised by extremely flat central current profiles, typical of highly elongated

plasmas.

Further work in optimising the current and pressure profiles with respect to the axisymmetric mode and the ideal beta limit is ongoing and has already resulted in a record elongation $\kappa = 2.8$. Two means to modify the current profile are presently analysed. Fast current ramp-up scenarios [73] and electron cyclotron heating and current drive [99], both, are used to broaden the current profile and consequently, decrease the growth rate of the axisymmetric mode. These experiments will provide a further test of the underlying theory and help to improve the plasma control capabilities.

Neoclassical tearing modes

Finally, neoclassical tearing modes which are feared to limit the attainable pressure in a fusion reactor, were analysed in TCV. Neoclassical tearing modes have been identified in plasmas which were characterised by a low electron collisionality, a medium ion collisionality, a medium value of beta and strongly peaked pressure and current profiles. The conditions at the onset of the mode are therefore similar to the conditions of the onset of NTMs in other experiments with dominant electron heating. In contrast to other tokamak experiments, where sawteeth, fishbones or ELMs generate the seed island, the trigger in TCV has been identified as a conventional tearing mode. The TCV results provide the first clear observation of such a trigger mechanism which can also explain the occurrence of “triggerless” NTMs observed in other experiments. The triggering by a conventional tearing mode explains the peculiar conditions under which NTMs were observed in TCV, since the initial current profile must also be unstable with respect to conventional tearing. The critical island width is observed to increase with increasing density, which is consistent with both currently discussed models of stabilising effects at small island width.

The TCV results allow to reconcile conventional and neoclassical tearing theory in order to describe the experiments. Means to control the current profile and consequently, the free energy available for the formation of magnetic island, can offer schemes to prevent or, if established, stabilise NTMs. A further analysis should expand the scanned parameter space in order to discriminate between the two stabilisation models. The role of sawteeth in triggering NTMs should also be addressed since the localised ECH heating in TCV applied in the vicinity of the $q = 1$ surface provides a tool to alter the sawtooth behaviour and, therefore, the size of a potential trigger island.

All of the stability limits presented in this thesis have implications for the performance of a tokamak, in particular by limiting local or global pressure gradients. The observations validate theoretical predictions and the applicability of models which are used to predict the stability and performance of a fusion reactor. The TCV results have pointed out

the strong influence that plasma shaping can have on local and global stability limits, thereby, a potential, offering a route to optimise the efficiency of a reactor. Furthermore, the TCV results showed new possibilities of an interaction between instabilities, therefore demonstrating the great difficulties involved in a simple and separate description of MHD phenomena in fusion plasmas.

Bibliography

- [1] J. A. Wesson. *Tokamaks*. Clarendon Press, Oxford, 2 edition, 1997.
- [2] L. A. Artsimovich et al. Experiments in tokamak devices. In *3rd Int. Conf. on Plasma Phys. and Controlled Nucl. Fusion Research, Novosibirsk 1968*, volume 1, page 157, Vienna, 1969. International Atomic Energy Agency.
- [3] G. Bateman. *MHD Instabilities*. MIT Press, Cambridge, Massachusetts, 1978.
- [4] J. P. Freidberg. *Ideal Magnetohydrodynamics*. Plenum Press, New York, 1987.
- [5] R. B. White. *Theory of Tokamak Plasmas*. North-Holland Physics, Amsterdam, 1989.
- [6] F. Hofmann and G. Tonetti. Tokamak equilibrium reconstruction using Faraday rotation measurements. *Nucl. Fusion*, 28(10):1871, 1988.
- [7] H. Lütjens, A. Bondeson, and G. Vlad. Ideal MHD stability of internal kinks in circular and shaped tokamaks. *Nucl. Fusion*, 32(9):1625, 1992.
- [8] M.N. Bussac, R. Pellat, D. Edery, and J.L. Soulé. Internal kink modes in toroidal plasmas with circular cross sections. *Phys. Rev. Lett.*, 35(24):1638, 1975.
- [9] J. Manickam, N. Pomphrey, and A. M. M. Todd. Ideal MHD stability properties of pressure driven modes in low shear tokamaks. *Nucl. Fusion*, 27(9):1461, 1987.
- [10] V.D. Shafranov. *Sov. Phys. Tech. Phys.*, 15:175, 1970.
- [11] F. Troyon, R. Gruber, H. Saurenmann, S. Semenzato, and S. Succi. MHD-limits to plasma confinement. *Plasma Phys. Control. Fusion*, 26(1A):209, 1984.
- [12] P. H. Rutherford. Nonlinear growth of the tearing mode. *Phys. Fluids*, 16(11):1903, 1973.
- [13] R. B. White, D. A. Monticello, M. N. Rosenbluth, and B. V. Waddell. Saturation of the tearing mode. *Phys. Fluids*, 20(5):800, 1977.

- [14] A. H. Glasser, J. M. Greene, and J. L. Johnson. Resistive instabilities in general toroidal plasma configurations. *Phys. Fluids*, 18(7):875, 1975.
- [15] B. Coppi, R. Galvão, R. Pellat, M. Rosenbluth, and P. Rutherford. Resistive internal kink modes. *Sov. J. Plasma Phys.*, 2(6):533, 1976.
- [16] F. Hofmann, M. J. Dutch, A. Favre, Y. Martin, J.-M. Moret, and D. J. Ward. Feedback stabilization of axisymmetric modes in the TCV tokamak using active coils inside and outside the vacuum vessel. *Nucl. Fusion*, 38(3):399, 1998.
- [17] T. P. Goodman, S. Alberti, M. A. Henderson, A. Pochelon, and M.Q. Tran. Design and installation of the electron cyclotron wave system for the TCV tokamak. In C. Varandas and F. Serra, editors, *Proc. 19th Symp. on Fusion Technology (Lisbon, 1996)*, volume 1, page 565, Amsterdam, 1997. Elsevier Science B. V.
- [18] S. Barry. *The extension of the FIR interferometer of TCV to a polarimeter and measurements of the Faraday rotation caused by the poloidal magnetic field*. PhD thesis, National University of Ireland, Cork, 1999. published as Lausanne Report LRP 638/99.
- [19] R. Behn, S. Franke, Z. A. Pietrzyk, M. Anton, C. Nieswand, H. Weisen, and B. Marlétaz. The Thomson scattering diagnostic on TCV. In M. Muruoka, editor, *Proc. 7th Int. Symp. Laser Aided Plasma Diagnostics (Fukuoka, Japan 1995)*, page 392, 1995.
- [20] S. Franke. *Application of Thomson scattering at $1.06\ \mu\text{m}$ as a diagnostic for spatial profile measurements of electron temperature and density on the TCV tokamak*. PhD thesis No 1654, Ecole Polytechnique Fédérale de Lausanne, 1997. published as Lausanne Report LRP 576/97.
- [21] M. Anton, H. Weisen, et al. X-ray tomography on the TCV tokamak. *Plasma Phys. Control. Fusion*, 38(11):1849, 1996.
- [22] I. Furno, H. Weisen, J.-M. Moret, P. Blanchard, and M. Anton. X-ray measurements of MHD activity in shaped TCV plasmas. In M. Schittenhelm, R. Bartiromo, and F. Wagner, editors, *Proc. 24th EPS Conf. on Controlled Fusion and Plasma Physics (Berchtesgaden, 1997)*, volume 21A part II, page 545, Geneva, 1997. EPS.
- [23] I. H. Hutchinson. *Principles of Plasma Diagnostics*. Cambridge Univ. Press, Cambridge, 1987.
- [24] J.-M. Moret, F. Buhlmann, D. Fasel, F. Hofmann, and G. Tonetti. Magnetic measurements on the TCV tokamak. *Rev. Sci. Instrum.*, 69(6):2333, 1998.

- [25] J.-M. Moret. private communication.
- [26] G. Flor et al. MDS-Plus - A comprehensive data acquisition and analysis system. In B. E. Keem, R. Huguet, and R. Hemsworth, editors, *Proc. 16th Symp. on Fusion Technology (London, 1990)*, volume 2, page 1272, Amsterdam, 1991. Elsevier Science B. V.
- [27] H. Reimerdes, J.-M. Moret, A. Pochelon, O. Sauter, and L. Villard. Reconstruction of magnetic islands in the TCV tokamak from magnetic measurements at the plasma edge. In *VIe Congrès Plasmas de la SFP (Orléans, 1999)*, 1999. A75.
- [28] O. Klüber et al. MHD mode structure and propagation in the ASDEX tokamak. *Nucl. Fusion*, 31(5):907, 1991.
- [29] T. Dudok de Wit, A.-L. Pecquet, J.-C. Vallet, and R. Lima. The bi-orthogonal decomposition as a tool for investigating fluctuations in plasmas. *Phys. Plasmas*, 1(10):3288, 1994.
- [30] J. S. Kim, D. H. Edgell, J. M. Greene, E. J. Strait, and M. S. Chance. MHD mode identification of tokamak plasmas from Mirnov signals. *Plasma Phys. Control. Fusion*, 41:1399, 1999.
- [31] M. Schittenhelm, H. Zohm, and ASDEX Upgrade team. Analysis of coupled MHD modes with Mirnov probes in ASDEX Upgrade. *Nucl. Fusion*, 37(9):1255, 1997.
- [32] J.D. Jackson. *Classical Electrodynamics*. Wiley, New York, second edition, 1975.
- [33] W. H. Press, B. P. Flannery, S. A. Teukolsky, and Vetterling W. T. *Numerical Recipes*. Cambridge University Press, Cambridge, 1986.
- [34] J.D. Callen Z. Chang. Global energy confinement degradation due to macroscopic phenomena in tokamaks. *Nucl. Fusion*, 30(2):219, 1990.
- [35] S. Von Goeler, W. Stodiek, and N. Sauthoff. Studies of internal disruptions and $m=1$ oscillations in tokamak discharges with soft x-ray techniques. *Phys. Rev. Lett.*, 33:1201, 1974.
- [36] H. Reimerdes, A. Pochelon, O. Sauter, T. P. Goodman, M. A. Henderson, and An. Martynov. Effect of triangular and elongated plasma shape on the sawtooth stability. *Plasma Phys. Control. Fusion*, 42:629, 2000.
- [37] H. Reimerdes, T. Goodman, A. Pochelon, O. Sauter, M. A. Henderson, and An. Martynov. Shape dependence of the sawtooth instability and neoclassical tearing

- modes in TCV. In *42nd Annual Meeting of the APS Division of Plasma Physics (Quebec City, 2000)*, 2000. HP1.010.
- [38] Z.A. Pietrzyk et al. Central electron temperature enhancements due to sawtooth stabilisation during counter electron cyclotron current drive in Tokamak a Configuration Variable. *Phys. Plasmas*, 7(7):2909, 2000.
 - [39] H. Weisen, D. Pasini, A. Weller, and A.D. Edwards. Measurement of light impurity densities and Z_{eff} in JET using X-ray tomography. *Rev. Sci. Instrum.*, 62(6):1531, 1991.
 - [40] G. L. Jahns, M. Soler, B. V. Waddell, J. D. Callen, and H. R. Hicks. Internal disruptions in tokamaks. *Nucl. Fusion*, 18(5):609, 1978.
 - [41] H. Weisen et al. Effect of plasma shape on confinement and MHD behaviour in the TCV tokamak. *Nucl. Fusion*, 37(12):1741, 1997.
 - [42] EQUIPE TFR. Internal disruptions and current breakdown in TFR. In *6th Int. Conf. on Plasma Phys. and Controlled Nucl. Fusion Research, Berchtesgaden 1976*, volume 1, page 279, Vienna, 1976. International Atomic Energy Agency.
 - [43] D.J. Campbell, R.D. Gill, C.W. Gowers, J.A. Wesson, et al. Sawtooth activity in ohmically heated JET plasmas. *Nucl. Fusion*, 26(8):1085, 1986.
 - [44] D. Edery, G. Laval, R. Pellat, and J.L. Soulé. Current-driven internal kink modes in cylindrical and helicoidal discharges. *Phys. Fluids*, 19(2):260, 1976.
 - [45] H. Weisen, R. Behn, J.-M. Moret, O. Sauter, and the TCV team. "Profile consistency" features in shaped sawtooth ohmic TCV plasmas. *Plasma Phys. Control. Fusion*, 40:1803, 1998.
 - [46] Z. A. Pietrzyk, A. Pochelon, et al. Behaviour of central plasma relaxation oscillations during localized electron cyclotron heating on the TCV tokamak. *Nucl. Fusion*, 39(5):587, 1999.
 - [47] A. Pochelon et al. Energy confinement and MHD activity in shaped TCV plasmas with localised electron cyclotron heating. *Yokohama Special Issue II (Nucl. Fusion)*, 39(11Y):1807, 1999. 17th IAEA Fusion Energy Conf. (Yokohama, 1998).
 - [48] F. Porcelli, C. Angioni, R. Behn, I. Furno, T. P. Goodman, M. A. Henderson, A. Pietrzyk, A. Pochelon, H. Reimerdes, E. Rossi, and O. Sauter. Model for hump-back relaxation oscillations. *Nucl. Fusion*, 40(10):1691, 2000.

- [49] A. Pochelon et al. Effect of localised electron cyclotron heating on energy confinement and MHD and TCV. In P. Pavlo, editor, *Proc. 25th EPS Conf. on Controlled Fusion and Plasma Physics (Prague, 1998)*, volume 22C, page 1170, Mulhouse, 1998. EPS.
- [50] G. Smith et al. In J. Lohr, editor, *Proc. 9th joint Workshop on Electron Cyclotron Emission and Electron Cyclotron Heating (Borrego Springs, 1995)*, page 651, Singapore, 1995. World Scientific.
- [51] J.-M. Moret et al. Influence of plasma shape on transport in the TCV tokamak. *Phys. Rev. Lett.*, 79(11):2057, 1997.
- [52] I. Furno et al. X-ray tomography of sawtooth activity during intense electron cyclotron heating experiments in TCV. In B. Schweer, G. Van Oost, and E. Vietzke, editors, *Proc. 26th EPS Conf. on Controlled Fusion and Plasma Physics (Maastricht, 1999)*, volume 23J, page 1069, Mulhouse, 1999. EPS.
- [53] F. Porcelli, D. Boucher, and M. Rosenbluth. Model for the sawtooth period and amplitude. *Plasma Phys. Control. Fusion*, 38:2163, 1996.
- [54] O. Sauter, C. Angioni, D. Boucher, I. Furno, A. Pochelon, and F. Porcelli. Sawtooth period simulations of TCV discharges. In J. W. Connor, E. Sindoni, and J. Vaclavik, editors, *"Theory of Fusion Plasmas", Proc. of joint Varenna-Lausanne Int. Workshop (Varenna, 1998)*, page 403, Bologna, 1998. Editrice Compositori.
- [55] C. Wahlberg. Analytical stability analysis for the ideal $m=n=1$ kink mode in a toroidal plasma with elliptic cross section. *Phys. Plasmas*, 5(5):1387, 1998.
- [56] An. Martynov and O. Sauter. Dependence of internal kink growth rate on tokamak plasma current and shape parameters. In J. W. Connor, O. Sauter, and E. Sindoni, editors, *"Theory of Fusion Plasmas", Proc. of joint Varenna-Lausanne Int. Workshop (Varenna, 2000)*, page 387, Bologna, 2000. Editrice Compositori.
- [57] An. Martynov. private communication.
- [58] L. Degtyarev, A. Martynov, S. Medvedev, F. Troyon, L. Villard, and R. Gruber. The KINX ideal mhd stability code for axisymmetric plasmas with separatrix. *Comput. Phys. Commun.*, 103(1):10, 1997.
- [59] C. Angioni, T. P. Goodman, A. Pietrzyk, and O. Sauter. Simulations of improved confinement discharges and sawtooth period with ECH and current drive in TCV. In J. W. Connor, O. Sauter, and E. Sindoni, editors, *"Theory of Fusion Plasmas", Proc. of joint Varenna-Lausanne Int. Workshop (Varenna, 2000)*, page 73, Bologna, 2000. Editrice Compositori.

- [60] H. Zohm. Edge Localized Modes (ELMs). *Plasma Phys. Control. Fusion*, 38:105, 1996.
- [61] W. Suttrop. The physics of large and small edge localized modes. *Plasma Phys. Control. Fusion*, 42:A1, 2000.
- [62] J. W. Connor. A review of models for ELMs. *Plasma Phys. Control. Fusion*, 40(2):191, 1998.
- [63] H. Reimerdes, A. Pochelon, W. Suttrop, Ph. Guittienne, and H. Weisen. Toroidally asymmetric ELM precursor oscillations in the TCV tokamak. In M. Schittenhelm, R. Bartiromo, and F. Wagner, editors, *Proc. 24th EPS Conf. on Controlled Fusion and Plasma Physics (Berchtesgaden, 1997)*, volume 21A part II, page 533, Geneva, 1997. EPS.
- [64] H. Reimerdes, A. Pochelon, and W. Suttrop. Toroidally asymmetric ELM precursors in TCV. *Nucl. Fusion*, 38(3):319, 1998.
- [65] E. J. Doyle et al. Modifications in turbulence and edge electric fields at the L-H transition in the DIII-D tokamak. *Phys. Fluids B*, 3(8):2300, 1991.
- [66] P. Gohil et al. Study of giant edge-localized modes in DIII-D and comparison with ballooning theory. *Phys. Rev. Lett.*, 61(14):1603, 1988.
- [67] H. R. Wilson et al. Ideal magnetohydrodynamic stability of the tokamak high-confinement mode edge region. *Phys. Plasmas*, 6(5):1925, 1999.
- [68] H. Weisen et al. Ohmic H-modes in the TCV tokamak. *Plasma Phys. Control. Fusion*, 38:1137, 1996.
- [69] R. J. Buttery et al. ELM related MHD activity on the COMPASS-D tokamak compared with ASDEX-Upgrade. In B. E. Keen, P. E. Stott, and J. Winter, editors, *Proc. 22th EPS Conference on Controlled Fusion and Plasma Physics (Bournemouth, 1995)*, volume 19C part III, Geneva, 1995. EPS.
- [70] T. Kass et al. Characteristics of type I and type III ELM precursors in ASDEX Upgrade. *Nucl. Fusion*, 38:111, 1998.
- [71] C. C. Hegna and J. D. Callen. Ideal ballooning stability near an equilibrium magnetic island. *Phys. Fluids B*, 4(10):3031, 1992.
- [72] R. Aymar. Outline of the new ITER design. *ITER EDA newsletter*, 9(10), 2000.

- [73] F. Hofmann et al. Stability and energy confinement of highly elongated plasmas in TCV. In *28th EPS Conf. on Controlled Fusion and Plasma Physics (Madeira, 2001)*, 2001. invited talk.
- [74] H. Reimerdes, L. Villard, F. Hofmann, O. Sauter, and A. Pochelon. MHD precursor to disruptions in highly elongated plasmas. In P. Pavlo, editor, *Proc. 25th EPS Conf. on Controlled Fusion and Plasma Physics (Prague, 1998)*, volume 22C, page 699, Mulhouse, 1998. EPS.
- [75] F. Hofmann, O. Sauter, H. Reimerdes, I. Furno, and A. Pochelon. Experimental and theoretical stability limits of highly elongated tokamak plasmas. *Phys. Rev. Lett.*, 81(14):2918, 1998.
- [76] A.D. Turnbull, A. Roy, O. Sauter, and F.S. Troyon. Current and beta limitations for the TCV tokamak. *Nucl. Fusion*, 28(8):1379, 1988.
- [77] ITER physics expert groups on confinement and transport and confinement modelling and database and ITER physics basis editors. Chapter 2: Plasma confinement and transport. *Nucl. Fusion*, 39(12):2175, 1999.
- [78] E. A. Lazarus. An optimization of beta in the DIII-D tokamak. *Phys. Fluids B*, 4(11):3644, 1992.
- [79] M. Chu and O. Sauter. private communication.
- [80] O. Sauter, F. Hofmann, H. Reimerdes, et al. Comparison of high current disruption limit in elongated plasmas with ideal and resistive MHD models. In A. Rogister, editor, "*Fusion theory*", *Proc. of the 7th European fusion theory conf. (Jülich, 1997)*, page 255. Forschungszentrum Jülich GmbH, 1998.
- [81] Z. Chang et al. Observation of nonlinear neoclassical pressure-gradient-driven tearing modes in TFTR. *Phys. Rev. Lett.*, 74(23):4663, 1995.
- [82] O. Sauter et al. Beta limits in long-pulse tokamak discharges. *Phys. Plasmas*, 4(5):1654, 1997.
- [83] H. Reimerdes, T. Goodman, A. Pochelon, and O. Sauter. Neoclassical tearing modes in TCV. In K. Szego, T. N. Todd, and S. Zoletnik, editors, *27th EPS Conf. on Controlled Fusion and Plasma Physics (Budapest, 2000)*, volume 24B, page 169, Mulhouse, 2000. EPS.
- [84] O. Sauter, C. Angioni, and Y. R. Lin-Liu. Neoclassical conductivity and bootstrap current formulas for general axisymmetric equilibria and arbitrary collisionality regime. *Phys. Plasmas*, 6(7):2834, 1999.

- [85] C. C. Hegna. The physics of neoclassical magnetohydrodynamic tearing modes. *Phys. Plasmas*, 5(5):1767, 1998.
- [86] R. Fitzpatrick and T. C. Hender. The interaction of resonant magnetic perturbations with rotating plasmas. *Phys. Fluids B*, 3(3):644, 1991.
- [87] H. R. Wilson, J. W. Connor, R. J. Hastie, and C. C. Hegna. Threshold for neoclassical magnetic islands in a low collision frequency tokamak. *Phys. Plasmas*, 3(1):248, 1996.
- [88] F. L. Waelbroeck and R. Fitzpatrick. Rotation and locking of magnetic islands. *Phys. Rev. Lett.*, 78:1703, 1997.
- [89] R. Fitzpatrick and F. L. Waelbroeck. Nonlinear dynamics of feedback modulated magnetic islands in toroidal plasmas. *Phys. Plasmas*, 7(12):4983, 2000.
- [90] A. Gude, S. Günter, S. Sesnic, and ASDEX Upgrade team. Seed island of neoclassical tearing modes at ASDEX Upgrade. *Nucl. Fusion*, 39(1):127, 1999.
- [91] R. Buttery et al. Onset and control of neo-classical tearing modes on JET. In B. Schweer, G. Van Oost, and E. Vietzke, editors, *Proc. 26th EPS Conf. on Controlled Fusion and Plasma Physics (Maastricht, 1999)*, volume 23J, page 121, Mulhouse, 1999. EPS.
- [92] R. J. La Haye et al. Practical beta limit in ITER shaped discharges in DIII-D and its increase by higher collisionality. In *Fusion energy 1996 (Proc. 16th Int. Conf. Montreal, 1996)*, volume 1, page 747, Vienna, 1997. International Atomic Energy Agency.
- [93] D. Kislov et al. Soft beta limits in T-10 tokamak. In K. Szego, T. N. Todd, and S. Zolotnik, editors, *27th EPS Conf. on Controlled Fusion and Plasma Physics (Budapest, 2000)*, volume 24B, page 584, Mulhouse, 2000. EPS.
- [94] D. A. Gates et al. Neoclassical islands on COMPASS-D. *Nucl. Fusion*, 37(11):1593, 1997.
- [95] P. A. Duperrex, A. Pochelon, A. W. Edwards, and J. A. Snipes. Global sawtooth instability measured by magnetic coils in the JET tokamak. *Nucl. Fusion*, 32(7):1161, 1992.
- [96] O. Sauter et al. Steady-state fully noninductive current driven by electron cyclotron waves in a magnetically confined plasma. *Phys. Rev. Lett.*, 84(15):3322, 2000.
- [97] C. D. Warrick et al. Complete stabilization of neoclassical tearing modes with lower hybrid current drive on COMPASS-D. *Phys. Rev. Lett.*, 85(3):574, 2000.

- [98] A. Degeling. private communication.
- [99] A. Pochelon et al. Plasma shape effects on sawtooth / internal kink stability and plasma shaping using EC wave current profile tailoring in TCV. In *Fusion energy 2000 (Proc. 18th Int. Conf. Sorrento, 2000)*, page EXP3/10, Vienna, 2000. International Atomic Energy Agency. to appear in Nucl. Fusion.

Acknowledgements

The final and maybe most important step of a thesis is reached when it comes to the acknowledgements. Although I am glad that it is over now, I have to say that the time was most of the times most enjoyable and it is my pleasure to thank the many people who contributed to the quality of the work and of my time at the EPFL.

This long list of people commences with Prof. F. Troyon, who, as the Director of the CRPP, gave me the opportunity to start a Ph.D. in Lausanne, and with Prof. M. Q. Tran, who succeeded Prof. F. Troyon after his retirement and continued to give me the same support.

I cannot stress enough my sincere gratitude to Dr. Antoine Pochelon who supervised my work. His advice and enthusiasm guided me through the thesis and boosted my motivation when it was in danger of decline. I have always appreciated the warm welcome I received anytime I called into his office with another question or idea. His vast experience has been invaluable to me.

I am also very grateful to Dr. Olivier Sauter from whom I have received a lot of support on the so-called “theory side”. Independent of the time of the day and his own work load, he never turned down a question and took the time to introduce me into the complexity of MHD theory, even though it occasionally required true multi-tasking on his part.

A big thank-you goes to Dr. Ferdinand Hofmann for all his help and support which ranged from designing discharges to scientific programs. I hope that he will excuse me for my constant nagging on the LIUQE code.

I also want to thank Dr. Jean-Marc Moret for all his help and support for the fast magnetic fluctuation diagnostic and, in particular, for his confidence in the calibration of the pick-up coils.

During this work I benefited from many discussions with colleagues. I appreciated, in particular, Dr. Tim Goodman’s interest in neoclassical tearing modes and Dr. Laurent Villard contribution to the work at high elongation carrying out many stability calculations. I am especially obliged to Dr. Wolfgang Suttrop (Max-Planck Institut für Plasmaphysik, Garching bei München) for his valuable collaboration on the analysis of ELM precursors during his 6 month visit at the CRPP.

This work would not have been possible without the help of the CRPP technical staff. Many people have helped me throughout the years and to all I am very grateful. In particular, the installation of new pick-up coils required a lot of extra effort. I would especially like to thank Jean-Michel Mayor and Erwin Bader for their help in designing and constructing the coils and Pascal Conti for installing them inside the TCV vessel. I also have

to point out Blaise Marletaz and Philippe Marmillod whose assistance has been essential for the calibration of the probes and the running of the magnetic fluctuation diagnostic.

After all I have to thank the whole TCV team for the great effort it takes to run the tokamak, to heat the plasma as well as diagnosing it. I know that much of this effort usually goes unaccounted for.

A big thank-you goes to the CRPP secretarial staff who has always been there when assistance was needed. I have to add a special "Merci" to Edith whose help often passed professional matters and I, here, promise to keep in touch.

This is also the place to include many thanks to Ivo Furno, who I shared the office with for the past five years. In addition to innumerable discussions about life, the universe and everything, I like to thank him for trying to fill me in into the subtleties of the Italian language which I resisted so successfully to learn, for convincing me of the greatness of Italian cuisine, and for letting my side of the office always look so much tidier. Among all the Ph.D. students, who form such a great team, I would also like to mention Clemente Angioni who I owe many thanks, not just for actually reading my sawtooth paper, but for sharing the joy and pain of thousands of kilometres on the bicycle.

After all I have to thank Siobhan for being much more supportive than she hoped to be when it was her turn two years ago. Without her, writing the thesis and the thesis itself would have certainly not been the same, just mind all these commas and paragraph-long sentences, only understood by non-anglophones.

The acknowledgements would not be complete without mentioning my parents who supported me throughout the countless years of school and university. I have always been very grateful for their encouragement, although it often meant to be far away from home. Vielen vielen Dank!

Curriculum vitae

I was born on the 4th of June 1969, in Hamburg, Germany. I attended both, primary and secondary schools in Celle. In 1986/87 I spent a year as an AFS exchange student in Tipton, Iowa, USA, where I obtained a highschool diploma. Back in Germany, I concluded my secondary education with an “Abitur” from the Kaiserin Auguste-Viktoria Gymnasium, Celle, in 1989. After my compulsory military service, I commenced my studies in physics at the Universität Bayreuth in 1990. During the 1993/94 academic year I spent two trimesters as an ERASMUS exchange student at the University of St Andrews, Scotland. After my return to Bayreuth I was given the possibility to carry out my diploma work at the Max-Planck-Institut für Plasmaphysik in Garching bei München, modelling transport processes in the ASDEX-Upgrade tokamak. In 1996, I received my degree as a “Diplom-Physiker” from the Universität Bayreuth. Since September 1996, I have been pursuing doctoral research at the Centre de Recherches en Physique des Plasmas in Lausanne. The subject of my research has been magnetic fluctuation measurements and the analysis of magnetohydrodynamic instabilities on the TCV tokamak.